ELECTRO-OPTICAL TECHNIQUES FOR

DIESEL ENGINE RESEARCH

ARNOLD ENGINEERING DEVELOPMENT CENTER
AIR FORCE SYSTEMS COMMAND
ARNOLD AIR FORCE STATION, TENNESSEE 37389

May 1977

Final Report for Period September 1971 — June 1975

Prepared for

U.S. ARMY TANK-AUTOMOTIVE RESEARCH AND DEVELOPMENT COMMAND
WARREN, MICHIGAN 48090

NOTICES

When U. S. Government drawings specifications, or other data are used for any purpose other than a definitely related Government procurement operation, the Government thereby incurs no responsibility nor any obligation whatsoever, and the fact that the Government may have formulated, furnished, or in any way supplied the said drawings, specifications, or other data, is not to be regarded by implication or otherwise, or in any manner licensing the holder or any other person or corporation, or conveying any rights or permission to manufacture, use, or sell any patented invention that may in any way be related thereto.

Qualified users may obtain copies of this report from the Defense Documentation Center.

References to named commercial products in this report are not to be considered in any sense as an endorsement of the product by the United States Air Force or the Government.
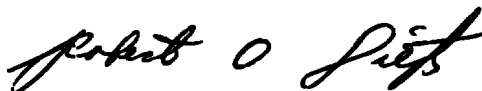
APPROVAL STATEMENT

This technical report has been reviewed and is approved for publication.

FOR THE COMMANDER

MARSHALL K. KINGERY
Research & Development
   Division
Directorate of Technology

ROBERT O. DIETZ
Director of Technology

REPORT DOCUMENTATION PAGE		·READ INSTRUCTIONS BEFORE COMPLETING FORM
1 REPORT NUMBER AEDC-TR-77-17	2 GOVT ACCESSION NO.	3 RECIPIENT'S CATALOG NUMBER
4 TITLE (and Subtitle) ELECTRO-OPTICAL TECHNIQUES FOR DIESEL ENGINE RESEARCH		5 TYPE OF REPORT & PERIOD COVERED Final Report – September 1971 – June 1975
		6 PERFORMING ORG. REPORT NUMBER
7 AUTHOR(s) A. E. Lennert, R. E. Sowls, R. A. Belz, W. H. Goethert, H. T. Bentley, H. M. Powell, A. B. Bailey, and T. D. McCay, ARO, Inc.		8. CONTRACT OR GRANT NUMBER(s)
9 PERFORMING ORGANIZATION NAME AND ADDRESS Arnold Engineering Development Center (DYR) Air Force Systems Command Arnold Air Force Station, Tennessee 37389		10. PROGRAM ELEMENT, PROJECT, TASK AREA & WORK UNIT NUMBERS Program Element 65807F
11 CONTROLLING OFFICE NAME AND ADDRESS Arnold Engineering Development Center (DYFS) Air Force Systems Command Arnold Air Force Station, Tennessee 37389		12. REPORT DATE May 1977
		13. NUMBER OF PAGES 161
14 MONITORING AGENCY NAME & ADDRESS(if different from Controlling Office) U. S. Army Tank-Automotive Research and Development Command Warren, Michigan 48090		15. SECURITY CLASS. (of this report) UNCLASSIFIED
		15a DECLASSIFICATION/DOWNGRADING SCHEDULE N/A

16. DISTRIBUTION STATEMENT (of this Report)

Approved for public release; distribution unlimited.

17. DISTRIBUTION STATEMENT (of the abstract entered in Block 20, if different from Report)

18 SUPPLEMENTARY NOTES

Available in DDC

19 KEY WORDS (Continue on reverse side if necessary and identify by block number)

electrooptics	Raman spectroscopy	mass spectrometry	internal combustion
lasers	infrared spectroscopy	combustion	engines
interferometry	mass spectroscopy	diagnostic equipment	particle sizing
holography	resonance absorption	diesel engines	laser anemometry

20 ABSTRACT (Continue on reverse side if necessary and identify by block number)

The results of research to determine the feasibility of applying electro-optical diagnostic techniques to the study of combustion phenomena in diesel engines is described and evaluated. The techniques that were investigated included: high-speed laser-augmented photography, holography, fringe techniques (laser anemometry and particle sizing), mass spectroscopy, and resonance absorption. A conventional Army TACOM diesel engine and a Turner engine were modified to acquire optical access by installing quartz

DD FORM 1473 EDITION OF 1 NOV 65 IS OBSOLETE
1 JAN 73

19. KEY WORDS (Continued)

high-speed photography

20. ABSTRACT (Continued)

windows in the combustion chamber. Droplet formation, breakup, combustion, and flow phenomena were observed in the combustion chamber in three dimensions using holographic techniques, whereas conventional high-speed photography provided only information in a plane. It was established that two-dimensional velocity measurements can readily be made in the combustion chamber but that additional development is required on the prototype particle-sizing instrument. The formation of certain hydrocarbons was observed in real time using resonance absorption techniques with a narrow-line, tunable helium-neon laser. Species determination, including total temperature, was realized with the application of mass spectroscopy.

AFSC
Arnold AFS Tenn

PREFACE

CONTENTS

ILLUSTRATIONS

5

TABLES

APPENDIX

1.0 INTRODUCTION

During the past decade, refinements in electro-optical instrumentation have proved to be an important source of diagnostic equipment for the study of physical and chemical processes. This advance in diagnostic instrumentation has been a direct result of the development of highly coherent, high-powered, monochromatic laser light sources. Techniques covering a wide range of applications have been developed for the observation and measurement of fluid and particle flow fields. Some of these techniques include the application of the laser as a high-energy, high-density light source for high-speed photography, laser velocity and particle-size measurements, holography, and laser spectroscopy.

To further the understanding of combustion phenomena, conventional instrumentation, such as temperature probes, pressure transducers, hot-wire anemometers, etc., has been augmented by laser instrumentation at the Arnold Engineering Development Center (AEDC). The research was originally concerned with the study of combustion phenomena in rockets and jet engines (Ref. 1). With the support of the Army Tank and Automotive Command (TACOM) the effort has been extended to include combustion diagnostics in diesel and other internal combustion engines with particular emphasis on applying these nonperturbing techniques for future engine development.

The TACOM instrumentation development program was subdivided into two major categories: interferometric and spectroscopic, as shown in Fig. 1. The interferometric
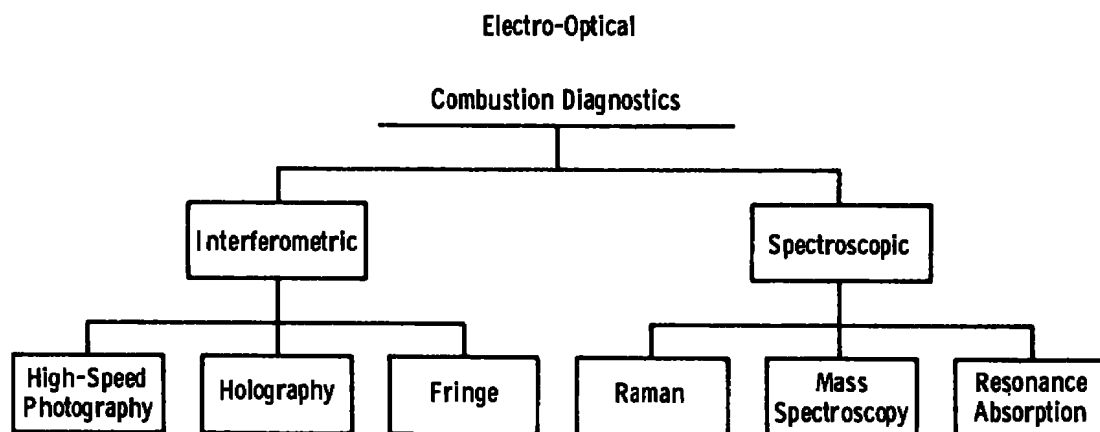
Electro-Optical

Figure 1. Electro-optical combustion diagnostic techniques.

techniques developed were (1) laser-augmented, high-speed photography to provide two-dimensional flow-visualization and particle-sizing measurements; (2) holographic techniques to provide three-dimensional flow-visualization and particle-sizing measurements; and (3) fringe techniques including laser velocimetry and particle-sizing measurements. The

development and application of spectroscopic techniques concerned the use of mass spectrometry and resonance absorption spectroscopy to provide a quantitative analysis of the constituents in incomplete combustion. Laser Raman spectroscopy has not as yet been attempted. Resonance absorption, because it provides in situ measurements and the mass spectrometry technique does not, appears feasible for use in studies of internal combustion.

In this report the work that has been completed will be summarized. The factors affecting the performance of the individual techniques, representative results, and recommendations for future developments are discussed. The theoretical basis necessary for quantitative evaluation of the molecular concentration of absorber gas is given in Appendix A.

2.0 DIESEL ENGINE MODIFICATIONS

A Turner diesel engine and a TACOM-LABECO diesel engine were both modified to obtain optical access to their combustion chambers for the study of combustion processes. Photography, holography, fringe techniques (laser velocimetry and interferometric particle sizing), and resonance absorption laser spectroscopy were then applied. Later, gas-sampling probes for mass spectrometry were installed in both engines. The Turner engine is a three-cylinder, two-stroke-cycle diesel engine with a 3.625-in. bore, a 3.500-in. stroke, and a total displacement of 108 in. Modifications to the Turner engine are described in Sections 5.0 and 8.0. The TACOM-LABECO research diesel engine is a single-cylinder, four-stroke-cycle engine with a 4.5-in. stroke, and a 71.5-in.^{3} displacement (Fig. 2). Descriptions of the modifications to this engine and their effect on its operation are given in the following subsections.

2.1 TACOM ENGINE COMBUSTION CHAMBER
VIEWPORT INSTALLATION

The difficulty of making a satisfactory viewport installation in an engine depends primarily upon constraints imposed by its geometry and by the requirement that the modification must not greatly disturb its operating characteristics. Viewport installations have been made for the combustion chambers of diesel engines (Refs. 2 through 6) and of stratified charge engines (Refs. 7 and 8) that were especially designed or modified for this purpose. Some engine geometries allow the utilization of a single viewport located in the top of the cylinder head (Refs. 5 and 6). Overhead valve engines (Refs. 2, 7, and 8) have been modified to utilize a single viewport located in the piston with optical access from below. After examining possible means of making viewport installations in the prechamber and in the direct-injected versions of the TACOM engine, it was concluded
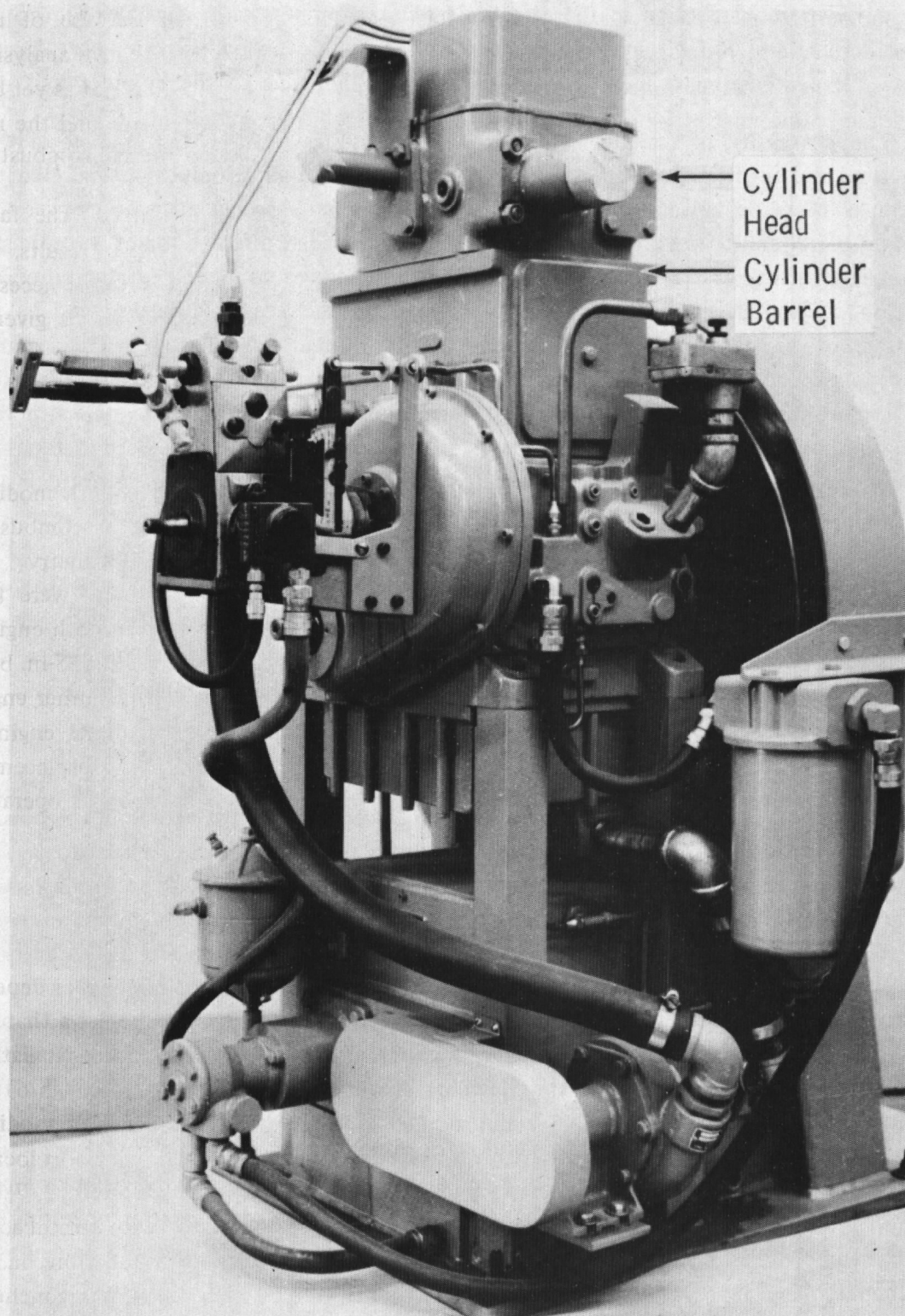
Figure 2. Photograph of TACOM engine.

that a viewport installation in the direct-injected version was more feasible. The Turner and other engines (Refs. 3 and 4) have been equipped with two opposed viewports looking across the combustion chamber in a direction perpendicular to the cylinder axis.

The possibility of installing viewports in the cylinder barrel itself was considered. Structural and functional requirements of the engine would allow only very small diameter viewports to be installed. The viewports were located in a spacer clamped between the cylinder barrel and the cylinder head. An extension threaded into the top of an unfinished piston was used to restore the standard combustion chamber volume. The orientation and location of the viewport openings were dictated by the headbolt pattern and by the locations of openings for the pushrods and for the oil and water passages. The thickness of the viewport spacer and the matching height of the piston extension were selected as a compromise between obtaining a large viewport aperture, supplying adequate structural strength around the window openings, maintaining a reasonably standard combustion chamber geometry, and not adding an excessive amount of reciprocating mass to the piston. A possible need to watercool the viewport spacer was considered. However, because of the design and fabrication difficulties involved, the viewport spacer was cooled by conduction to the cylinder head and the cylinder block. This has not caused any structural or operational problems to date. The special components required for the viewport installation include a viewport spacer, an extended piston, two special headbolts, four headbolt spacers, two longer pushrods, two window plugs, two window retainers, two window flanges, and a supply of fused quartz windows.

Figure 3 is a dimensioned drawing of one viewport spacer that was made. It shows how the headbolt pattern and the various pushrod, oil, and water passages limit the possible viewport locations. The viewport passage shown is parallel to the crankshaft axis and perpendicular to the cylinder axis. A second spacer was made with the viewing passage 0.500 in. to the left of that shown in Fig. 3 so that it passed through the extended axis of the combustion chamber bowl. Four 9.75-in.-long headbolts (LABECO Part No. 8523) with spacers and two special 11.00-in.-long headbolts made to the same specifications of strength and finish were used to clamp the viewport spacer between the cylinder head and the cylinder barrel. Satisfactory sealing was obtained with one head gasket (LABECO Part No. 8667) on each side of the viewport spacer.

In an attempt to provide larger window openings, a third viewport spacer was made. A deformable metal O-ring was used in place of the headgasket to seal the viewport spacer cylinder head interface. However, a tight seal was not achieved, and after operating the engine for a short period of time the viewport windows would become fouled with lubricating oil. With some additional work, this condition should be correctable.
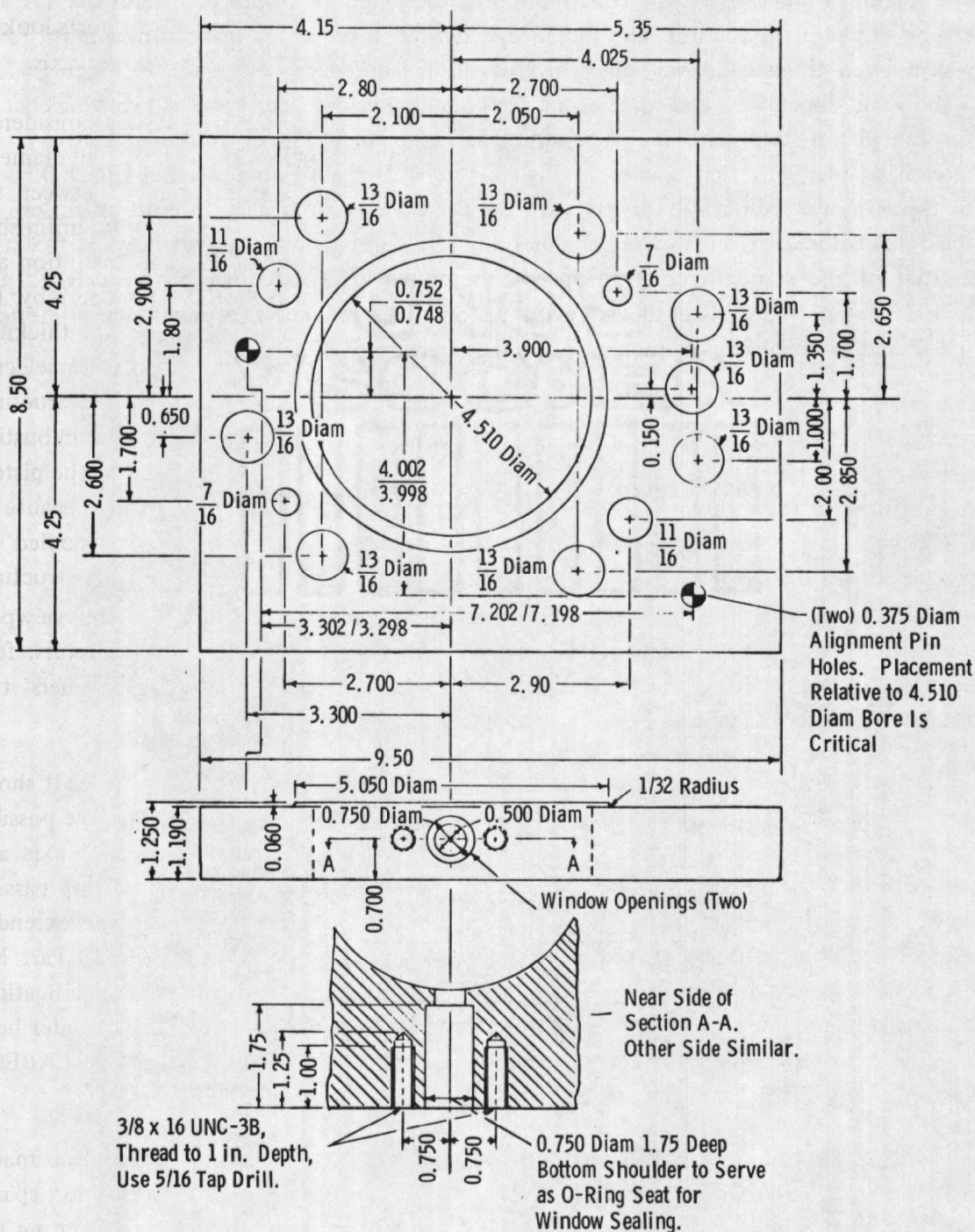
Figure 3. TACOM engine viewport spacer.

Figure 4 shows the basic construction of the extended piston used with the TACOM engine viewport installation. The threaded extension is prevented from turning in the lower piston by a threaded dowel pin which is itself secured by a set screw. Figures 4 and 5 show the dimensions and location of the combustion chamber bowl and viewing channel for the piston used with the viewport spacer shown in Fig. 3. A similar piston crown interchangable with that shown in Fig. 5, but with the viewing channel offset 0.55 in. to the left, was fabricated for use with the other viewport spacer. In both piston crowns the total volume of the viewing channel and the combustion chamber bowl is the same as that of the standard combustion chamber bowl. The extended piston weight 2.068 lb (938.4 gm) more than the standard piston. This reduces the maximum safe engine speed and is a source of engine test stand vibration.
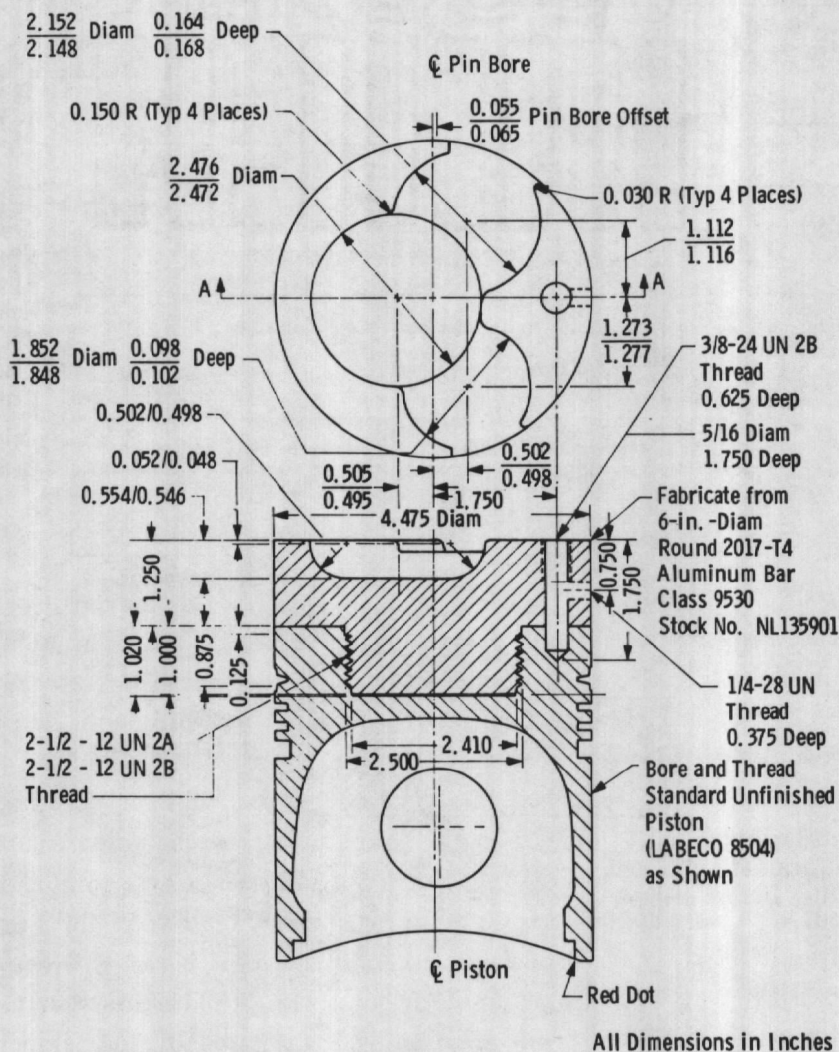
Figure 4. TACOM engine basic viewport piston.
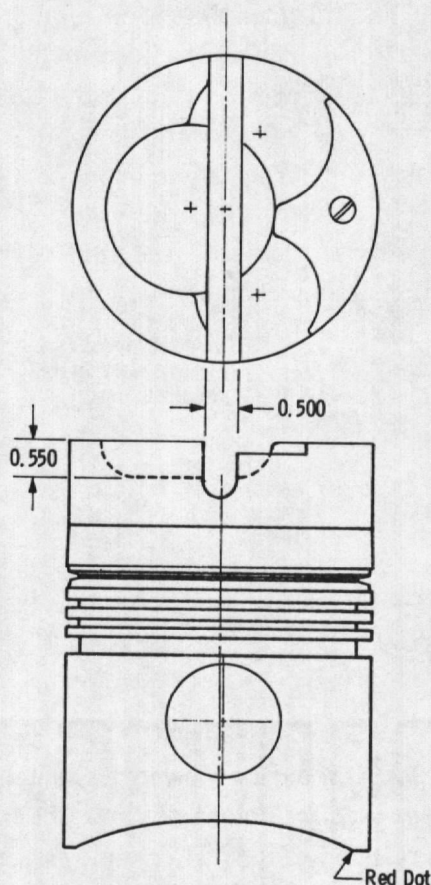
Figure 5. TACOM engine offset viewport piston.

Figure 6 shows most of the special small parts required for the viewport installation. The two special pushrods were made by cutting pushrods for an International Harvester DT 429 engine near the ball end, trimming the tubes to length and reaming them, and pressing in the extensions (shown in Fig. 6) to obtain a pushrod length of 14.39 in. The window flanges and window retainers shown in Fig. 6 are used to hold the fused quartz windows in place in the viewport spacer. It was later found that the bore of the window retainer could be increased to 19/32 in. without damage to the fused quartz windows. The window plugs shown in Fig. 6 are used when optical access to the combustion chamber is not required, such as when warming up the engine in preparation for a data run. The inside edge of each fused quartz window or each window plug is sealed with a 9/16-in.-ID by 3/4-in.-OD Buna N® 70 Durometer O-ring or a silicon 70 Durometer O-ring of the same size. Although these O-rings are eventually deteriorated by the temperatures they encounter, it is not necessary to replace them very often.

Viewport Window Flange
Material: Mild Steel
Required: Two

Viewport Window Retainer
Material: Mild Steel
Required: Two

Headbolt Spacers
Material: Mild Steel
Required: Two of Each Length

0.70

0.500 Diam Through

13/32 Diam Through

1.40

0.760 Diam, 0.060 Deep

0.70   0.750   0.750

0.75   1.25   1.25

2.50

1.250

0.500 ID

0.746 OD

$\frac{13}{16}$ ID

1-3/8 OD

1.63   Long Spacer

1.13   Short Spacer

Viewport Window Plug
Material: Mild Steel
Required: Two

Pushrod Extension
Material: Use Shank of an 8-30
          or Similar Bolt
Required: Two

0.500

0.330

30°

1/8   0.75   0.75

0.210

1.750   1-1/4

Drill 5/16 Diam, , 1-1/4 Deep
3/8 x 16 UNC 1.0 Deep

0.746 Diam

All Dimensions in Inches

Figure 6. TACOM engine viewport assembly small parts.

For best results windows used for holography must be free of voids, have very uniform optical density, and have very flat surfaces. The windows for the TACOM engine viewport installation were fabricated from disks of T15 Homosil obtained from Amersil Inc. The finished windows are 0.745 in. in diameter by 0.500 in. thick. To minimize chipping, the outside edge of each window has a 0.030-in.-wide bevel at 45 deg to the flat surface. To help maintain satisfactory contact with the O-ring the inside edge of each window has a 0.100-in.-wide bevel at 45 deg to the flat surface. Each side of each window is flat within 1/10 wave of green light, and the two sides are parallel within five seconds of arc. Although it would be advantageous in some ways, the windows are not antireflection (AR) coated since this would make them move susceptible to damage.

2.2 TACOM ENGINE COMBUSTION CHAMBER GAS-SAMPLING PROBE INSTALLATION

The modifications required to sample gas from the TACOM engine combustion chamber for analysis using mass spectrometry and Raman spectroscopy techniques are similar to those previously described. In fact, all the cylinder headbolts and headbolt spacers, the lengthened pushrods, one of the window flanges, and one of the window plugs are common to both the viewport installation and to the gas-sampling probe installation.

The gas-sampling probe was mounted in a spacer as shown in Fig. 7. The port at the right side of the spacer is used for evacuating the combustion chamber before each data run. Otherwise it is closed with one window plug and one window flange from the viewport installation. The gas-sampling probe is mounted in the port shown at the bottom edge of the figure. Sealing is handled using head gaskets and O-rings. Dimensions not included in Fig. 7 correspond to the dimensions shown in Fig. 3. The location of the gas-sampling probe was chosen to make the distance from its orifice, at the edge of the combustion chamber bowl, to the mass spectrometer apparatus in the vacuum chamber as short as possible.
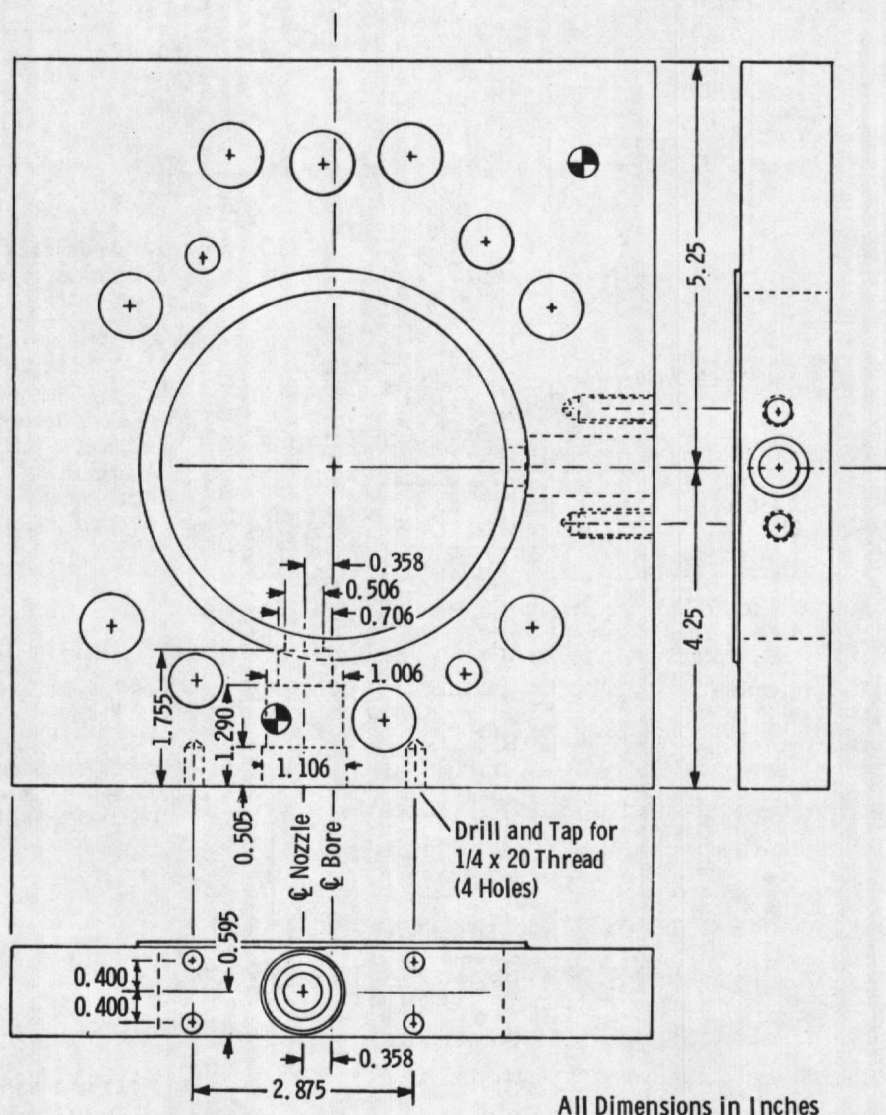
Figure 7. TACOM engine gas-sampling spacer.

Engine vibration is a more serious problem in the mass spectrometer work than in the optical experiments since it causes misalignment between the gas-sampling probe orifice and the mass spectrometer skimmer and ionizer. For this reason an effort was made to minimize the added reciprocating mass attributable to the engine modifications. Figure 8a shows the construction of the extended piston used for this installation. Figure 8b
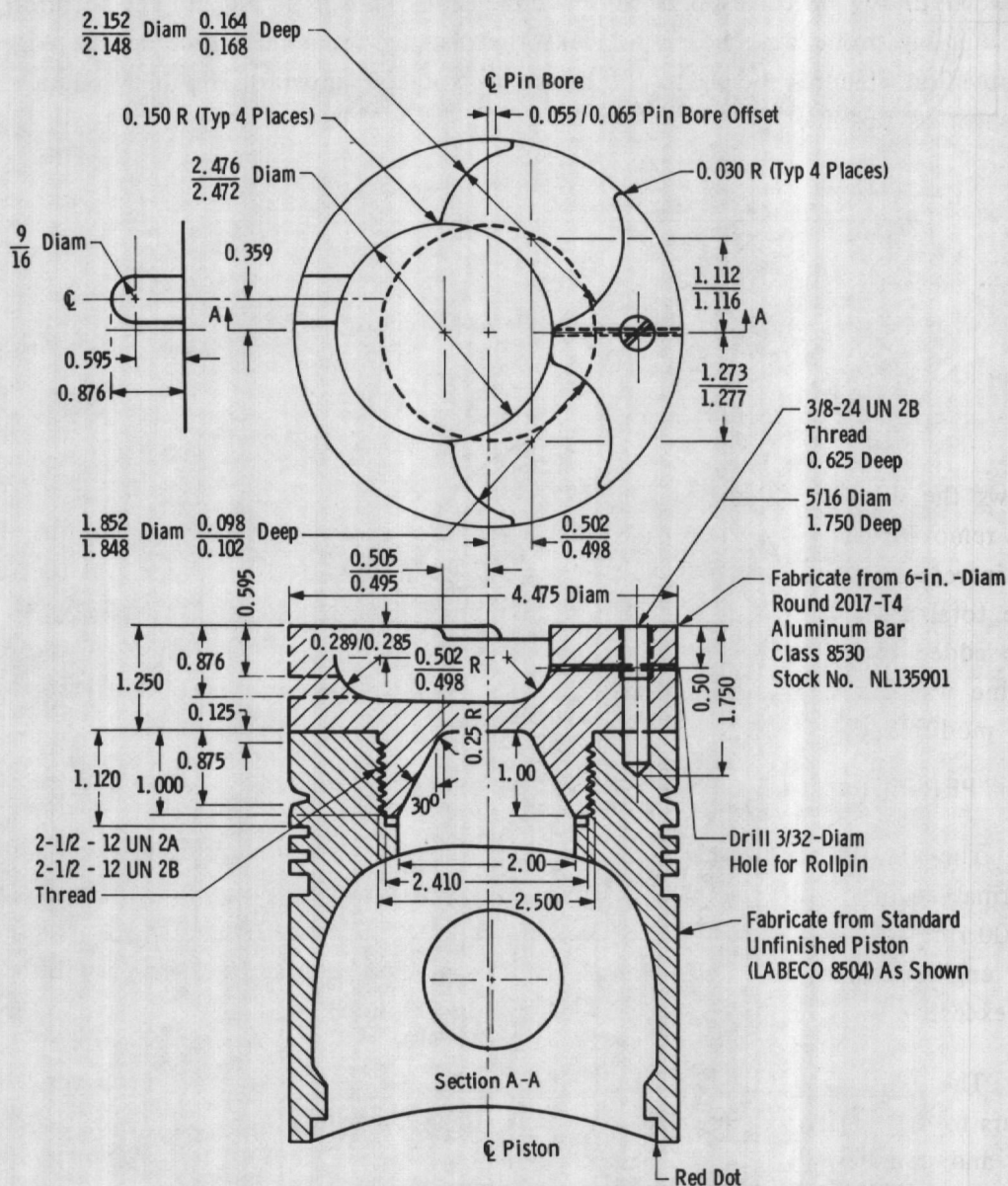
All Dimensions in Inches

a. Gas-sampling piston
Figure 8. TACOM engine modifications.

All Dimensions in Inches

b. Connecting rod modification
Figure 8. Concluded.

shows the dimensions of the small end of the connecting rod after material (0.31 lb) was removed. The largest contribution to reduced reciprocating mass (0.88 lb) was obtained by increasing the diameter of the hole through the piston pin from 0.700 to 1.250 in. The total reduction in added reciprocating mass from these three sources was 1.50 lb. The added reciprocating mass for the gas-sampling probe modification of the TACOM engine was 0.57 lb compared with 2.07 lb for the viewport modification. Vibration of the modified engine and test stand was found to be very reasonable.

2.3 PERFORMANCE OF THE MODIFIED ENGINE

The viewport-equipped TACOM engine has operated for approximately 350 hours. Normal engine speed was usually 1,000 rpm; but the engine was often run at 2,000 to 2,100 rpm while being brought up to temperature. Although the overweight piston caused the engine and test stand to vibrate badly on many occasions, there was no evidence of excessive wear or stress when it was disassembled.

The gas-sampling probe modification of the TACOM engine has been run about 50 hours to date. Data runs are being made at 1,000 rpm and because of the lightened piston pin and connecting rod the engine will not be run at more than 1,600 to 1,700 rpm. The operation of the modified engine has been completely satisfactory so far.

To determine the effect of modifications to the engine on its performance, motored compression pressures were measured and compared with the standard, unmodified engine. Motored compression pressures that were obtained for the standard and modified TACOM engine are shown in Table 1.

Table 1. Motored TACOM Engine Compression Pressures

Intake Air Temperature = 78°F

Barometer = 28.8 in. Hg

Coolant Temperature = ~100°F

	RPM				
	500	750	1,000	1,250	1,500
Configuration			Psig		
Standard	479	499	500	518	530
Viewport	445	470	485	500	515
Gas Sampling - No Orifice	390	410	430	435	450
Gas Sampling - 0.013-in. Orifice	380	403	425	431	445

The compression pressures for the viewport-equipped engine are 15 to 34 psi (2.8 to 7 percent) below those for the standard engine. Small differences in combustion chamber volume and in heat transfer probably are the explanation. The compression pressures for the gas-sampling modification of the engine fitted with a plug in place of the sampling nozzle are 68 to 89 psi (15 to 18.5 percent) lower than those for the standard engine. This indicates too large a combustion chamber volume. Evidently an error was made in the design or fabrication of the piston extension used for this engine configuration. The compression pressures for the gas-sampling modification of the engine fitted with a nozzle having a 0.013-in.-diam orifice are 5 to 10 psi (0.7 to 2.5 percent) lower than those for the same engine configuration fitted with a plug in place of the sampling nozzle. This indicates that the volume of gas sampled through a 0.013-in.-diam orifice should not greatly affect the performance of the engine.

3.0 HIGH-SPEED PHOTOGRAPHY

The experimental study of the characteristics of fuel sprays under actual engine combustion chamber conditions presents many difficulties. Some of these arise from the

complex structure of the spray itself, which is made up of a large number of droplets having a wide range of sizes that are continuously undergoing collisions, ligamentation, evaporation and/or burning. Other difficulties arise from the high temperatures, pressures, and turbulence in the combustion chamber, from fuel injection through the exhaust process, which makes viewing difficult. The turbulence conditions also affect many properties of the fuel spray as well as causing index-of-refraction gradients that affect the quality of optical data. The critical series of experiments centered in taking high-speed photographs in the engine operation; these experiments will be evaluated in the following section.

High-speed photography has been used to study fuel injection and combustion in diesel engines (Refs. 2 through 6) and in stratified charge engines (Refs. 7 and 8) that were designed or modified especially for this purpose. Similar work has been done using viewport-equipped spark-ignition engines and special pressure vessels designed to simulate engine combustion chambers. Fused quartz is the transparent material used in most engine viewport installations. A single viewport allows photographing only self-luminous and front-lighted subjects, and two opposed viewports allow backlighted photography as well. Backlighting has a decided advantage when very short exposure times must be used to prevent motion blur.

The studies mentioned above (Refs. 2 through 8) used incandescent light sources and the camera shutter to control the exposure time. The photographs covered in this report differ mainly in that a pulsed argon-ion laser was used to provide more intense illumination, and photographic exposure time was controlled by the length of each laser pulse.

3.1 EXPERIMENTAL APPARATUS AND TECHNIQUE

Figure 9 is a diagram of the setup that was used to make high-speed photographs of fuel injection and combustion in the TACOM engine. A 6-in. focal length f/3.8 Elgeet lens and a 100-mm focal length f/4.5 Kodak® Ekton enlarging lens were used with the Model 41 Hycam® 16-mm high-speed movie camera. Extension tubes were used with the lenses to magnify the images by 0.75 and 3.50 on the film. A shutter-open signal provided by the camera was used to trigger a Hewlett Packard Model 1901A pulse generator. Signals from the pulse generator were amplified by the Spectra Physics Model 465 Bragg cell driver which was used to control the timing and duration of the laser pulses. A Spectra Physics Model 166 laser equipped with a Model 365 output coupler was used to backlight the scene. Timing marks were placed on one edge of the film at millisecond (msec) intervals. During the last several data runs, magnetic pickup signals generated by crank-angle markings on the flywheel were amplified and marked at 1-deg intervals of crankshaft rotation on the other edge of the film. A missing mark just ahead of top dead center (TDC) was used to establish the correspondence between film frames and engine crank angles.
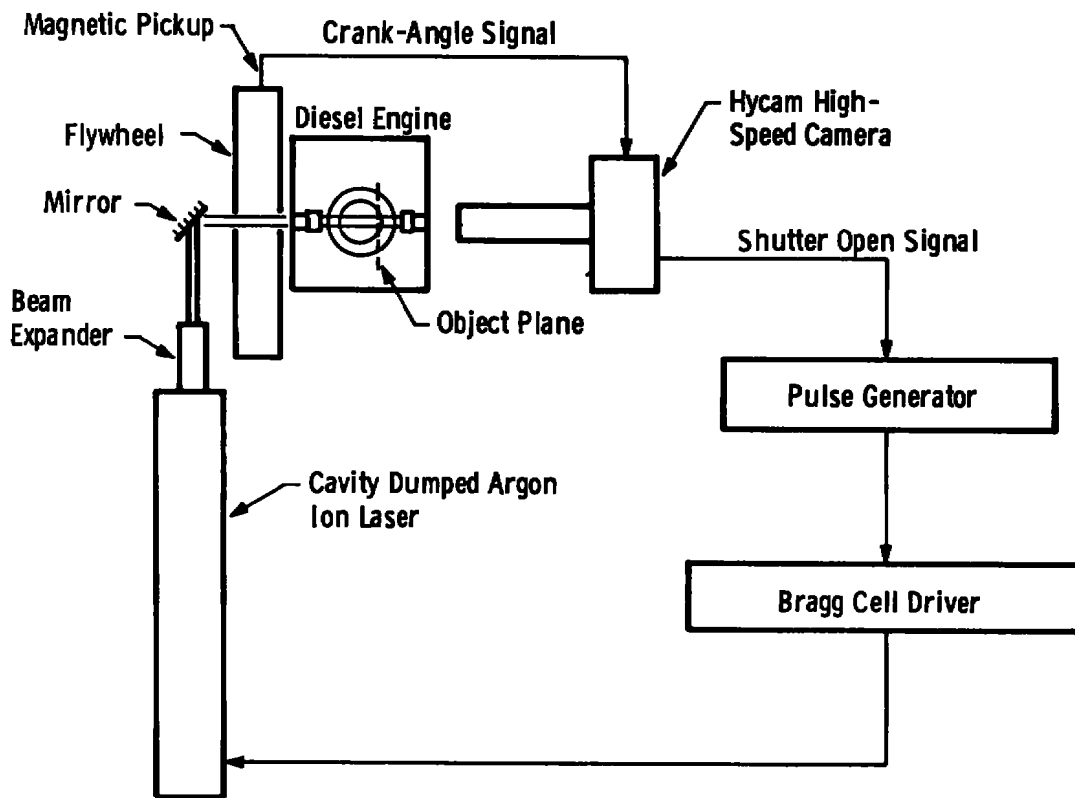
Figure 9. Schematic diagram — high-speed photography setup.

Kodak 7242 Ektachrome® film was used for the high-speed photographs. By adjusting exposure time and film processing, several film speeds were evaluated. Data were taken with both 0.4-microsecond (μsec) exposures and 500 ASA processing and 0.2-μsec exposures and 1,000 ASA processing. Framing rates were 2,500, 5,000, and 10,000 frames/sec. The best combination of time and spatial resolution was obtained using the 5,000-frame/sec rate.

The orientation of the fuel spray pattern relative to the optical axis of the TACOM engine viewport installation is shown in Fig. 10. The viewport aperture was 0.50 in. in diameter. The fuel injection nozzle has four 0.0138-in.-diam spray holes arranged symmetrically on a conical surface with a 145-deg included angle. For some of the photographs a nozzle having a 130-deg included angle was installed in its place. As expected the photographs showed that the 130-deg spray covered a substantially greater fraction of the visible area, whereas dynamometer readings showed that the performance of the engine was changed only slightly.
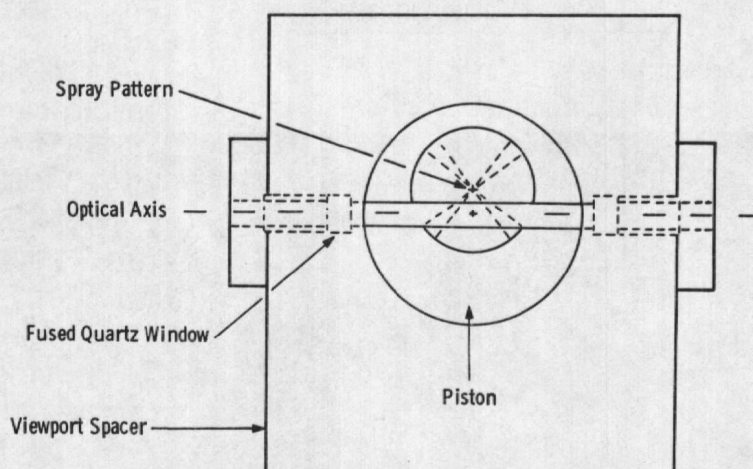
Figure 10. Intersection of optical axis with fuel spray.

Before the high-speed photographs were taken, the engine was operated with steel plugs sealing the viewport openings until the coolant temperature reached 150°F. The steel plugs were then replaced by fused quartz windows, and the throttle stop was set at 0.400 on a micrometer scale which was approximately full throttle. After bringing the engine up to speed using the Varidrive® motor, the fuel was turned on and the camera was started. At 2,500, 5,000, and 10,000 frames/sec, the 400-ft roll of film lasts about 6.4, 3.2, and 1.6 sec, respectively. Engine rpm increased only slightly during a data run. Thirty 400-ft rolls of film were exposed in this way while camera speed, laser pulse duration, film processing, and lenses were varied to optimize the technique.

3.2 EXPERIMENTAL RESULTS

The data were carefully examined using a Model 224A Mk. II photo-optical data analyzer which is a 16-mm stop-motion projector. Several pertinent events are clearly revealed in the photographs. In fact the photographs are shadowgraphs and record information concerning the second derivative of the index of refraction and therefore the second derivative of the density of the gas. Consequently, they show regions of the flow where the gas density gradients change very rapidly. Such regions were found to develop during the compression stroke. They appear to move with the flow and allow one to visualize the gross motion of the gas. Figure 11 shows prints of film frames that correspond to four crank angles in a single compression stroke which illustrate the development of the density gradients and their effect upon a wavefront. The degree of turbulence will limit the ultimate accuracy that can be expected when applying photographic and holographic methods to study processes in the combustion chamber of an engine.

23
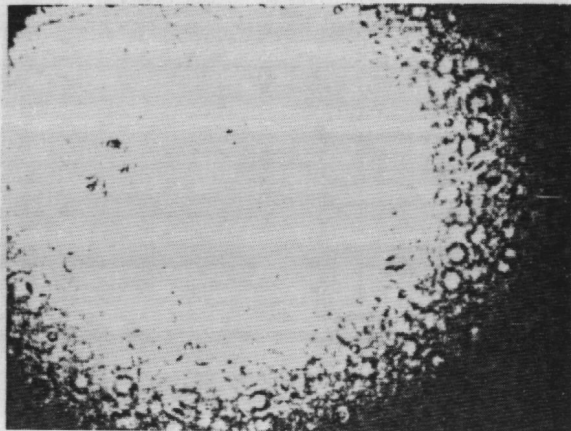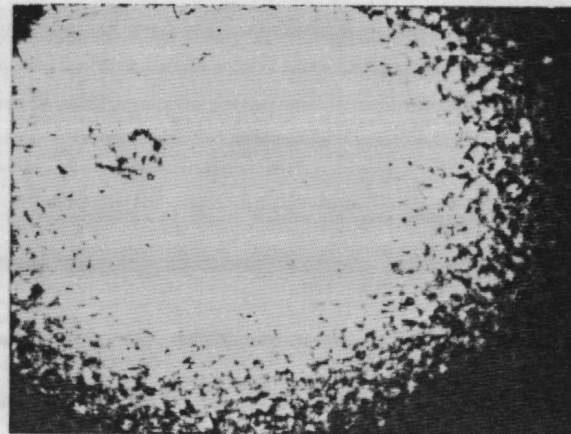
a. 85 deg BTDC

b. 55 deg BTDC
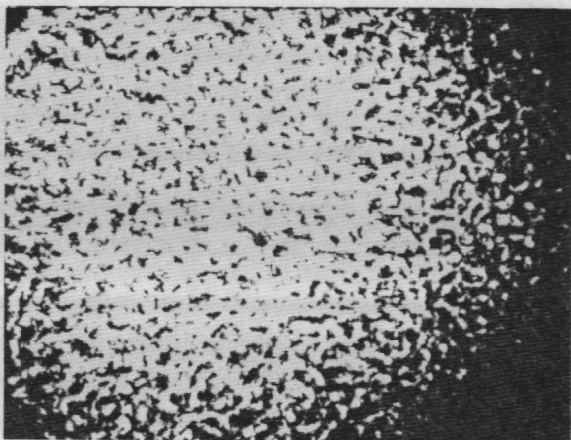
c. 25 deg BTDC
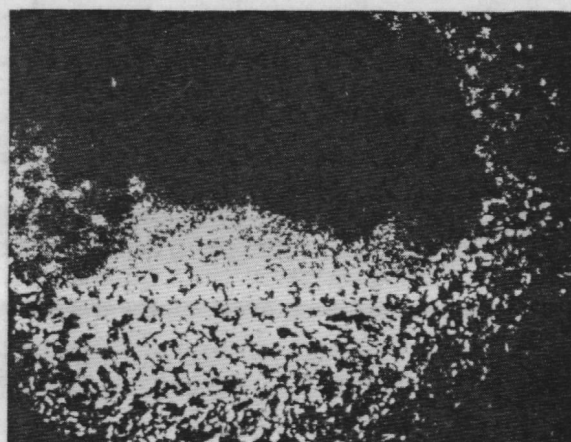
d. 5 deg BTDC

Figure 11. Photographs of gas density and turbulence effects.

The movement of the spray plume across the field-of-view and the beginning and duration of combustion are quite clearly shown in the high-speed photographs. These events can easily be correlated with the timing and crankshaft position marks on the edges of the film. Figure 12 shows four frames that illustrate the progress of a spray plume. From the film, the lower edge of the spray plume was estimated to be moving horizontally at about 1,100 cm/sec and vertically at about 1,120 cm/sec. Data showing the onset and duration of combustion are not included because black and white prints from the colored film do not show the effect very well.

The camera, optical system, and film that were used to take photographs at a linear magnification of 0.75 should be able to resolve droplets as small as 33 microns (μ) in diameter. The appearance of the edge of the spray in these photographs does suggest the presence of individual droplets, but they are too small to produce measurable images on photographic film. Droplets as small as 40 μ in diameter were measured by projecting the film at a magnification of 50.

An examination of the film frames revealed that solid particles and liquid droplets can occur in the engine almost anytime in its cycle. The particles/droplets size varied from 50 to 500 μ and were often seen following the gas motion when the intake or exhaust valve was open. Occasionally large fuel droplets appeared after combustion while the piston was still on the expansion stroke. Figure 13 shows some of these droplets moving from right to left across the viewport aperture. Smoke or dense vapor can be seen streaming to the left from the upper droplet. The paths of these and other droplets that appeared in a 45-frame sequence of one film series are shown in Fig. 14. Sizes and velocities that were measured are also presented.

These photographs actually are low-resolution in-line holograms. The images of some large droplets that appear during parts of the engine cycle where gas density gradients and turbulence are minimal show the well-defined concentric interference patterns that are characteristic of in-line holograms of droplets. Attempts to reconstruct images of these droplets were of limited success. Distortion of the reference beam by fouling of the windows and by density gradients in the gas as well as the inherent limitations of the camera, film, and optical system appear to be responsible for the low resolution that was obtained. It will be possible to improve the resolution somewhat by operating the engine at lower throttle settings to reduce the window fouling.
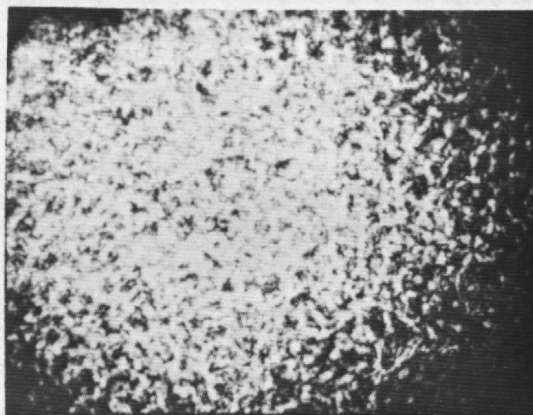
a. 0.0000 sec, 7.7 deg BTDC
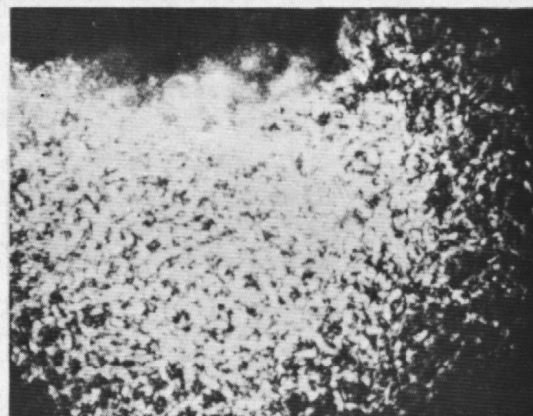
b. 0.0002 sec, 6.5 deg BTDC
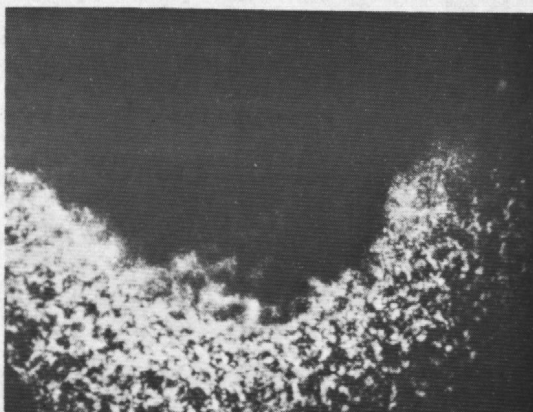
c. 0.0006 sec, 4.0 deg BTDC

d. 0.0008 sec, 2.7 deg BTDC

Figure 12. Photographs of fuel spray crossing the viewport aperture.
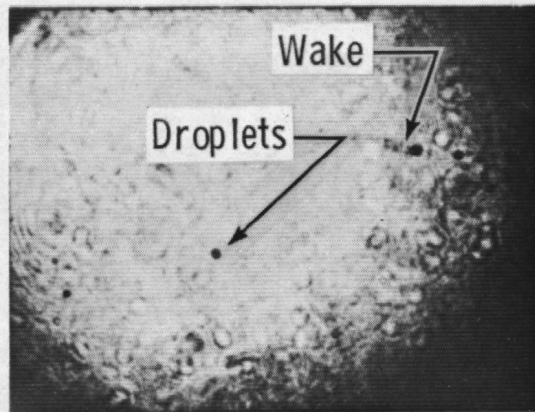
a. 0.000 sec, 129.0 deg ATDC
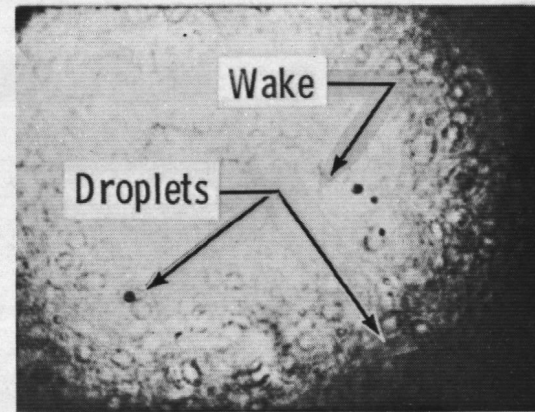
b. 0.001 sec, 135.2 deg ATDC
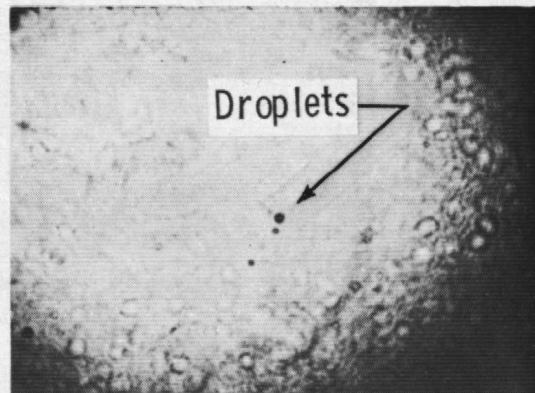
c. 0.002 sec, 141.4 deg ATDC
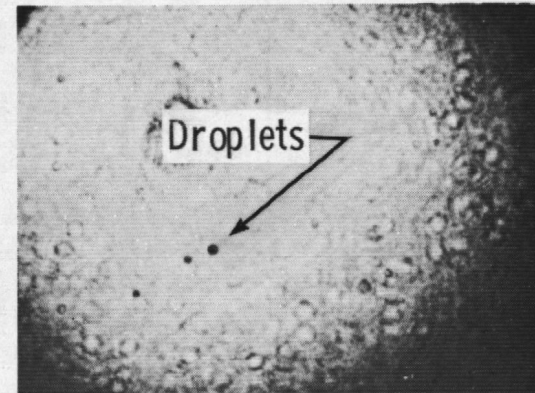
d. 0.003 sec, 147.6 deg ATDC

Figure 13. Photographs of large fuel droplets crossing the
viewport aperture.

O − at 1-msec intervals
Frames 1 and 45 at 103 and 153 deg ATDC on the expansion stroke.
Engine Speed = 1000 rpm

Droplet		A	B	C	D	E	F	Units
Diameter	D initial	196	231	156	280	234	230	μ
	D final	180	230	156	264	204	194	μ
Velocity	V x	224	170	348	157	206	277	cm/sec.
	V y	133	107	206	86	93	94	cm/sec
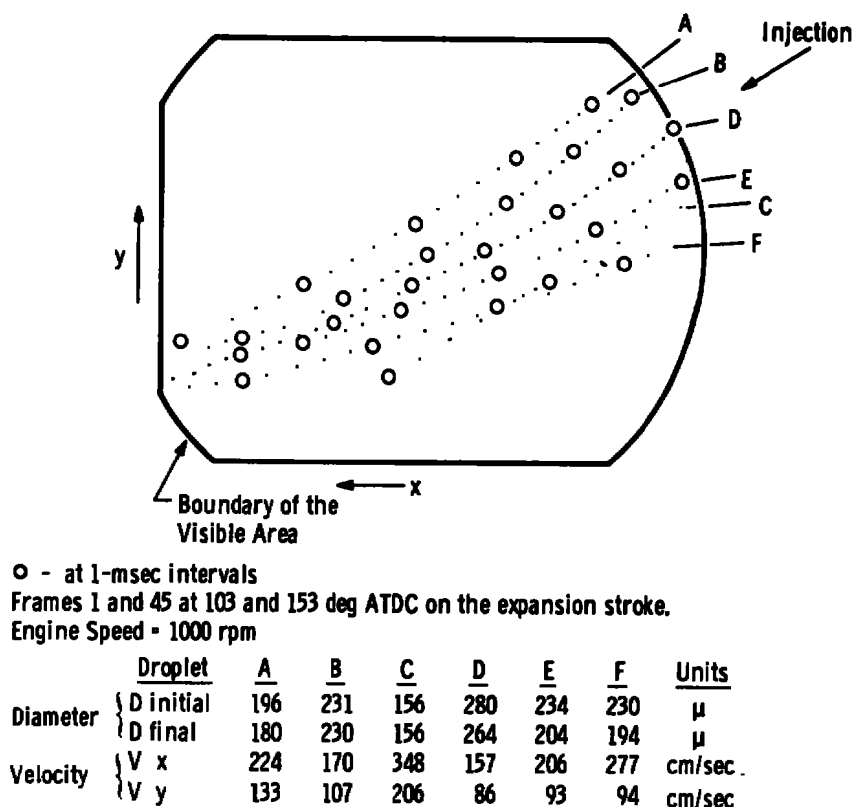
Figure 14. Instantaneous droplet sizes and velocities.

4.0 APPLICATION OF HOLOGRAPHIC TECHNIQUES

In this section the feasibility of holographically sizing fuel droplets in the combustion chamber of a diesel engine is presented. A sideband holography system was utilized to record holograms of the fuel injection and combustion process in a four-cycle, single-cylinder, diesel engine supplied by the Army Tank and Automative Command. The effects of the combustion chamber environment were expected to be more severe than those encountered in previously reported work (Ref. 4) because of higher pressures and temperatures that exist in the TACOM engine and a longer distance over which the object beam must travel. The degree of degradation is manifested by a decrease in resolution of the reconstructed images. The extent to which this occurred could be somewhat controlled by choking the airflow into the engine. Feasibility was considered to be proven when 8-μm-diam particles were reconstructed at the periphery of the spray. The resolution degradation attributable to speckle noise generated by large number density regions within the spray was also of interest.

Two sideband holography optical systems were designed and applied to the TACOM engine. The first system illuminated the spray from the back and incorporated object field magnification to reduce image degradation by the film resolution. The change in magnification with object distance, which is characteristic of a thin lens and which is carried over into the reconstruction when the reference and reconstruction beams are collimated, was eliminated by using a reference beam having spherical wavefronts. The constant magnification in the reconstruction eliminated the necessity of recording reconstruction distances and additional calculations to determine droplet image sizes. Reconstructed image resolution of 8 μm and better was verified with an Air Force tri-bar resolution chart, and by reconstructing fuel spray droplets of this size. It was concluded from the data that sideband holography is applicable to studies of in-situ diesel engine fuel sprays. The second optical system utilized front illumination of the injector spray in order to observe droplets which would not normally reconstruct because of the large droplet density. Point reflections from the droplets could only be reconstructed, making direct image size measurement impossible. However, velocity can conceivably be obtained from those images as well as indirect size data by multiple-pulse holography.

The sideband, constant magnification, optical system will be described along with the experimental apparatus and the procedure for taking and reconstructing the holograms. The quality of the data in terms of the effects of the engine parameters will also be discussed. The front-lighted holocamera which was also applied to the diesel will be described and the results of the holographic study will be summarized.

4.1 HOLOCAMERA OPTICAL CONFIGURATION

The resolution of any hologram recording system (whether it is inline or sideband) is basically limited by the ability of the film to faithfully record the light scattered by the illuminated objects. For microscopic droplet fields this can be caused by the droplets being too far from the film plane, a limiting aperture in the recording imaging system, low film resolution, and poor laser coherence. The latter is not significant when the object and reference beam pathlengths are equal and the laser is operating in the fundamental traverse electromagnetic (TEM_{00}) mode. To reduce all but the last limitation, a lens is used to magnify the droplet field and image it near the film. However for planar reference and reconstruction light the magnification in the reconstruction is functionally dependent on the image position.

A sideband holocamera that was designed for constant magnification in the reconstruction of a hologram is illustrated in Fig. 15. The object field is illuminated with collimated laser light, and lens L_1 images a plane outside of the fuel spray region, but inside the combustion chamber, on the hologram film plane. Lens L_2 changes the plane

29
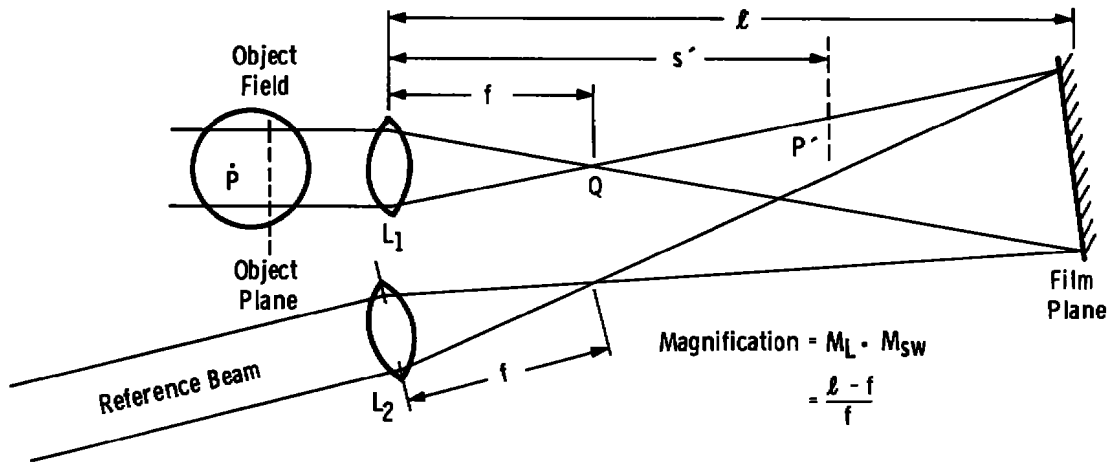
Figure 15. Schematic of constant magnification holocamera.

wavefronts of the collimated reference beam to spherical, which have the same radius of curvature at the film as the object wave. This is done by placing matched lenses of equal focal lengths at the same distance from the film.

Magnification on the hologram is equal to the produce of the magnification, M_L, attributable to the lens used in the recording and the magnification, M_{sw}, associated with spherical reference and object beam illumination (Ref. 10), i.e.,

$$M_{sys} = M_L \cdot M_{sw} \tag{4-1}$$

(The lens is considered to be imaging a magnified object field which is, in turn, illuminated by spherical waves emanating from a source at point Q as shown in Fig. 15 in the focal plane.) Considering a droplet at an arbitrary position, P, in the object field the lens will produce an image at P' which is magnified according to the thin-lens equation,

$$M_L = \frac{S' - f}{f} \tag{4-2}$$

where S' is the image distance from the lens which has a focal length f. In addition, objects illuminated by a spherical wavefront are magnified in the recording according to

$$M_{sw} = \frac{1}{1 - (z_1 / R_1)} \tag{4-3}$$

30

where z_1 is the distance of the hologram object (lens image, P') from the film, R_1 is the radius of curvature of the reference wave, and it is assumed that a collimated beam will be used in the reconstruction. From the geometry in Fig. 15

$$z_1 = \ell - S'$$ (4-4)

and

$$R_1 = \ell - f$$ (4-5)

where ℓ is the distance from the imaging lens to the film plane. Substituting these equations into Eq. (4-1) yields

$$M_{sys} = \frac{\ell - f}{f}$$ (4-6)

The magnification in the reconstruction is therefore constant, depending only on the film distance from the imaging (or reference beam) lens and the lens focal length. Therefore, droplet images will be reconstructed by the hologram with the same magnification irrespective of their position in the object field.

It should be noted that Eq. (4-6) specifically pertains to the magnification of objects that are focused on the film plane. This is consistent with the results since these images can be considered to reconstruct on the hologram plane and therefore must have the same magnification as the remainder of the reconstructed volume. This identity between the magnification of the image focused on the film plane and the rest of the reconstructed volume allows the magnification to be easily remembered.

The reconstructed image distance, z_r, from the hologram plane, is given by

$$z_r = (\lambda_1 / \lambda_2) M_{sys}^2 \, z$$ (4-7)

where λ_1 and λ_2 are the recording and reconstruction wavelengths, respectively, and z the distance from the object to the hologram plane. This result is significant in that the actual volume depth will be increased by M_{sys}^2 in the reconstruction. This could make it difficult to bring images of droplets relatively distant from the film into focus on a finite length optical bench.

Recording fuel spray droplets in the diesel engine places a number of severe requirements on the resolution of the hologram recording optical system. First, the hologram must be capable of resolving droplet images on the order of 10 μm, since these sizes and those below this value are generated by the fuel spray. Second, the droplets must be resolved in a turbulent density volume. The resolution of a hologram can be

no better than that resolution associated with the object information transferred to the film. Density gradients within the combustion chamber refract the object illumination producing areas of light and dark in the background as in a shadowgraph which can be confused with images or could obliterate the images altogether. These gradients can also distort the image information before it is recorded on the hologram. The severity of the aberration is a function of the strength of the density gradients and the distance over which the light beam must travel through them. During the fuel injection, turbulent gradients were found to be less harsh than in the combustion portion of the engine cycles. In the latter case it was impossible to identify a droplet image because of the turbulence-induced speckle.

4.2 EXPERIMENTAL ARRANGEMENT

The holocamera optical system is shown schematically in Fig. 16. The ruby laser is q-switched with a Pockel's cell and emits a 30- to 40-nanosecond (nsec) light pulse. An etalon and a 1.0-mm aperture in the laser cavity were provided to make the emitted wavefront single mode. As shown, this was not always accomplished because fringes caused by multimoding were present in the reconstruction. A 5X microscope objective, 10-μm pinhole, and collimating lens expand the light beam, smooth any spatial variations of the wavefront, and collimate it to a 1-in.-diam beam, respectively. A cube beam splitter separates the light into a reference beam and an object illumination beam. The reference beam is reflected to mirror M_1 and then to the film. Pathlengths of the object and reference beams were matched in order to reduce the effects of temporal incoherence of the laser radiation. The spherical reference wavefront is generated by lens L_2, which has a focal length of 21 cm and was 123 cm from the film plane.
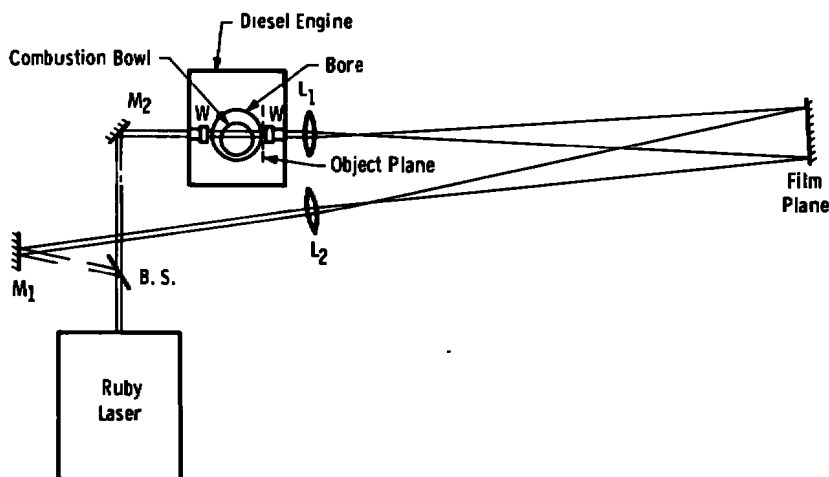
Figure 16. Optical configuration of fuel injection holocamera.

Object illumination is directed to the combustion chamber of the diesel engine by mirror M_2. Optical access was gained by means of two ports on opposite sides of the combustion chamber. During fuel injection and combustion the top of the piston was above the field-of-view; therefore, in order to observe the fuel being injected into the combustion bowl, a channel 0.5 in. wide and 0.800 in. deep was cut across the top of the piston. Optical ports on the engine had a clear aperture of 5/8 in. and were 1/2-in.-thick laser-quality quartz. (Laser quality implies minimal striae and bubble content within a homogeneous material. The surface was parallel to 5 arc sec and flat to $\lambda/10$.) The windows were separated by 5 in. and were 1-1/4 in. inside the piston head. A plane immediately inside the combustion chamber was focused by L_1 onto the film with a magnification of 5X. The normal to the film plane bisected the 12-deg angle between the reference and object wavefronts to minimize shrinkage effects in the reconstruction (Ref. 11).

Figure 17 shows the front of the holocamera optical system in-place around the TACOM engine. The ruby laser is to the right of the engine. A 3-mw helium-neon (He-Ne) laser beside the ruby laser head was used to align the optical system. The flywheel and a magnetic pickup for timing of the laser firing are pointed out on the front of the engine. The reference beam lens L_2 is immediately to the right on the far side of the engine head.

Holograms were recorded on Agfa-Gevaert® 10E75 film plates and developed in Kodak D-19 solution for approximately four minutes. In order to increase the diffraction efficiency (the amount of light diffracted into the reconstructed image) the holograms were bleached in bromine vapor (Ref. 12). No loss of resolution was evident in the reconstruction after bleaching. The time to bleach each hologram clear was found to be dependent on the density of the recording and the density of the vapor. This varied from 15 minutes to several hours. It was found to be essential that the plates be removed once bleaching had occurred since leaving the holograms in the caustic bromine atmosphere too long caused destruction of the emulsion.

In some cases where the developed hologram recordings were so dense that the reconstruction beam was significantly attenuated and image reconstructions were very dim, bromine bleaching brought the reconstructed image brightness to the same level as those holograms that were bleached from a much lighter density. In all cases, the reconstructed object beam was significantly brighter after bleaching.

Holograms were initially reconstructed with the optical arrangement shown in Fig. 18. Collimated light from a 15-mw He-Ne laser was used to reconstruct the holographic images. The laser, beam expanding and collimating optics, and hologram were on a common optical bench that was rotated with respect to the optic axis of the television (TV) camera
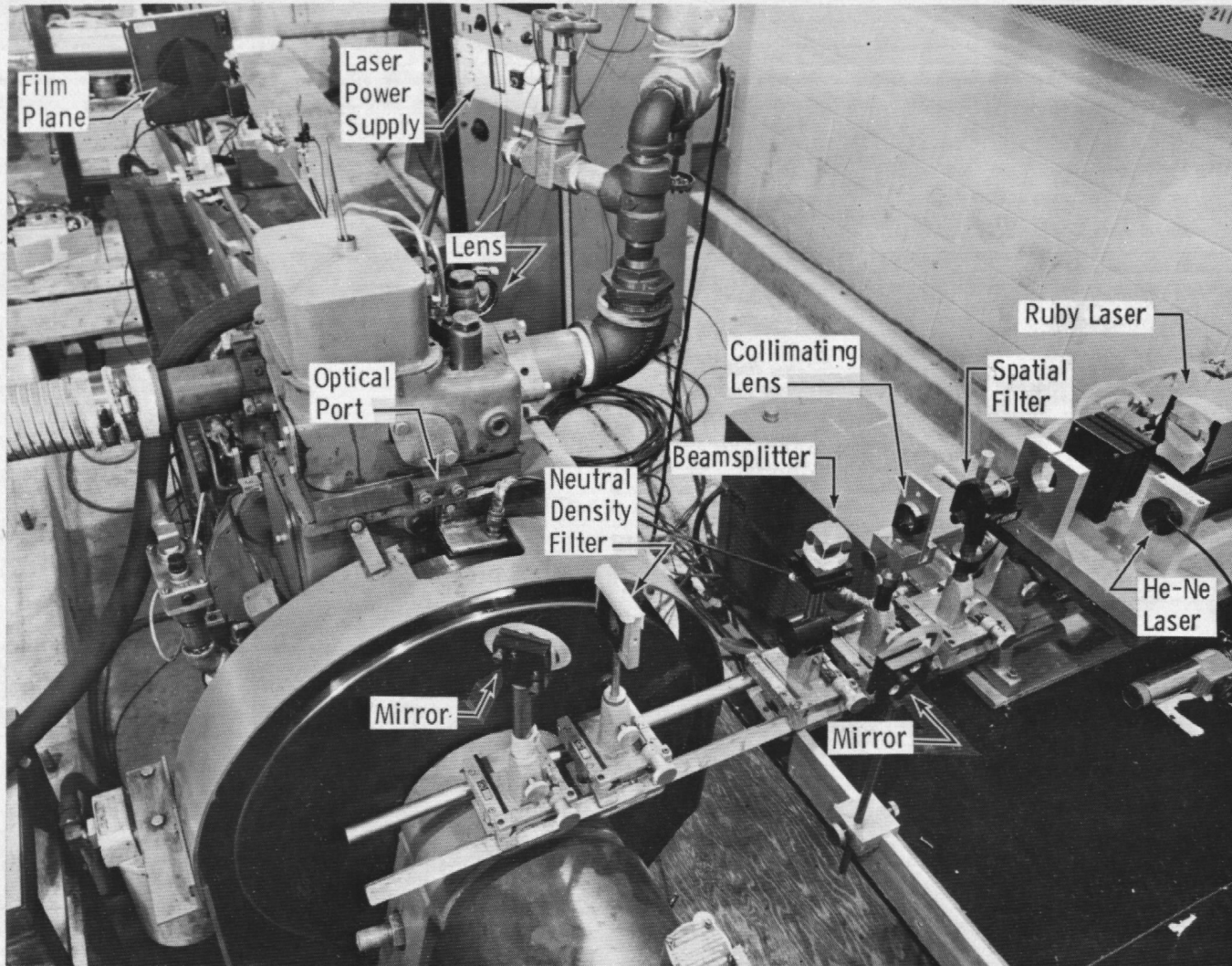
Figure 17. TACOM diesel engine side-band holocamera — front view.
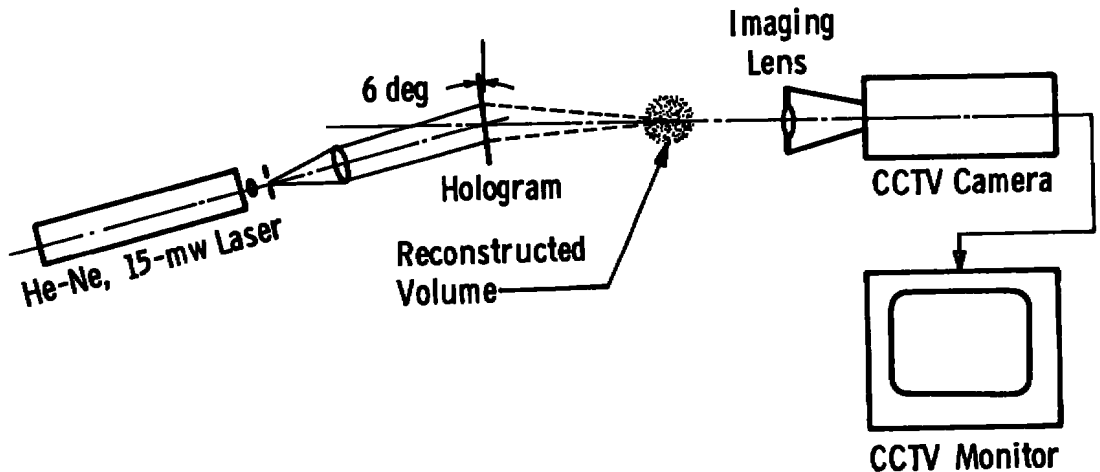
Figure 18. Side-band reconstruction system.

and imaging lens. This reconstruction angle (12 deg) was set equal to the angle between the reference and object beams in the recording. The hologram was then tilted half this amount (6 deg) to allow the reconstructed volume to lie along the TV camera optical axis. The camera was used to focus on various planes within the reconstructed volume. Images were then observed and measured from the screen of the closed-circuit (CC) TV monitor.

The hologram could not be moved along either the laser or TV camera optical axes because of the ensuing lateral motion of the images across the camera vidicon. Therefore, traversing the camera was a necessity. However, focusing was difficult because of the bulk and weight of the camera which produced jittering of the images. To remedy this situation, a self-aligning traverse system was designed and built. This device, shown in Fig. 19, allows the laser, lenses, and TV camera to be placed along a common optical axis on the reconstruction bench. Two mirrors on the traverse system direct the light to the hologram. These could be adjusted to illuminate the hologram at the appropriate horizontal and · vertical angles. Rotation of the mirrors around the vertical axis is geared such that the lower mirror rotates half as much as the upper mirror to keep the reflected light on the upper mirror. For three-dimensional scanning of the reconstruction the entire hologram traverse is motor driven along the optical axis to provide depth-of-field scanning, whereas the hologram moved in the x-y plane.

To determine the resolution achieveable with the holocamera a hologram was recorded of an Air Force tri-bar resolution chart placed in the combustion chamber of the engine. Two 100-μm-diam wires were also fixed to the outer surface of each window to determine the amount of magnification variation in the reconstruction. The resulting reconstructed images are shown in Fig. 20. Bars in Group 6, Element 3, were observable, indicating
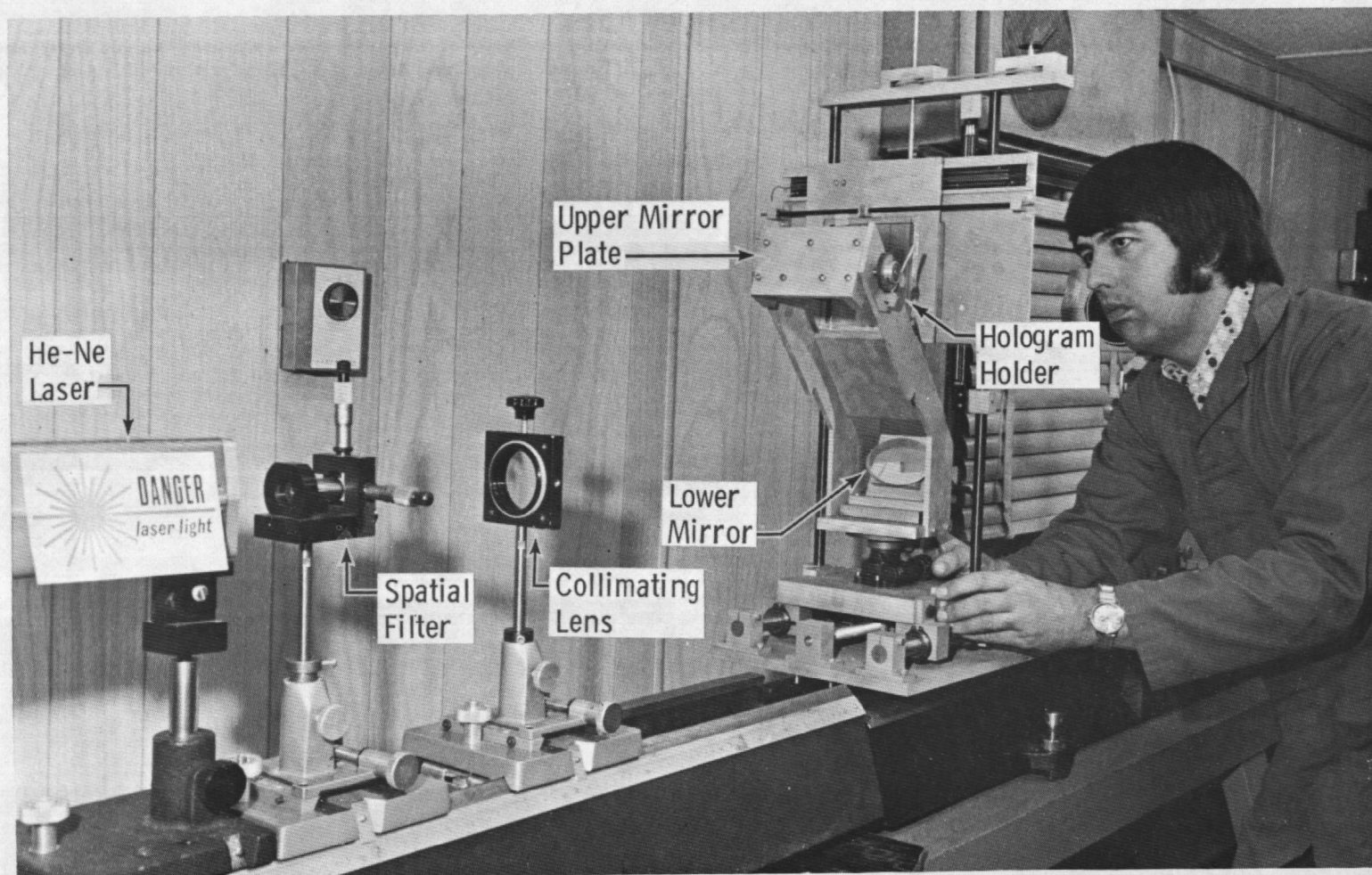
Figure 19. Side-band reconstruction traverse system.

Group 6
Element 3

Diffraction
Rings (Noise)
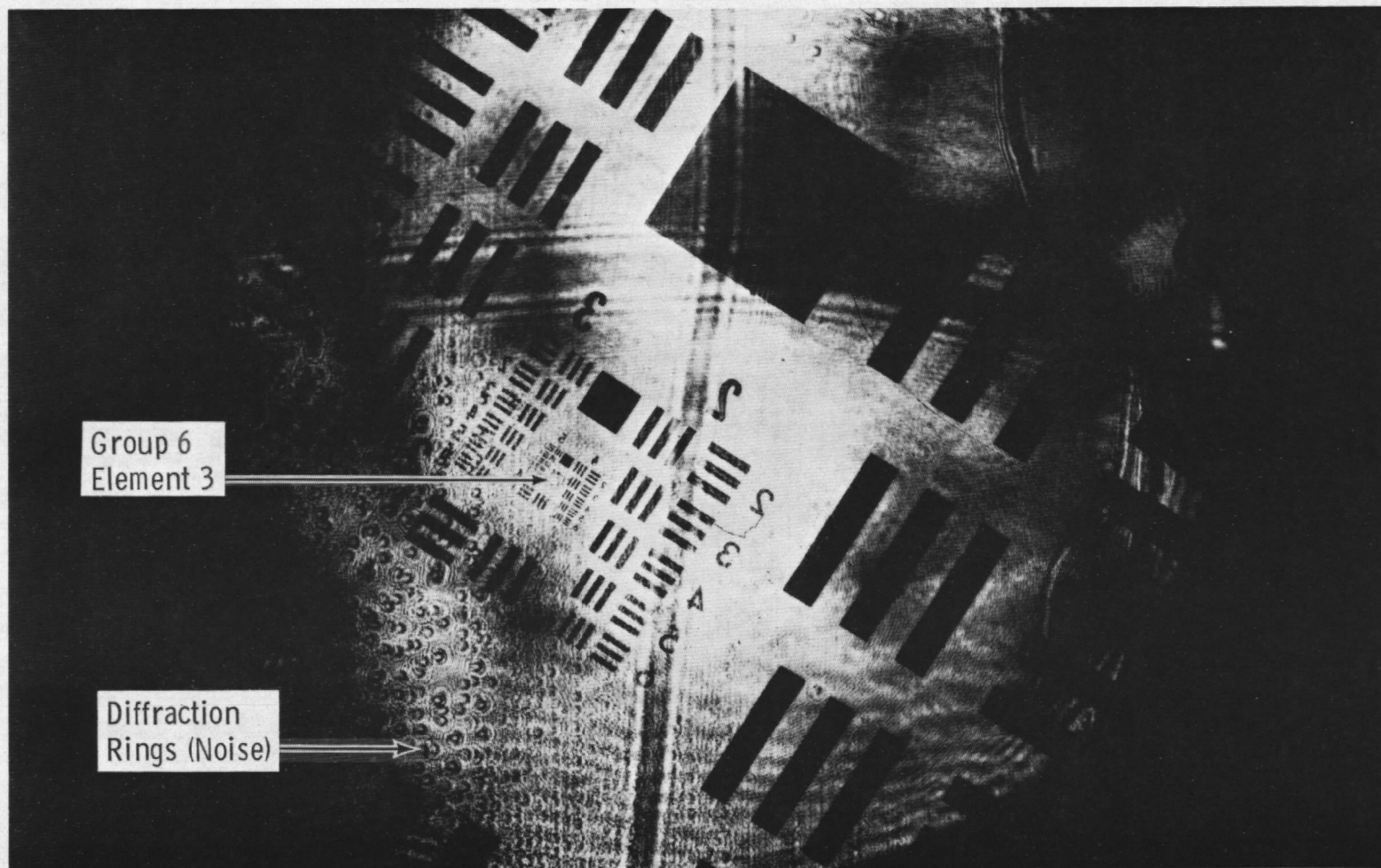
Figure 20. Reconstruction of Air Force tri-bar resolution chart
within combustion chamber of diesel, M = 15.6.

a resolution of 6.2 μm. The chart image reconstructed 97cm from the hologram. Dark areas on the photograph in Fig. 20 were caused by multimoding of the laser. In the lower left corner are diffraction rings of dust particles and fuel droplets on the window nearest to the film. The wire images reconstructed with diameters of 9 and 11 mm on the TV monitor and were separated by 429 cm. This corresponds to a percent magnification change per cm of reconstruction length of 0.05 which, over the depth of the fuel spray, was considered to be insignificant.

4.3 HOLOGRAPHIC DATA RECORDING PROCEDURE

Timing of the hologram recording to the engine cycle was achieved by means of a magnetic pickup mounted adjacent to the perimeter of the flywheel and a photodiode-LED (light-emitting diode) pair mounted on the cam-shaft. The magnetic pickup generated one pulse for each degree of crank-angle rotation, and the photodiode produced one pulse every two engine cycles. A Strobotac® triggered by the amplified pulse from the photodiode illuminated the marks on the flywheel so the crank angle could be read while the engine was running. This pulse also initiated the laser firing. The laser pulse energy and the pulses from the magnetic pickup were detected by another photodiode, and the resulting signals stored on an oscilloscope to verify proper laser firing and timing. An example of these data is shown in Fig. 21. The upper trace indicates the energy emanating from the laser including the flash lamp light and the laser pulse. The bottom trace shows the crank-angle pulses. The large amplitude pulse corresponds to the top-dead-center groove passing under the pickup. These pulses are delayed by 10 deg with respect to the actual engine crank angle because of the mechanical offset of the pickup on the flywheel.
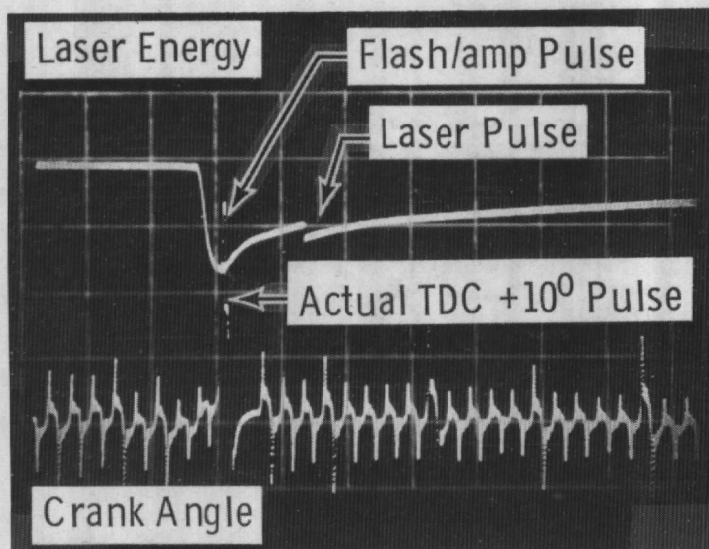
Figure 21. Hologram timing waveforms.

The appropriate crank angles for recording holograms of the fuel injection and combustion were initially determined from the high-speed photographs and then verified experimentally with ruby laser exposures on Polaroid® film. Essentially these latter recordings are laser shadowgraphs. The timing delay was adjusted until the appropriate condition within the combustion chamber was observed on the film. Figure 22 illustrates one of the shadowgraph recordings showing the initial portion of fuel injection. Injection is occurring from the upper right of the photograph, diagonally across the field-of-view. The top of the piston has risen above the field-of-view. Gross characteristics of the fuel spray and the refraction of the coherent beam as it passes through the pressure and temperature gradients within the combustion chamber are evident. The latter generate the mottled background surrounding the spray which is also present in the hologram reconstructions.
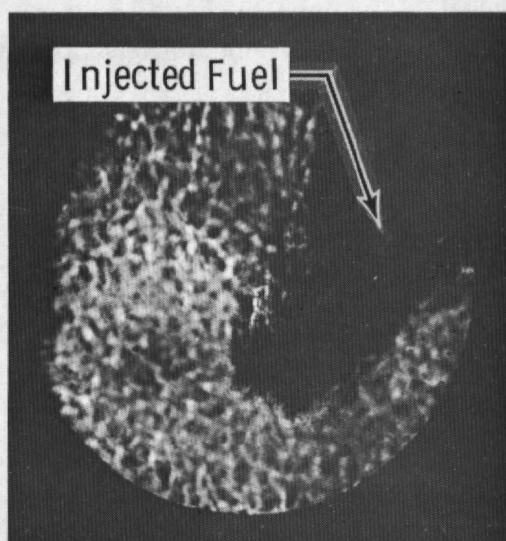
Figure 22. Laser shadowgraph of diesel engine fuel injection (air-choked).

Holograms were taken with the engine driven by a Varidrive motor at the proper rpm. Fuel injection was allowed to take place only during the cycle where a hologram was to be recorded. This prevented the windows from being coated by spray droplets and reducing the quality of the hologram recording. After each laser firing, the engine was stopped and the windows were removed and cleaned.

4.4 HOLOGRAPHIC DATA ANALYSIS

Sideband holograms were initially recorded of the onset of fuel injection with the air choked almost completely off. Since density gradients would not be as severe under these conditions, this would provide the best chance for reconstructing fuel droplets. After

the successful holographic reconstruction of spray droplets under these conditions, data were recorded with full air, at three speeds (500, 1,000, and 1,500 rpm) at full throttle (0.40) and lean (0.25) fuel settings on a micrometer dial, and at crank angles where combustion occurred. A summary of these conditions is presented in Table 2.

The reconstructed image of the fuel injection within the TACOM engine running at 1,000 rpm with the fuel set at 0.4 and the air at 0.5, which is midway between choked and full air, is shown in Fig. 23. The tip of the spray was in focus 132 cm from the hologram plane. Fuel droplets 8 μm in diameter at the outer periphery of the spray could be quite easily reconstructed. Close-ups of two planes of focus of peripheral droplets are shown in Fig. 24. The mottled background attributable to refraction by density gradients across the combustion chamber does not severely degrade these droplet reconstructions. A more significant parameter is the number density. Moving inward from the edge of the spray, droplet images were increasingly more difficult to discern from optical (speckle) noise. This speckle was a result of interference of light scattered by droplets which precede those being observed. This results in a loss of image resolution since the diameter of the speckle pattern is on the order of the droplet size (Ref. 13). Droplet illumination can be considered to progress from a uniform wavefront (since the scale of the mottling is larger than the droplets) in low-density regions to a diffuse wavefront in the higher density regions. As a consequence, an image in a low-number-density region comes into focus with characteristic diffraction rings converging to its edge. These rings are not present under diffuse illumination.

Table 2. Crank-Angle Degrees Corresponding to TACOM Engine Hologram Recordings

500 rpm	Air	
Fuel	Choked	Full
0.25	–	4,5,6,7 deg
0.40	7 deg	4,5,6,7 deg
1,000 rpm		
Fuel		
0.25	–	9,10,11 deg
0.40	12 deg	12 deg
1,500 rpm		
Fuel		
0.25	–	5,6,7,8.5 deg
0.40	18 deg	15,16,17,18 deg

NOTE: All values are taken before top dead center (BTDC).
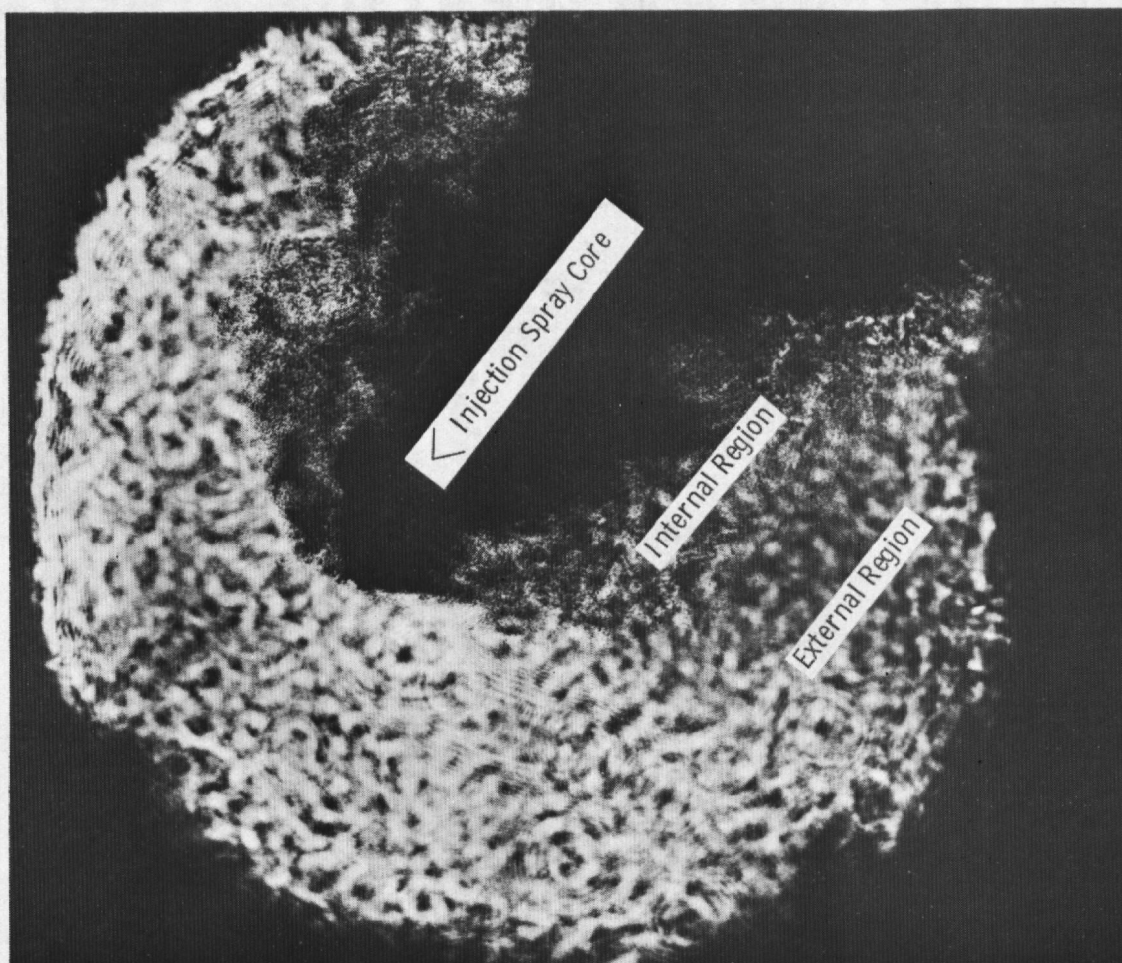
Figure 23. Side-band hologram reconstruction, TACOM diesel engine.
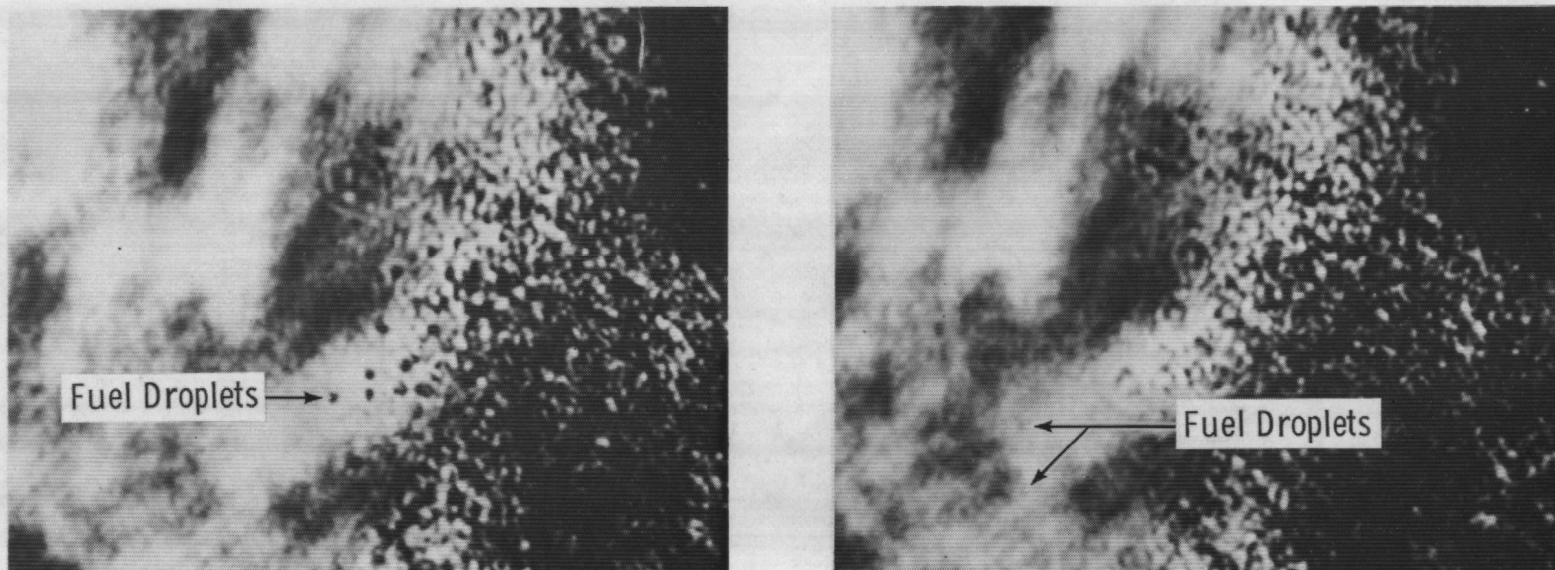
Figure 24. Fuel droplets in two reconstructed planes.

Coupled with the droplet-induced speckle is multiple scattering of droplet information (the diffraction pattern) by other droplets in the field. This optical information can therefore be distorted when it reaches the film plane or can be, in the worse case, completely blocked from the film. The large number density of the core of the spray (Fig. 23) completely blocked the illumination from the film. However, the edges of this central region could be focused upon even though individual droplets were not discernible. By selectively focusing on the tip of the spray and then on the peripheral region near the back edge, the angle of injection can be found; for Fig. 23 this was approximately 45.5 deg. This corresponds to the spray focusing lengthwise over a distance of 20.8 cm in the reconstruction.

Peripheral droplets in Fig. 23 were measured, and histograms of the data are presented in Fig. 25. The data in the higher density regions were plotted separately from those
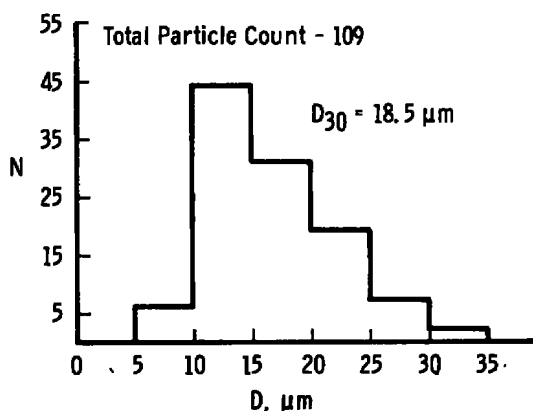
a. External
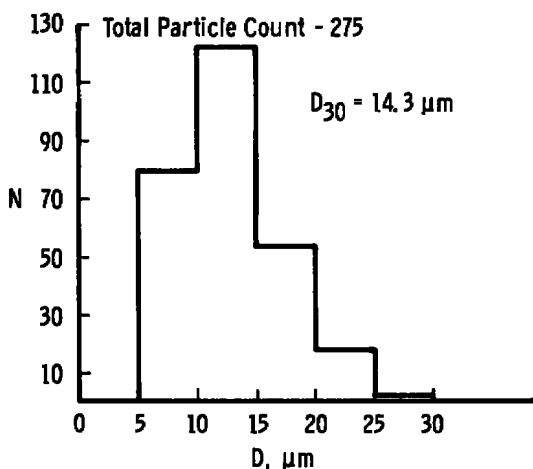
b. Internal

Figure 25. Histograms of fuel droplets near periphery
of injector spray.

43

in the low-density areas because of the inability to positively identify droplet image in the former regions. In both, the droplets followed a log-normal distribution with the greatest number between 10 and 15 μm. The volumetric mean diameter, D_{30}, was 15.8 μm for the outer region droplets and 14.3 μm for those in the higher density region. It is believed that speckle noise contributed to the large number of 5- to 10-μm measurements in Fig. 25b.

Under all engine conditions, the resolution of the sideband hologram images was approximately 8 μm. Although droplets smaller than this limit did not individually reconstruct, their collective presence at the periphery of the fuel spray was observed. These regions perturbed the wavefront, producing interference patterns which would not produce a recognizable image when focusing was attempted.

Image degradation from turbulent density gradients was not as severe during fuel injection as was expected. Even with the air intake valve fully open the scale of the background mottling was larger than the droplets. They, therefore, were observable in most areas around the spray perimeter. Figure 26 illustrates the difference in the reconstructed image backgrounds for choked and fully open air intake valve conditions. Refraction by the turbulence caused the edges of the viewing aperture to be less distinct in Fig. 26b than in 26a. The darker regions of the background did not focus, and therefore should not be confused with droplet images.

Figures 27, 28, and 29 illustrate the images reconstructed from holograms recorded at three engine speeds and at three BTDC crank angles during fuel injection. The fuel setting was 0.25 for the first two figures and 0.4 in the third. In all cases, the air valve was wide open. The crank angle of the photographs in each figure coincides with the experimentally determined point of initial injection. The dark areas were caused by multimoding of the ruby laser and prevented a portion of the fuel spray shown in Fig. 28b from being reconstructed.

Figure 30 illustrates the effects of combustion gases within the diesel engine on the image reconstructions. The hologram was recorded much later into the injection cycle as compared with those of Fig. 29 and combustion should be taking place. The finely speckled areas in the photographs are due to the gas density gradients. It was impossible to conclusively identify droplet images anywhere in the reconstructed volume under these conditions. However, regions void of the combustion gases can be observed and are pointed out in Fig. 30. This same structure is evident in Figs. 27a and c and 28a. The fact that combustion was taking place during this time was only assumed and not verified during the experiments.
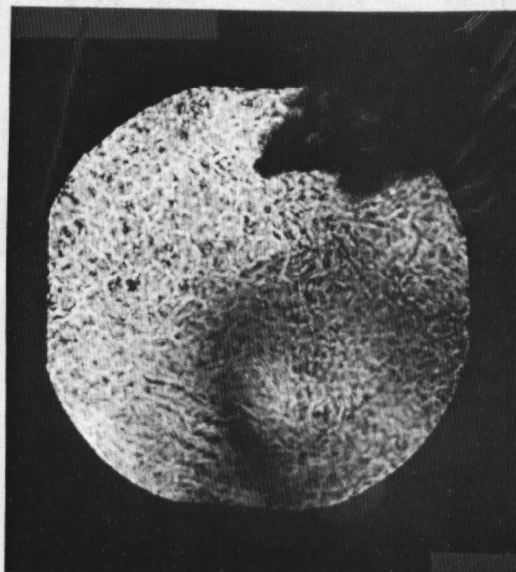
a. Choked air
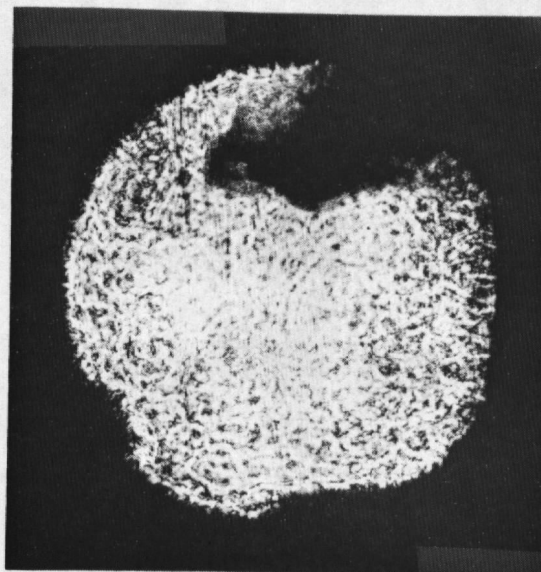
b. Full air

Figure 26. Background variations associated with air density;
1,000 rpm, fuel − 0.4.
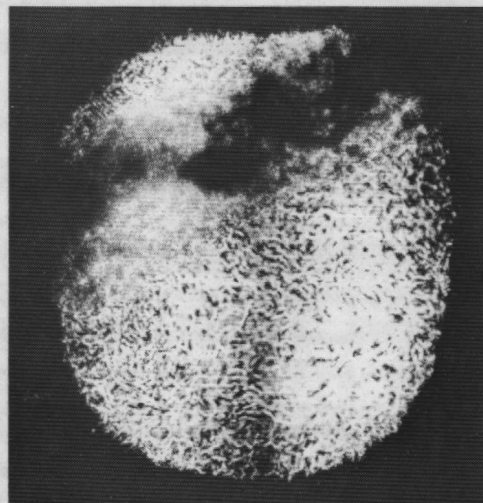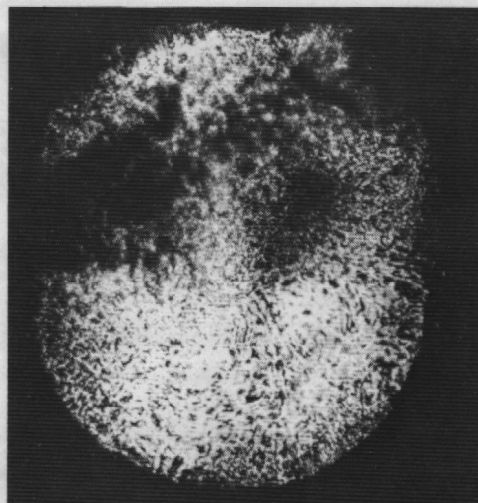
a. 7 deg BTDC b. 5 deg BTDC c. 4 deg BTDC
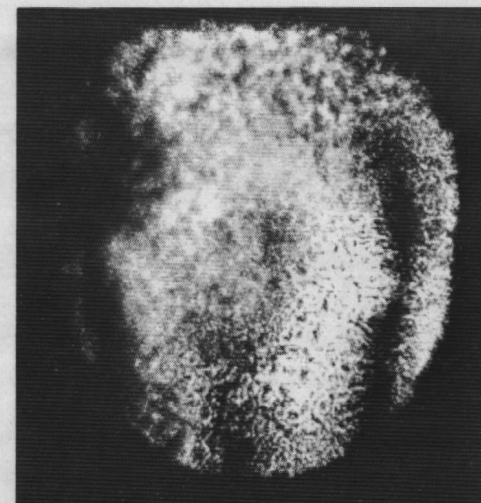
Figure 27. Side-band hologram reconstructions, TACOM diesel engine;
500 rpm, fuel setting = 0.25, full air.
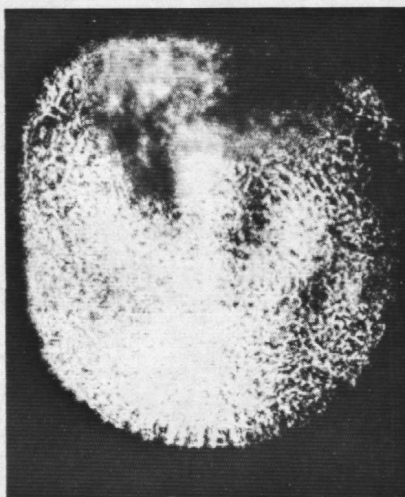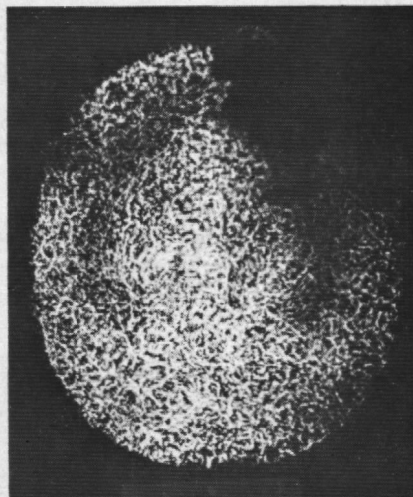
a. 11 deg BTDC   b. 10 deg BTDC   c. 9 deg BTDC
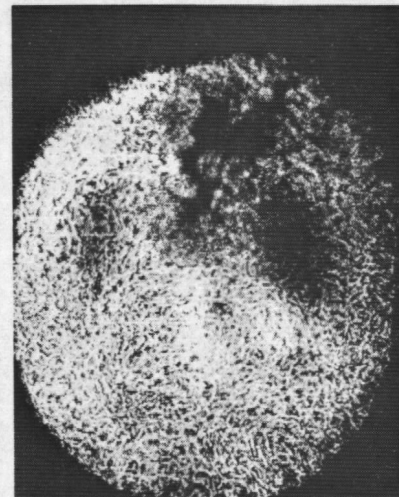
Figure 28. Side-band hologram reconstructions, TACOM diesel engine;
1,500 rpm, fuel setting = 0.4, full air.
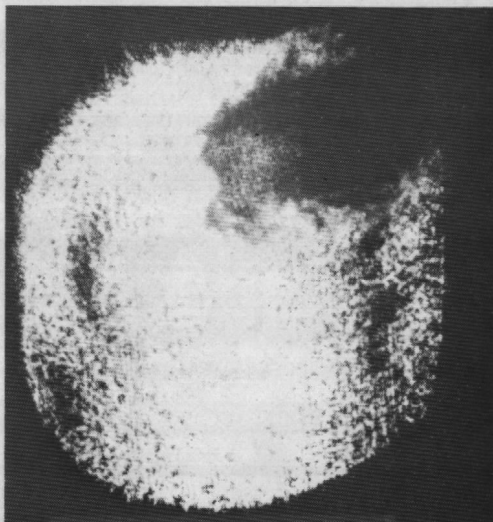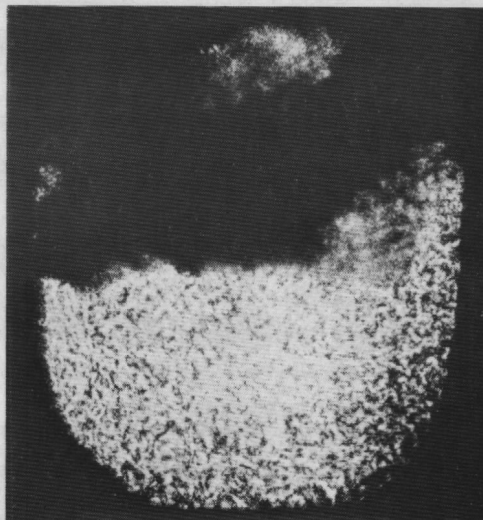
a. 18 deg BTDC   b. 17 deg BTDC   c. 16 deg BTDC
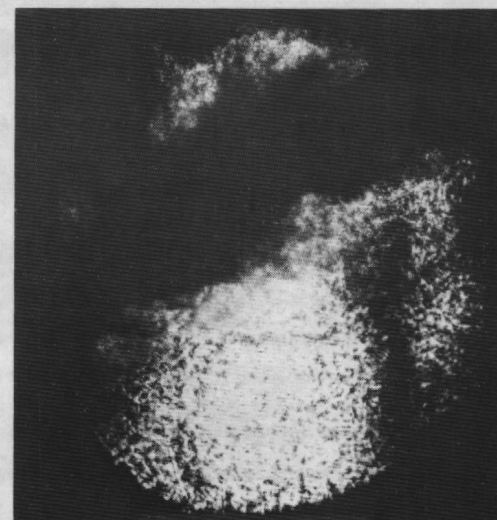
Figure 29. Side-band hologram reconstructions, TACOM diesel engine;
1,000 rpm, fuel setting = 0.25, full air.
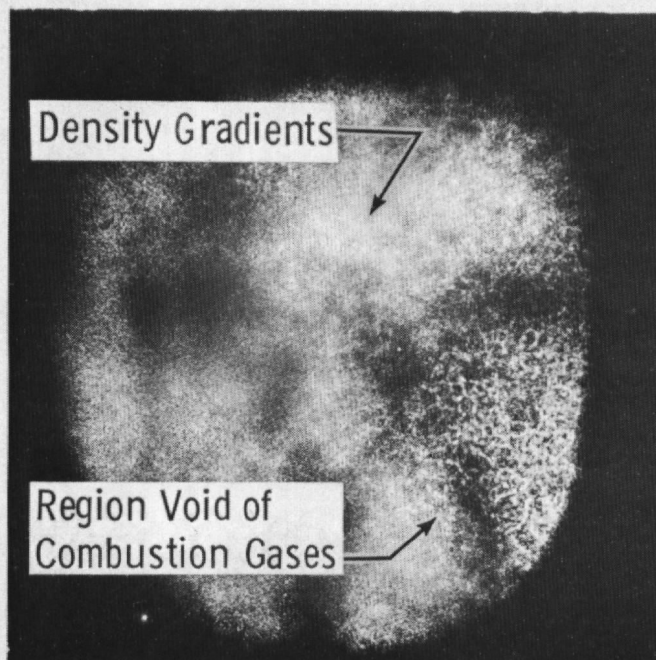
Figure 30. Side-band hologram reconstructions, TACOM diesel engine; 1,500 rpm, fuel setting = 0.25, full air (5.0 deg BTDC).

The various spray patterns that were reconstructed are shown in Fig. 31. The engine operating conditions were the same in all three cases with the only variations being the air mixture varying from choked to 0.5 and full air (1.0) or throttle fully open. The injector in the engine when these data were recorded was a replacement for the one used when Fig. 23 was recorded. The speckled region below mid-center of Fig. 31b was caused by fuel droplets on the window closest to the film (as in Fig. 20). These droplets focused 49 cm from the film on the side opposite to the fuel spray image because of the location of the object plane in the combustion chamber.

4.5 BACKSCATTER HOLOGRAPHY

Droplets within the optically dense regions of the fuel sprays could not be reconstructed from either sideband or in-line holograms for probably one of two reasons: either the light that is scattered by the droplet is blocked by intervening droplets or the droplet field prevents illumination of droplets on the far side of the spray near the film plane. A proposed solution to this problem was to illuminate the droplets from the front and mix the backscattered (and reflected) light with a reference beam. The front portion of the dense field could then conceivably be probed to a limited depth. On this premise, a front-lighted holography system shown in Fig. 32 was designed and used to take holograms of fuel droplets.

a. Air choked   b. Air = 0.5   c. Air = 1.0
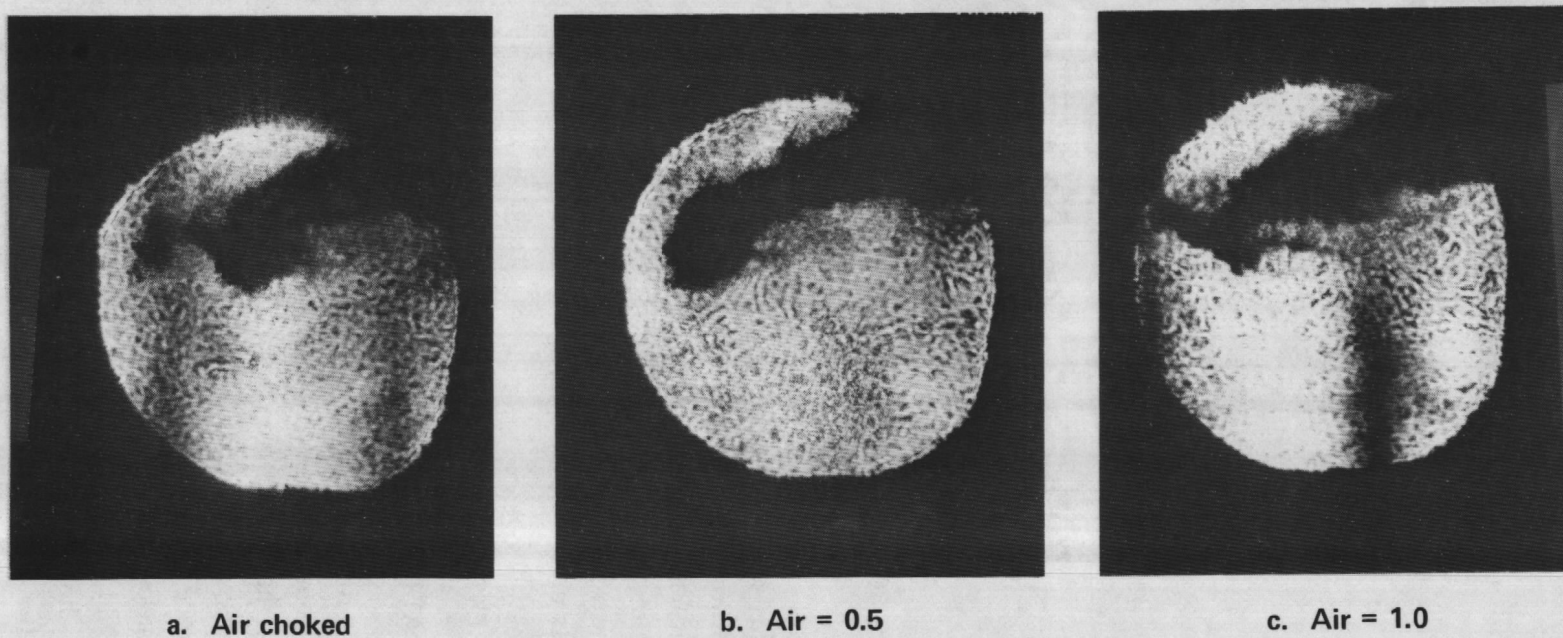
Figure 31. TACOM engine spray patterns; 1,000 rpm, air choked,
fuel = 0.4, crank angle = 12 deg BTDC.
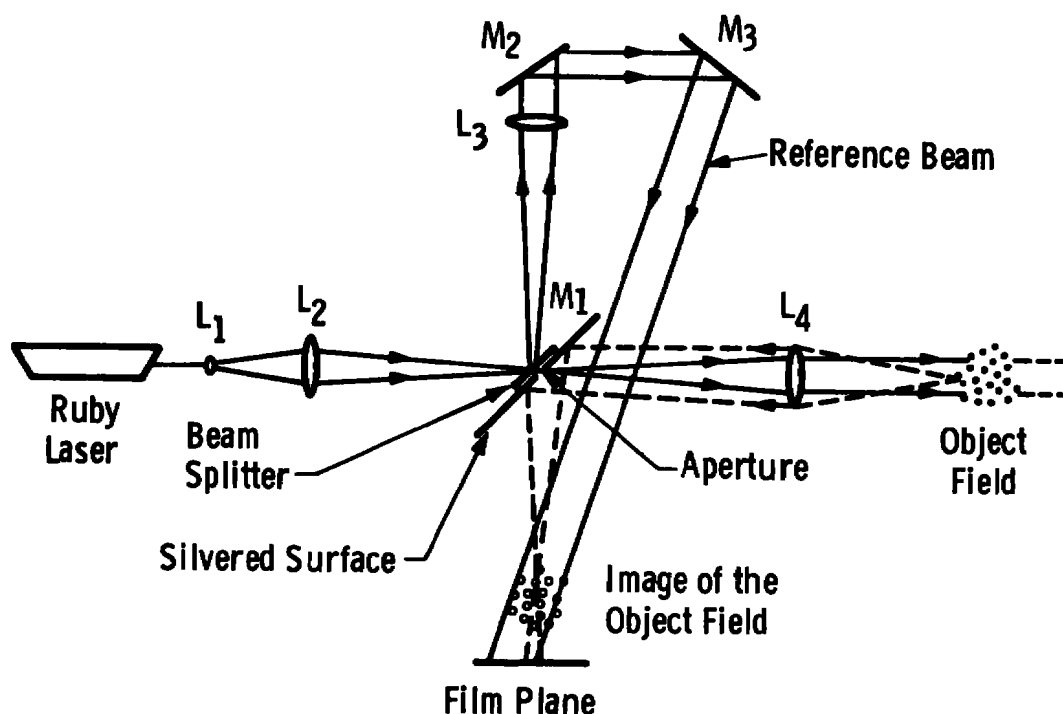
Figure 32. Front-lighted holocamera optical configuration.

The holocamera optical system allows the light from the ruby laser to be expanded and focused through a hole in the center of first surface mirror. A glass plate over the hole in the rear of the mirror reflects approximately seven percent of the light to a lens which collimates it. Mirrors M_2 and M_3 reflect this radiation onto the film for a reference beam. The object field is illuminated by light collimated by lens L_4. This lens also images the backscattered field near the film plane by means of M_1 to improve the resolution of the hologram.

Reconstructions from holograms recorded using this optical configuration were not of droplet images but rather of aberrated points of the light reflected by the droplet back to the film plane. The scattered field which would allow the individual droplet images to be reconstructed was not recorded even though 93 percent of the laser light served to illuminate the droplet field. As a consequence, droplet diameter information could not be measured from the data. Part of this problem can be explained by the fact that the aperture, in the mirror through which the object illumination passed, filters the reflected and scattered light from the object field. Therefore, low-frequency information about the field is removed before the image is formed. The effect of this aperture on the reflected light is to decrease the point image intensity.

It is conceivable that an indication of droplet size could be obtained with this technique by measuring the amount of light in each reconstructed spot, since the total light collected by lens L_4 is proportional to the particle radius (Ref. 14). However, in order to eliminate the effects of the hologram recording, developing, and reconstruction processes a known intensity calibration beam would also have to be recorded. This third light beam would be split from the illumination light and recorded on the film. The power density diffracted into the reconstruction of this wavefront would then provide intensity calibration for size measurements (Ref. 15).

Velocity and propagation of individual droplets can also be determined by recording a multiple exposure front- (or side-) lighted hologram of the droplets. Individual point images would not necessarily have to be reconstructed if the droplet moved on the order of a resolution spot between exposures since the images would merge together in the reconstruction into a line indicating the propagation path. In high-density regions where individual droplet paths are indiscernible, the trajectories of the droplet field could be observed collectively to determine the degree and location of swirl in the combustion chamber. Reference 16 describes a side-lighted system which was used to record 100 separate exposures on a single film plate. Because only the reflected light was recorded, the increase in noise normally associated with the square root of the number of exposures was not observed.

If particle size is not important it would be possible to determine the propagation paths of droplets smaller than the resolution limit of the film (Ref. 16). However, this is predicated on the ability of the film to record the backscattered or reflected radiation.

Although the front-lighted holographic technique was not successful in recording and reconstructing fuel droplet images for size measurements, it does appear to be applicable to determining droplet size (indirectly) and droplet trajectories for spray regions that are too dense for back illumination. In addition, the presence of droplet sizes below the resolution limit of the hologram can be observed from the reconstruction of the diffraction-limited point images. The feasibility of these indirect object measurements for combustion analysis still must be proven in an engine environment, however.

5.0 APPLICATION OF FRINGE TECHNIQUES

5.1 LASER VELOCIMETER

Laser Doppler velocimeters (LDV) are interferometer systems which have demonstrated great versatility and practical value in a number of applications (Refs. 19 through 28). Velocities have been measured over a speed range of mm/sec to km/sec (Refs. 22 and 27). These devices have also been used to measure velocity in hostile environments

such as over long transmission atmospheric paths or over short transmission path flame environments (Refs. 26 and 29). Basically, there are two types of interferometer systems that are used as LDV instruments; these are shown in Fig. 33. The first type of interferometer (Fig. 33a) is called the local oscillator or reference beam LDV. This device has been found to work well when a large number of scattering particles are in the region of measurement (henceforth called the probe volume) and the density variation of the fluid containing the particles is small. The Doppler shift of the light scattered from a single illumination beam is measured by mixing the scattered light stemming from a particle traversing the probe volume with an unperturbed local oscillator beam to remove the fundamental laser frequency at the photodetector. The second type of interferometer is called the dual-scatter or differential Doppler LDV (Fig. 33b). This instrument has been

To Signal Processor ← Detector

b. Local oscillator observation mode

Beam Splitter

Laser

α

k_{si}

Solid Lines – Reference Beam
Dotted Lines – Scattered Radiation

a. Dual-scatter observation mode

Detector

To Signal Processor
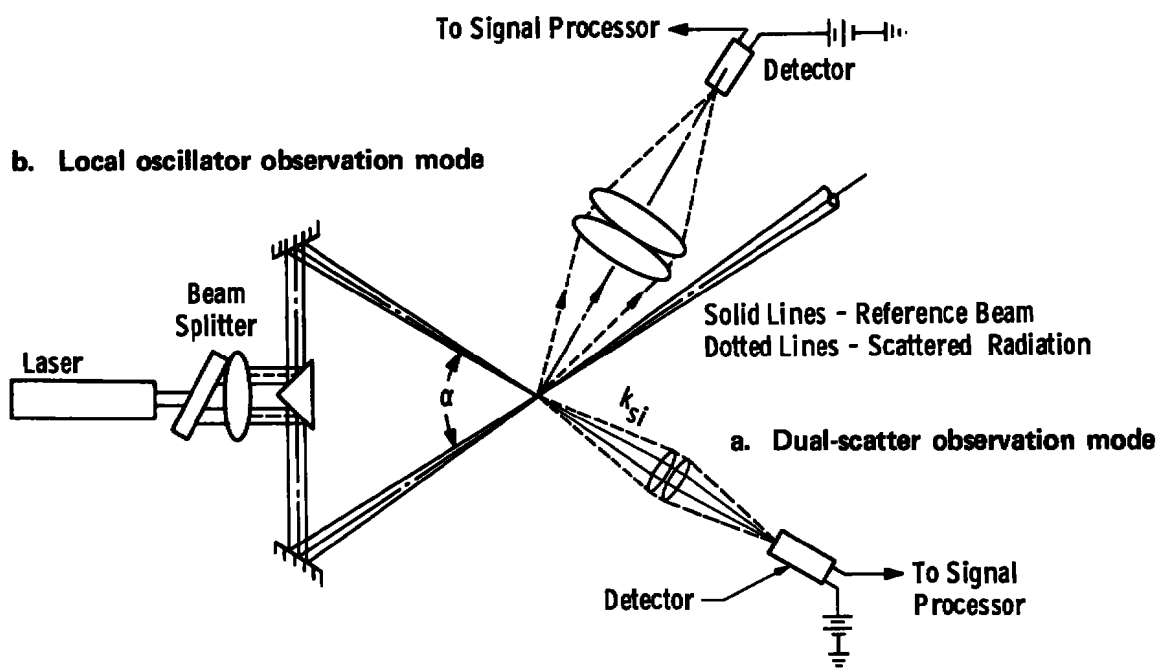
Figure 33. Multi-beam interferometer arrangement and different observation modes.

found to work well when the number of scattering particles in the probe volume is small and when density variations of the medium surrounding the particle are "large" (Ref. 30). This device measures the difference in Doppler-shifted frequencies from two or more beams simultaneously illuminating the particle. This difference can be shown to be constant for any viewing angle. Therefore, the velocity signal from such a device does not have the usual frequency dispersion commonly associated with the Doppler signal measured with local oscillator LDV systems. Furthermore, it has the added advantage that the scattered light collection system can be made as large as desirable. Dual-scatter LDV

systems have been shown to have a number of additional practical advantages other LDV systems do not have. These advantages relate primarily to simplicity in optical design and an insensitivity to vibrations that have commonly degraded the signal quality of other LDV systems.

A convenient way to visualize the operation of these interferometers for most applications is called the "fringe model." In this model interference fringes (either real or virtual) exist in a region of measurement designated the probe volume (Fig. 34). For example, for dual-scatter LDV, it is straightforward to show that real interference fringes exist in the region of the beam crosspoint. These fringes lie in planes parallel to the bisector between the beams and perpendicular to the plane of the beams. As particles traverse successive bright and dark fringes they are said to scatter light proportionately to the light intensity contained in the interference fringes. Thus, the reciprocal of the time period required for a particle to traverse a fringe cycle, δ, is identical to the Doppler difference frequency. The model, while adequate to account for fringe frequency, does lead to some misleading conclusions when scatter signal intensities are desired. This is particularly true for large included angles, a, between the illuminating beams.

$$\text{Frequency of Cutting Stationary Fringes} = \frac{v}{d}$$
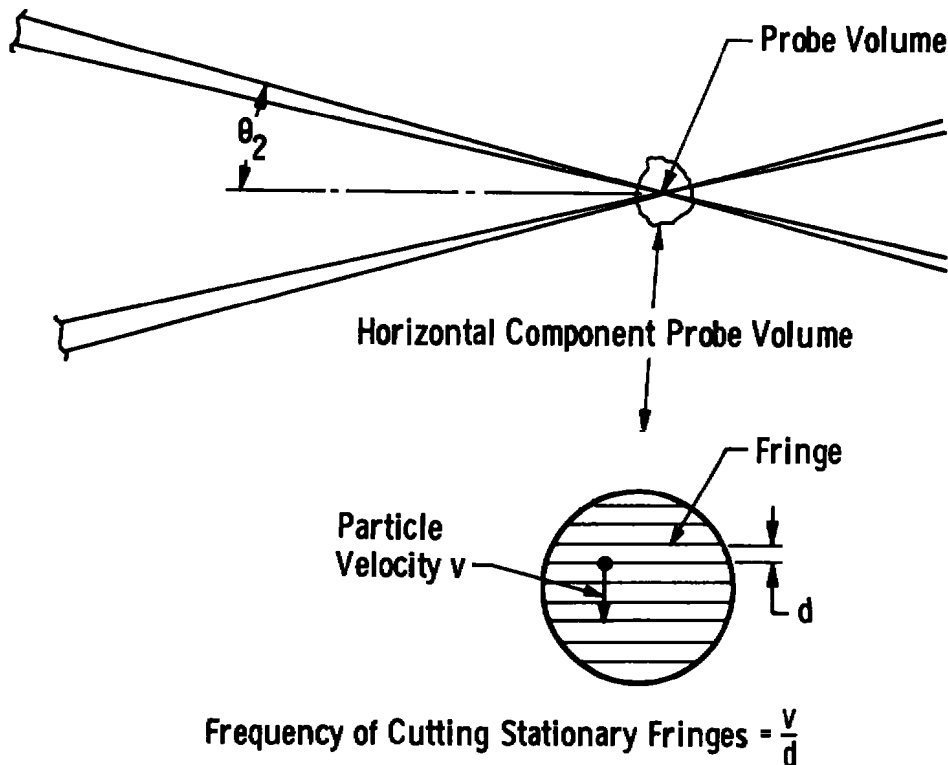
Figure 34. Fringe analysis of laser velocimeter.

Once the scattered light is collected and converted into an electrical current, the Doppler frequency must be measured. The specification of a particular electronic technique to measure the frequency of the current containing the Doppler frequency depends strongly on the type of interferometer used to transmit the illumination and collect the scattered light. Nevertheless, experience has shown that even under conditions where the number density of scattering particles is high, the LDV signal can be processed effectively. A schematic of such a pulse is shown in Fig. 35. The high-frequency term contains the Doppler shift information; the envelope describes the trajectory of the particle as it passes through the illumination beam or beams. Devices such as phase lock loops which depend on continuous signals obviously do no work well with discrete signal burst, especially if the frequency varies. A device which has been found to work extremely well with this type of LDV signal, filters the envelope (which contains no velocity information) and measures the period of the high-frequency portion of the burst (Ref. 31).
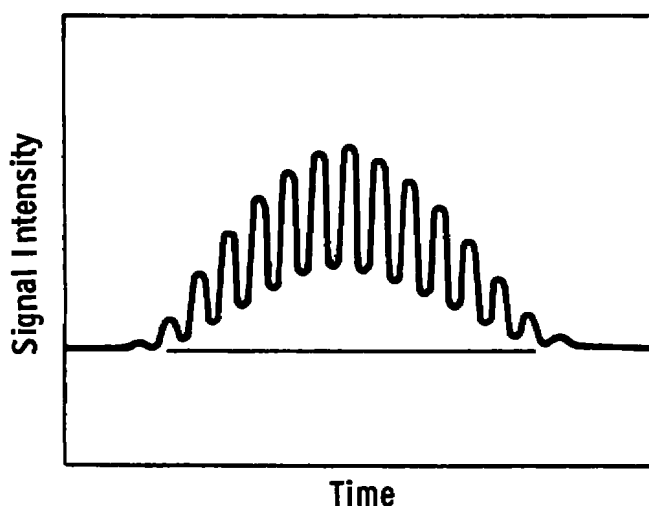
Figure 35. Example of an LDV Doppler pulse.

5.2 THEORY OF THE DUAL-SCATTER LASER VELOCIMETER

The detailed theory of both the local oscillator and the dual-scatter LV is well understood and will not be reviewed (Refs. 19 and 20). However, for the sake of clarity, an alternative analysis of the dual-scatter technique is presented. The laser source is split up into two beams (Fig. 34), for each velocity component, and focused to a diffraction-limited region of Gaussian intensity containing essentially planar wavefronts of radiation. In view of the coherence characteristics of the source, the beams will interfere constructively and destructively to establish a set of closely spaced, planar, stationary

interference fringes at the beam crossover, or focal, region. The peak-to-peak fringe spacing, d, is

$$d = \frac{\lambda_o}{2\eta \sin \theta/2} \qquad (5\text{-}1)$$

where λ is the wavelength, η the index of refraction of the medium, and θ the angle between the beams. As a particle traverses the focal volume at a velocity v the interference fringes are cut at a rate equal to

$$f_D = \frac{2\nu\eta \sin \theta/2}{\lambda_o} \qquad (5\text{-}2)$$

the measured modulation frequency. It has also been shown that only one component of velocity, namely the component normal to the interference fringes, is measured. It is straightforward to add additional optics to determine the second and third velocity components (Ref. 32).

The $1/e^2$ diameter of the focal region is given by

$$D_f = \frac{4}{\pi} \lambda_o \frac{F.L.}{d_B} \qquad (5\text{-}3)$$

where F.L. is the focal length of the lens and d_B is the beam diameter at the focusing lens. The number of fringes contained in the probe volume can be determined by dividing the peak-to-peak fringe spacing into the focal diameter as follows:

$$N_s = \frac{8}{\pi} \frac{FL}{d_B} \eta \sin \theta/2 \qquad (5\text{-}4)$$

This can be further simplified since $\theta/2 \ll 1$ such that $2 \sin \theta/2 \simeq \theta$, With this approximation,

$$N_s = \frac{4}{\pi} \eta \frac{d_s}{d_B} \qquad (5\text{-}5)$$

where d_s is the spacing between the beams at the transmitting lens. The number of fringes in the focal volume is important as a minimum number (nominally 10) are required for processing.

5.3 BRAGG CELLS

The measurement of two orthogonal velocity components is a relatively straightforward procedure using the dual-scatter LDV just described. However, the fundamental problem to be resolved is the ambiguity in the direction of the velocity vector. The signals yield the absolute value of frequency, the magnitude of velocity, not the direction. With the application of Bragg cells the directional ambiguity is resolved. Using this technique, light from the laser is simultaneously split and frequency-shifted into four beams with a two-dimensional ultrasonic Bragg cell (TDBC). The TDBC consists of distilled water through which two independent ultrasonic sound waves propagate. The acoustical wavefronts are equivalent to two linearly superimposed moving phase gratings, or fringes. As the light beam interacts with these wavefronts a portion is diffracted. The resultant interaction produces four beams. In practice, a multiplicity of beams will produce higher orders of diffraction. Each order is shifted from the undeviated beam by Nf_0 where f_0 is the Bragg modulation frequency and N the order (Fig. 36). The lenses which focus the beams to the crossover region (probe volume) essentially image the traveling waves as moving, mutually orthogonal, interference fringes.
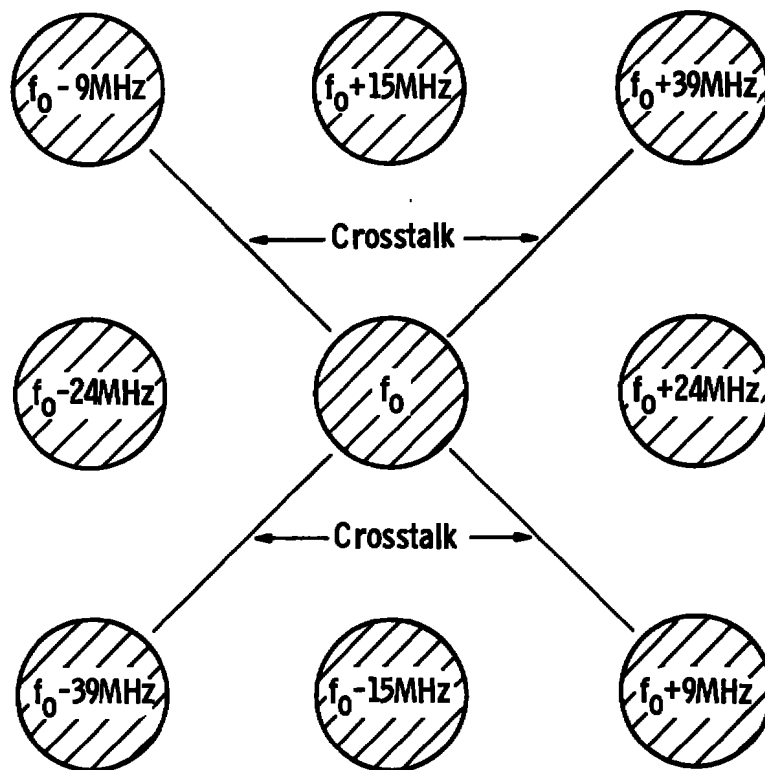
Figure 36. Diffracted beams from Bragg cell showing wave propagation.

Briefly the technique, with recourse to Fig. 37, is analyzed as follows (Ref. 4):

$$f_{D1} = f_o \pm \nu \eta - (\vec{k}_{s1} - \vec{K}_{o_1})$$

(5-6)

$$f_{D2} = f_o \mp f_m \pm \nu \eta \cdot (\vec{k}_{s2} - \vec{K}_{o_2})$$

where f_o is the light frequency, f_m the Bragg modulation frequency, and η the index of refraction. Since the particles scatter light from the same point, the original $\vec{K}_o$ propagation vector disappears ($K_{o1} = k_{o2}$) when the difference frequency is obtained, e.g.:

$$f_D = (f_{D2} - f_{D1}) = \mp \nu \cdot (\vec{K}_{s2} - \vec{K}_{s1}) + f_m$$

(5-7)

rearranging and performing the analysis results in

$$f_D = f_m \pm \frac{2 \nu \eta \sin \theta/2}{\lambda_o}$$

(5-8)
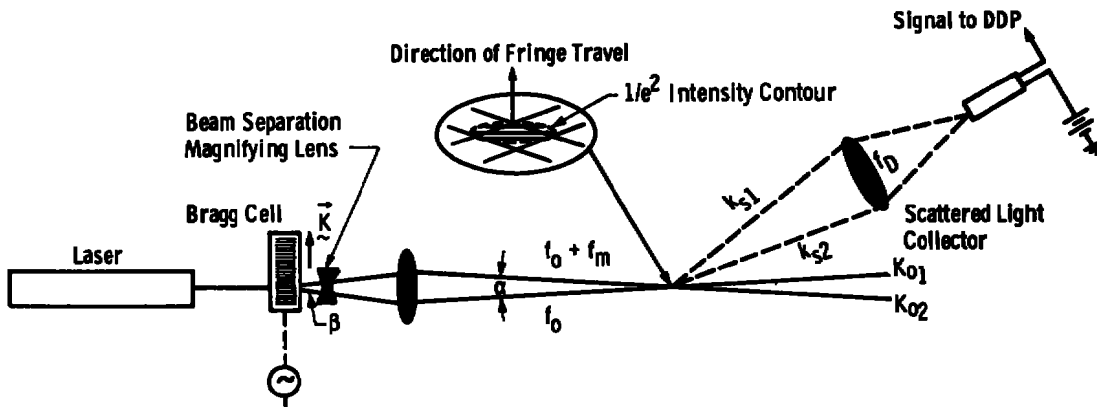
Figure 37. Schematic of the Bragg cell LDV system.

When the particles are traversing the focal volume in the direction of the moving fringes, the signal frequency will be lower than the modulation frequency. Conversely, if the particles are traversing opposite the direction of the traveling fringes, the measured frequency will be higher than the modulation frequency. Furthermore, since the modulation frequency is superimposed upon stationary fringes, the number of effective fringes (N_e) (stationary plus traveling) within the focal volume becomes

$$N_e = N_s (f_m/f_D \pm 1)$$

(5-9)

N_s is obtained from Eq. (5.4). A given range of particle velocities thereby defines a band of corresponding frequencies center at f_m. By using two different frequencies in the two different TDBC water columns, two discrete frequency bands (along with sum and difference crosstalk bands) are produced. A particular velocity component in the scattered light can then be identified electronically by frequency separation techniques (Ref. 33). Thus, both velocity components can be observed with a single photodetector. This fact considerably simplifies the scattered light detection and collecting system.

5.4 EXPERIMENTAL ARRANGEMENTS IN A DIESEL COMBUSTION CHAMBER

The lack of access to the combustion chamber with physical probes makes the LDV system an ideal velocity measurement device. The constantly varying velocity gradients in the combustion chamber makes the Doppler "burst" type readout ideal for obtaining the statistical trends at points in the combustion cycle. These velocity trends will determine the general flow field in the combustion chamber with varying piston position.

It must be remembered that the LDV system data stem from the motion of particles trapped in the fluid media in the combustion chamber. The origin of these particles is from several sources: (a) fuel droplets, (b) ambient dust particles in the air, (c) oil particles, (d) combustion products, and (e) water droplets. These particles appear in various portions of the cycle and contribute to a highly varying particle density field. Velocity measurements under these conditions must therefore accommodate these particle density changes.

5.4.1 Diesel Engine Modifications

The engine used for the velocimeter experiments was a Turner diesel, two-cycle, three-cylinder engine. Each cylinder consists of a 3-5/8-in. bore with a 3-1/2-in. piston excursion. Originally this engine was modified for holographic particle-sizing studies, and no attempts were made to optimize the design for LDV applications. The modification consisted of a 1-in.-diam hole bored 1 in. from the bottom of the 2-1/2-in.-thick cylinder head to accommodate the viewing ports. The viewing ports are made of quartz, 1 in. thick and 1 in. in diameter. A 7/8-in. vertical hole bored in the center of the head and into the viewing port chamber provides the link to the combustion chamber. Figure 38 shows the general layout of the viewing port and cylinder.

Opening of the port in the two-cycle engine occurs at 105 deg before top dead center (BTDC) for the intake and 88 deg after top dead center (ATDC) for the exhaust. Initially, the operating procedure was to start the engine (cold), but the windows fogged-up almost immediately because of the fuel and oil that collected on them. Later, other techniques were investigated to alleviate this problem. Currently, the procedure requires running the
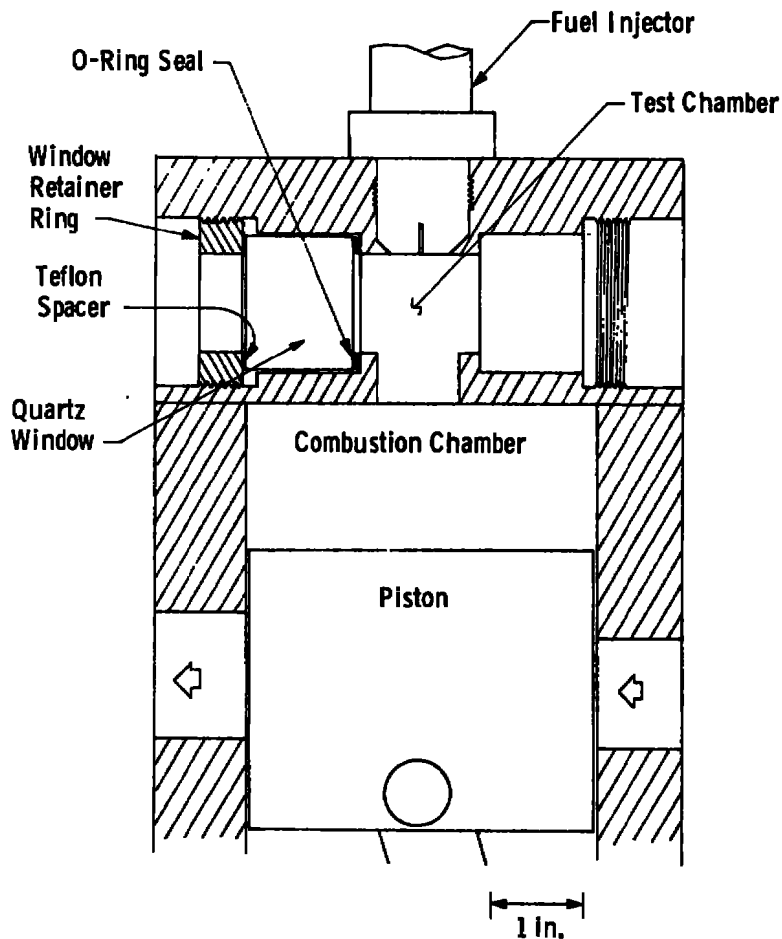
Figure 38. Test cylinder modification of Turner engine.

engine to operating temperature and subsequently shutting down for window cleaning. Operating the engine immediately after window cleaning greatly reduces fogging and allows engine operation and data taking for at least 10 minutes. Velocity measurements were made in a plane passing through the center of the cylinder and perpendicular to the laser beams. A photograph of the experimental arrangement is shown in Fig. 39.

5.4.2 Crank-Angle Encoder

The crank-angle position indication is obtained by attaching a synchro-transmitter on the flywheel of the engine. This synchro drives a receiver synchro located on a stable, nonvibrating table near the engine. One- and 1.5-deg resolution may be obtained with the indicator wheel which was fabricated by photographing a standard 8-in. circular protractor. The photographic negative is cut out and mounted on the receiver synchro. A small photodiode detector senses the markings on the negative.
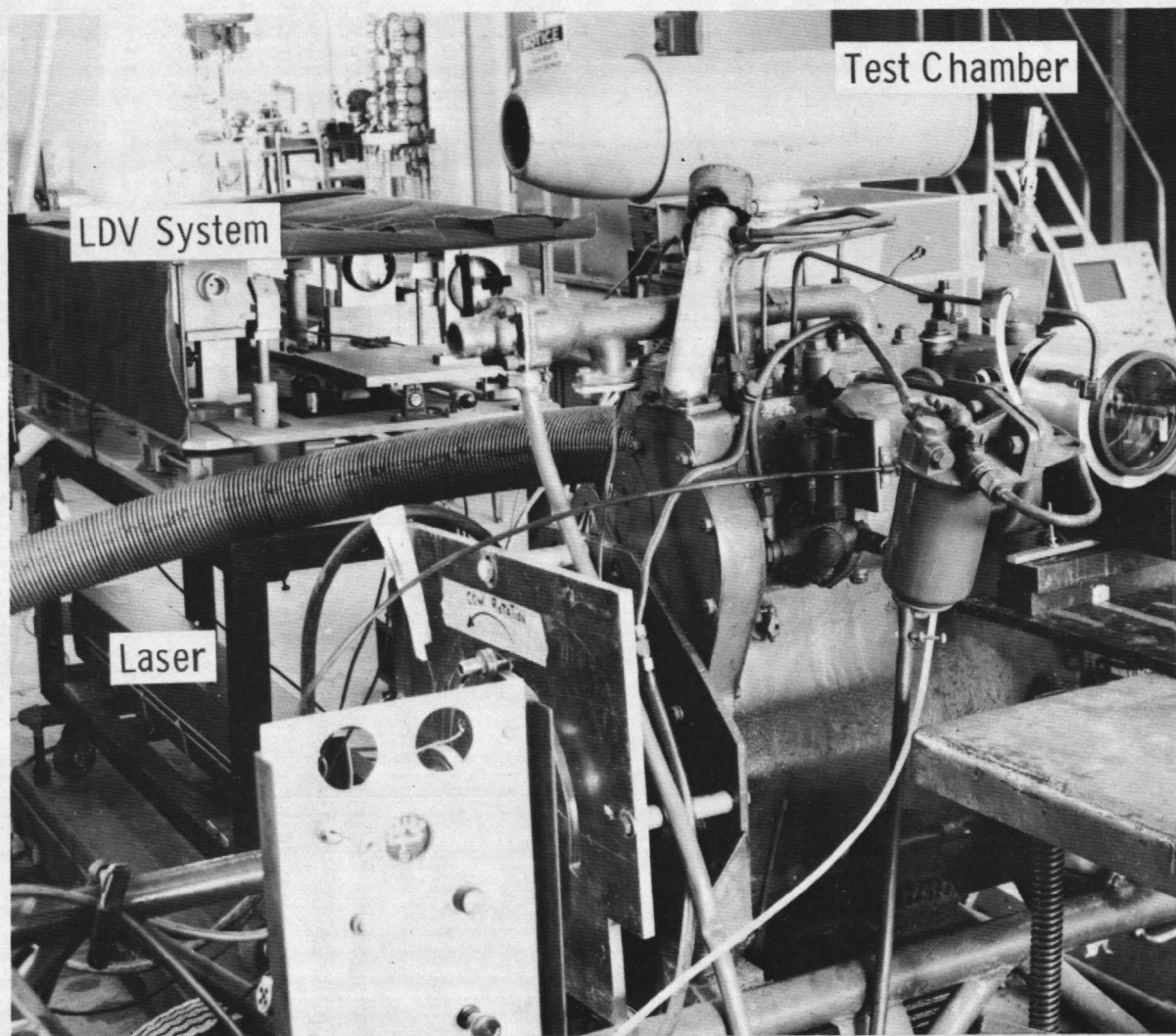
Figure 39. Turner diesel test setup.

Although simple·in concept, the synchro technique for crank-angle indication is quite accurate and results in better control of the crank-angle pulses than previous techniques. The synchro drive also smooths out the small erratic angular motion of the engine flywheel. Calibration was effected with a strobe triggered by the re-set pulse occurring at the 0-deg mark of the crank-angle indicator wheel. By rotating the receiver synchro relative to the photodiode sensors, accurate bottom dead center (BDC) was determined. Figure 40 shows the crank-angle indicator wheel with a synchro drive system on the transmitter and the receiver.

5.4.3 Probe Volume Alignment Gage

In order to determine the precise location of the LDV probe volume in the combustion chamber, an alignment gage was built. This device has a 10-mil wire suspended at the location where the measurement is to be made. The wire is attached to an arm reaching to the center plane of the combustion chamber. An xyz micrometer-positioning device allows accurate placement of the wire. Initial calibration was effected by removing the injector and gaging to the center of the chamber. The xyz positioner was mounted on the engine with dowel pins to allow accurate replacement of the alignment gage after removal.

The probe volume was aligned by positioning the crossover point on the wires such that an equally intense diffraction pattern appears on both sides of the wire. Figure 41 shows the alignment gage and its installation on the engine.

5.4.4 Signal-Processing System

The signal from the photomultiplier tube (PMT) is introduced to a signal separation spectrum translator system (SSST) and to a visibility processor schematically shown in Fig. 42. The objective of the SST system is to separate signals from the two components of velocity that are simultaneously being detected by the photomultiplier tube and to translate these signals to frequencies which will allow accurate determination of each signal period by Doppler processor. Figures 43 and 44 give the LDV frequency spectra before and after translation and separation for the two ranges of the velocities which are covered with this particular setup. In the figures all frequencies accepted by the photomultiplier tube are shown; that is, the information beams I1 and I2 in addition to the crosstalk CT1 and CT2 are shown.

Sources of digital data include a crank-angle counter, a Model 6 LV (Ref. 20) Data Processor (horizontal velocity component), a Model 8 LV Data Processor (Ref. 28) (vertical velocity component), and a visibility processor (particle size) (Ref. 36). Each data source requires a gate pulse to initiate a reading.
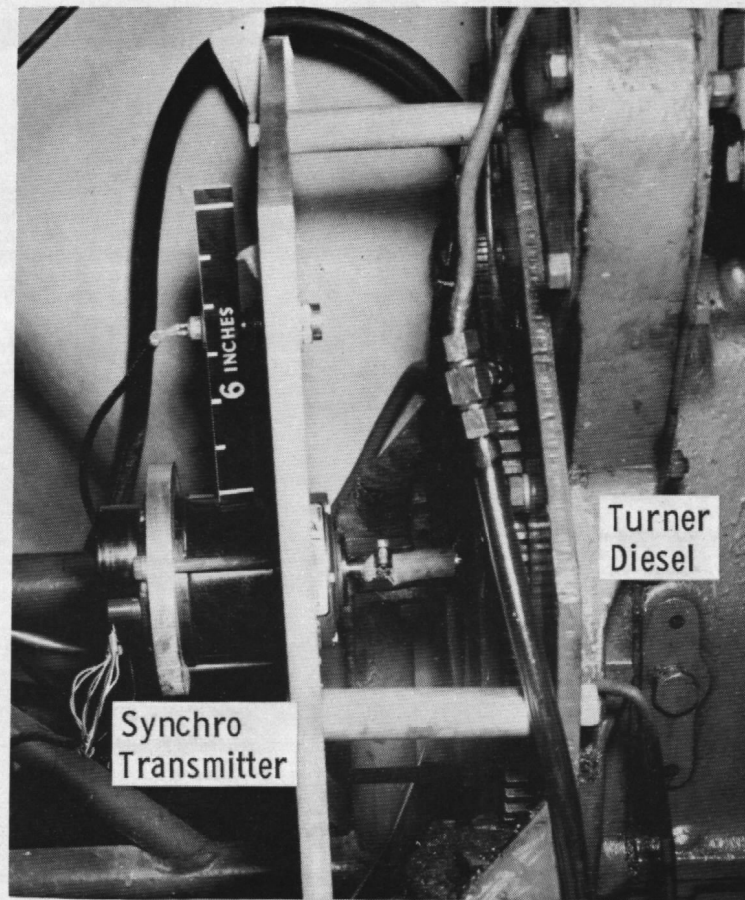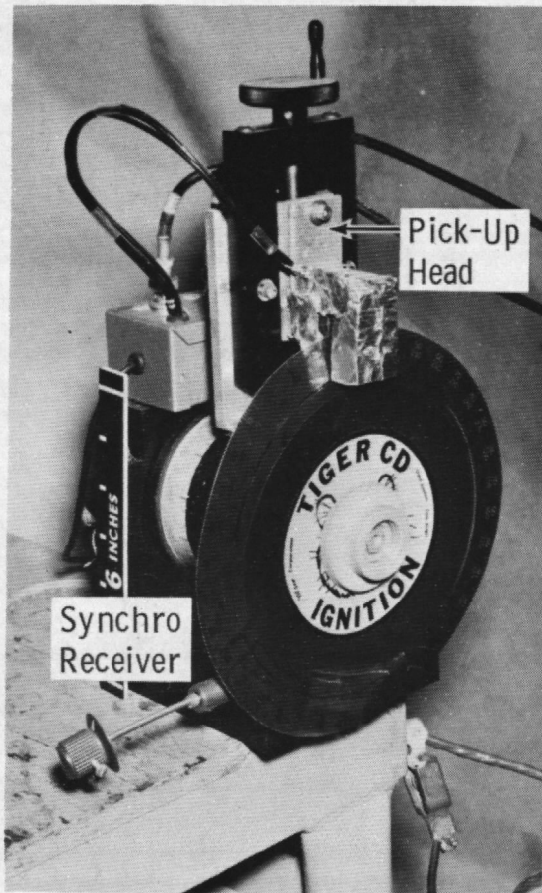
Figure 40. Synchro-crank-angle encoder.
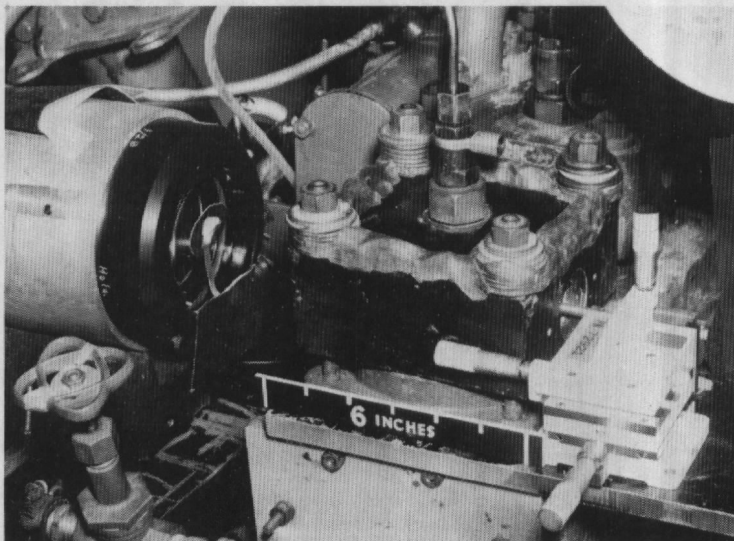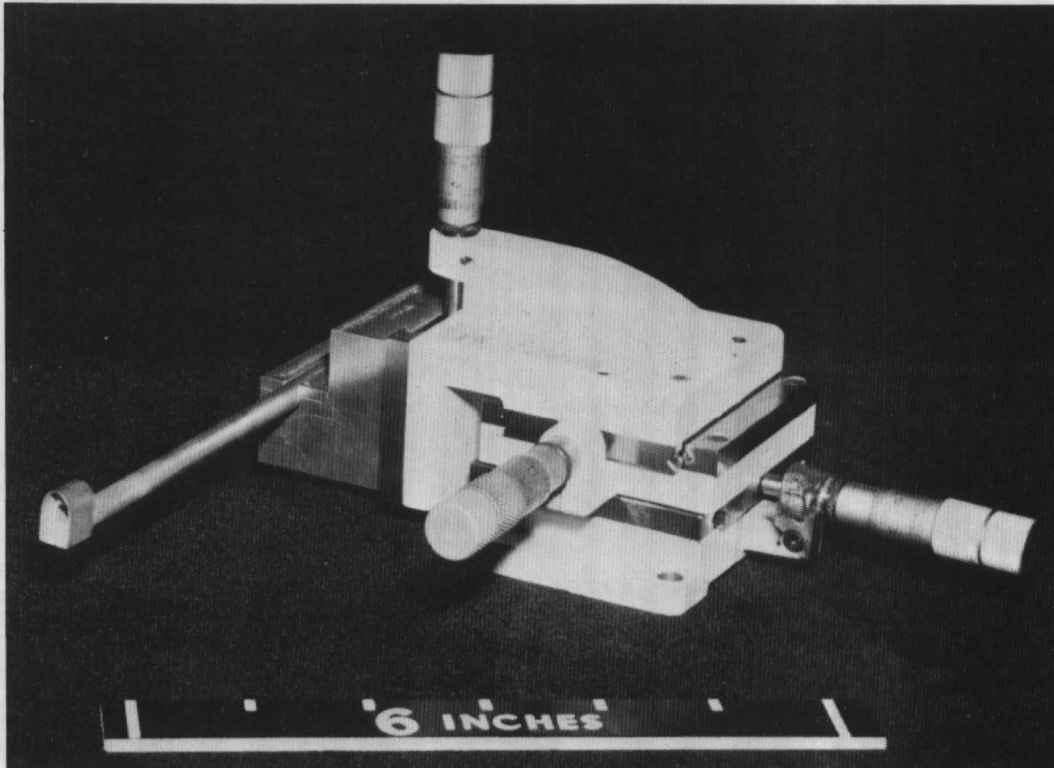
Figure 41. Probe volume alignment gage.
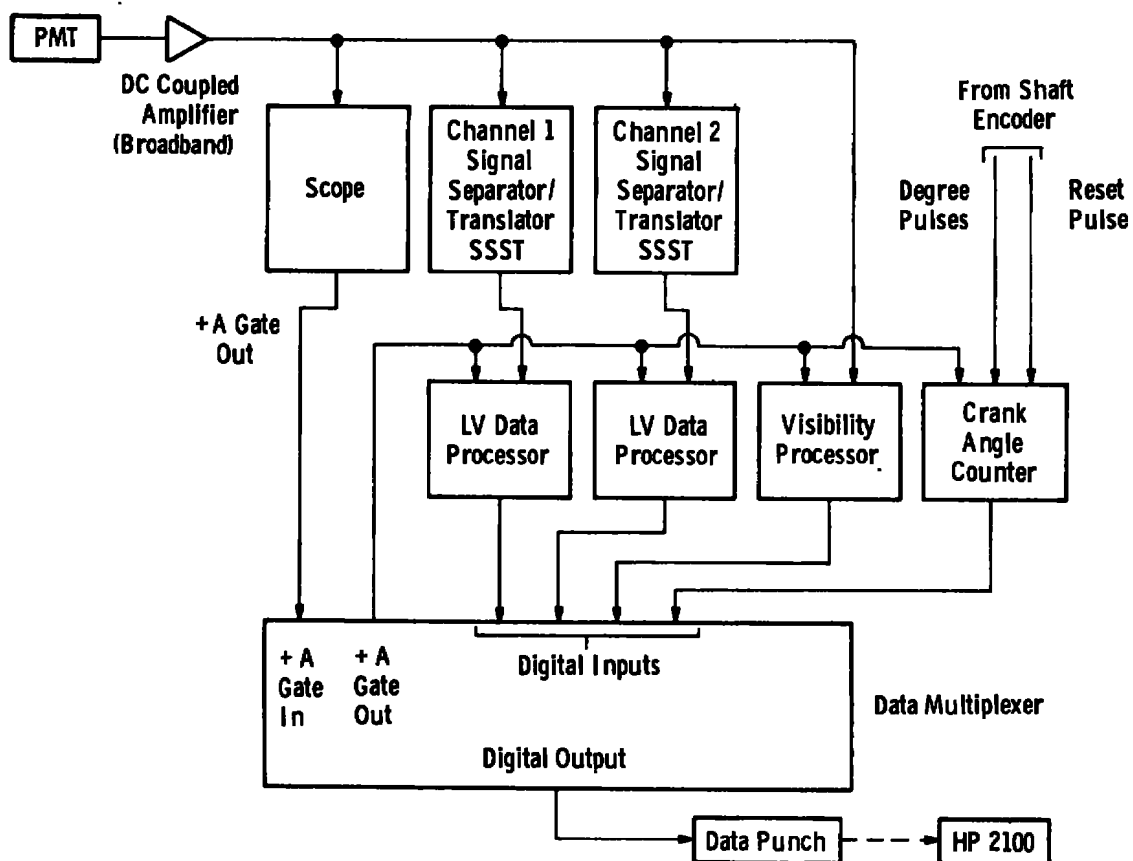
Figure 42. LV and particle-size signal processing/data acquisition system.
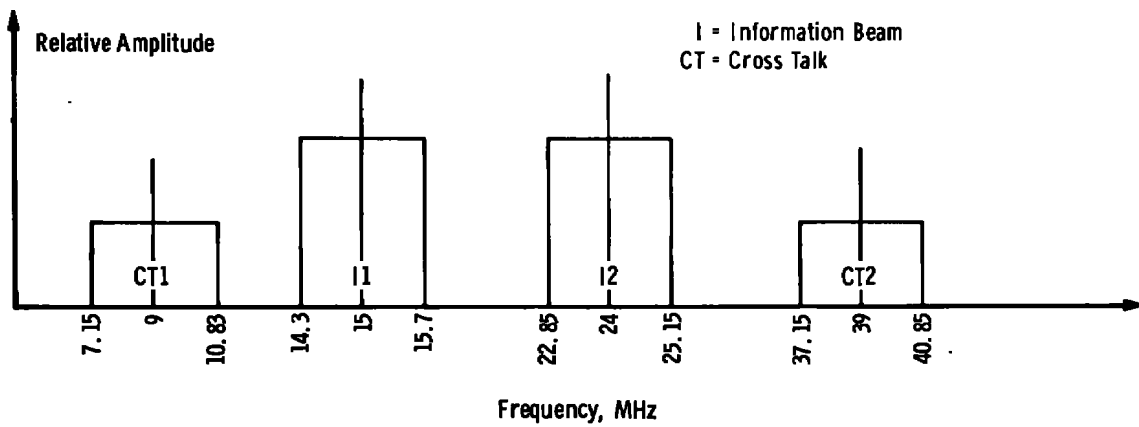
a. Spectra for ±70 m/sec velocities
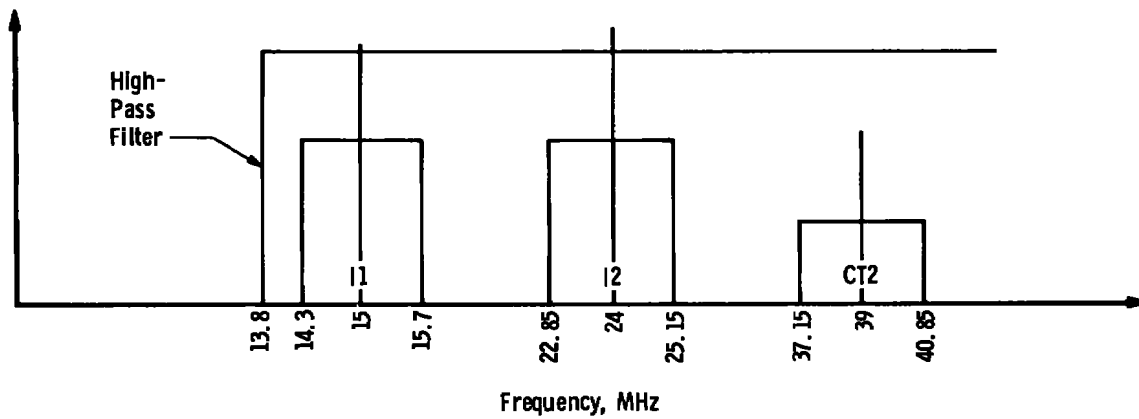
b. Ch. 1 spectra following 13.8-MHz high-pass filter
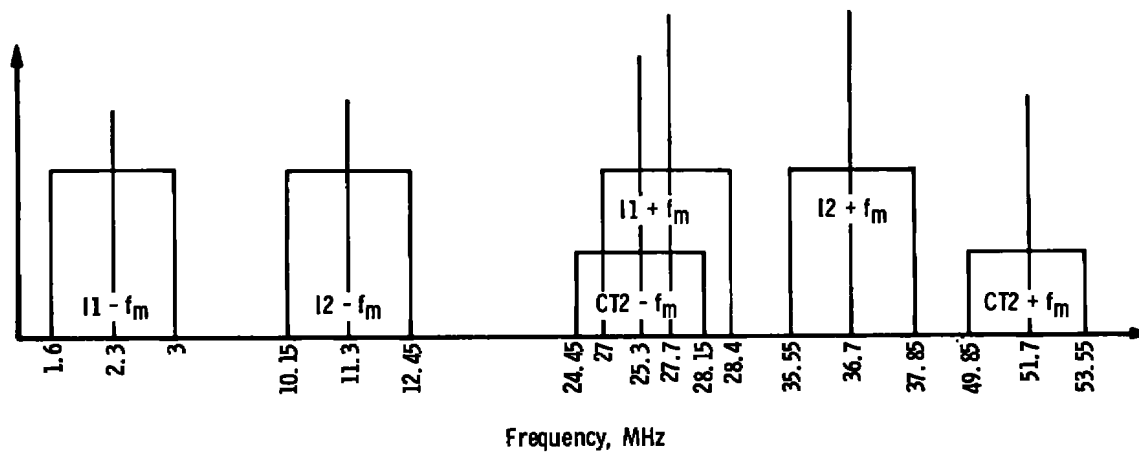
c. Ch. 1 spectra after mixing with f_m = 12.7 MHz

Figure 43. Signal processing for ±70 m/sec at
15 and 24 MHz.

Low-Pass Filter

$I1 - f_m$

1.6 23 3

Frequency, MHz

d. Ch. 1 spectra after mixing and low-pass filtering at 5 MHz

High-Pass Filter

I2

CT2

21.00 22.85 24 25.15 37.15 39 40.85
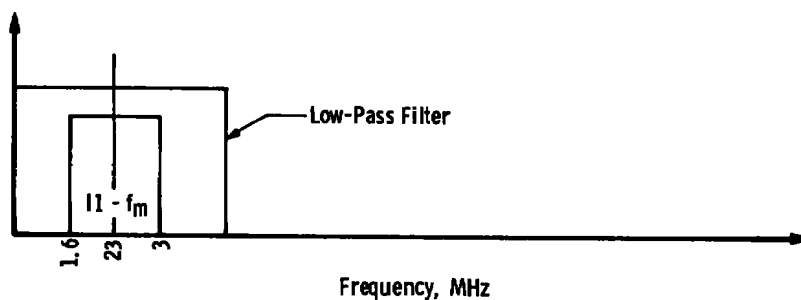
Frequency, MHz
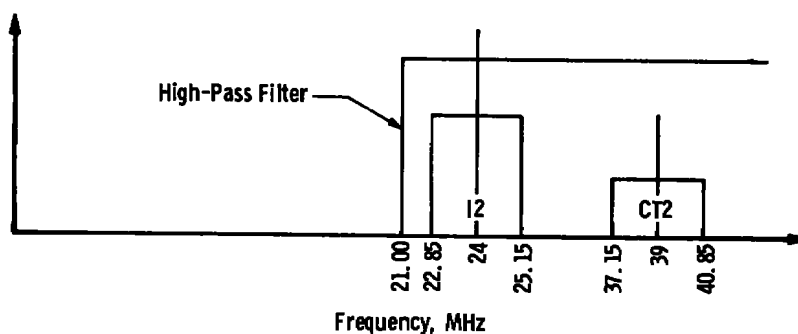
e. CH.2 spectra following 21-MHz high-pass filter

$I2 - f_m$

$CT2 - f_m$

$I2 + f_m$

$CT2 + f_m$

1.85 3.0 4.15 16.15 18.0 19.85 43.85 45.00 46.15 58.15 60.00 61.85

Frequency, MHz
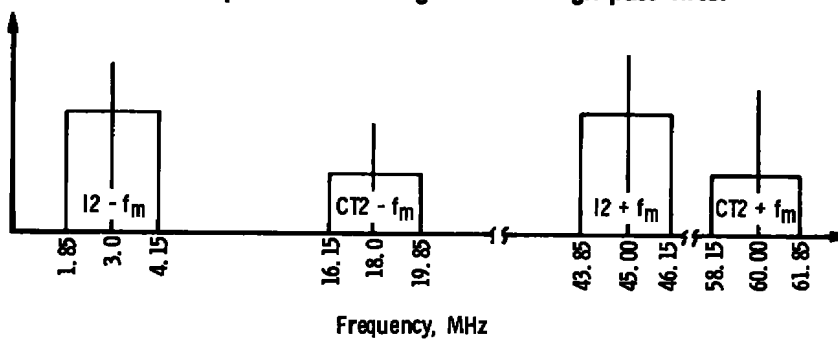
f. Ch. 2 spectra after high-pass filtering and mixing with f_m = 21 MHz

Low-Pass Filter

$I2 - f_m$

1.85 3.0 4.15 9.00

Frequency, MHz
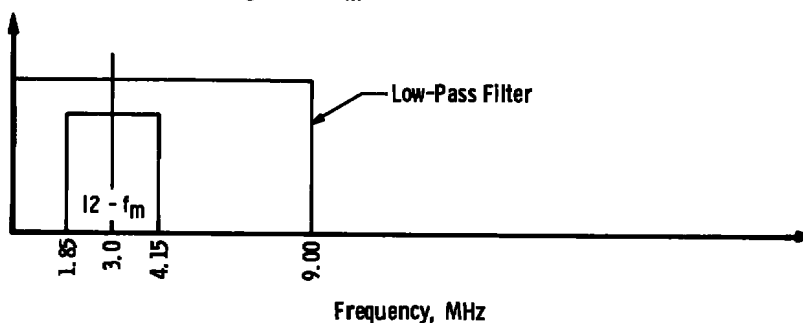
g. CH. 2 spectra after mixing and low-pass filtering at 9 MHz

Figure 43. Concluded.

Relative Amplitude

CT1 I1 I2 CT2

8.68 9 9.32   14.88 15.0 15.12   23.8 24.0 24.2   38.68 39 39.32

Frequency, MHz
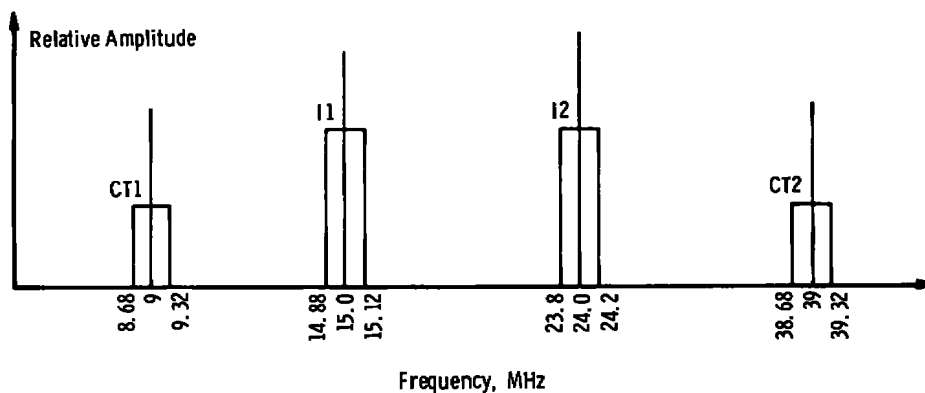
a. Spectra for ±12 m/sec velocities

I1 - f_m

0.11 0.230 0.35

Frequency, MHz
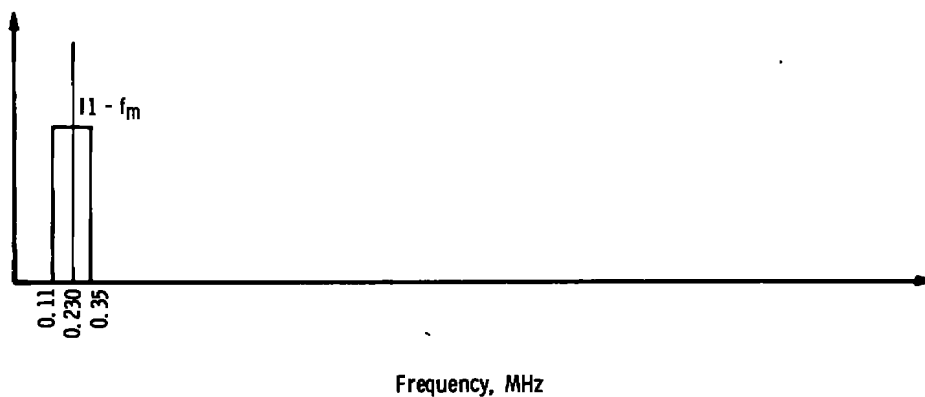
b. Ch. 1 spectra following high-pass filtering at
13.8 MHz, mixing with f_m = 14.77 MHz, and
low-pass filtering at 5 MHz

I2 - f_m

0.1 0.300 0.5

Frequency, MHz
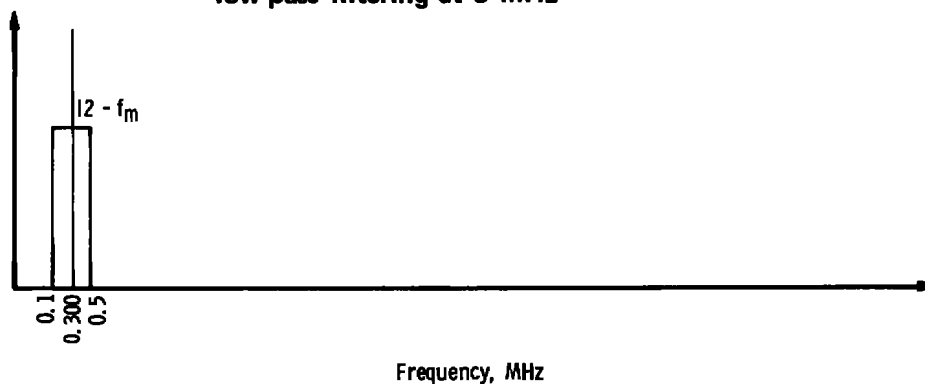
c. Ch. 2 spectra following high-pass filtering at
21 MHz, mixing with f_m = 23.7 MHz, and
low-pass filtering at 9 MHz

Figure 44. Processing for ±12 m/sec at 15 and 24 MHz.

68

The gate pulse for the LV and visibility processors (Fig. 42) is normally obtained (when a multiplexer is not used) from the +A gate output of an oscilloscope which is triggered on the burst waveform produced when a particle enters the LV probe volume. This causes the processors to initiate a reading. However, each of these data sources independently determines whether or not the data obtained from a given burst waveform are valid, based on such parameters as signal-to-noise ratio and particle acceleration. The processors do not print the crosstalk terms.

The crank-angle counter continuously indicates crank angle as determined by degree pulses and a reset pulse (produced once per engine revolution) obtained from the optical-shaft encoder. When a gate pulse is applied to the counter, the counter contents are recorded in a temporary output storage register. If this gate pulse is obtained from the scope +A gate, the contents of the storage register also indicate the crank angle at which the measurement was made.

5.4.5 Data Multiplexer

The purpose of the data multiplexer is to synchronize operation of the four data sources and to arrange the data in a format acceptable to a data recorder. Synchronization of the data sources is accomplished by gating the multiplexer with the scope +A gate and allowing the multiplexer to gate all data sources simultaneously via its gate output (Fig. 42).

Since crank-angle data are always present following the application of a gate pulse, the basic function of the multiplexer involves gating the counter at the same time that the other sources are gated and formating the crank-angle data for output. Of the other three data sources, it is possible to require that certain of the sources always have valid data before the multiplexer will accept and output the data. This is done by moving appropriate data select switches on the front panel to the up position. For example, if both LV processor switches are up but the size data switch remains down, valid data must be present at the output of both LV processors, after a given input waveform has passed, before the multiplexer will pass all the data to the recording device. Valid data do not necessarily have to be present at the output of the visibility processor in this case. If none of the three sources is selected as "required," the multiplexer will initiate a data-transfer cycle when any of the three sources makes a measurement.

Following the gating of all data sources, the multiplexer waits an interval of time, nominally 900 μsec, for all units to complete a measurement. At the end of this interval a logic network within the multiplexer determines if record commands have been received from the required data sources. If all required sources have provided record commands

(or if any provides a command when none of the data select switches is up), the multiplexer proceeds to output data from those sources along with any other data which may exist from nonrequired sources. Nonrequired data sources which failed to obtain readings at a given gating will have zeroes for their readings (zero would never be a valid reading from any unit). Following a data-transfer cycle, all processors are reset. The next gate pulse produced by the scope will be passed to the processors and a new cycle will begin.

If any of the required data sources selected on the multiplexer fails to provide a record command after 900 μsec from the gating signal, then all data sources are reset and the gate line is activated for another sample. Coordinating the data sources in this way ensures that any set of readings from the multiplexer was taken on the same particle traversing the LV probe volume. The multiplexer can cycle the processors at a rate up to 1 kHz.

Another feature incorporated into the multiplexer is the capability of disabling the multiplexer output gate with a logic signal generated by the crank-angle counter. This signal can be set to disable the gate line at all times except where the engine crank angle falls between specified lower and upper limits selected by a pair of thumbwheel switches on the crank-angle counter front panel. Operated in this manner, the multiplexer allows data to be taken only within a selected range of crank angles.

5.4.6 Data Recording

When the multiplexer indicated that an acceptable block of four readings (crank angle, two-velocity components, and particle size) occurred, a high-speed data punch recorded the block as a string of American Standard Code for Information Interchange (ASCII) characters on paper tape. At the end of a data run, the paper tape produced was fed into a minicomputer data acquisition system through a high-speed photoreader. An assembly language subroutine written for the minicomputer then separated the ASCII string into its individual readings which were either stored on magnetic tape or processed immediately by data analysis programs written for the computer.

5.5 EXPERIMENTAL RESULTS

Two-component velocity measurements were taken to determine feasibility of making LDV measurements inside a combustion chamber. A problem unique to the time-varying particle motion was the varying particle density through the engine cycle. This was first discovered from crank-angle-dependent data rates and signal intensities. Figure 45 is a typical plot of the Doppler data rate versus crank angle. As shown in the figure, the data are grouped before and around top dead center (TDC). High-light scattering, for the case where the cylinder was not firing, is clearly shown in each cycle and was initially
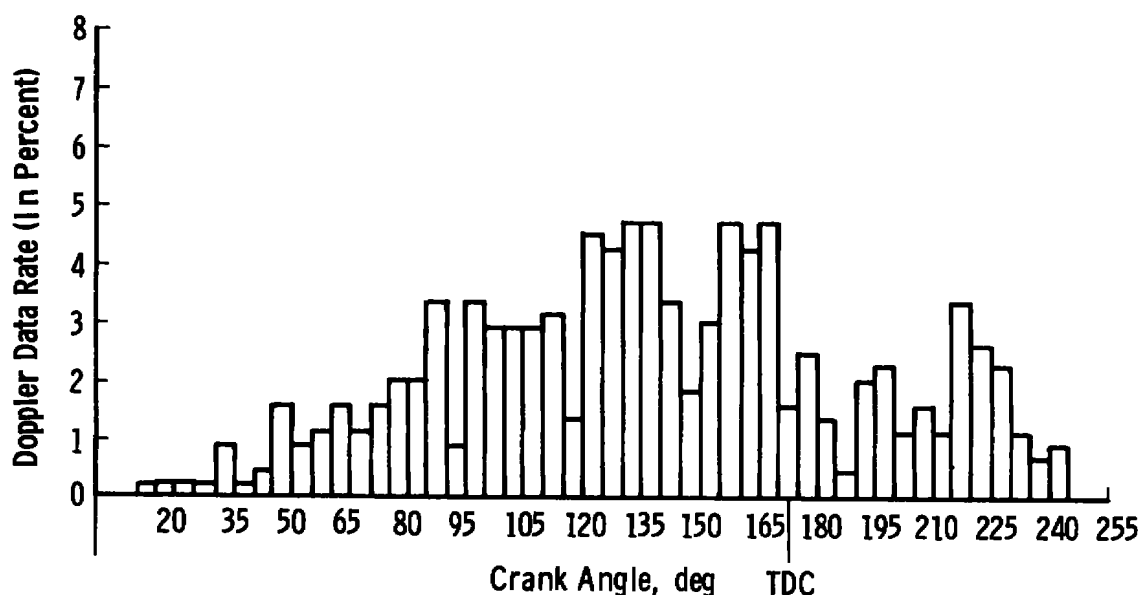
Figure 45. Doppler data rate versus crank angle.

believed to be high particle density generated during the compression portion of the cycle. To verify this assumption the percentage data rate as a function of crankshaft angle was measured with the Bragg cell turned off. This results in only one beam passing through the probe volume. A trigger pulse from the scope represented the passage of a particle or droplet through the probe volume. The crank angles were then recorded. The data (Fig. 46) show that high light-scattering intensities occurred at the beginning and end of each cycle. The data represent a statistical sampling of many cycles without the engine firing. Data processing bias may apply since the signal processor would only produce an output when the signal level was above a threshold value.

Photographs of phototube output taken throughout the engine cycle show large amplitude fluctuations and also indicate the portion of the cycle where scattering centers first appear. Furthermore, these data indicate that the phototube saturates during portions of the cycle because of sporadic large particle number densities which scatter too much light. The top two photographs in Fig. 47 clearly show tube saturation with increasing particle density. Referring to Fig. 46, the light-scattering peak beginning at the 274-deg mark is believed to represent the leading edge of the moisture condensation point. Based on the photographs of one cycle with no fuel injection, it is shown that the high particle concentration remains throughout the rest of the cycle with some residue left at the beginning of the compression stroke. The "moisture" peak shown in Fig. 46 results in (1) phototube saturation and/or (2) data processing bias. It should be noted that the large "moisture peak" is a characteristic of this particular nonfiring engine condition and
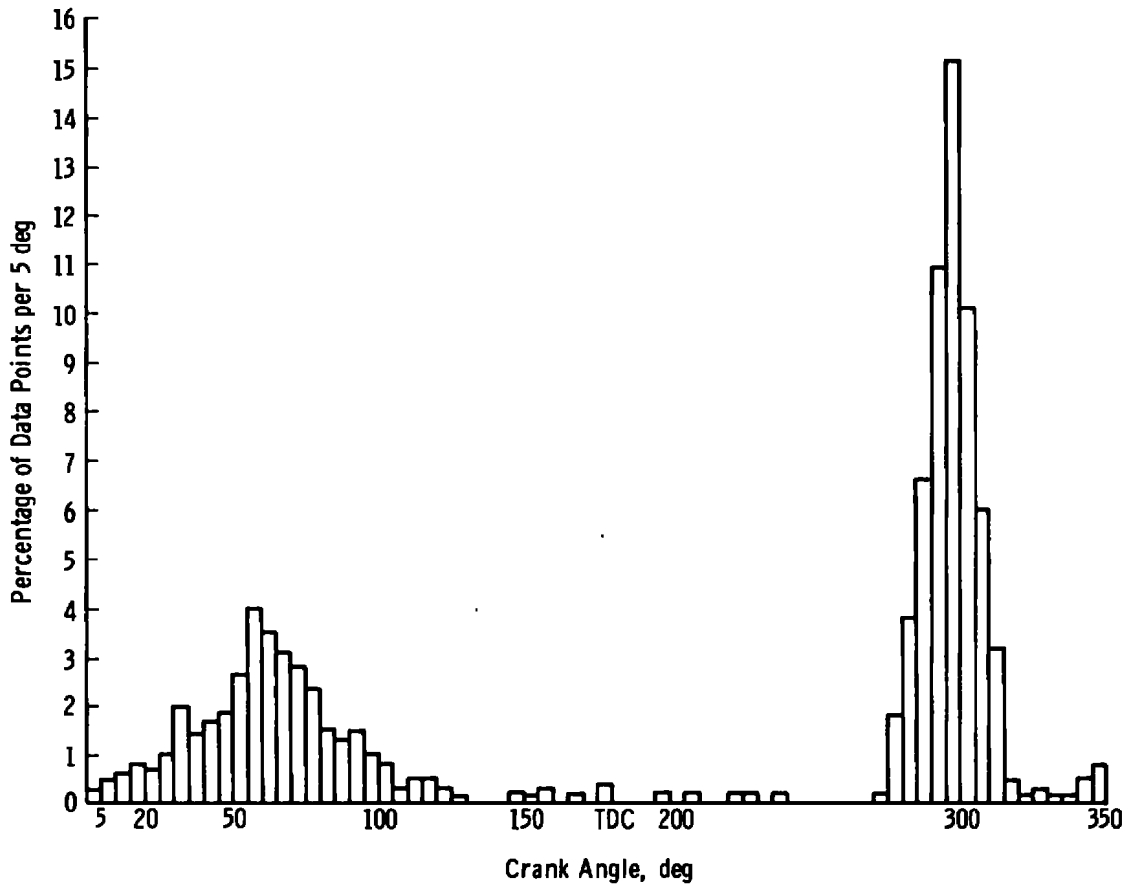
Figure 46. Light-scattering occurrence versus crank angle
(engine not firing).

is greatly reduced when data were taken on the firing runs. This characteristic is evidenced in the bottom two photographs in Fig. 47 taken during firing conditions. The large peak in the center of the two photographs indicate combustion at approximately 170 deg. The one "blurb" on the third photograph at approximately 324 deg indicates phototube saturation. Similarly, in the last photograph three blurbs, or saturation points, are evidenced at 30, 150, and 350 deg.

Two-component velocities were measured during the portion of the diesel cycle where phototube saturation does not occur. The results indicate no insurmountable difficulties in obtaining the data during this portion of the cycle. Figures 48a through l show the vector velocity flow, of a typical run, for airflow in the prechamber without fuel injection. Future efforts will comprise taking a large sample, over a series of 5- or 10-deg intervals, until a sufficient quantity of data, to be statistically significant, is acquired.

Saturation

Laser Power 75 mw

Photomultiplier Tube (PMT) Output 20 mv/div

BDC Marker

Amplified "AC" Output (Signal) 100 mv/div

No Fuel Injection

Saturation Occurs at ~ 274 deg

Saturation

Laser Power 150 mw

PMT Output

BDC Marker

Amplified "AC" Output

No Fuel Injection

Laser Power 200 mw

PMT Output   20 mv/division

BDC Marker

Amplified "AC" Output   100 mv/div

With Fuel Injection

Laser Power 75 mw

PMT Output   20 mv/div scale

BDC Marker

Amplified "AC" Output 100 mv/div scale

With Fuel Injection

Intensity ⟶

Time (10 msec/div)
36-deg Crankshaft/div
10 msec/div

Figure 47. Photographs of signal parameters for one cycle.
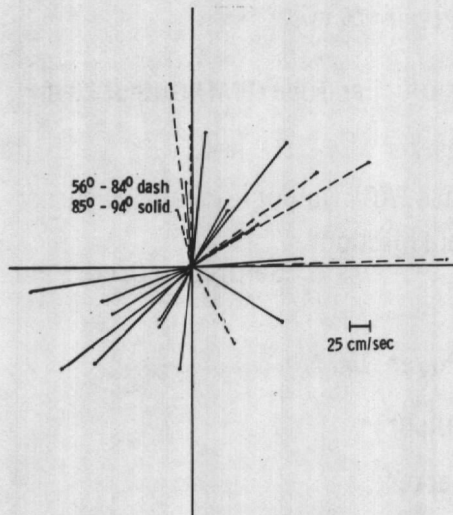
a. Crank angles of 56 to 94 deg
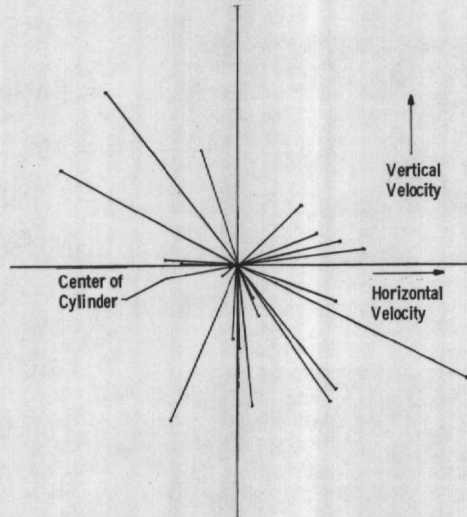
b. Crank angles of 95 to 104 deg
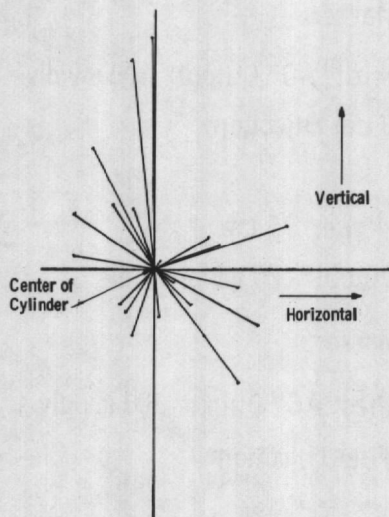
c. Crank angles of 105 to 114 deg
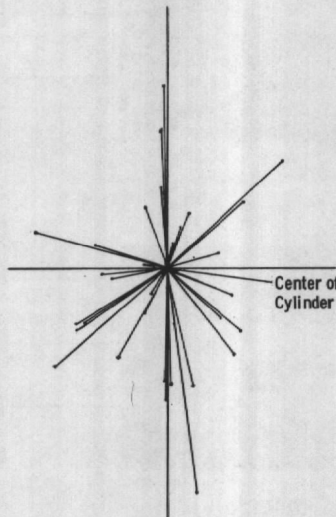
d. Crank angles of 115 to 124 deg

Figure 48. Vector velocities as a function of crank-angle windows in center plane of test cylinder (no fuel injected).

74
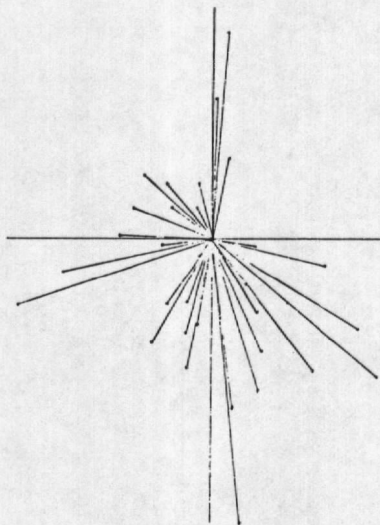
e. Crank angles of 125 to 134 deg
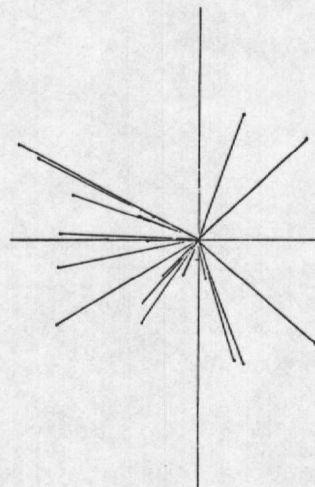
f. Crank angles of 135 to 144 deg
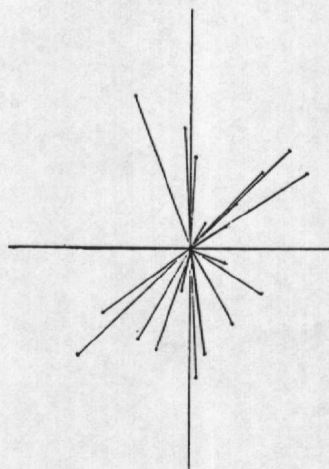
g. Crank angles of 145 to 154 deg
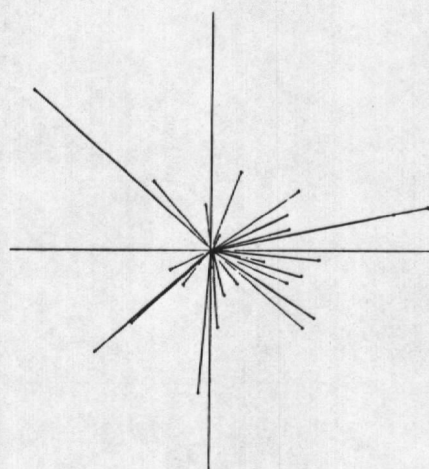
h. Crank angles of 155 to 164 deg

Figure 48. Continued.
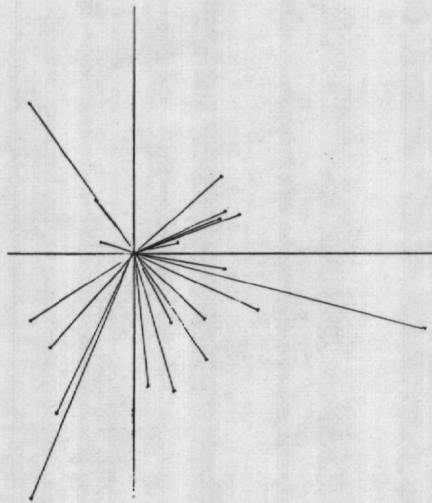
i. Crank angles of 165 to 174 deg
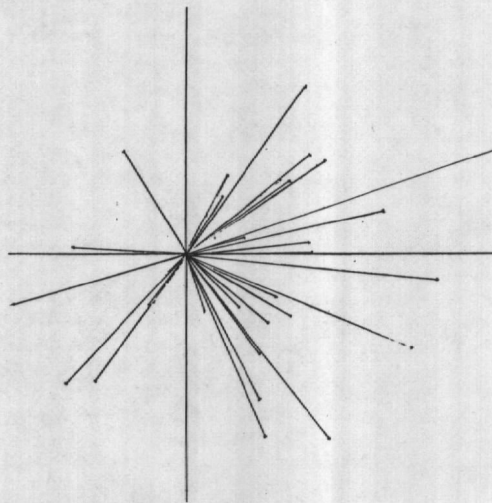
j. Crank angles of 175 to 185 deg

50 cm/sec

216° - 220° solid
221° - 231° dash

50 cm/sec
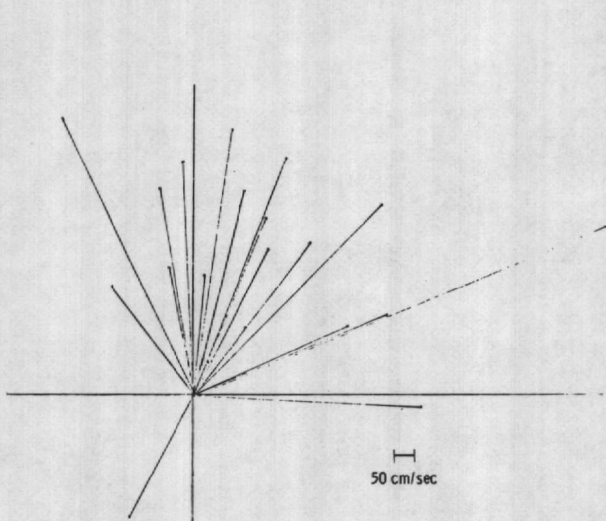
k. Crank angles of 206 to 215 deg
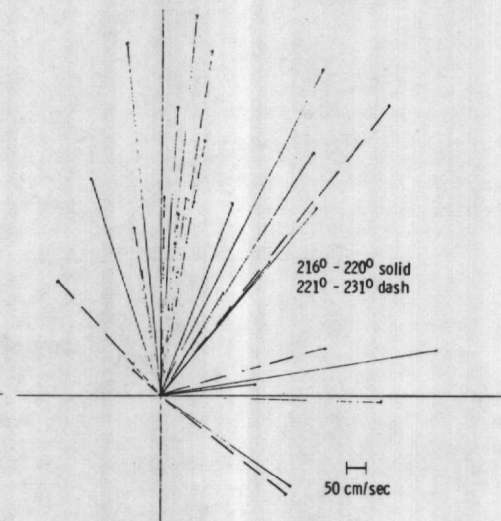
l. Crank angles of 216 to 231 deg

Figure 48. Concluded.

Crank-shaft angles where fuel injection and combustion occurred were determined by passing the laser beam through the fuel spray and collecting the scattered light and light from combustion with a photodiode. Figure 49 illustrates the resulting oscilloscope signals. The center trace shows the output of the diode. Complete blockage of the beam was found to occur in each photograph at a 158-deg crank-angle position with engine firing occurring 13 to 18 deg later. Combustion was always observed to occur before top dead center. The combustion signal was obtained with the photodiode set 3 ft from the window and with no light-collecting optics or filters.
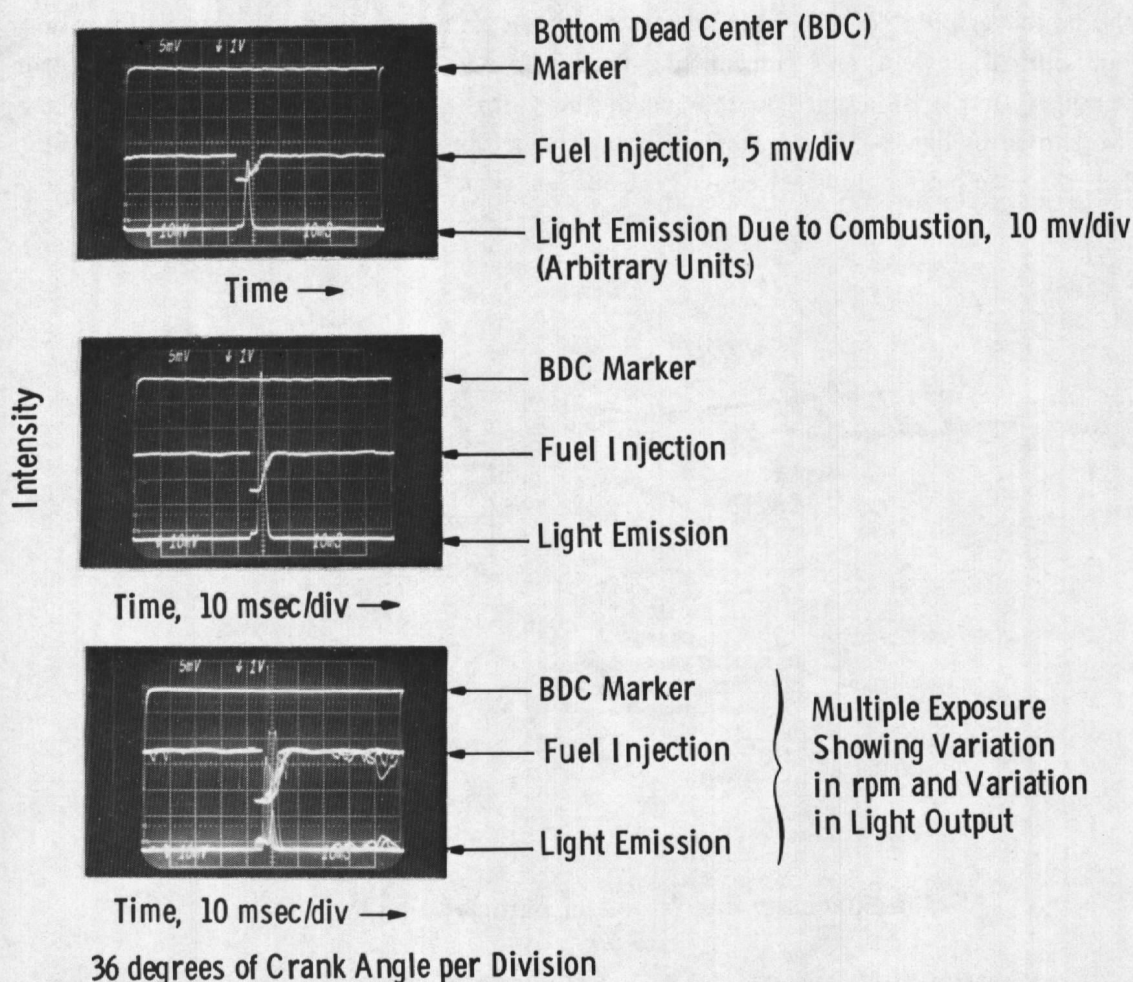
Figure 49. Fuel injection and combustion versus crank angle.

5.6 PARTICLE SIZING

It has been shown that particle size and number density of particles suspended in fluids can also be measured using interferometric techniques (Ref. 34). This light-scattering technique has the advantages that the measurement is (1) independent of the absolute magnitude of the scattered light, (2) independent of particle composition, and (3) utilizes the same optical system as that of a laser velocimeter. This offers the possibility of acquiring simultaneous velocity and particle-sizing data.

Figure 50 is a diagram of an optical arrangement for making interferometric particle-size measurements. When a particle traverses the set of interference fringes formed at the crossover point of two laser beams, it scatters light. The light is collected by means of an optical system and transmitted to a photodetector. Scattered light waveform ("Doppler burst") of a particle moving in the y-direction and through the z = 0 plane is also shown in Fig. 50. The waveform comprises a Gaussian modulated cosine component called the "ac" on a lower frequency Gaussian signal called the "pedestal," or "dc."
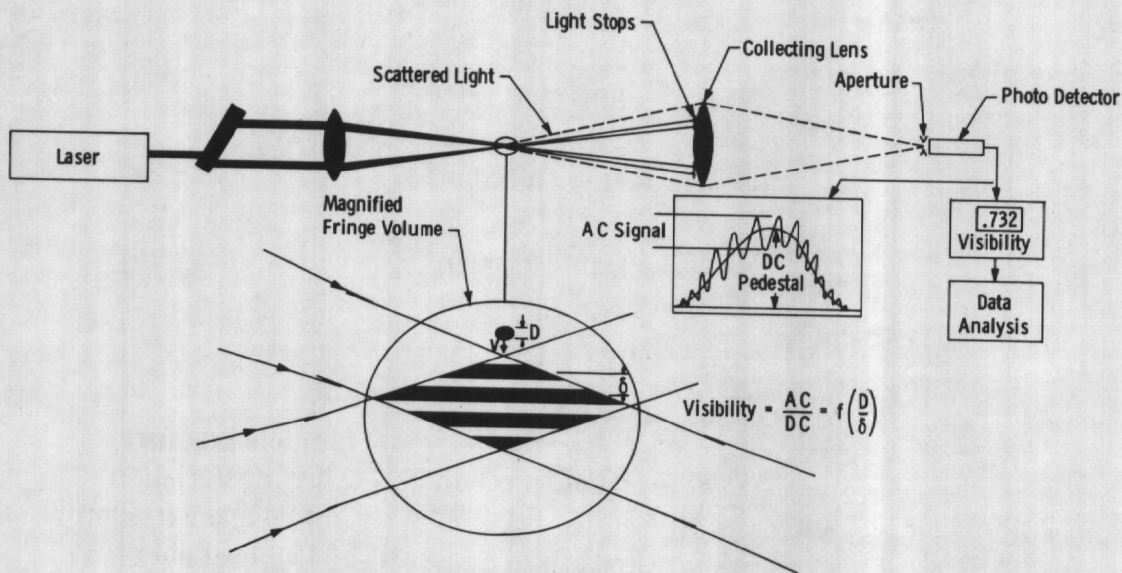
Figure 50. Laser interferometer particle-sizing instrument.

The "visibility" of the waveform is defined as the ratio of the magnitude of the ac component (one-half peak-to-peak value) to the magnitude of the dc component. The ac signal amplitude is defined through the equation

$$ac = (I_{max} - I_{min})/2 \qquad (5\text{-}10)$$

where I_{max} is the value of the signal at a peak and I_{min} is the following half-cycle minimum. The dc amplitude is defined as

$$dc = (I_{max} - I_{min})/2 \qquad (5\text{-}11)$$

The signal visibility, V, is then

$$V = \frac{I_{max} - I_{min}}{I_{max} - I_{min}} \qquad (5\text{-}12)$$

The relative amount of oscillation on the waveform, and therefore the visibility, is dependent upon the ratio of the particle size to the fringe spacing. It is also a function of the particle trajectory through the probe volume and of the geometry of the collection optics. Figure 51 shows the theoretical relationship between the visibility, V, and the ratio of particle diameter to fringe spacing (D/δ) for a particle passing through the center of the probe volume, for a particular optical configuration. For a spherical particle the curve may be approximated as (Ref. 35):

$$V = \frac{2J_1(\pi D/\delta)}{(\pi D/\delta)}$$

where

$$\delta = \frac{\lambda_o}{2\eta \sin(\theta/2)} \qquad (5\text{-}13)$$

and $J_1()$ is a first order Bessel function of the first kind, D is the particle diameter, δ is the fringe spacing, λ_o is the wavelength of the illuminating beam, η is the index of refraction of the surrounding medium, and θ is the angle between illuminating beams. Figure 52 contains the scattered waveform of several particles moving a probe volume and their respective visibilities.

The fringe particle-sizing technique is currently under development; however, a prototype system was applied to the Turner engine. Attempts to acquire meaningful data of the particulate and droplet sizes in the combustion chamber were unsuccessful. A number of problems were uncovered which must be resolved before the technique can be developed for this application. With the diesel engine operating, the background light, and hence the dc level, varied widely during a complete cycle. With recourse to the definition of the visibility function [Eq. (5-12)] it can be readily seen that based on subtracting out a constant background level the results would be erroneous.
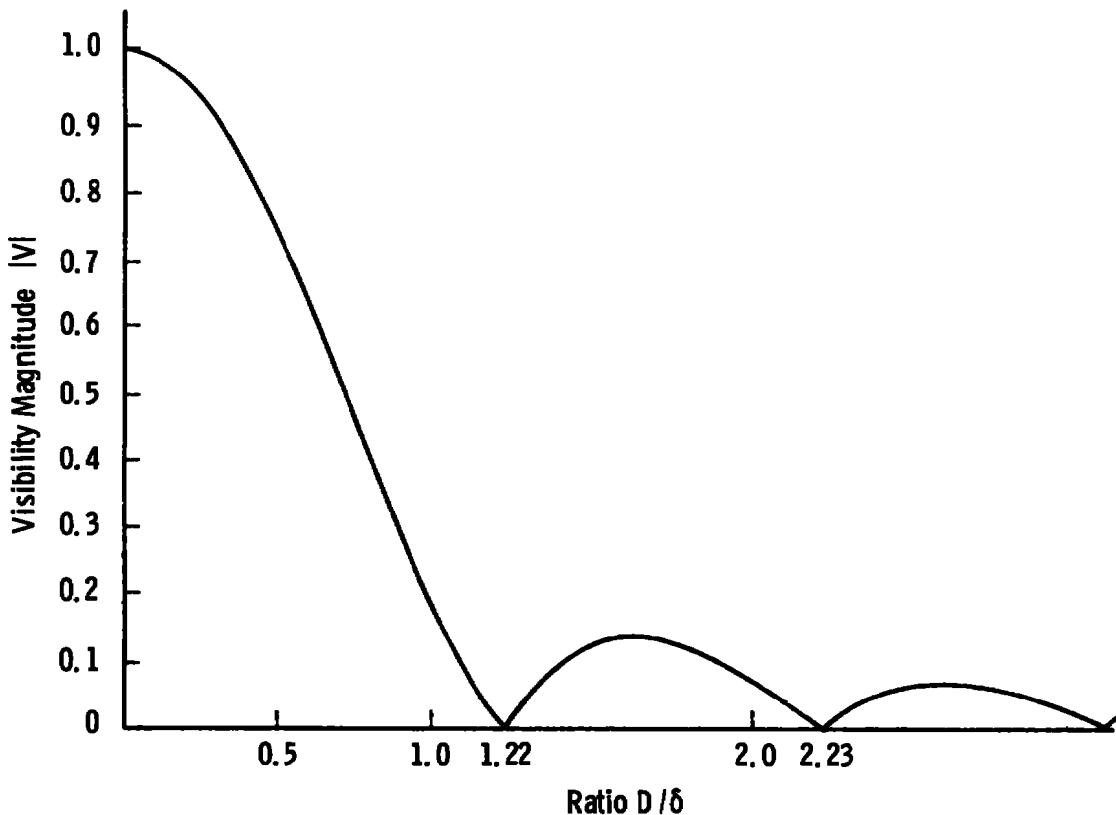
Figure 51. Theoretical visibility versus ratio of particle
diameter to fringe spacing.

Although attempts to observe the signal bursts of particulates within the combustion chamber were unsuccessful, it was possible to observe signals when the fuel was shut off and one of the windows was removed from the engine. In this case the background light was low and constant. Examples of these data are shown in Fig. 53. The isolated burst in the center of Fig. 53b was caused by a single particle passing through the probe volume; however, the bursts in other photographs appear to be a result of a multiplicity of particles traversing the focal region. The visibility under these conditions cannot, at present, be evaluated for each of the particles.

Additional photographs of signal burst data taken with one window removed are shown in Fig. 54. These waveforms were taken after the signals were filtered in the visibility processor to separate the ac component from the dc pedestal. The upper trace in each photograph is the dc pedestal and the lower trace the ac magnitude. The complicated waveform in Fig. 54a is similar to that shown in Fig. 53a and is due to multiple particle scattering. Figures 54b and c show waveforms attributable to isolated particles passing through the probe volume.
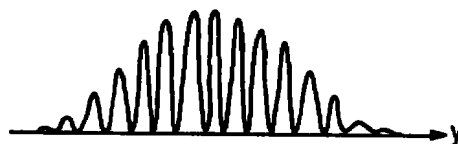
a. Visibility = 1.0
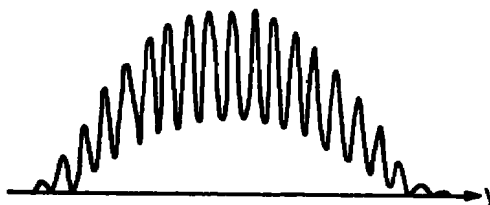
b. Visibility = 0.47
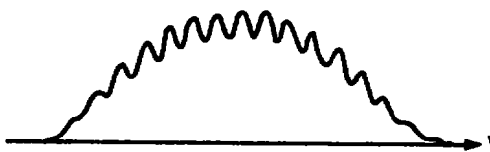
c. Visibility = 0.17
Figure 52. Scattered intensities for three values of
D/δ at z = 0.

In Fig. 54c, the fluctuations appearing simultaneously in both traces is attributed to illuminating laser beam intensity variations. Such fluctuations, appearing on the signals of both the ad and dc components, do not affect the visibility determination. The visibility of the waveform shown in Fig. 54c is approximately 0.32. For a fringe spacing equal to 60 μ this visibility indicates a particle diameter of approximately 50 μ.

6.0 MASS SPECTROMETER TECHNIQUES FOR COMBUSTION ANALYSIS

Improvement in performance and emissions for internal combustion engines requires improved understanding of engine combustion processes. Knowledge of the spatial distribution and temporal variation of chemical species, temperature, and pressure in engine combustion chambers are necessary prerequisites. Instrumentation capable of obtaining

Continuously Varying
Bursts, Multiple
Particles in Probe
Volume

Isolated Burst
Single Particle

Intensity
(5 mv/div)

a.

b.

Continuously Varying Bursts, Multiple
Particles in Probe Volume

Intensity
(5 mv/div)

θ

θ

Time ⟶
(20 μsec per div)

Time ⟶
(20 μsec per div)

c.

d.
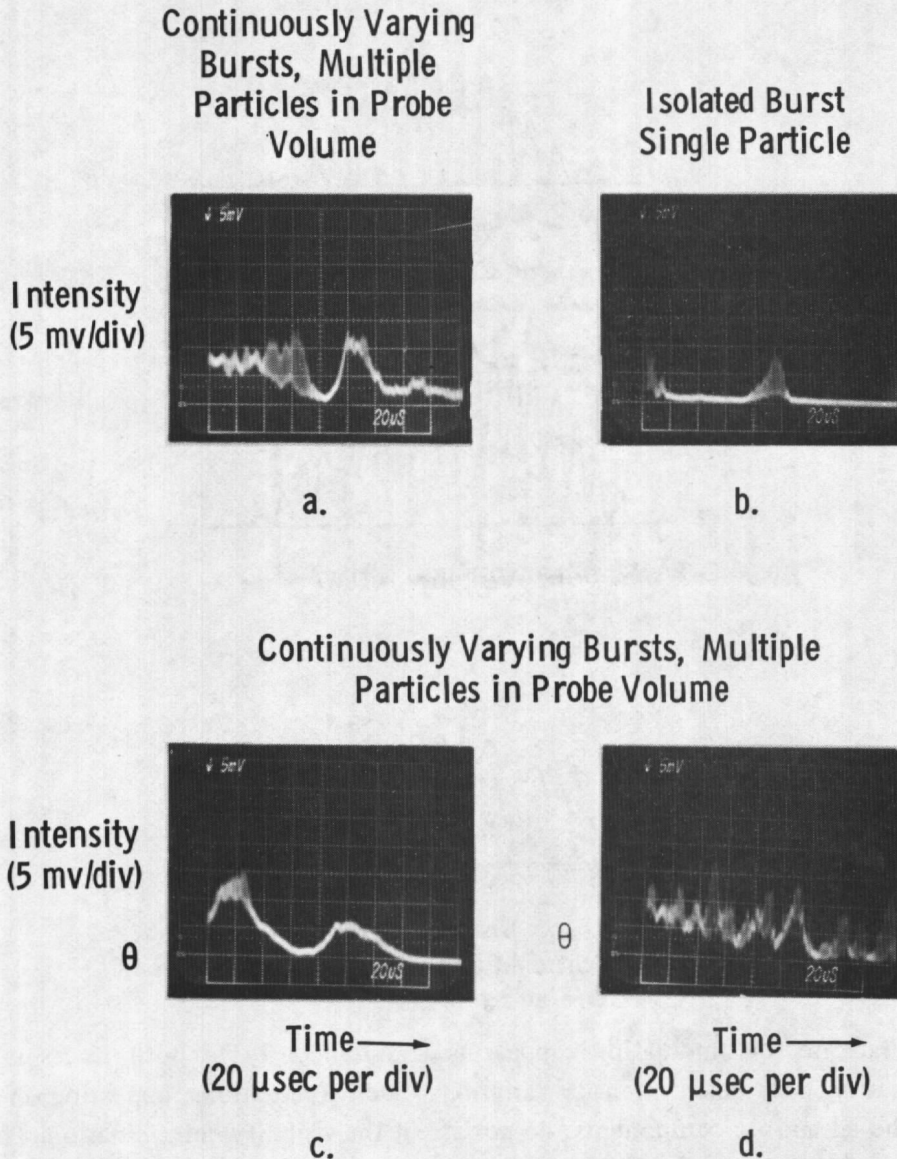
**Figure 53. Light scattered from particles in probe volume
(window removed from cylinder wall).**

these data would assist in evaluating the effects of engine design modifications, operating characteristics, and fuel composition as well as providing the means for evaluating mathematical modeling of engine operation.

Gas samples withdrawn from the combustion chamber can be analyzed outside the engine. In most gas-sampling/external analysis methods, composition changes attributable to chemical reactions during transport from the combustion chamber to the analytical
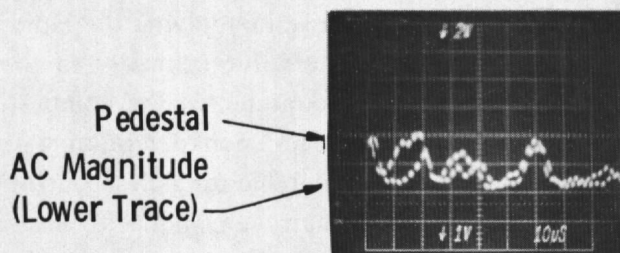
a.
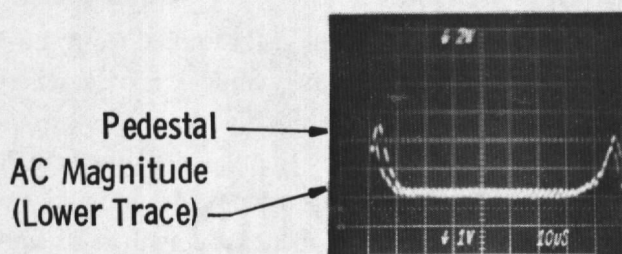
b.
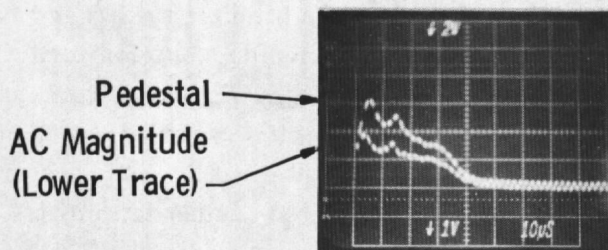
c.

Figure 54. A-C magnitude and pedestal scattered from probe volume (window removed).

instrument are inevitable, and all temperature information of the sample at the time it left the combustion chamber is lost. The molecular beam mass spectrometry technique used for the present work minimizes the composition change by using a rapid expansion to stop the chemical reactions as quickly as possible to preserve total temperature information of the sample at the time it left the combustion chamber.

A number of problems and questions arise in applying the rapid expansion sampling technique to operating diesel engines. These are due primarily to the wide ranges of gas pressure, temperature, and composition encountered in the combustion chamber during the engine cycle. The present work is focused upon determining the feasibility of (1) designing a rapid expansion sampling system suitable for a diesel engine combustion camber and (2) using molecular beam mass spectrometry techniques to measure the composition and temperature of the sample.

6.1 SUMMARY OF TECHNIQUE AND INSTRUMENTATION

6.1.1 Rapid Expansion Sampling

In the rapid expansion sampling technique, gas sampled from the combustion chamber passes through a small orifice into a diverging conical nozzle where it expands into a hard vacuum. The temperature decreases very rapidly as the gas expands, with a minimum of collisions, so that after a few microseconds the chemistry is virtually frozen. Molecular beam mass spectrometry, electron beam fluorescence, and laser light-scattering techniques (Refs. 36 through 45) can each be used to identify constituents and make temperature measurements representative of conditions existing at the point and time of sampling. Figure 55 shows how these techniques are related and the region of the expansion plume to which each applies.

A critical feature of the technique is the ability of the pumping system to provide a hard vacuum for the nozzle expansion while handling the gas and heat loads of a cyclic, high-temperature and pressure source. The requirement for hard vacuum ($<10^{-4}$ torr) conditions in the expansion chamber is essential in molecular beam mass spectrometer measurements. By operating gaseous-helium (GHe)-cooled cryopumps at temperatures between 14 and $20^{\circ}K$ in conjunction with oil diffusion and mechanical vacuum pumps, it is possible to pump the gases occurring in the combustion process, thereby maintaining the required vacuum conditions.

6.1.2 Molecular Beam Skimmers

The successful application of the molecular beam mass spectrometry technique also depends upon obtaining a representative sample of the combustion products by skimming from the core of the expansion plume. If a closed container with a cryogenic ($20^{\circ}K$) skimmer or a sharp-lipped conical skimmer in conjunction with a proper internal pumping system is suitably located in the expansion, a molecular beam is formed. For maximum beam intensity, it is best to cryopump the skimmer when the condensation level (caused by a large isentropic temperature drop, T_i, during expansion) is significant. For sampling a high-temperature source a warm conical skimmer produces high-intensity molecular beams
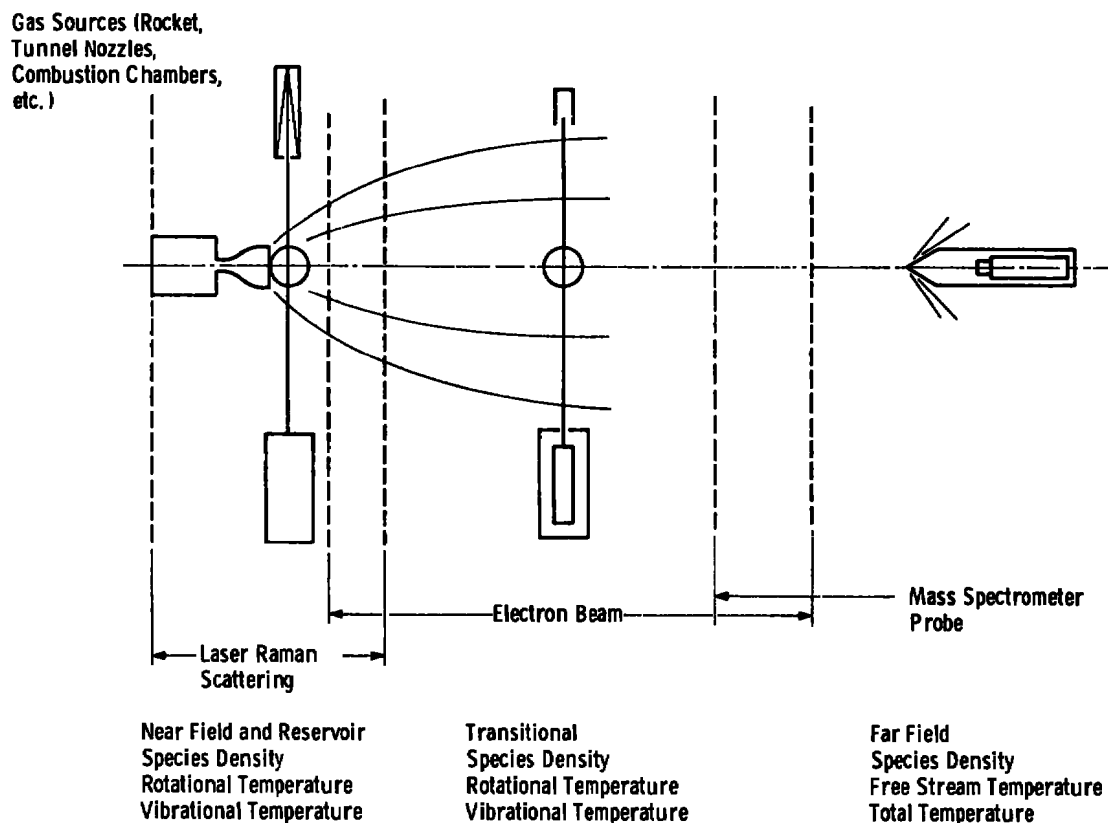
Figure 55. Test regimes for diagnostic techniques.

with unaltered gas properties. Both types of skimmers were used in the present work, e.g., a cryogenically cooled skimmer with the Turner engine and a warm conical skimmer with the TACOM engine.

6.1.3 Mass Spectrometer

The mass spectrometer ionizes a portion of the molecules in the molecular beam, filters the resulting ions according to their mass-to-change (m/e) ratio and collects and detects the filtered ions. A quadrupole mass spectrometer, because of its small size, simplicity, excellent resolution, and mass range, and high efficiency was selected for this application. It consists of (1) an Extranuclear Laboratories cross-beam ionizer, (2) an EAI Quad 200 mass filter, (3) an Extranuclear paraxial multiplier and enclosure, and (4) a preamplifier with a high-frequency response.

As the molecular beam traverses the mass spectrometer ionizer it is bombarded by electrons which cause a small fraction of the atoms and molecules to become positive ions. Either an axial or a crossed-axis configuration may be selected for the ionizer section

of the mass spectrometer. In the axial ionizer configuration the molecular beam traverses the entire length of the ionizer/quadrupole filter/particle multiplier assembly. In the crossed-axis ionizer configuration the ions are extracted on the ionizer/quadruple filter/particle multiplier axis which intersects the molecular beam at a right angle; the molecular beam traverses only the width of the ionizer assembly. In a later discussion, it will be shown that a crossed axis ionizer is preferred for this work.

The filter section of a quadrupole mass ·spectrometer contains a quadrupole lens comprising four parallel cylindrical electrodes arranged in a square array (Fig. 56). Positive ions with different m/e ratios are introduced into the entrance aperture of the quadrupole lens. A static potential, U, (dc) superposed with a radio frequency (rf) potential, V cos wt, is applied between adjacent pairs of electrodes to comprise the total potential, ϕ. Ions with the proper m/e ratio have bounded trajectories and pass through to the exit aperture of the quadrupole lens. Ideally, all other ions have divergent trajectories and are collected on the electrodes. Increasing the ratio of dc to rf increases the resolution; for proper operation the dc is about one sixth the peak r-f amplitude. When the r-f frequency is fixed, increasing the d-c and r-f potentials together to maintain the same ratio tunes the filter to pass ions with larger m/e ratios. The ions that reach the exit aperture are collected by the ion collection system.
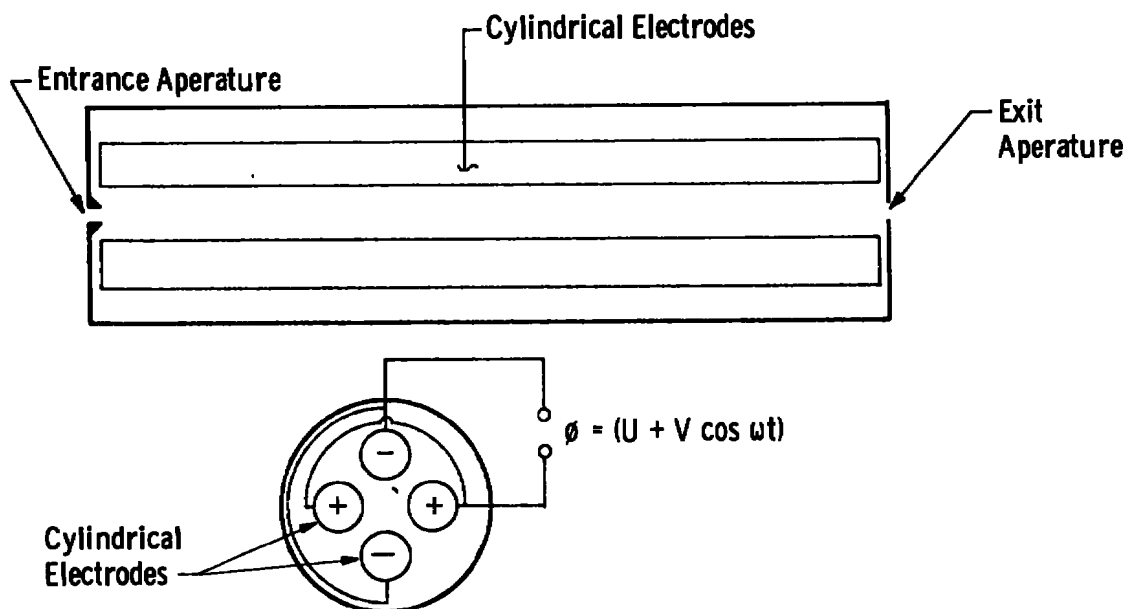
Figure 56. Quadrupole mass spectrometer tube.

For a typical ionizer/mass filter configuration, ions of a given species that reach the exit aperture of the mass filter carry currents of approximately 10^{-13} to 10^{-12} amp. Current amplification by means of a particle multiplier is required in order to record these currents with a frequency response compatible with the expected output signals. The particle multiplier enclosure is designed so that neutral and metastable molecules and photons leaving the filter section cannot strike the first dynode of the multiplier, thus preventing the associated random untunable noise.

In the ionizing region of the mass spectrometer, crossing of the electron beam with the molecular beam results in (1) the production of ions which are drawn into the mass filter and mass analyzed and (2) the production of metastables which are unaffected by electric fields. A chopped metastable beam can be generated by pulsing the ionizer electron beam for durations of approximately 10^{-5} sec. The flight time of the metastables can be detected with a copper beryllium electron multiplier located a known distance along the flight path behind the ionizer. Using this measurement of the velocity the total temperature of the process under study can be calculated from the expression for the velocity of gas expanded to the adiabatic limit (Refs. 39 and 40).

6.1.4 Instrumentation Systems

Figure 57 is a block diagram showing the instrumentation systems used for this work. The quadrupole mass spectrometer has previously been described. The signal-averaging systems used were a waveform eductor and/or a boxcar integrator. These are analog devices using resistance-capacitance (RC) filtering curcuits. They were used to extract weak signals from the background noise and to average signals which fluctuated because of cycle-to-cycle variations in the combustion characteristics of the engine. A magnetic pickup provided a flywheel position signal that was used to synchronize the mass spectrometer output and the signal-averaging systems with engine crank angle. An oscilloscope and a strip-chart recorder provided for viewing and recording the data. Essentially the same instrumentation was used for both the Turner engine and the TACOM engine experiments.

6.2 TURNER ENGINE MASS SPECTROMETER AND TEMPERATURE MEASUREMENTS

6.2.1 Turner Engine Experimental System

The initial experiments were concerned with the application of the mass spectroscopy technique to the Turner engine. The Turner engine is a three-cylinder, two-stroke-cycle, loop-scavenged diesel engine. Each cylinder has a separate cylinder head. The front cylinder head was replaced with a special head (Fig. 58) so that a gas sample could be extracted from the precombustion chamber. The gas expanded through the sampling nozzle into
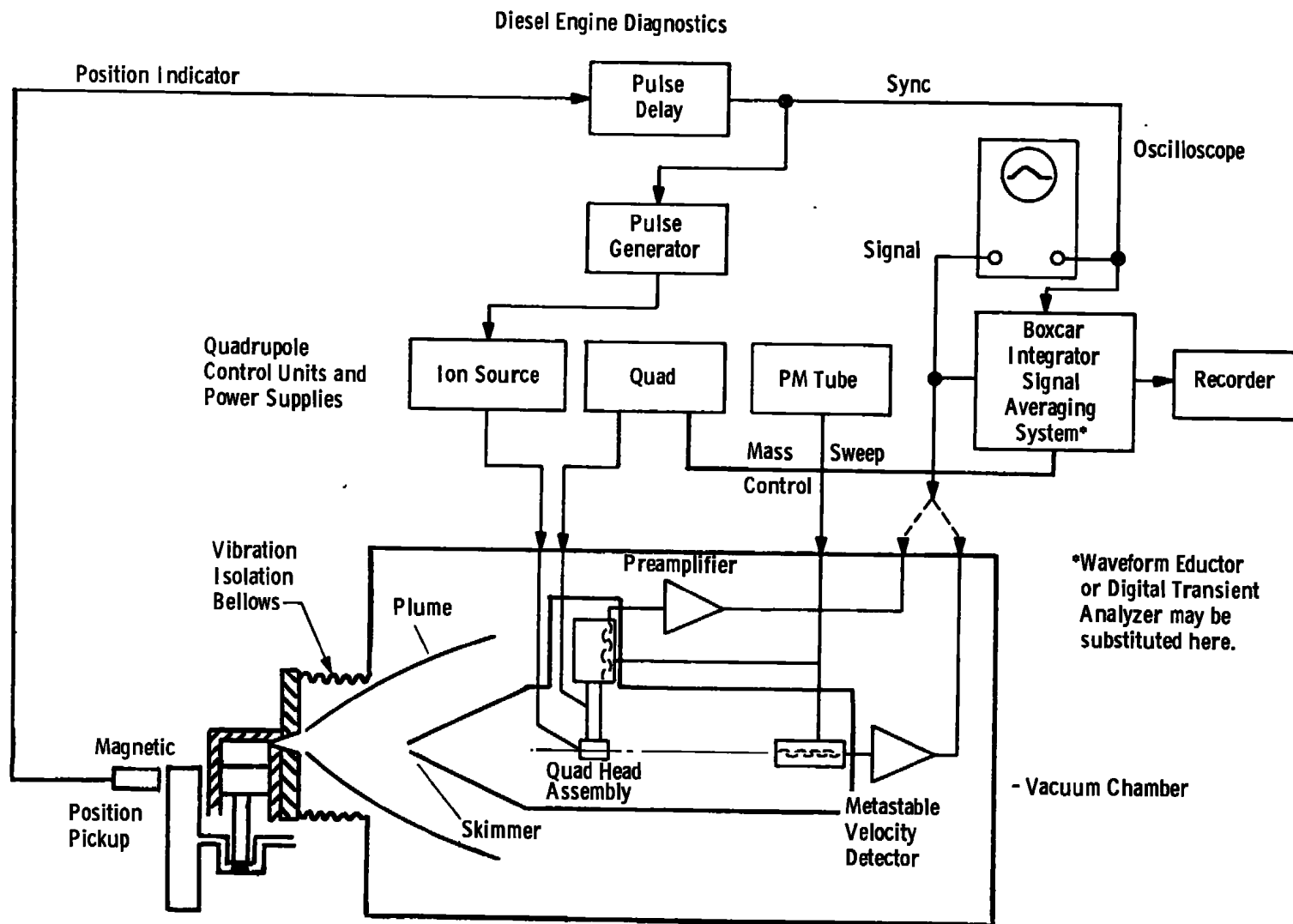
Figure 57. Block diagram of instrumentation systems.
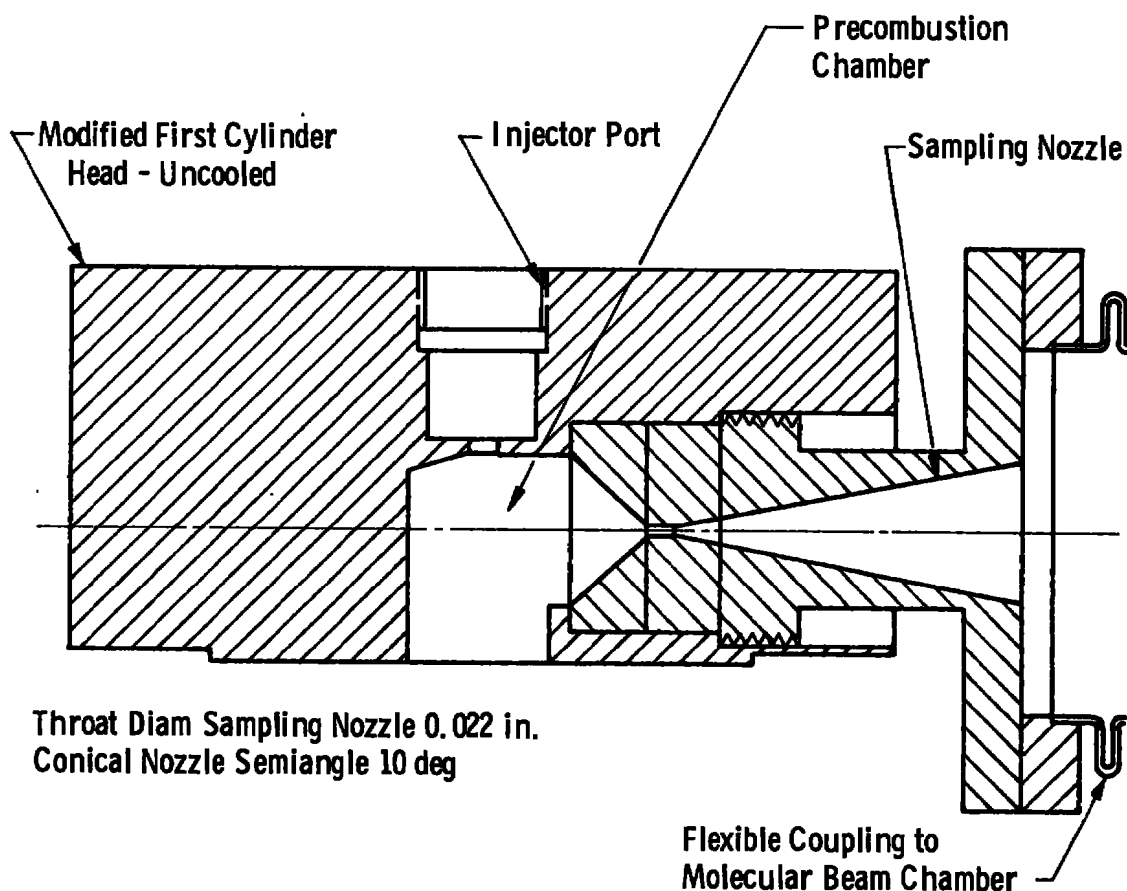
Figure 58. Schematic of modified cylinder head and sampling nozzle.

the source chamber of the AEDC Aerodynamic Molecular Beam System to be analyzed using molecular beam mass spectrometry techniques.

The AEDC Aerodynamic Molecular Beam System is a 3-1/2-ft-diam, 6-1/2-ft-long stainless-steel chamber divided into two sections by a removable bulkhead. Vacuum conditions are maintained by mechanical pumps, oil diffusion pumps, 77°K liquid-nitrogen (LN_2) cryoliners and 14 to 20°K GHe cryoliners. This pumping system can maintain pressures of 1×10^{-4} and 3×10^{-8} torr in the source and test sections, respectively, during testing.

Figure 59 shows the overall features of the experimental installation. Note the cylinder head, sampling nozzle, bellows for vibration isolation, and 6-in. gate valve for chamber isolation during pumpdown. Note also the two sections of the test chamber, the source end which pumps most of the combustion gases and the test end containing the mass
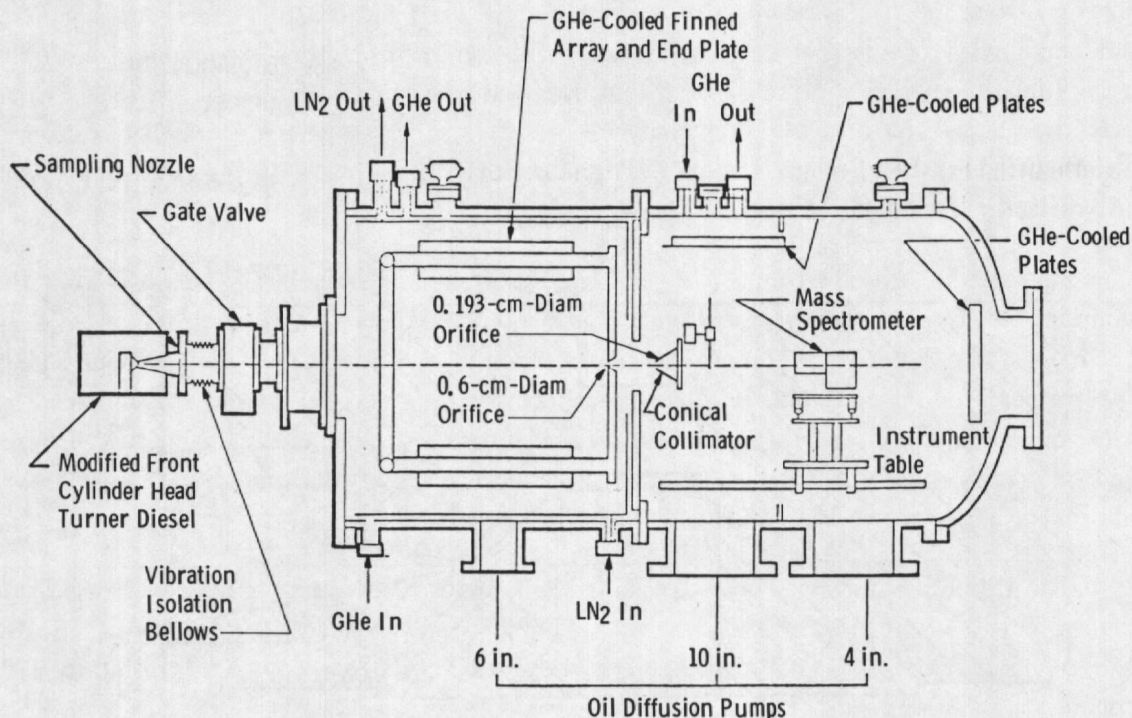
Figure 59. Schematic of molecular beam chamber.

spectrometer assembly. The two sections are separated by a 0.25-in.-thick cryogenic skimmer plate and have independent GHe pumping systems. The gas to be analyzed enters the source chamber through the sampling nozzle. The core of the expansion passes through the 0.6-cm-diam orifice in a cryogenically cooled plate (14 to 20°K). This beam then passes into the test chamber where it is collimated by a 0.193-cm-diam orifice in the conical collimator before entering the detection systems.

6.2.2 Turner Engine Results

In the studies of the combustion process in the Turner engine precombustion chamber, attention was confined to species having masses of 18, 26, 28, 30, 32, 34, and 44 amu. All measurements were made with the engine idling at 600 rpm. The engine could not be loaded since the test stand was not equipped with a dynamometer.

The first series of measurements was made with an axial ionizer, the molecular beam passing through the ionizer directly into the quadrupole section. The results showed that the axial ionizer configuration was unsatisfactory in this application. It was suspected that large charged particles passed through the quadrupole section and interfered with the measurement. The existence of something other than a gas phase in the spectrometer head was verified when significant signals were obtained with the ion source electron energy below the threshold for ionization, and even with the ionizer turned off. In addition,

the signal obtained with the mass spectrometer tuned off showed that mass was in general independent of the mass spectrometer operating conditions. Other experiments with the axial ionizer configuration indicated that resolved spectra could not be obtained when mass number scans at fixed crank angle were attempted. Only a noise background was obtained over the entire mass range, with no resolved mass peaks during the compression stroke or at top dead center (TDC).

Microscopic examination of a glass slide that had been exposed to flow from the sampling nozzle confirmed the presence of particulates in the flow (some as large as 30 μ). It was thought that particles of this type reaching the quadrupole section of the mass spectrometer could affect its performance. Accordingly, the axial ionizer was replaced by a crossed-axis ionizer. In this configuration the molecular beam passes through the ionizer and only ionized particles are drawn into the quadrupole section for analysis. Considerably improved performance was obtained with this configuration.

The variation of species intensity with crank angle as measured using the crossed-axis ionizer for the fueled case is shown with sample data in Fig. 60 for masses of 18, 28, and 32 amu. The data are normalized to the peak signal to show their variation with engine crank angle.

Some measurements of molecular velocity distributions were made using the metastable velocity analyzer. The translational velocity derived from the time-of-flight measurements is qualitatively shown as a function of crank angle in Fig. 61. Note from the bottom plot in Fig. 61, that the measured velocity peak, which corresponds to a total temperature of approximately 1,100°K, occurs at approximately 40-deg BTDC.

6.2.3 Evaluation of Turner Engine Results

The mass spectrometer measurements made with fuel supplied to the test cylinder of the Turner engine all show an abrupt decrease in signal intensity beginning near 40-deg BTDC. This decrease, which cannot be correct, is probably due to molecular beam breakdown and is evident in the data shown in Fig. 60. This suggests that the increased combustion chamber pressure which occurs during compression and combustion is related to the molecular beam breakdown. The time-of-flight velocity measurements shown in Fig. 61 are typical of background chamber gas effects and also indicate complete molecular beam breakdown. The cause of the molecular beam breakdown lies in the experimental configuration.

Several items could account for the observed behavior:

a. Shock structure forming in the bellows coupling between the cylinder head and the gate valve.

No Load – Idle
Engine rpm 600
Diesel No. 2 Fuel

Signal Normalized with
Respect to Peak Signal

28 amu – N_2 /CO

32 amu – O_2

18 amu – H_2O

Signal Intensity

Crank Angle, deg

TDC
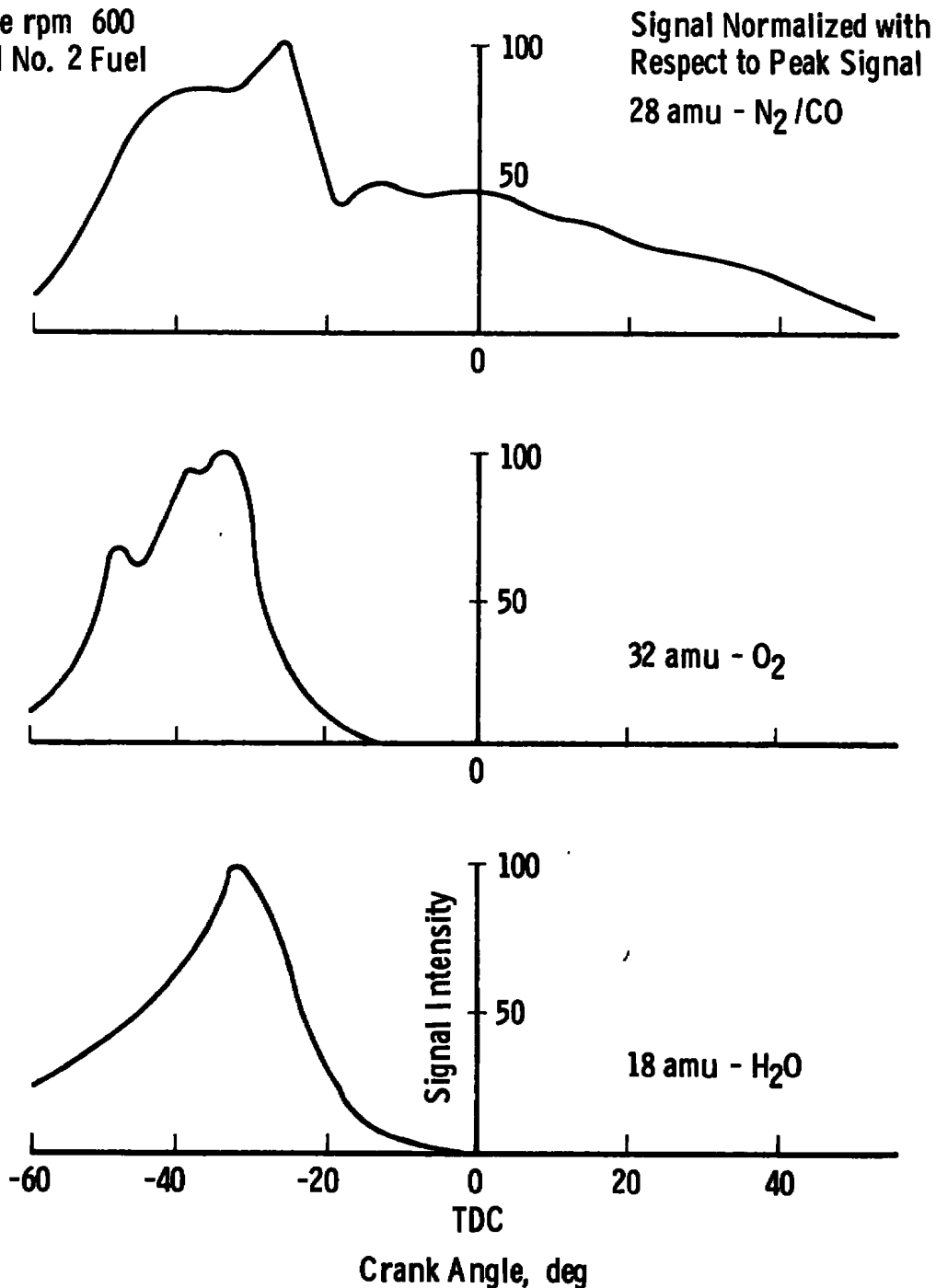
Figure 60. Turner engine-species intensity versus crank angle
(cross beam ionizer).
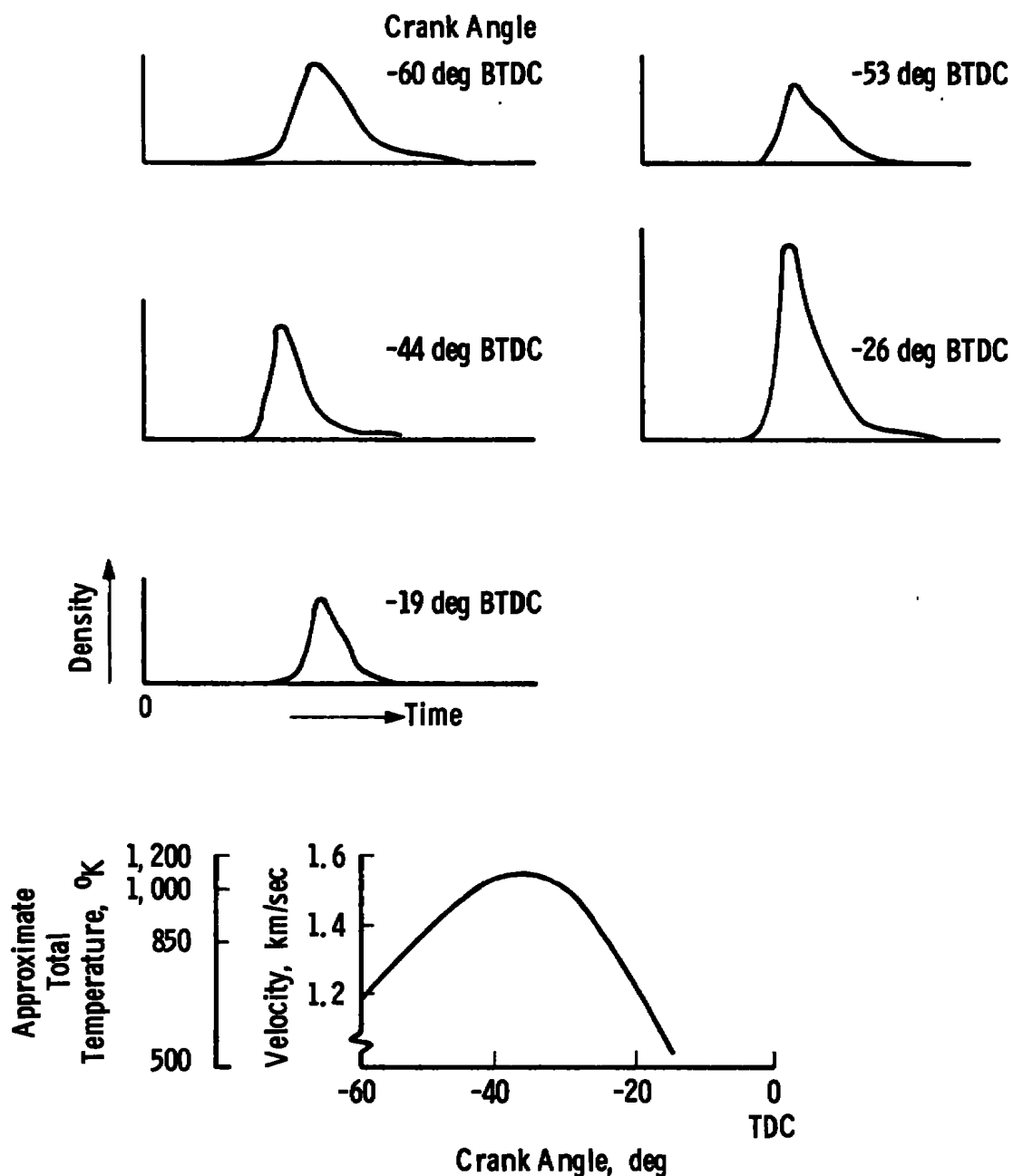
Figure 61. Time-of-flight velocity measurements (Turner engine).

b.   Impact pressure limitation on cryogenic bulkhead.

c.   Mach disk moving between source and skimmer.

Item "a" is mentioned because of the small diameter of the bellows relative to the plume diameter at high combustion chamber pressures. Concerning item "b", subsequent

93

experiments have indicated that impact pressures of 150 to 200 μHg at the cryogenic bulkhead containing the skimmer will cause beam breakdown from molecular backscattering. Calculations indicate that these pressures are not unreasonable for the experiment. Item "c" appears to be the most important.

Figure 62 shows an idealized arrangement for the formation of a molecular beam. When a high-pressure gas expands into a vacuum, the resulting flow field is contained within a barrel shock and a normal shock. The location of the normal shock with respect to the source depends on the ratio of the source pressure to the chamber pressure. When the skimmer is located upstream of the normal shock, it absorbs all the flow and an intense molecular beam is formed. If the flow is completely randomized before beam formation by a normal shock ahead of the skimmer, the beam intensity is significantly attenuated. Ideally, the beam should be formed by skimming upstream of the normal shock. This is normally achieved by maintaining a low pressure in the source chamber and keeping the source-to-skimmer distance small. In this feasibility study, only a cursory attempt was made to optimize the components (i.e., source diameter, skimmer diameter, and source skimmer distance) of the molecular beam system. The resulting source-to-skimmer distance was so large that at moderately high source pressures the normal shock moved upstream of the skimmer, resulting in significant attenuation of the molecular beam. It is suggested that this could be the reason for the abrupt decrease in mass spectrometer signal intensity beginning near 40-deg BTDC.
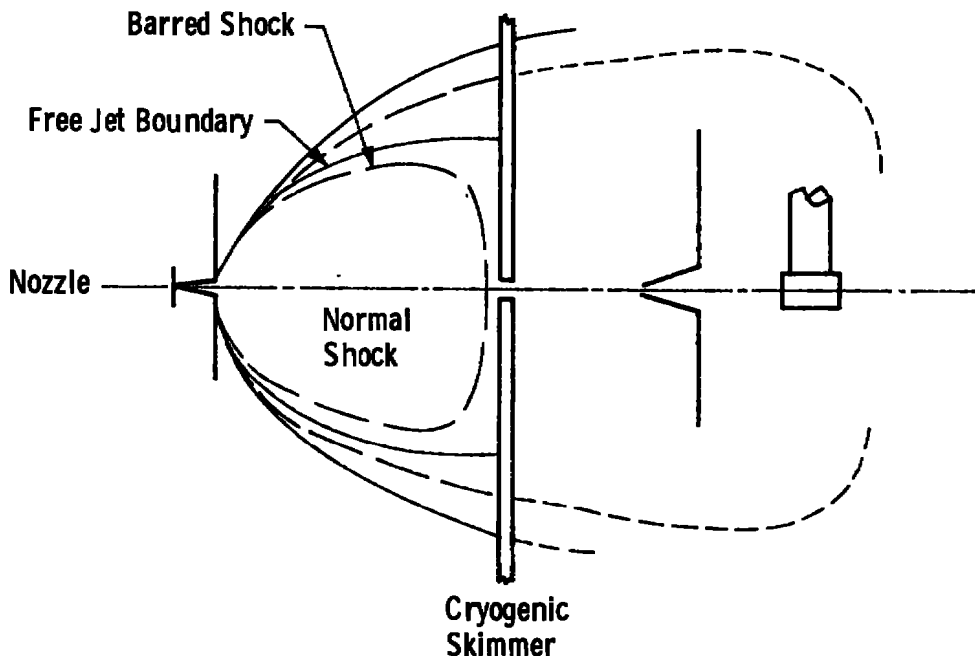
Figure 62. Schematic of molecular beam system.

The data in Fig. 61 support the ideas presented above regarding beam attenuation effects. The expanding flow from the nozzle appears to experience shock interactions after 40-deg BTDC, as evidenced by lower velocities and inferred total temperatures even though the temperature in the combustion chamber is certainly increasing.

The Turner engine experiments were not very successful. However, the need to use a crossed-axis ionizer was established, and the feasibility of extracting a gas sample from the combustion chamber of a diesel engine and of using molecular beam mass spectrometry techniques to measure species intensity, mass spectra, and translational velocity was demonstrated. The results of the Turner experiments also suggested changes that will better match the sampling nozzle orifice size, nozzle angle, source skimmer distance, and skimming technique to the ranges of pressure and temperature that occur in diesel engine combustion chambers. The beam attenuation problems discussed earlier suggested the following:

1. Using a much larger coupling bellows diameter.

2. Resizing the sampling orifice.

3. Using a slender (22-deg) warm conical skimmer.

4. Decreasing the separation between sampling nozzle and skimmer.

These improvements and others were used in applying mass spectrometry to the TACOM research engine.

6.3 TACOM ENGINE MASS SPECTROMETER MEASUREMENTS

6.3.1 TACOM Engine Experimental System

A second experimental arrangement was developed to overcome the previously discussed problem areas. A LABECO-TACOM research engine was interfaced with the 4-deg by 10-ft Research Vacuum Chamber (RVC). Figure 63 shows the general configuration of the experimental installation.

The LABECO-TACOM research engine is a single-cylinder, four-stroke-cycle diesel engine. The engine system includes a Varidrive electric motor for starting and for running unfueled, an eddy current dynamometer, and an air ejector for removing the exhaust gases. A spacer clamped between the cylinder head and the cylinder barrel and an extended piston adapt the engine for this work. The engine modifications are described in detail in Section 2.3. A sampling nozzle with an adapting flange fits into a socket in the spacer (Fig. 64). The nozzle throat assembly reaches the edge of the combustion bowl through a slot in the piston crown.
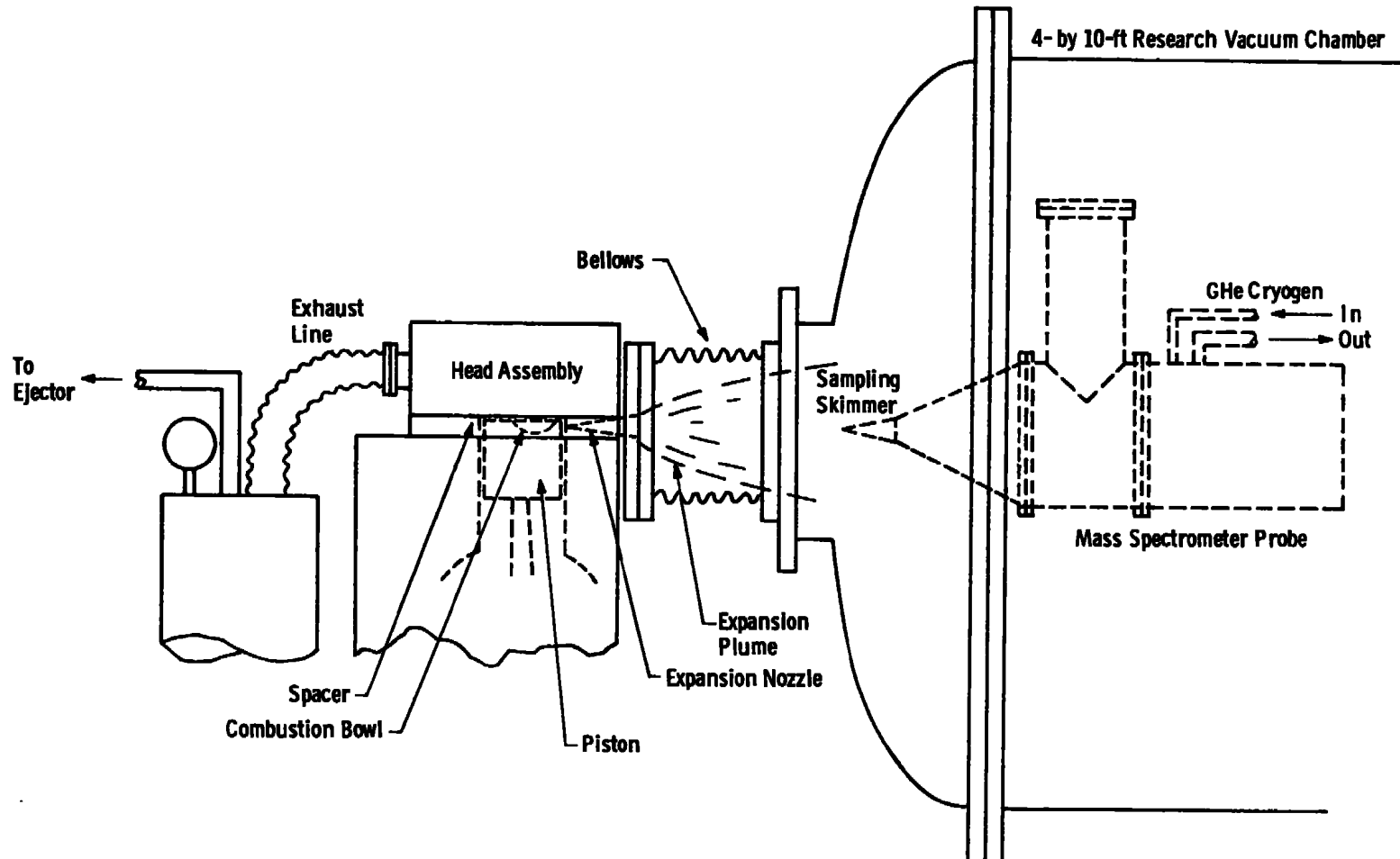
Figure 63. Schematic of 4- by 10-ft research vacuum chamber with
TACOM diesel engine installation (for mass spectrometer
measurements).
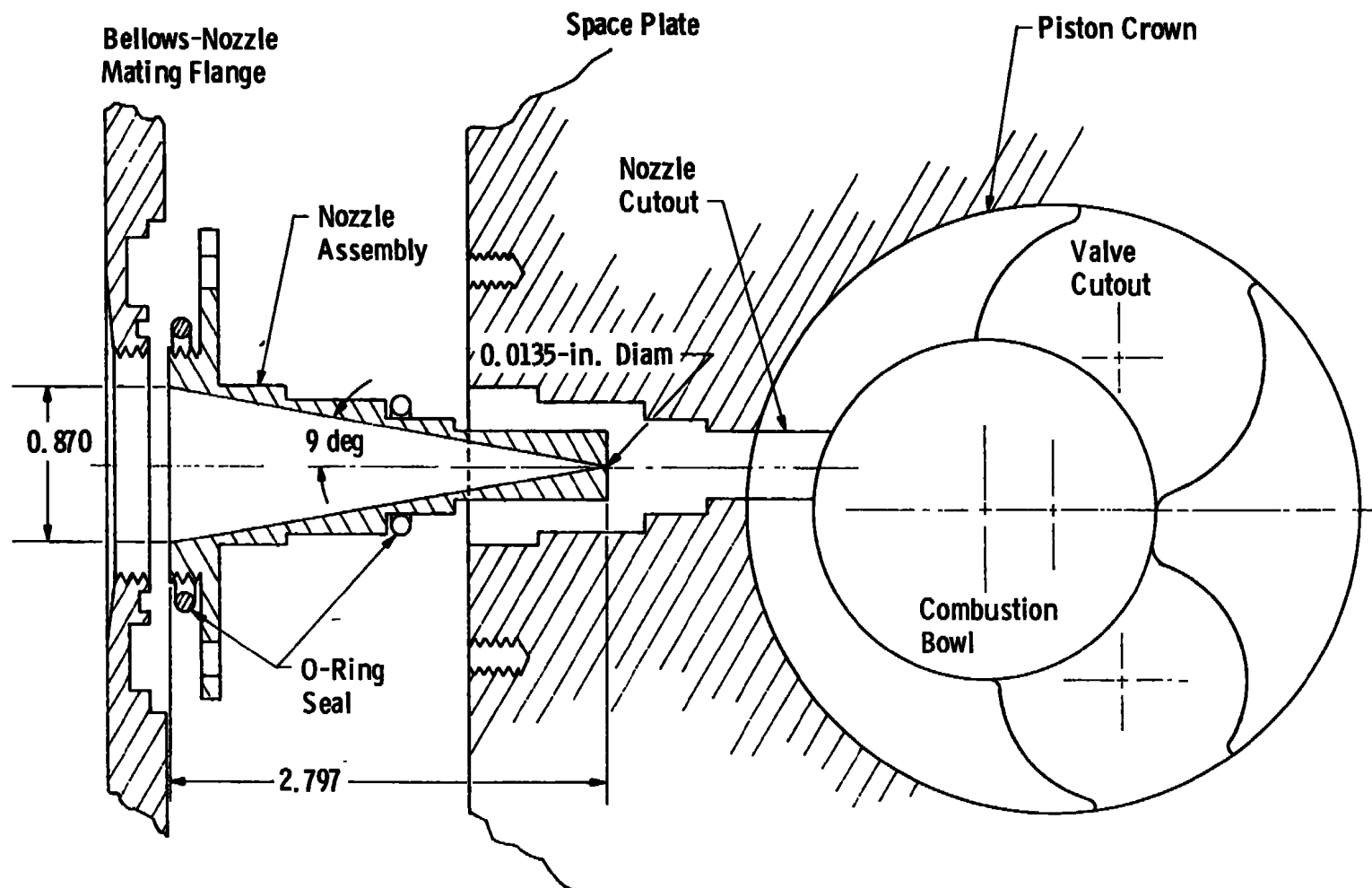
Figure 64. Top view of nozzle, spacer interface with TACOM diesel engine.

Conflicting considerations required a compromise design of the sampling nozzle:

1. A short length to minimize chemical effects is limited by the engine configuration, and

2. A large mass-flow rate from the nozzle for measurement sensitivity conflicts with a minimum disturbance of engine operating characteristics.

Compatibility with the engine configuration and dimensions was the most restrictive requirement. This limited any nozzle design to a minimum length of 2.5 in. and a maximum exit diameter of 1.0 in. Nozzle gas-dynamic calculations were made to optimize all possible effects. The following design was used:

1. 9-deg half-angle

2. 0.0135-in. throat diameter

3. 3/32-in. throat length

4. 2.797-in. total length

5. 0.870-in. exit diameter

The sampling nozzle throat diameter was selected for minimum effect on engine performance and minimum leakage into the vacuum chamber during nonoperating periods.

In designing the experimental arrangement for the TACOM engine, a 10-in.-diam bellows, the largest practical, was used to couple the sampling nozzle flange to the vacuum chamber. A special procedure was developed so that a gate valve previously used in the Turner engine experiments for vacuum chamber isolation could be eliminated. To minimize the rather large leak from the engine's combustion chamber into the vacuum chamber through the sampling nozzle during pumpdown, provision was also made to pump directly on the combustion chamber. With the engine's piston at TDC and its intake and exhaust valves closed, a 375-liter/minute mechanical pump reduced the combustion chamber pressure to 10 to 15 mm Hg. Thus, leakage through the 0.0135-in.-diam nozzle throat was minimized during pumpdown. Elimination of the gate valve cut the distance between the nozzle exit and the skimmer in half. Figure 65 shows this interface between the engine and the vacuum chamber.

The AEDC 4- by 10-ft RVC (Fig. 63) cryopumping is supplied by a radial-finned GHe-cooled to (14 to 20°K) aluminum cryoarray, an LN_2-finned GHe-cooled to (14 to 20°K) aluminum cryoarray, an LN_2-cooled (77°K) aluminum cryoliner, a 6-in. oil diffusion pump with refrigerated trap, and a 300-cfm mechanical vacuum pump. The chamber pretest

4- by 10-ft Research Vacuum and Engine Interfacing Flange Assembly

Head Assembly

Bellows Assembly

Spacer Assembly

A E D C
5180-75
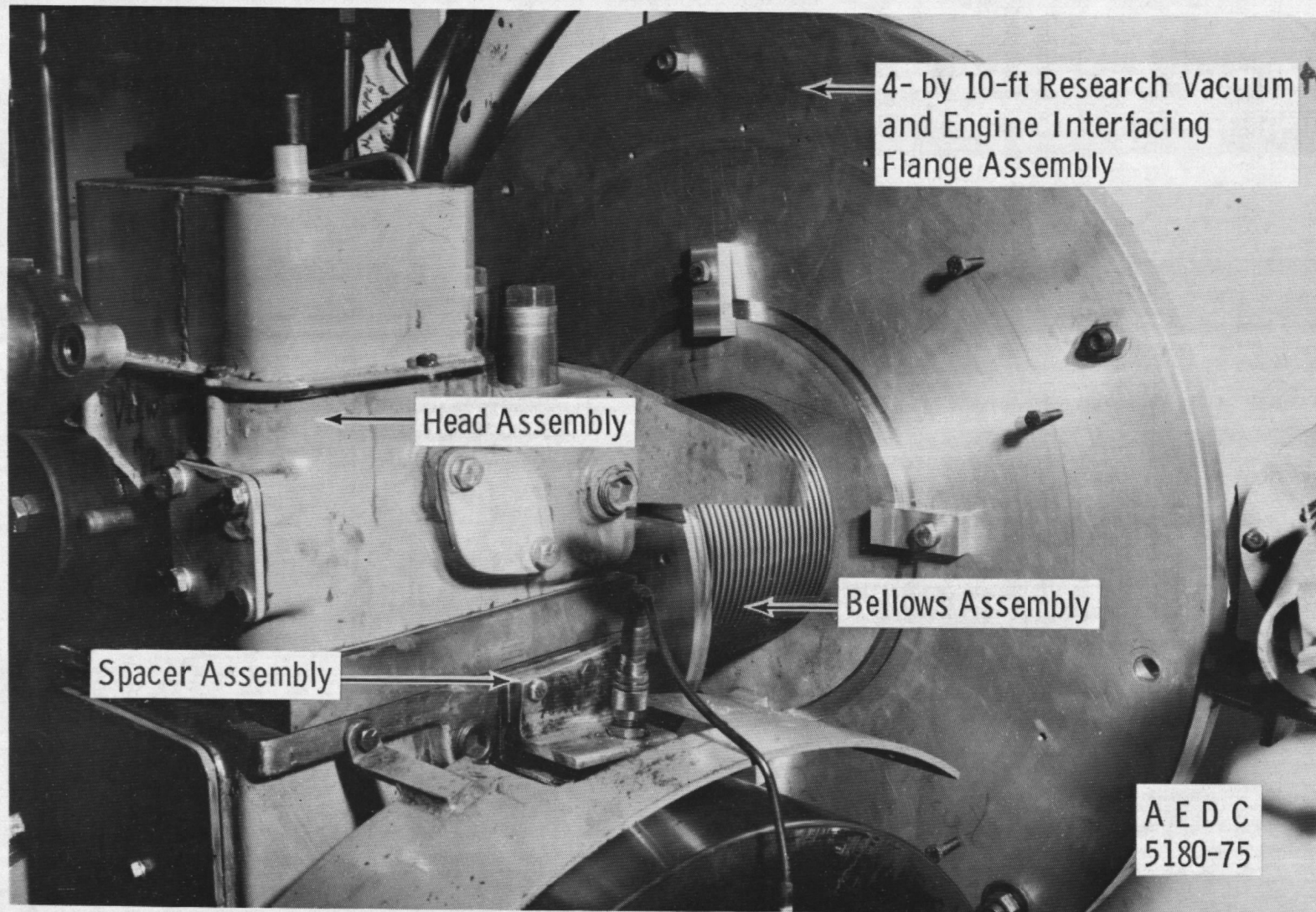
Figure 65. Bellows, spacer, and head assembly, TACOM diesel engine.

conditions, with the engine system isolated, would nominally give background pressures of 2×10^{-7} torr. With atmospheric pressure in the TACOM engine combustion chamber and not isolated from the vacuum chamber, the vacuum chamber pressure was approximately 2×10^{-5} torr.

Figure 66 is a schematic of the mass spectrometer probe assembly used for the TACOM experiments. It combines elements to provide for molecular beam formation, ionization, ion mass filtering and detection in a compact package which has an internal pumping system to provide a hard vacuum for the spectrometer head assembly. The probe originally used axial ionization but was converted to cross-beam ionization by adding a T-transition piece. The cryogenic GHe cryopump was attached to and thermally isolated from the T-transition section at the aft end of the probe assembly. A small opening in the end of the cryopump was provided for laser sighting and alignment procedures. The mass spectrometer head was mounted in the elevated section of the probe, and the skimmed molecular beam passed directly through the ionizer.
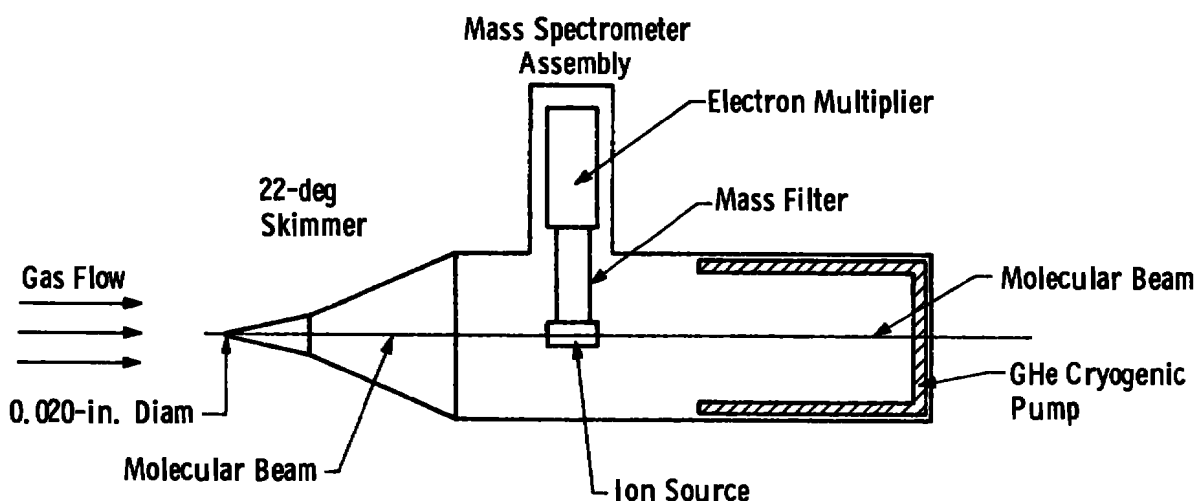
Figure 66. Schematic of mass spectrometer probe assembly.

The molecular beam probe assembly provided more flexibility for ideally locating the sampling point relative to the expansion nozzle than did the type of system used for the Turner experiments. The probe did not employ a cryogenic skimmer as in the Turner engine experiments. Its location in the vacuum chamber is schematically shown

in Fig. 63 and photograph of the installed system is shown in Fig. 67. The skimmer was located 9 in. from the sampling nozzle exit plane. The skimmer orifice, 0.020 in. in diameter, minimized the probe gas load at the short separation distance required. The 22-deg total cone angle was selected for an attached shock at the skimmer for the anticipated flow conditions. The thin-walled skimmer was fabricated by.electroplating a machined aluminum cone with nickel and using a lye solution to remove the aluminum.

6.3.2 TACOM Engine Results

All data for the TACOM engine, both unfueled (motored) and fueled, were taken with the engine turning at 1,000 rpm. Engine load was varied to maintain the speed constant during test. The fuel used was Diesel No. 2, and the throttle setting was identical for each run. The initial tests were used to assess the problem areas suggested by the Turner engine experiments.

The concept of minimizing sampling nozzle-to-skimmer separation by not using a gate valve proved satisfactory. New pumpdown procedures permitted adequate vacuum chamber performance without isolating it from the sampling nozzle during pumpdown. The most serious consideration during the initial checkout was the maintenance of a molecular beam through the entire engine cycle, particularly during combustion. The initial tests indicated that breakdown of the flow ahead of the skimmer, which attenuated the molecular beam in the Turner engine setup, did not occur in the TACOM engine gas-sampling system.

Mass spectrometer measurements were confined principally to mass species 18, 28, 30, 32, 44, and >60 amu. Relative measurements of crank-angle variations of number density for mass numbers $18(H_2O)$, $28(N_2$ and CO), $30(NO)$, and $44(CO_2)$ are presented in Figs. 68a through c. Kistler pressure transducer measurements of combustion chamber pressure and photodetector measurements of light emission are also shown. Note that time and crank-angle increase from right to left in this figure. Mass scans from 2 to 60 amu at fixed crank angles were also accomplished. Typical results are shown in Figs. 69a through c for a 26- to 44-amu mass range and for crank angles of 5, 35, and 65 deg after top dead center (ATDC).

6.3.3 Evaluation of TACOM Engine Results

An error in fabricating the piston's combustion bowl resulted in reducing the compression ratio to 14 to 1 rather than the desired 16 to 1. The error was not discovered until after the data were taken, which made interpretation of some of the data difficult. The reduced compression ratio resulted in delayed ignition and late combustion. The effect is evident in Figs. 68a through c where the peak combustion pressure and light emission occur significantly after TDC.
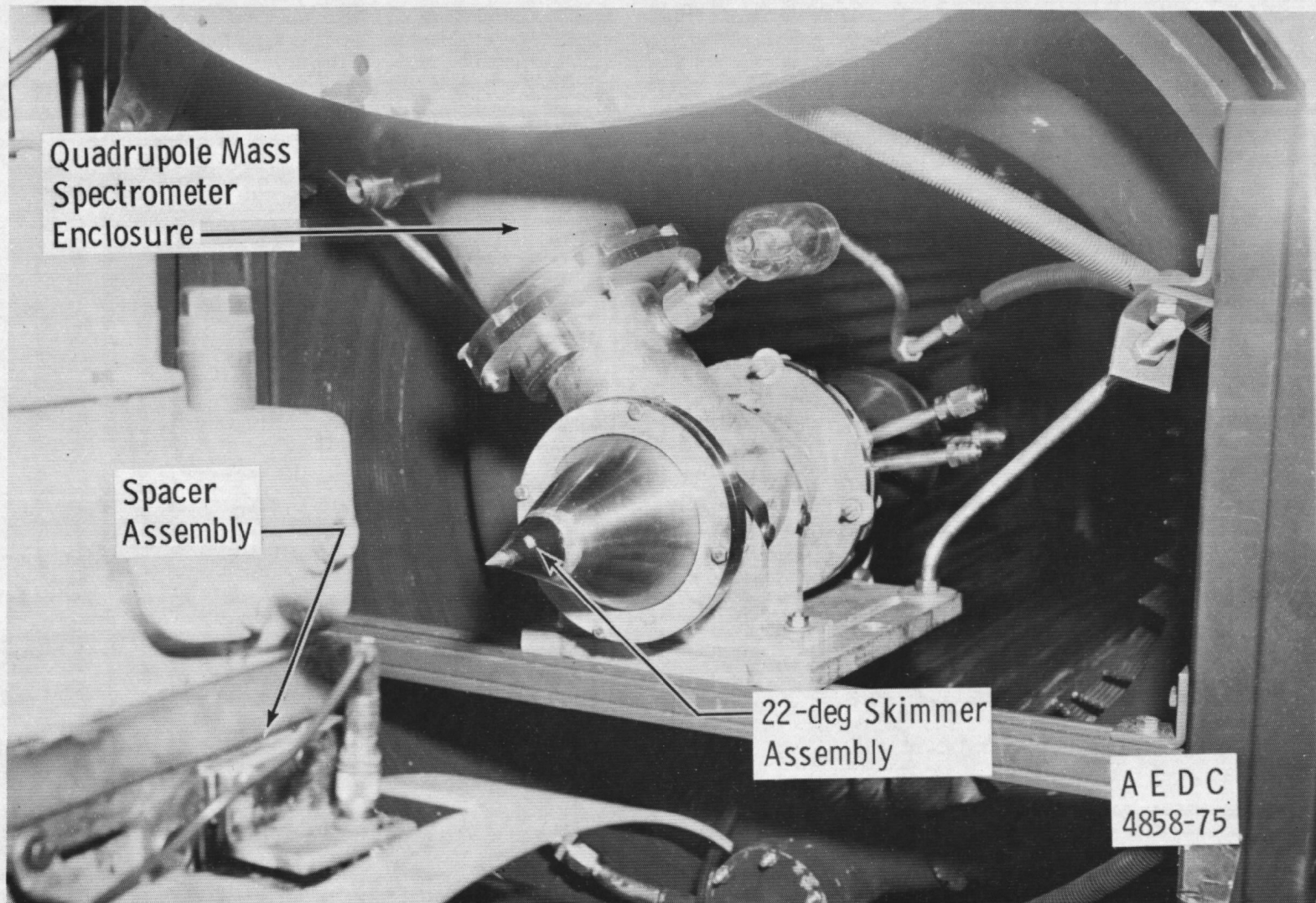
Figure 67. Mass spectrometer probe — 4- by 10-ft research vacuum chamber.
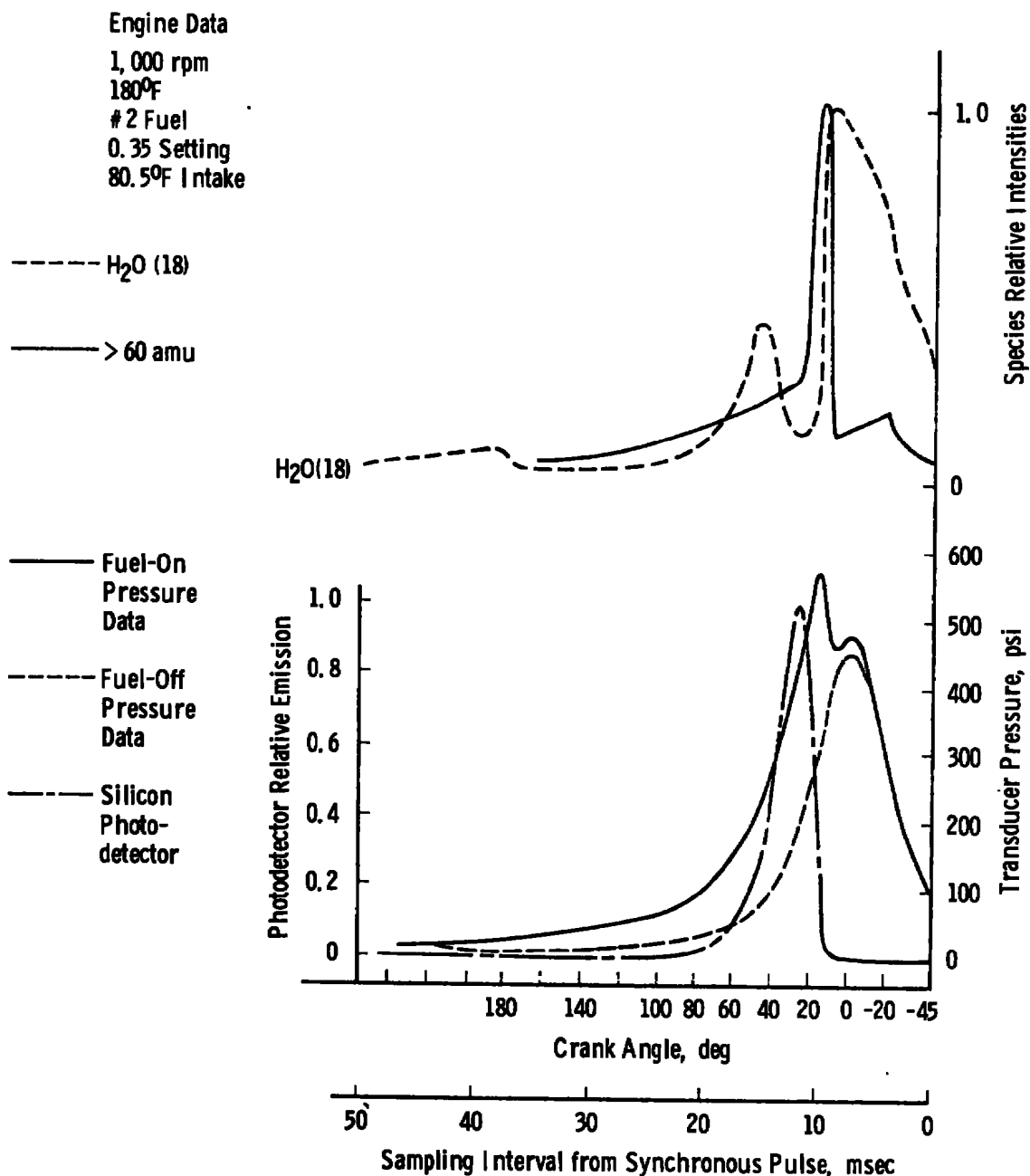
a. H_2O

Figure 68. Mass spectrometer, pressure transducer, and photodetector signals versus crank angle.

Engine Data
1, 000 rpm
180°F
2 Fuel
0. 35 Setting
80.5°F Intake
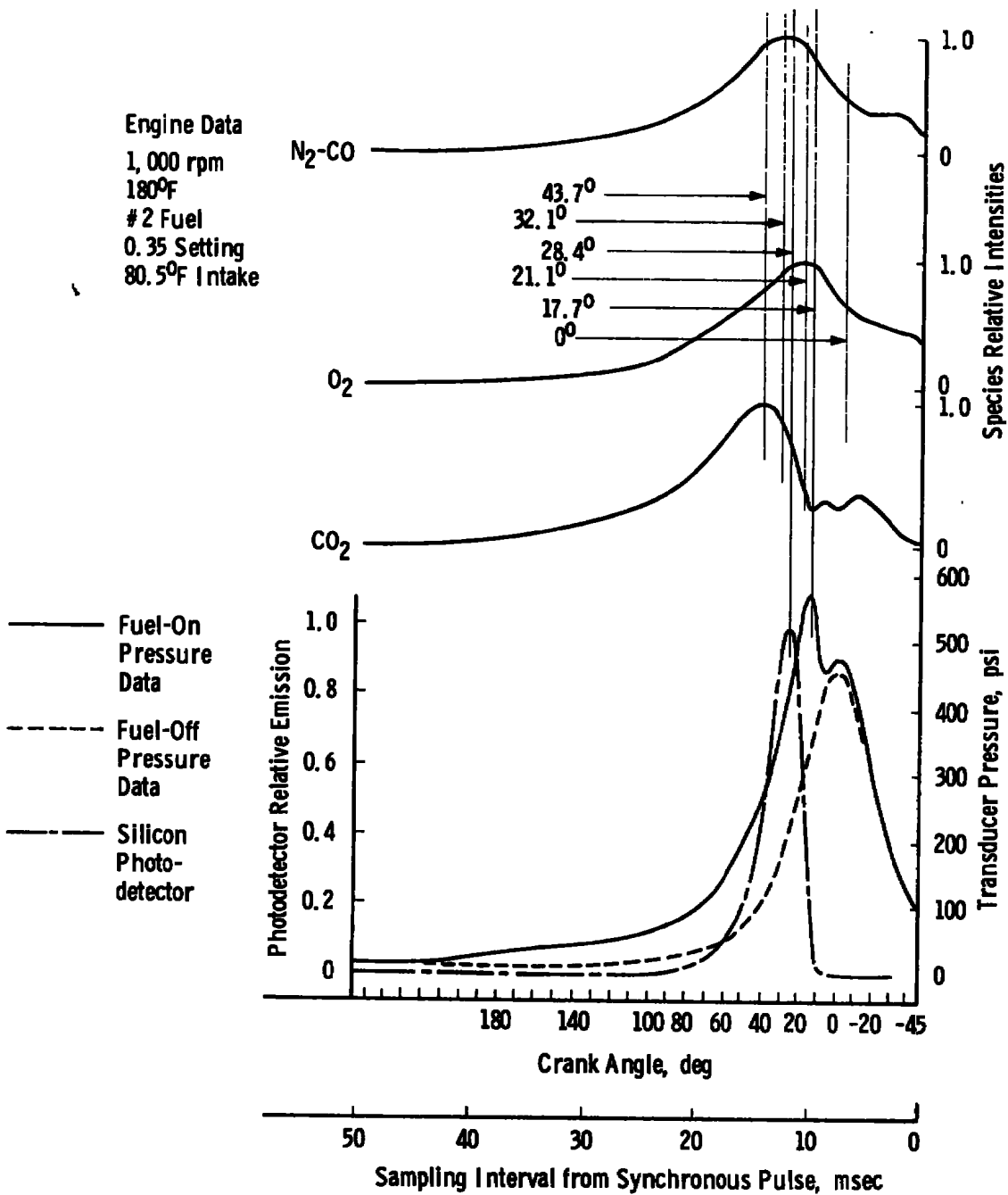
b. N_2-CO, O_2 and CO_2
Figure 68. Continued.

104

--- Engine Data
1,000 rpm
180°F
#2 Fuel
0.35 Setting
80.5°F Intake

——— 30-amu Species
(Averaged Signal)

------- Fuel Fragment
(C_2H_6)

—-—- NO

——— Fuel-On
Pressure
Data

----- Fuel-Off
Pressure
Data

—-—- Silicon
Photo-
detector
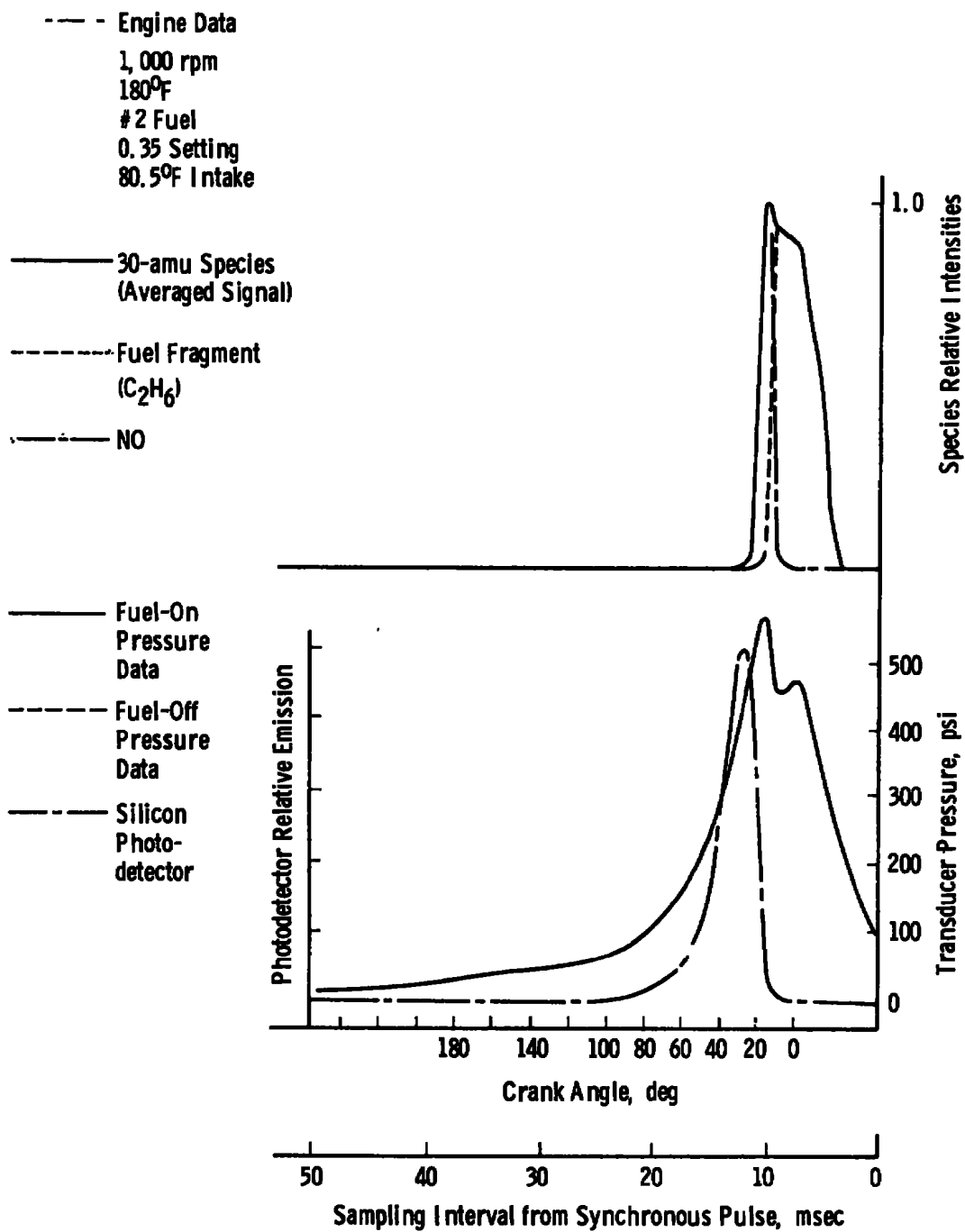
c. NO
Figure 68. Concluded.
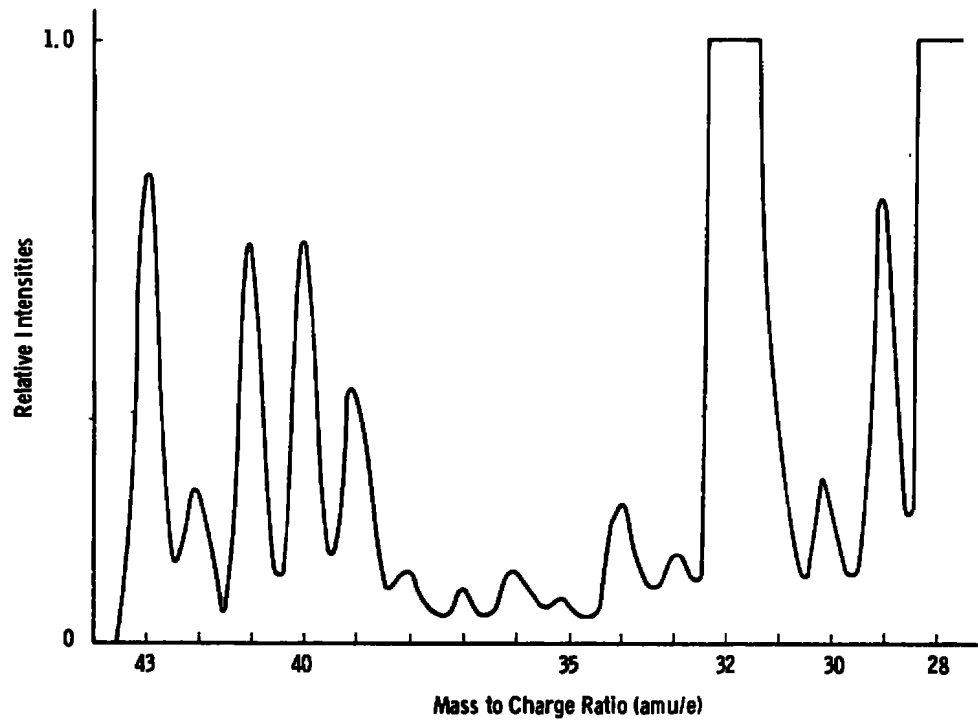
a. Crank angle of 5 deg
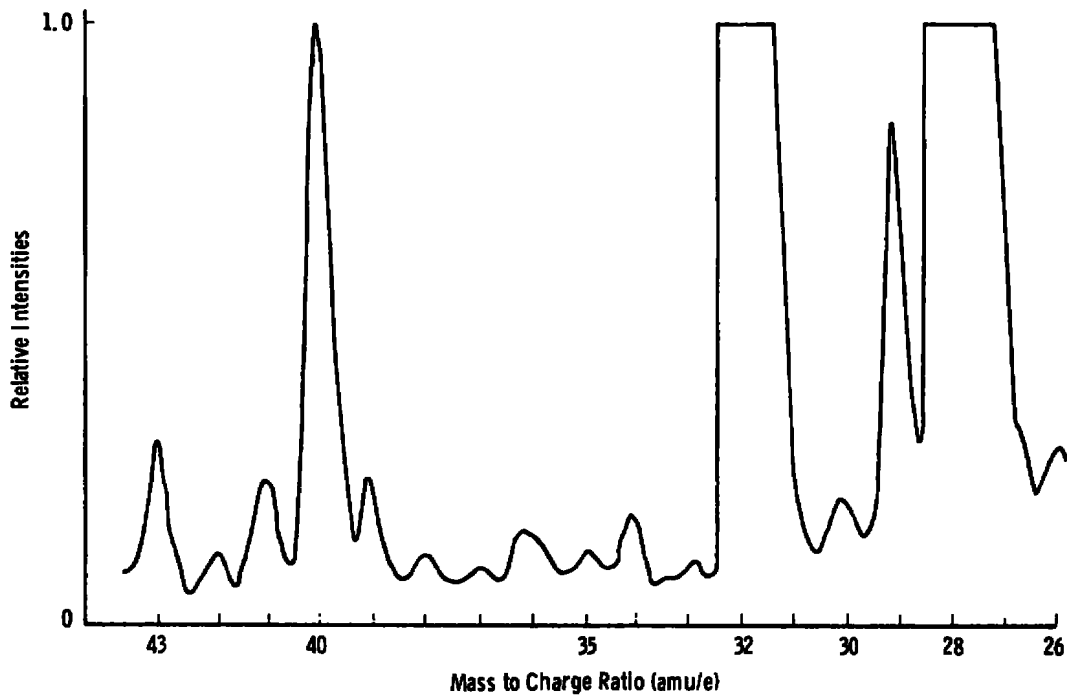
b. Crank angle of 35 deg

Figure 69. Mass spectra 26 — 43 AMU at 5, 35, and 65 deg ATDC.
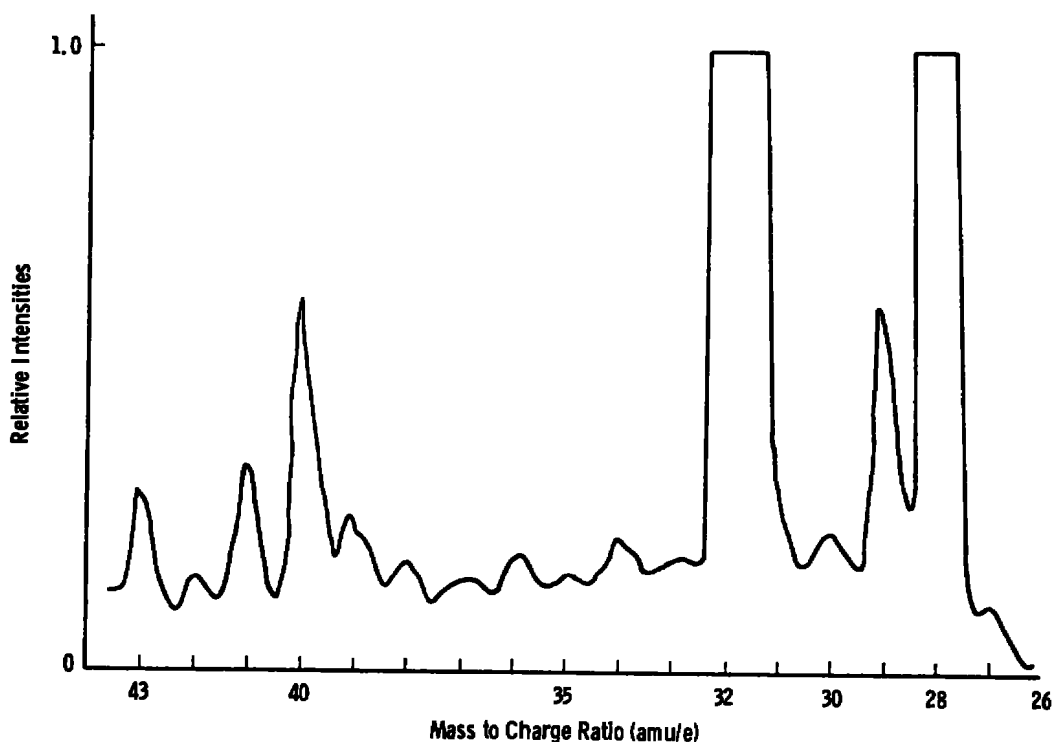
c. Crank angle of 65 deg
Figure 69. Concluded.

Examination of Fig. 68 reveals phenomena which cannot be attributed directly to engine performance. Since the mass spectrometer signal relates directly to species number density in the combustion chamber at an earlier time, which is separated from real time by the time of flight, it should be a simple representation of volumetric changes in the combustion chamber superposed on the species modifications attributable to combustion or to the heat of compression. Examination of the 28-amu N_2-CO curve (Fig. 68b) reveals the general trend expected. However, the peak signal occurred at a later crank angle than anticipated. This shift could be caused by a lower-than-expected temperature plus a large production of CO during the latter part of combustion. The delay in the 44-amu (CO_2) (Fig. 68b) peak is similar and can be explained accordingly, since it is also a major combustion constituent and corresponds favorably with the light emission measured by the photodetector. However, the occurrence of the O_2 peak at later-than-expected crank angles tends to suggest the presence of other potential problems. Two easily corrected problems which may explain the delayed peaks are:

a. Poor skimming at the warm skimmer of the mass spectrometer probe.

b. Combination of insufficient probe internal pumping speed and nonoptimum skimmer orifice size and skimmer source separation.

Concerning the former, posttest microscopic examination of the skimmer did reveal an orifice diameter to lip thickness ratio less than desirable. Replacement of the skimmer with one of "molecular beam" quality should assist in shifting the signal curves to the expected shape and position. Concerning the latter, the pumping problem coupled with a possible skimmer re-expansion implied by item "a," above has the effect of beam attenuation by molecular scattering processes from probe background gases. Indeed all constituents, except O_2 and N_2-CO, which require 22°K pumping surfaces, appear to behave well within reason. Constituents CO_2, H_2O, NO, and $C_m H_n$ cryopump at temperatures above 55°K and are thus pumped more readily.

The H_2O (18-amu) curve in Fig. 68a gives an indication of an advantage of the expansion nozzle technique over tube sampling techniques. Water is known to dissociate into H and OH at temperatures below those experienced in diesel combustion, the H and OH acting as catalytic ions during combustion. The H_2O curve (Fig. 68a) demonstrates the initial compression and production, then dissociation of water. Dissociation appears to become pronounced where the pressure curve indicates combustion is accelerating rapidly. Recombination is also evident later during the cycle, corresponding to the light emission curve and during probable low-temperature combustion. Tube sampling techniques do not quick-freeze the composition, and details of dissociation would be lost during sample transit.

The production of NO during the cycle is typified by the NO curve in Fig. 68c. The details of the 30-amu waveforms are characterized by two effects, one of which was observable via an oscilloscope display of the instantaneous spectrometer signal. The initial response shown of the averaged waveform occurred exactly at fuel injection. This component was evidently a fuel fragment. The second component occurred exactly with combustion as indicated by Fig. 68c and corresponded to the peak combustion pressure. Direct observation showed this component to be rather narrow and erratic on successive engine cycles. This coupled with the 3-deg crank-angle resolution of those data caused the spike to be relatively small in comparison to the overall curve.

The depletion of O_2 caused by combustion is implied by the N_2/CO and O_2 waveform peak separation shown in Fig. 68b. An effect not shown but observed during O_2 data acquisition occurred during fuel on-off-on transitions. The reduction of O_2 waveform peaks during fuel-on was appreciable. This effect might be used to determine the utilization of O_2 during combustion.

The feasibility of extracting a gas sample from the combustion chamber of a diesel engine, and of analyzing the sample using molecular beam mass spectrometry techniques, was demonstrated for a much wider range of combustion chamber conditions than had

previously been demonstrated with the Turner engine. Analysis of the TACOM data also suggested changes to the experimental system that should improve future measurements. The results show, however, that:

1. A gas sample can be extracted from the combustion chamber of a diesel engine and analyzed in a quadrupole mass spectrometer.

2. Species intensity measurements can be made as a function of engine crank angle.

3. Mass spectra can be determined for fixed engine crank angles.

4. Molecular translational velocity (which can indicate combustion chamber temperature) can be measured as a function of engine crank angle.

The results also indicate that a new warm skimmer, more internal cryogenic pumping surface, and a time-of-flight detector should be added to the mass spectrometer probe for future studies. These changes should produce very reliable molecular beams from which more meaningful qualitative and quantitative combustion measurements can be obtained.

7.0 RAMAN SPECTROSCOPY

The mass spectrometric analysis of the combustion process gives a measure of the relative intensity of the various species. Because of the large dynamic range of the system, minor species may also be monitored. To convert these relative values to absolute number densities, it is necessary to provide an in situ calibration of the mass spectrometer. Considerable experience has been gained in the application of laser Raman scattering techniques in the measurement of gas specie concentration. Although the feasibility of applying the Raman spectrographic technique was not established during this portion of the program, it is proposed to use this technique to calibrate the mass spectrometer and to make major species concentration measurements.

When a monochromatic laser light beam strikes a molecule, scattering processes take place which make it possible to determine the identity, density, and the vibrational and rotational temperatures of the scattering media. In this scattering process (1) there is a particular wavelength shift associated with each gas and (2) the amount of scattered light at the characteristic wavelength can be associated with the absolute number density of the gas. (The wavelength shifts for the gases of interest are well documented.) Thus, this technique permits the identification of gas species and also a determination of their absolute number density.

The energy associated with the vibrational and rotational degrees of freedom in an expanding gas is manifested in the detailed spectra structure of the scattered light. Through the use of high-resolution spectral devices it is possible to derive the rotational and vibrational temperatures. It is reasonable to assume that the vibrational mode is frozen at the nozzle throat such that it should be possible to determine the vibrational temperature associated with the combustion process. Additionally, knowledge of the specie density and temperature values will enable more accurate corrections to be made of the effects of chemical reactions occurring in the expansion process.

In the present application a pulsed laser beam which is synchronized with crank position is focused on the sampling nozzle centerline in the exit plane. A spectral element and a photomultiplier measure the light intensity from the scattering volume on the nozzle centerline. The spectral element may be a spectrometer, interferometer, or simple optical filters.

A schematic of the laser-Raman system is shown in Fig. 70. Not shown in this schematic but shown in Fig. 63 for the mass spectrometer, is the sampling nozzle and the vacuum chamber into which the combustion gases are expanded. The Raman measurements will be made as close to the nozzle exit plane as the physical constraints of the vacuum system will permit. Both the continuous-wave (CW) argon laser and the
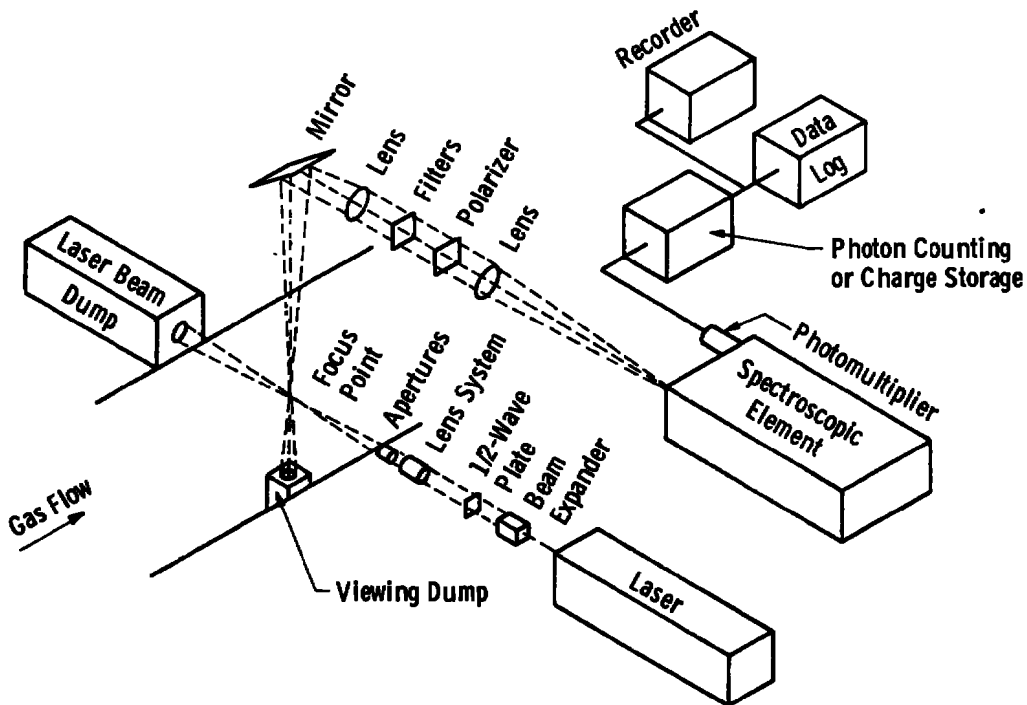
Figure 70. General setup for Raman diagnostic applications.

pulsed ruby laser will be used in these measurements. Synchronization and time circuits will be incorporated in the system such that the variation of density with crank angle can be determined. To date, a design concept has been developed for laser beam injection into the flow field and collection of the scattered light.

8.0 RESONANCE ABSORPTION

With the advent of tunable lasers, increased attention is being focused on the development of resonance absorption techniques as another spectroscopic method for determining gaseous concentrations. Initially, for diesel engine applications, it was felt that the fortuitous match between helium-neon (He-Ne) infrared laser transition at 3.39 μm and a fundamental vibration mode found in most hydrocarbons could be exploited. Two basic approaches have been followed in exploring the capabilities of the resonance absorption technique to time-resolved hydrocarbon concentration studies (Ref. 4). The first of the basic goals was to construct a visualization system which would have the required flexibility to obtain qualitative information concerning the hydrocarbon concentrations over an optical path through the cylinder of a diesel engine. Such a system requires a fairly rapid response time and suitable timing circuitry in order to obtain data only during a very small portion of the engine cycle. The second goal was to obtain accurate quantitative gaseous concentration data within the diesel engine environment. Initial experiments were directed toward obtaining stable laser operation centered on the methane absorption line, since the feasibility of using the He-Ne transition at 2947.903 cm^{-1} has been demonstrated (Refs. 46 and 47).

It was found that a number of gases absorb light in the 2947.8- to 2948.0-cm region, which is a portion of the rotation-vibration absorption band of carbon-hydrogen bonds. Tuning of the optical frequencies was effected by applying a varying external magnetic field. In the preliminary experiments, a number of absorption maxima for several hydrocarbons were found. One of particular interest is methane (CH_4) which has an absorption maximum at 2947.888 cm^{-1}. Absorption constants for methane were found to be 0.17 and 0.18 cm^{-1} torr^{-1} at room temperature at the respective resonance lines. Within this same spectral region a large number of gases also exhibit broadband absorption coefficients. However, they are generally several orders of magnitude lower than that of CH_4. Some of the significant constituents and their interaction cross sections are presented in Table 3.

Table 3. Gas Constituents and Their Interaction Cross Section

Propane	0.01 cm⁻¹ torr⁻¹	Cyclohexane	0.038
Butane	0.015	Cyclohexene	0.017
Cyclopentane	0.017	Methylcyclohexane	0.026
Cyclopentene	0.01		

It is interesting to note that a previous investigator (Ref. 47) was unable to resolve structure in propane or butane. This can be attributed to three causes: (1) the laser was lasing at more than one frequency as it was not stabilized to a particular output frequency, i.e., more than one longitudinal mode was in operation at a time; (2) the heavier gases which have an increased number of peaks caused by the increased number of almost degenerate vibration levels and the closer spacing of the rotational levels and the small level splittings caused by anharmonic forces absorb light in a near continuous spectrum; (3) Doppler broadening which is inversely proportional to the square root of the molecular mass also affects the line shape. Methane, however, which was resolved (Ref. 46), has a greater line width due to its low molecular weight. The increase in the number of individual lines in the heavier gases tend to outweigh the Doppler broadening effect. This illustrates that for the heavier organic molecules, limitations on resolving power in the laser are not important.

Methane has an absorptivity that is at least three times larger than the gases tabulated in Table 3. It is also very close to the untuned He-Ne laser frequency (3.39 μm). Even if other hydrocarbons are present in abundnace, overshadowing the methane absorption line, the resonance absorption technique can define fuel-rich regions within combustion cells and during combustion processes. Therefore, the technique, rather than being specie specific, e.g., for methane, is hydrocarbon specific.

The frequencies and relative line widths of the laser and methane are shown in Fig. 71. The laser Doppler profile is centered at 2947.903 cm⁻¹ with an approximate width of 0.05 cm⁻¹. The methane line is represented at a partial pressure of 7.6 torr (0.147 psi) with nitrogen the foreign gas responsible for broadening, making the total pressure 760 torr (14.7 psi). The methane line is centered at 2947.888 cm⁻¹ with a full width at half maximum of 0.012 cm⁻¹. The separation between modes for the Jodon HN-15 laser is 0.0062 cm⁻¹. The Spectra Physics Model 120 initially used had a mode spacing of 0.0129 cm⁻¹. While the latter had approximately four longitudinal modes in operation at any one time, as many as eight modes in the HN-15 laser could be expected.

Methane at 7.6 torr, 760 torr Total
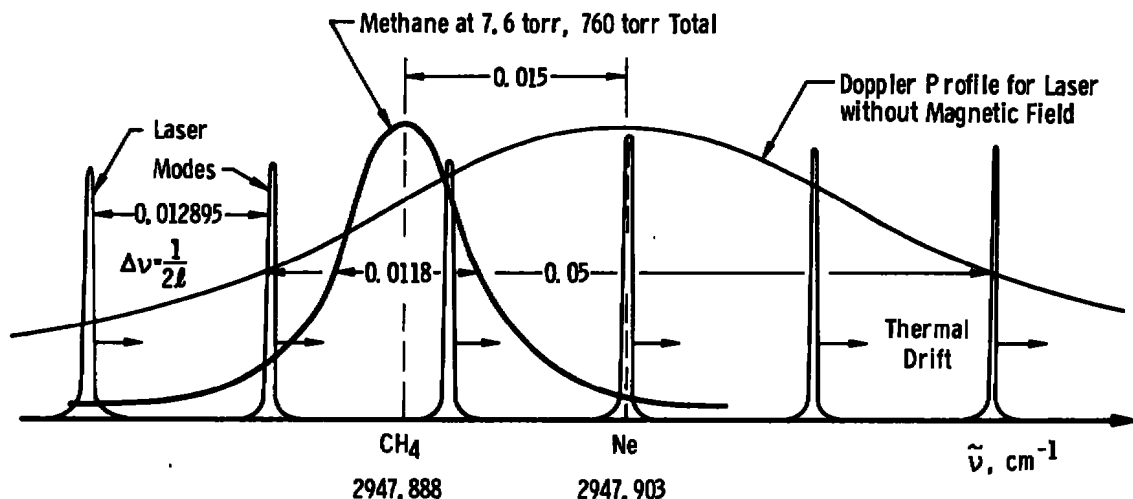
Figure 71. Relative line width and mode spacing.

For the case where pressure broadening becomes predominant, as illustrated in Fig. 72, the laser line width becomes small when compared to the absorption line. Here, the line width (full width at half maximum) and the line centers are shown for the laser and CH_4. For this example, a temperature of 2,250°K and a pressure of 352 psi were assumed in a gas mixture of CH_4 and combustion gases typical of diesel exhaust. The laser can therefore be used to accurately measure the absorption line center since the ratio of halfwidths is 17.14:1. Under these conditions the narrow line absorption technique is applicable (Ref. 48). This technique, as modified for use in diesel engine environments, will be outlined in a later section.
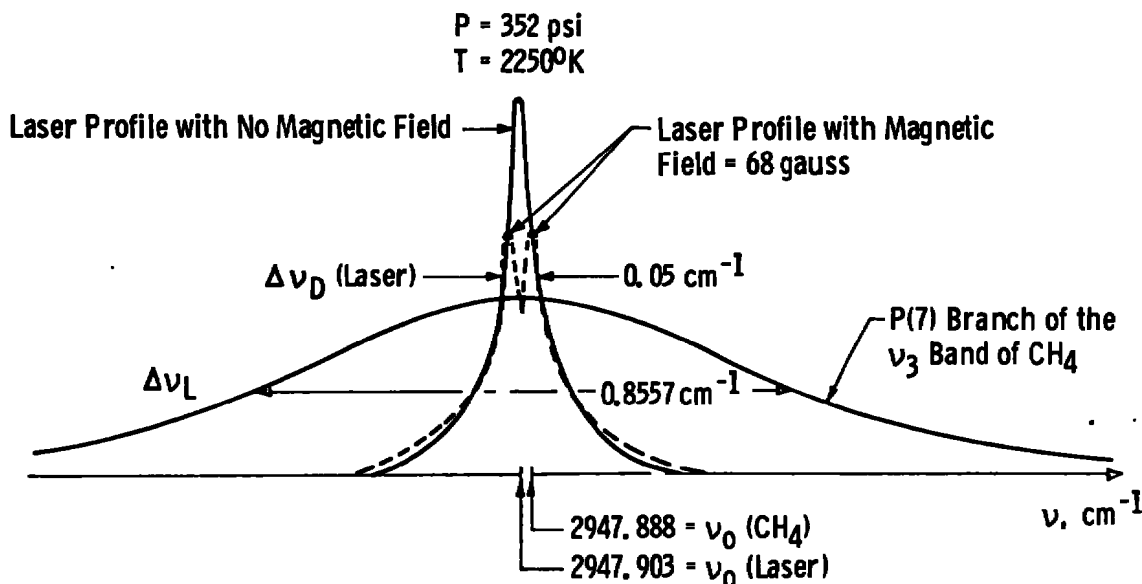
Figure 72. Laser Doppler profile compared to collision broadened profile of methane (with and without magnetic field).

113

Initial experiments were concerned primarily with the methane molecule for several reasons: (1) Methane has been detected in the exhaust products of internal combustion engines, (2) methane has a well-documented line structure, (3) the absorption coefficient of methane is very strong relative to other known molecules, and (4) little shifting is required in the basic laser frequency to obtain resonance. The technique, as applied to high temperature and pressure regimes, may best provide a measure of only the total hydrocarbon content.

8.1 METHANE MOLECULE

Consideration will now be given to the energy levels of the methane molecule (CH_4). The methane molecule is a member of the point group having tetrahedryal symmetry. Furthermore, the molecule is a symmetrical top as it has no identifiable figure axis (Refs. 3, 49, and 50).

8.1.1 Vibrational Infrared Spectra

The symmetry of the molecule gives rise to only three possible vibrational modes. They are the A_1 which is nondegenerate, E which is doubly degenerate, and F which is triply degenerate. The vibrational frequencies associated with each of these species are as follows: A_1 is the $\tilde{\nu}$, band centered at 2,914 cm^{-1}; E is the $\tilde{\nu}_2$ band centered at 1,526 cm^{-1}; and F_1 has two frequencies, the $\tilde{\nu}_3$ band centered at 3,020 cm^{-1}, and the $\tilde{\nu}_4$ band centered at 1,306 cm^{-1}. Of these four frequencies only two are active in the infrared; these are the $\tilde{\nu}_3$ and $\tilde{\nu}_4$. It is the ν_3 band centered at 3,020 cm^{-1} which is of interest to resonance absorption experiments.

8.1.2 Rotational Infrared Spectra

The rotational energy levels of methane can be described by the following equation:

$$F(J,K) = BJ(J+1) + (A-B)K^2 \qquad (8\text{-}1)$$

where J is the total angular momentum quantum number and K is the angular momentum quantum number associated with the figure axes of the molecule. A and B are defined in terms of the moments of inertia, I_a and I_b, of the molecule, as follows:

$$A = \frac{h}{8\pi^2 c I_a} \qquad (8\text{-}2)$$

$$B = \frac{h}{8\pi^2 c I_b} \qquad (8\text{-}3)$$

where h = Planck's constant and c the speed of light. However, for methane $I_a = I_b$ implying A = B and also K = 0 because there is no identifiable figure axis. The equation for the energy levels simplifies to

$$F(J) = BJ(J+1) \tag{8-4}$$

The statistical weight g_i of the energy level is $(2J + 1)^2$ for symmetric and spherical tops.

8.1.3 Vibration-Rotation Infrared Transition

In general when the vibration and rotational transitions occur simultaneously in a molecule, fine structure splitting of the vibrational band occurs because of interactions with the rotational states. When centrifugal and coriolis forces are considered, Eq. (8-1), for the rotational energy levels, becomes

$$F^+(J) = BJ(J+1) - DJ^2(J+1)^2 + 2B\rho(J+1) \tag{8-5}$$

$$F^\circ(J) = BJ(J+1) - DJ^2(J+1)^2 \tag{8-6}$$

$$F^-(J) = BJ(J+1) - DJ^2(J+1)^2 - 2B\rho J \tag{8-7}$$

where B, δ, and D are empirically determined constants. In methane, B has a representative value of 5.25 cm^{-1}, δ has a value of 0.056, and D has a value of 9×10^{-5} cm^{-1}.

The selection rule for the quantum number J is

$$\Delta J = 0, \pm 1 \tag{8-8}$$

Additionally ΔJ is restricted to be +1 for $F^-(J)$, 0 for $F^\circ(J)$, and -1 for $F^+(J)$, corresponding to the R, Q, and P branches of the band structure, respectively. The equations for the energy associated with these branches are as follows (Ref. 51):

R branch

$$R(J) = \nu_3 + 2B_2 - 2B_2\rho + J(3B_2 - 2B_2\rho - B_1 - 12D)$$
$$+ J^2(B_2 - B_1 - 12D) - 4DJ^3 \tag{8-9}$$

For the Q branch

$$Q(J) = \nu_3 + 2B_2 - 4D + J(3B_2 - B_1 - 12D)$$
$$+ J^2(B_2 - B_1 - 12D) - 4DJ^3 \tag{8-10}$$

115

and for the P branch

$$P(J) = \nu_3 + 2B_2 + 4B_2\rho - 4D - J(3B_2 - B_1 - 12D - 2B_2\rho)$$

$$+ J^2(B_2 - B_1 - 12D) - 4DJ^3 \qquad (8\text{-}11)$$

where B_1 and B_2 are empirically determined constants and, because of the slight convergence in the branches, have values of 5.210 cm^{-1} and 5.241 cm^{-1}, respectively.

8.2 RESONANCE ABSORPTION APPARATUS

The initial resonance absorption experiments were performed in the laboratory using the system shown in Fig. 73 (Ref. 57). A 0.5-mw He-Ne, Spectra Physics Model 120 gas laser was used as the source. Two modifications were made to the laser: first, the output mirrors were replaced by dielectric-coated mirrors for 3.39-μ operation, and second, the internal permanent magnets used to enhance operation at the visible wavelength 0.6328 μ were removed (Ref. 57). The magnets were used to create inhomogeneous magnetic fields which would, through Zeeman splitting, produce a wider gain profile at the normally unwanted 3.39-μ transition.
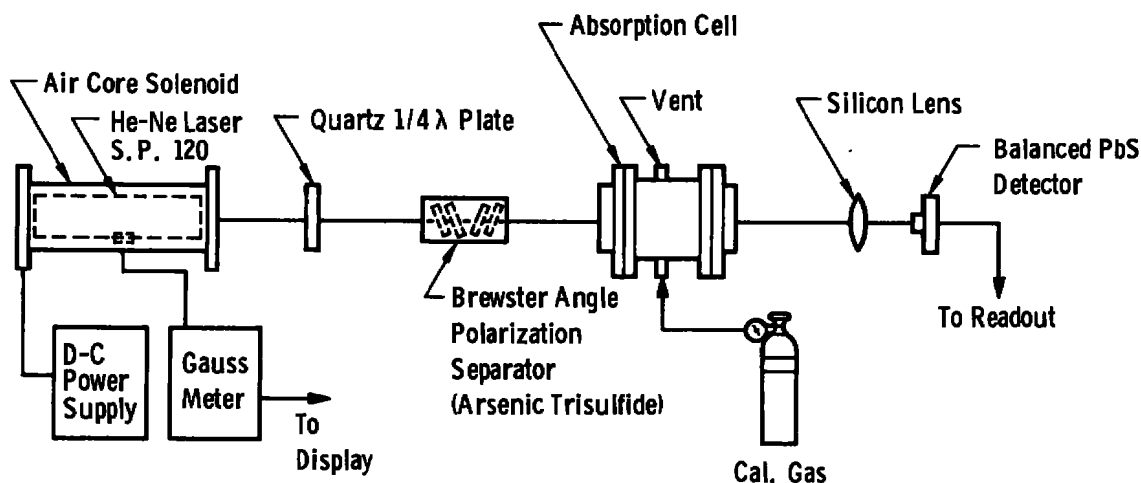
Figure 73. Original resonance absorption instrumentation.

A balanced lead sulfide detector in conjunction with a simple bridge circuit was used for optical signal detection. Such a detector system suffers greatly from lack of sensitivity in addition to thermal drift; however, to avoid this latter problem a chopper wheel and a synchronous detector were used (Ref. 46). For purposes of diesel engine research, the response characteristics of this technique were not compatible with the transient times encountered within the combustion chamber. The system was suitable, however, for the proof-of-principle tests that were performed.

A series of four arsenic trisulfide glass plates oriented at their Brewster angles composed the first ·polarization separator. The efficiency of polarization separation was rather low and as much as 10 percent of the radiation was still of the undesired polarization. Nevertheless, the separation was considered to acquire sufficient design criteria and to perform feasibility studies.

8.2.1 Diesel Engine System

The resonance absorption optical system together with the data handling equipment are shown schematically in Fig. 74. The overall system will be first described with attention being focused on those components which were critical to its operation. The system was designed so that not only could stationary path data be obtained but x-y scan data for visualization purposes could also be obtained.
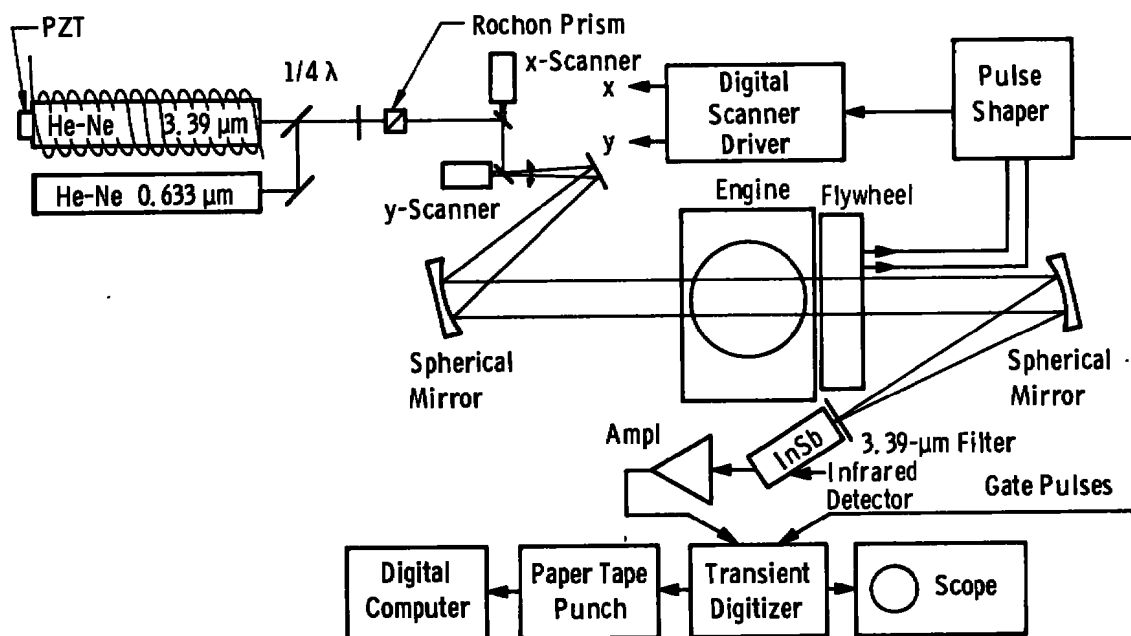
Figure 74. Resonance absorption optical system and data processor schematic.

A Jodon HN-15 He-Ne laser was used which incorporated the following special features. First, the mirrors were coated for 3.39-μ operation and second, the Brewster angle windows were removed and replaced with flats normal to the propagation direction. This latter modification allowed circularly polarized light to propagate within the laser cavity. This was not possible with the off-the-shelf, commercially available laser previously used. A pizeoelectric drive element was also incorporated into the rear mirror assembly to allow scanning. The voltage required to scan over the free spectral range, that is to

say, from one longitudinal cavity model to another, was 385 v. An auxiliary He-Ne laser operating at the 0.6328-μ wavelength was used in conjunction with a slide mirror assembly to provide alignment for the infrared laser.

An air core solenoid was constructed of aluminum tubing to house the laser and provide for Zeeman-split tuning of the output radiation frequency. The current through the coil, which was limited to 10 amp by the power supply, generated a field strength of only 150 gauss. The power dissipation was approximately 360 w, and the excess heat was removed by means of a small fan located in one end. Frequency separation was obtained in a manner similar to the initial system. A quarter-wave plate followed by a Rochon prism was used to provide single frequency output. Early proof-of-principle tests indicated that the Rochon prism, because of the high absorption of natural quartz at 3.39 μ, attenuated the power by approximately 10 db. The Rochon was then cut in length with a subsequent reduction in usable free aperture. This provided a 6-db gain over the original configuration.

The optical system included two scanners to provide orthogonal beam scans when desired. The beam, upon reflection from the scanners, was directed by the first spherical mirror parallel to the optical axis. The individual beam focused to a point within the engine. The second spherical mirror collected the radiation and passed it on to the indium antimonide detector assembly. All mirrors were at least a quarter-wavelength flat and were front surfaced. The spherical mirrors had a focal length of 30 in. (76.2 cm). Because of slight spherical aberrations induced by the off-axis configuration of the spherical mirrors, the x and y scanner focal points differed. This proved advantageous as the scanner positions could be adjusted so that upon final refocusing by the second mirror the image would appear stationary, independent of scanner orientation.

A transient digitizer was used to store the array of intensity information. The data were transferred to punched paper tape. This in turn was transferred to a digital computer for data reduction.

8.2.2   Digital Matrix x-y Galvanometer Driver

The desired format of an x-y matrix of absorption data required a power driver with a voltage output to two scanners which could be incremented in discrete steps. External trigger pulses incremented the driver position. The driver output voltages are obtained in the following manner (Fig. 75). The input pulse is counted with a binary counter, and the count is fed to a digital-to-analog converter. This signal is then amplified and fed to the x-y driver. The matrix dimensions are switch-selectable from 16 to 128 resolution elements in the x- and y-directions. The output voltages follow a simple step ramp for both the x and y. After the x has incremented through a full scan the y scanner is
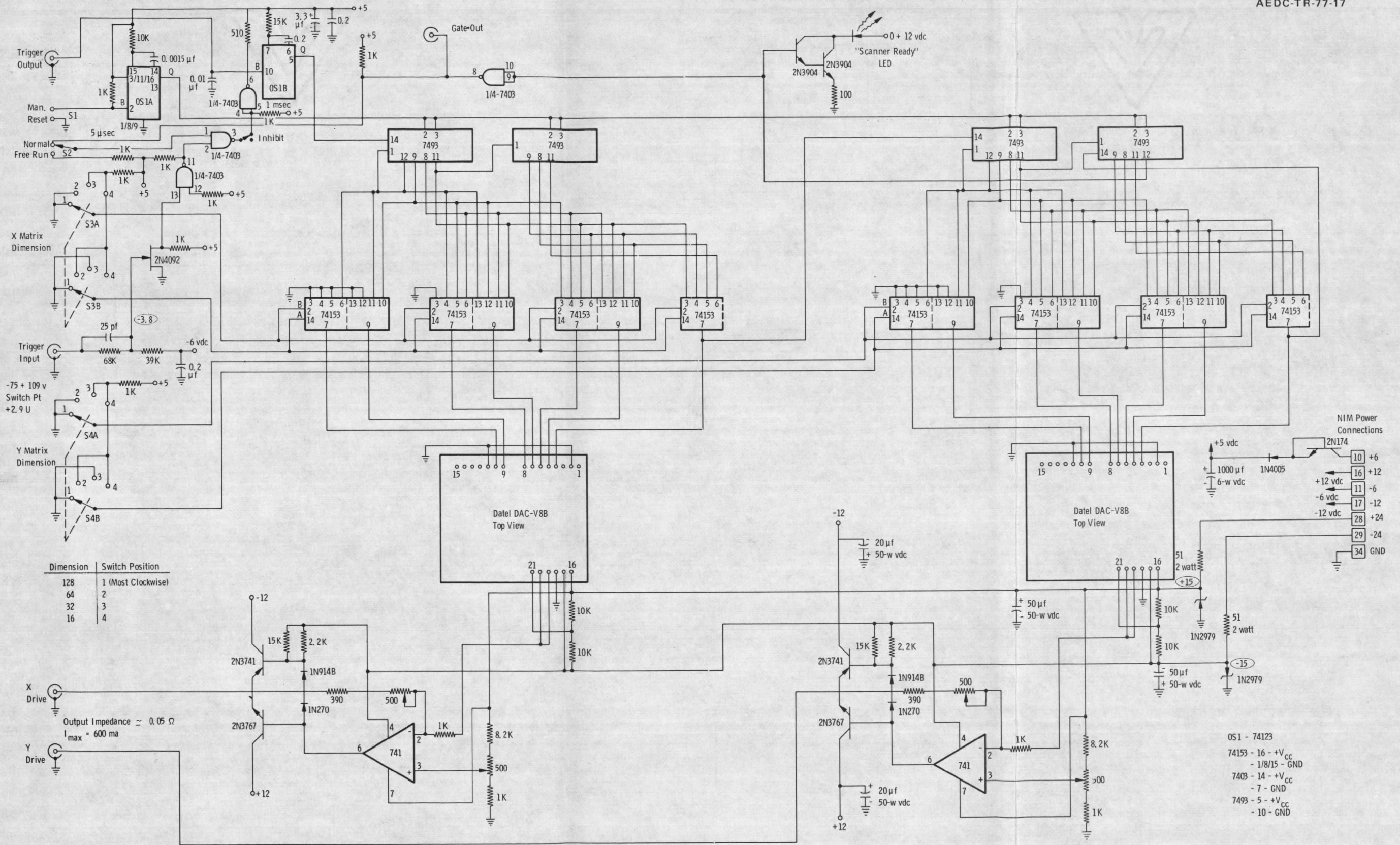
Figure 75. Schematic of digital scanner (x-y driver).

incremented by "1". The system resets upon completion of scanning the entire preselected array. Two modes of operation are possible: a normal or a free-run mode. In the normal mode, upon completion of a single x-y scan, the input pulses are inhibited and the driver is held in a ready state. In the free-run mode, scans are continuously made as long as input trigger pulses are available. A manual reset button allows the state of the counters to be reset to their standby state.

The input trigger logic voltage levels may vary from -75 to 109 v with a crossover point of +2.9 v. This makes the trigger compatible with transistor-transistor logic (TTL) levels or higher. Output trigger pulses of TTL logic levels were also made available. When the scanner is in the standby mode, these pulses are inhibited. A gate-out signal goes to a logic 1 during the scanning and in the standby mode is a logic 0. A light-emitting diode indicates when the scanner is in the standby mode. A manual advance button will cause the initiation of a scan. The galvanometer scanner derives its power from Nuclear Instrument Module-Standard module (NIM) bin. Required voltages are ±6, ±12, and ±24 v dc.

8.2.3 Digital Pulse-Shaping Logic

Trigger pulses were required both for the digital scanner and for the transient digitizer. The signals were derived from light-emitting diodes and a photodiode pair. The output from one of the light-emitting diodes is interrupted by a chopper wheel mechanically coupled to the engine. The pulse from the photodiode is shaped so that it can be utilized by the TTL compatible input circuitry of the scanner and the transient digitizer. Two such pairs of diodes are used to provide pulses at bottom dead center (BDC) and at a preselected variable crank angle, θ.

The input voltage levels to the digital pulse-shaping circuitry (Fig. 76) are on the order of 20 mv dc. A 741 operational amplifier boosts the signal levels to a point where a 2N4092 FET switch can be gated. The BDC pulse, the preselected variable crank-angle pulse, and the ORed combination of the two are available as outputs. All signals were TTL compatible and were used to directly drive a scanner or transient digitizer. The ORed output is used for the transient digitizer as two pulses per engine cycle. A gate input was used to hold off the ORed output pulses and was obtained from the output of the digital scanner. In this manner, the transient digitizer would not accept data until the scanner operation was initiated. As with the digital scanner, the circuitry is located in an NIM bin and derives the required -6, +6 power supply voltages from the NIM bin connectors.
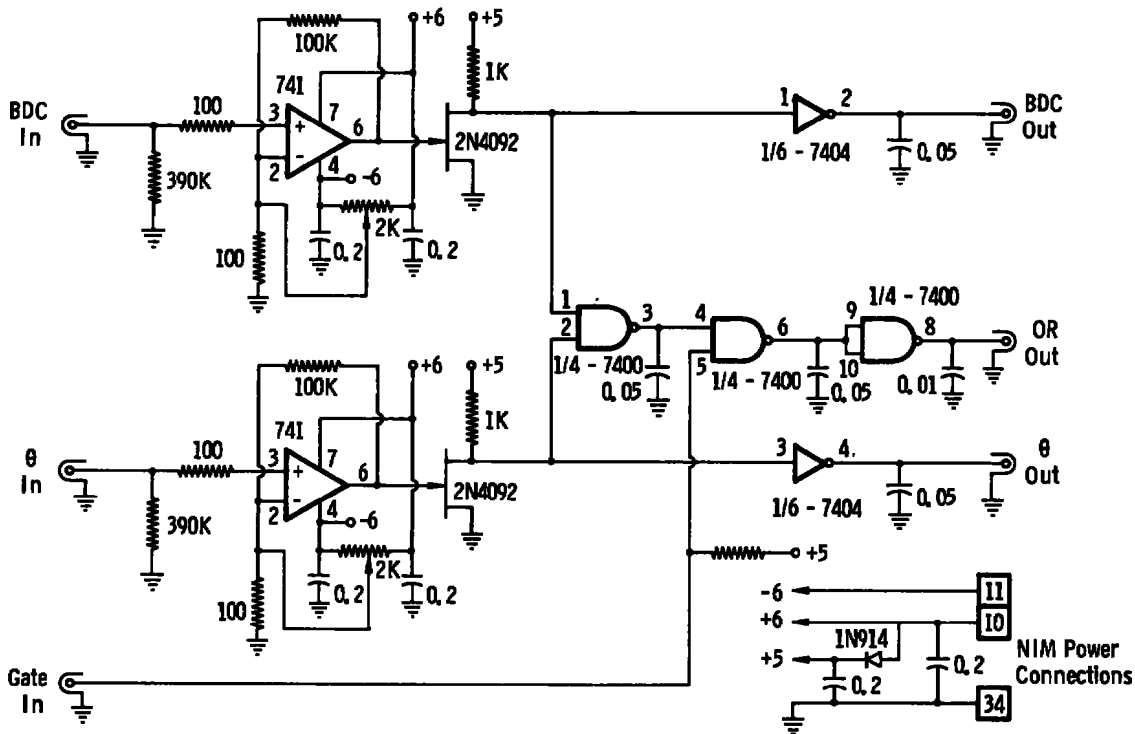
Figure 76. Schematic of digital pulse shaper.

8.2.4 Beam Scanners

The beam-scanning function was handled by two galvanometer-type scanners. The galvonometers utilize quarter-wave, flat, front-surfaced mirrors. The operating characteristics are summarized in the following table:

Coordinate	Max Freq., Hz	Rotation Peak-to-Peak, deg	Mirror Dimensions, in.	Coil Resistance, ohms	Sensitivity, ma/deg	Full Scan Current, amp
x	1,500	8	0.25 by 0.25	8 ± 1	150	1.2
y	300	6	1.00 by 1.00	8 ± 1	170	1.02

The scanners were typically operated over only 2 deg, a fraction of the available range. This corresponds to a 1-in. (2.54-cm) linear scan with the 30-in. (76.2-cm) focal length collimating mirror. Utilizing the full scan capability of the galvonometers would allow linear scans as large as 4.2 in. (10.7 cm) in x and 3.14 in. (8.0 cm) in y without a change in mirrors. The scan was electrically restricted by the addition of a series resistor. In addition, through the proper selection of optical components, the scanning array size can be made as large or as small as required.

122

The spacing between points in an x-y scan is readily determined from the range of the scan and the number of resolution elements into which it is broken up, i.e., 16, 32, 64, or 128. For the transient recorder, a 32 by 32 array was utilized since this was the storage capacity (32 by 32 or 1,024 data pairs or 2,048 data points) of the transient digitizer. Typical spacing for a 1-in. scan was 0.03125 in. (0.079 cm).

8.2.5 Detector Amplifier System

The detector was an indium antimonide semiconductor manufactured by the Santa Barbara Research Corporation. It responds to wavelengths from 2 to 5.5 μ and has an active diameter of 1.25 mm with a total sensitive area of 0.0123 cm^2. The detector sensitivity was 2.26 amp/w with a noise equivalent power of 0.109 x 10^{-11} $Hz^{1/2}$. The window material was silicon with an antireflective (AR) coating peaked at 3.9 μ. The response time constant was less than 1 μsec. Its operating temperature was 77°K, which was maintained through the use of a Joule-Thompson cryostat. The cryostat provided LN_2 to the detector through the conversion of 1,200-psi bone-dry nitrogen gas. Run times on the order of 4 to 5 hr were possible when a fully charged k bottle (2,200 psi) was used.

A line filter at 3.39 μm with a bandpass of 0.1579 μm in conjunction with a silicon lens was used to reduce the effect of background radiation. Under engine operating conditions the background radiation from the combustion constituted approximately 1/25 of the signal level at the peak. This corresponded to a blackbody radiation level of 100 μw or less. A tare method was used to reduce its effect on the data.

The infrared detector amplifier schematic is shown in Fig. 77. The amplifier was designed to operate in the "short circuit" mode, whereby the photodiode voltages were kept near zero. This provides a linear output with incident intensity. The circuit was also designed to protect the photodetector from electrical transients. Five gain settings and corresponding frequency responses were selectable by means of an external switch. A response time less than 50 μsec was measured in the laboratory using an optical chopper wheel. The maximum output voltage was 10 v, which was compatible with the analog-to-digital converter. The detector amplifier system was compatible with a small photodiode detector sensitive in the visible range. This allowed laboratory experiments and optical alignment studies to be made using the 0.6328-μ He-Ne laser. This capability proved to be quite advantageous when a checkout of the data acquisition and the digital scanner driver systems was made.
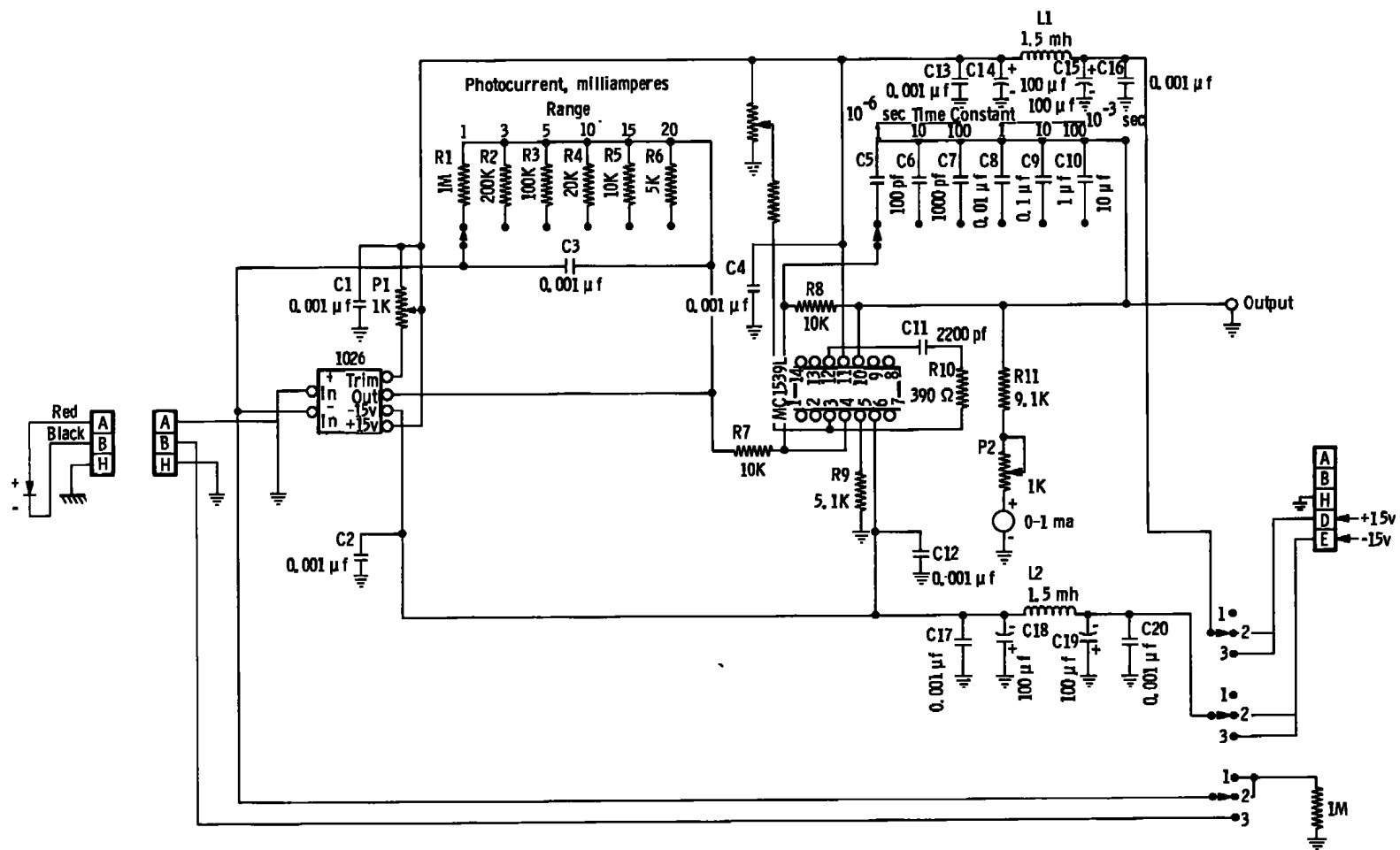
Figure 77. Schematic of infrared detector amplifier.

8.3 LABORATORY EXPERIMENTS

Several techniques were developed for displaying the two-dimensional absorption data. The first technique, shown in Fig. 78a, involved intensity modulating a cathode ray tube (CRT) spot. The output from the photodetector amplifier varied the intensity while the spot was scanned with the x-y galvanometer signals. This technique does not provide quantitative data directly, and the contrast was found to be very poor.

A second technique produced a "three-dimensional" picture of the intensity field. It utilized a resistor network to combine the x- and y-position voltages with the amplifier voltage. This method produced semi-quantitative data as shown in Fig. 78b. The object in this figure is a tri-bar resolution chart which has a maximum dimension of 1 in. (2.54 cm). The visible 0.6328-μ laser transition was used in conjunction with the photodiode for purposes of this recording. The matrix dimensions were 128 by 128 which produced a very high resolution image. The ability to obtain quantitative data from such a system was limited, and therefore digital techniques were employed.

The approach adopted was to record digitally, point-by-point, the attenuated intensity together with the background intensity. This was accomplished by means of the transient digitizer. The data taken in this manner could be ratioed numerically on the HP2100 computer and for purposes of visualization were printed out in a 32 by 32 array of numbers ranging in value from -9 to 9. Each number corresponded to a ratio of intensities (Fig. 79). Although some resolution is lost in this visualization technique, quantitative data can be obtained from the numerical grid. At engine speeds normally encountered, i.e., 1,000 rpm, approximately two minutes were required to obtain a full array of data. At the end of this time, window degradation became noticeable and accounted for approximately 50 percent of the attenuation. However, because of the ratioing technique this results only in a reduced overall signal-to-noise ratio and does not affect the basic measurement.

Figure 80 shows the results for an asymmetric methanol flame obtained in this manner. Areas of high absorption are readily seen and representative transmissivities are indicated. The asymmetry in the flame is obvious in these data.

Further experiments were carried out in the laboratory before entry in the diesel engine installation. Most of these experiments were conducted at relatively low pressures and therefore did not reflect the increased line width found in a typical diesel engine operation (Fig. 81). At these lower pressures, i.e., at less than 30 psi, the absorption maxima could be readily obtained by scanning the applied magnetic field. During these tests, drift of the laser from one mode to the next was noticeable as is evidenced by the variations during retrace. This is not a problem, however, at the higher engine pressures.
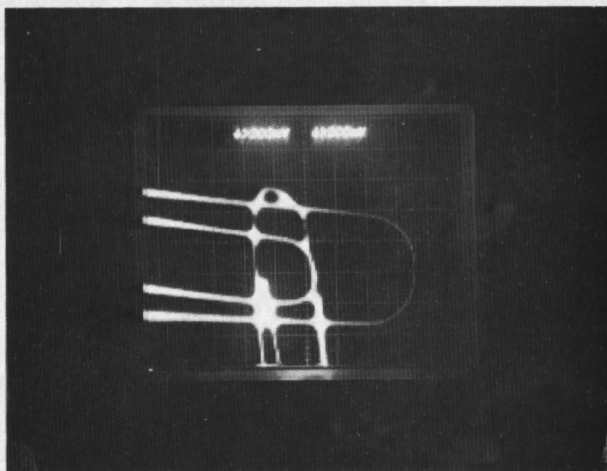
a. Scope intensity modulation
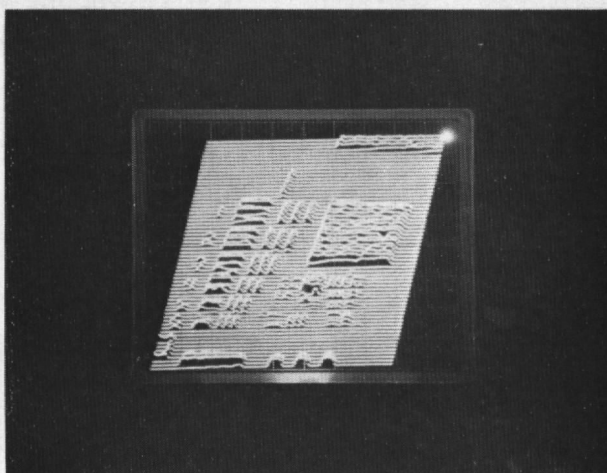
b. Y-axis modulation

Figure 78. Preliminary data from resonance absorption
optical system.

a. 13 deg BTDC, Run 1, 4/15/75
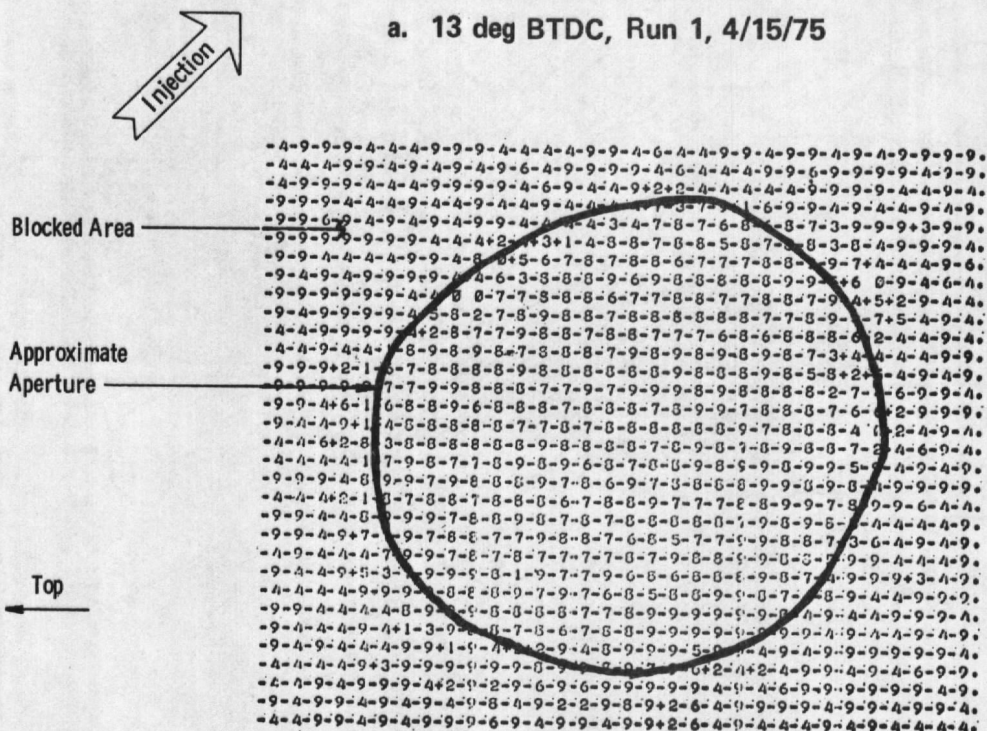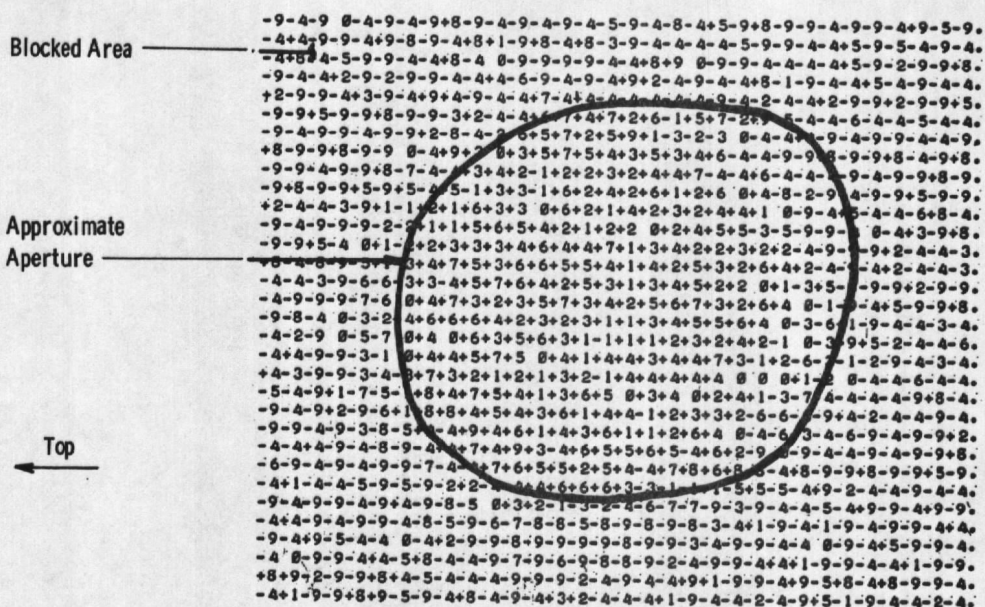
b. 40 deg ATDC, Run 3, 3/5/75
Figure 79. x-y numerical grid.

127
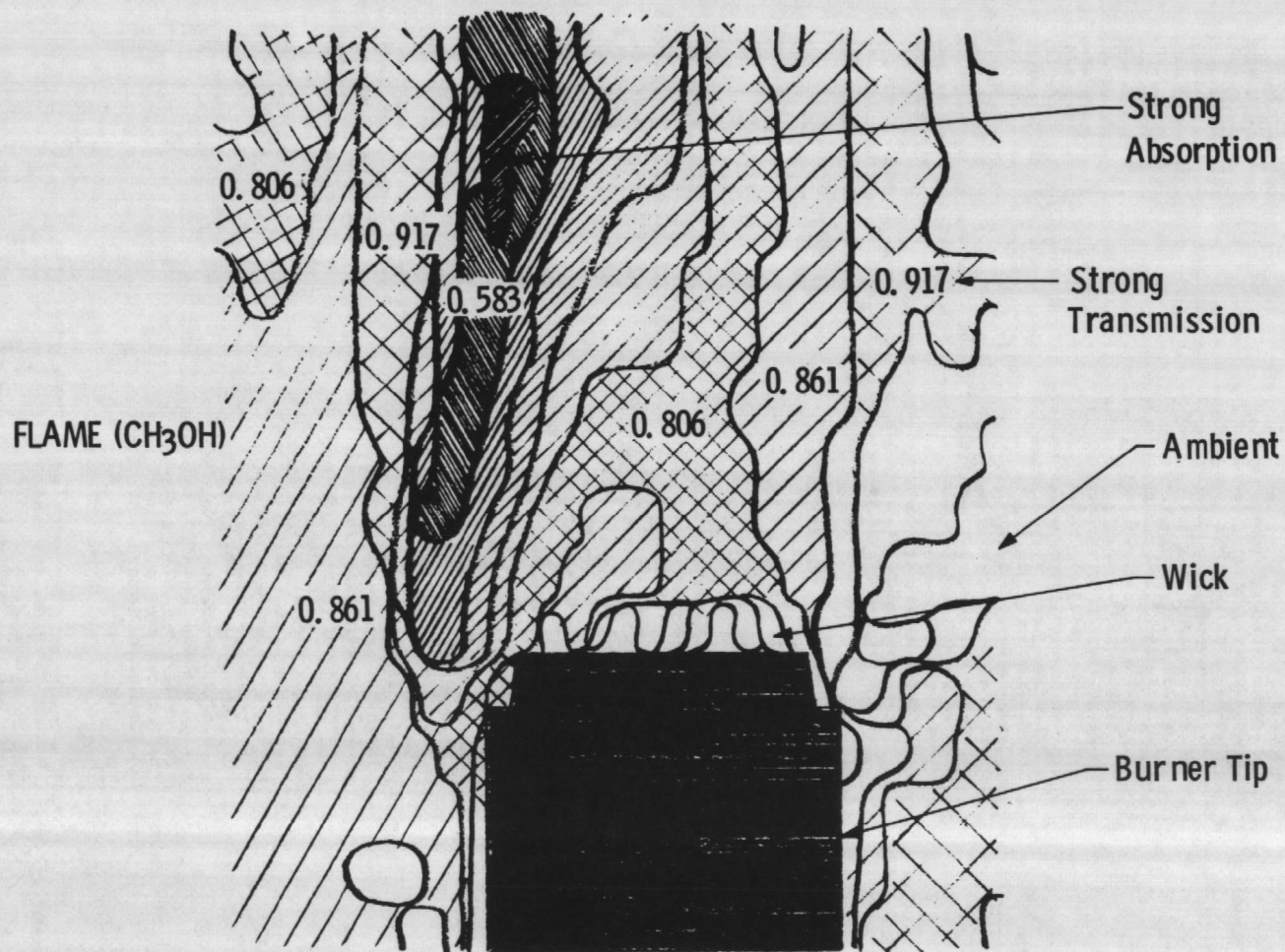
Note: Numbers Represent Amount of Transmission

Figure 80. Asymmetric methanol flame transmissivities.
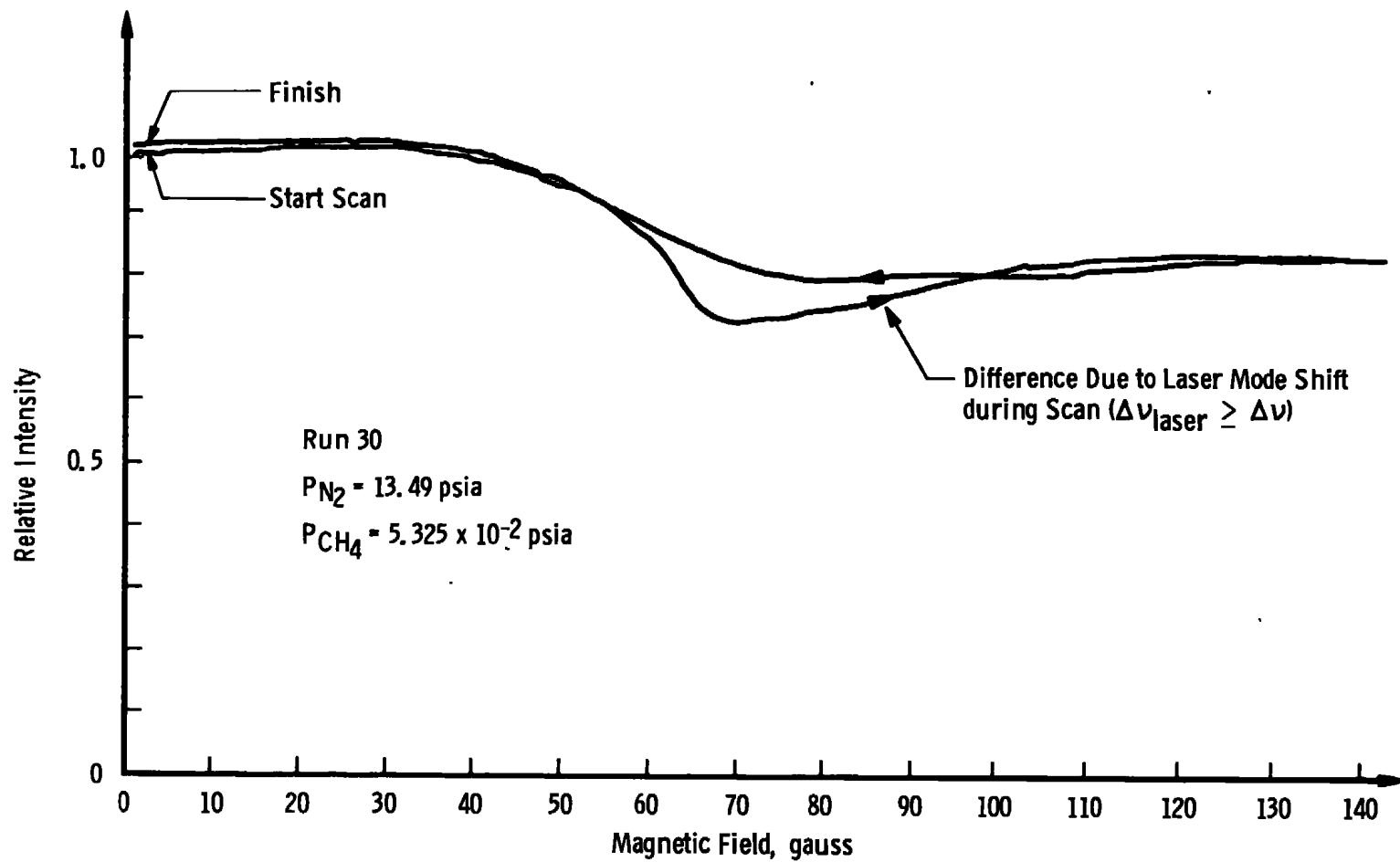
Figure 81. Typical line scan for a low temperature and pressure.

Of primary importance was the ability of the optical system to track and accurately scan a rapidly changing environment. To test the high-frequency response of the system an optical chopper wheel was used to generate an optical modulating frequency of 333 Hz. Some image blur appeared in the data near the chopper blade that was accountable in part by jitter in the timing pulses and is not necessarily representative of the frequency response of the system. These experiments led to the development of digital pulse-shaping electronics which provided a much cleaner crossover response to input timing pulses because of a reduction in noise.

A feasibility study was performed to determine if laser line stabilization and narrowing could be accomplished in the Jodon HN-15 laser. Stabilization can be accomplished through the introduction of a small amount of methane into the cavity of the laser. This will cause absorption to be selectively higher at all frequencies except for that frequency corresponding to a zero Doppler-shifted component, i.e., the center of the methane line. Laser radiation at the frequency corresponding to the absorption of zero velocity molecules will selectively burn or deplete the lower state methane molecules and therefore become transparent to this radiation. The net effect is one in which this central component appears enhanced because of the repression of all other modes.

Using CH_4-N_2 mixtures at atmospheric pressures, the laser was scanned over a free spectral range (one longitudinal mode spacing), and broad peaking of the laser light occurred. Sharp line profiles could not be achieved because of the requirement that the modified plastic intracavity absorption cell be at atmospheric pressure. However, with the addition of antireflection coated windows and a small low-pressure cell, it is believed this technique could be used to reduce the laser line width.

8.4 DIESEL ENGINE EXPERIMENTS

Diesel engine data were taken in several different formats, one of which is shown in Fig. 82, which is a crank-angle-resolved absorption history for the firing engine. The data were stored on paper tape and then averaged over three cycles. An intensity reading was taken for each crank-angle degree through the approximate center of the optical ports. Initial laser (I_o) values were not obtained simultaneously but were obtained from a second run taken a short time later under as identical conditions as possible, as shown in Fig. 83. The only difference between the two plots is in the fact that the background data were obtained from an unfired engine. The rpm was maintained by means of a Varidrive motor to obtain the ratio of final-to-initial intensity values (I/I_o) so these two profiles could be ratioed point by point. Some variation, perhaps associated with turbulence or engine vibration, gave rise to very rapid oscillations as evidence in both profiles. Data were taken under a wide variety of fuel settings with the representative plots for a rather high fuel setting of 0.4 being shown in Figs. 82 and zero fuel in Fig. 83.
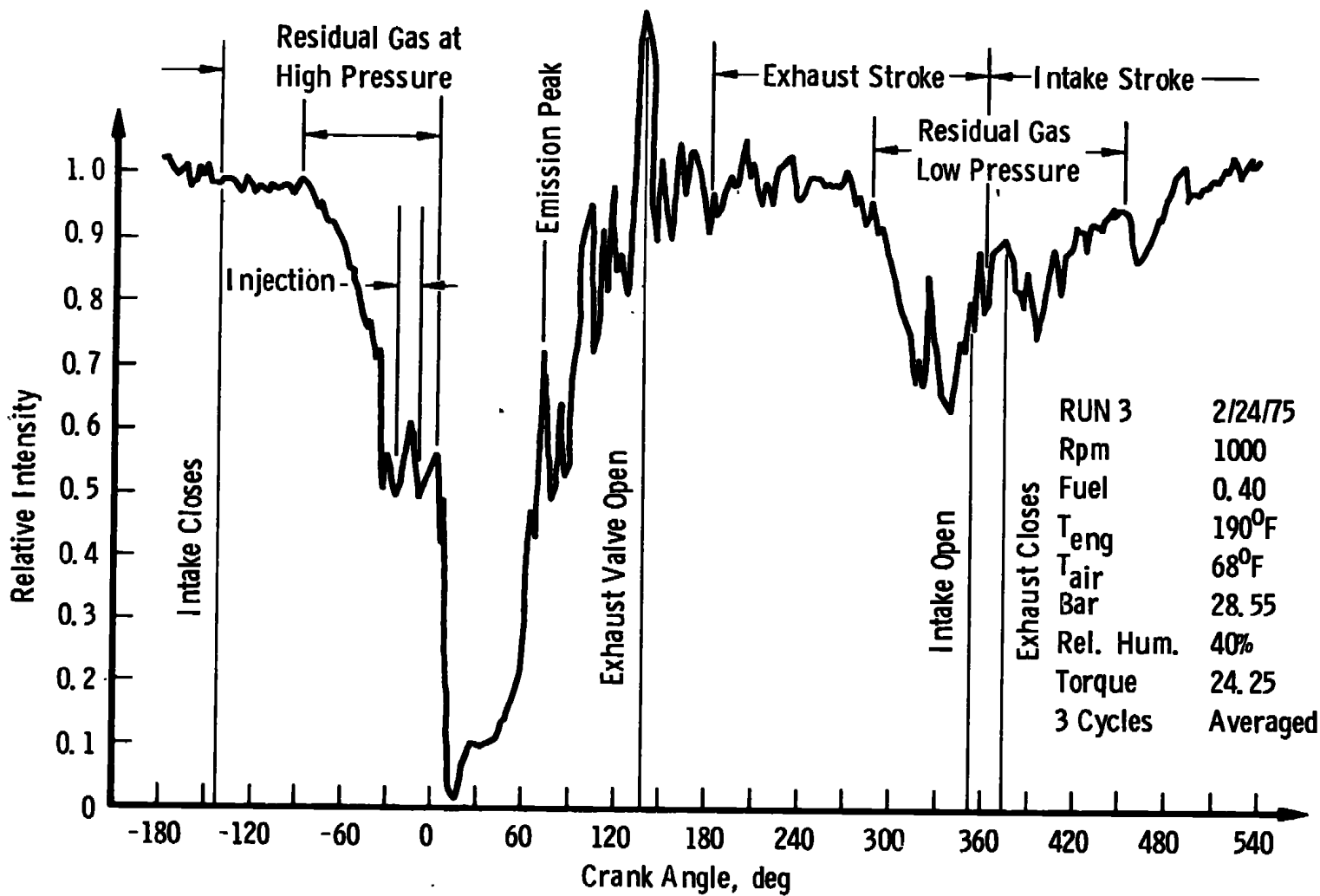
Figure 82. Relative light intensity versus crank angle
for firing engine.
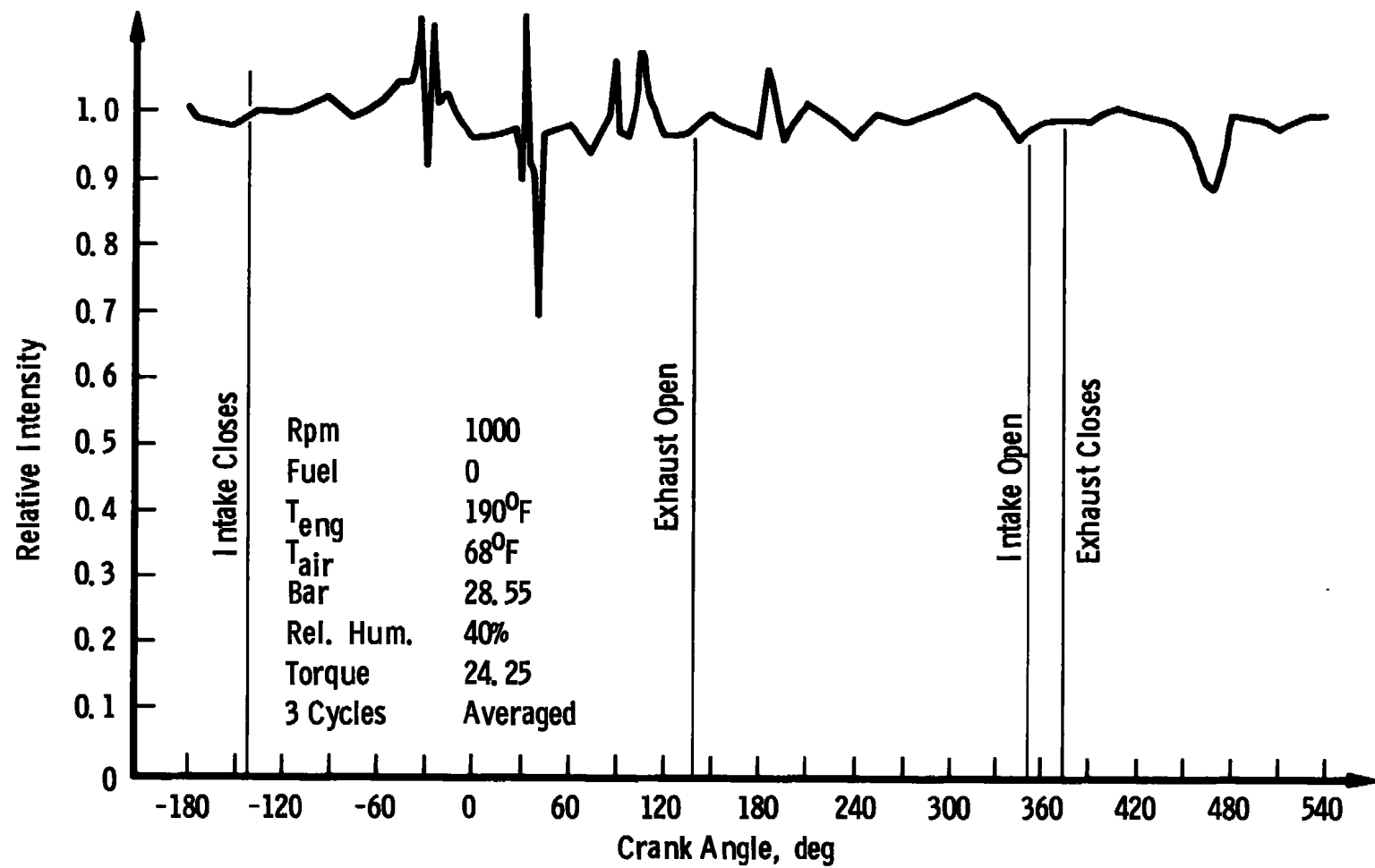
Figure 83.   Relative intensity versus crank angle for unfired engine.

Background radiation had to be considered, as the line width of the bandpass filter on the detector did allow some emission radiation to be recorded. Figure 84 shows the amplitude of this radiation versus crank angle for various fuel settings. Some cycle-to-cycle variations were found for fuel settings between 0.25 and 0.35, which are common to diesel engine operation.

In Fig. 82, a number of interesting features of the profile should be noted. Apparently a large amount of residual gas was carried from one cycle to the next as can be seen from the decrease in transmission during the compression stroke between -90 deg and 0 deg BTDC. This is attributed to residual gas since it was not present in data recorded for an unfired engine (Fig. 83). The increase in absorption with pressure is also evident in Fig. 82. It is seen that as the density increases the absorption also increases. A similar absorption decrease is shown in the area between the exhaust and intake stroke. The residual gases present are obviously not totally cleared during the exhaust stroke and remain into the next cycle. It is felt that these residual gases are closely associated with the boundary layer associated with the piston head. Also, some residual gases have been found in and around the piston ring areas. Some of the high-frequency structure in this area may be due to swirl and turbulence carrying a locally varying concentration of hydrocarbons.

A number of runs were made to acquire data of the pressure as a function of crank-shaft angle under various fuel settings. The data, required to correct for these pressure variations, are shown in Fig. 85.

Combustion was initiated slightly after fuel injection, which occurs nominally at 20 deg before top dead center (BTDC) with ignition occurring nominally at 10 to 12 deg BTDC. Following ignition a rapid increase in the amount of absorption by the gas is observed, reaching a maximum at approximately 25 deg after top dead center (ATDC). Expansion then begins to peak in the neighborhood of 60 to 70 deg ATDC.

From the emission data, temperatures can be inferred using the blackbody radiation equation and taking into account the filter profile. Figure 86 shows the calculated blackbody irradiance at 3.35 μm, the bandpass filter center frequency. Although estimates of the temperature can be made from the geometry of the system, uncertainty in the effective detector area precludes an absolute temperature measurement. In Fig. 87 temperature versus crank angle is plotted. The temperature was normalized to a peak temperature of 3,360°K. An absolute calibration of the system is required using a calibrated blackbody source to make the measurements more accurate.
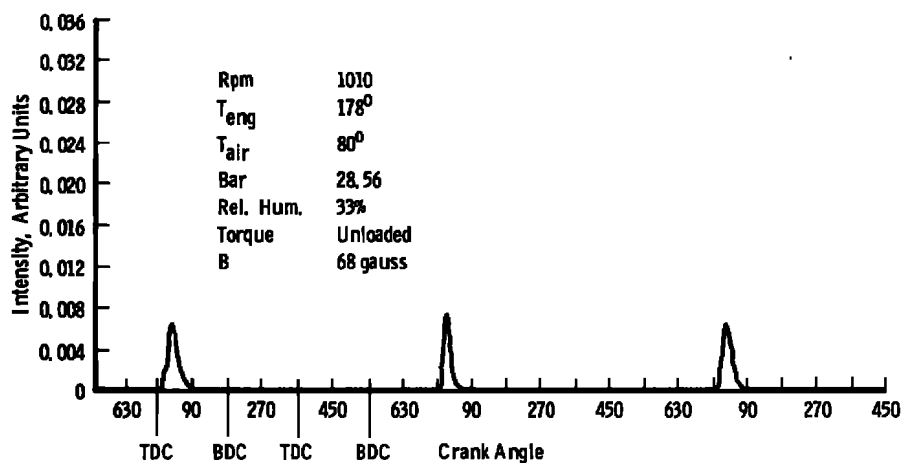
a. Fuel 0.25
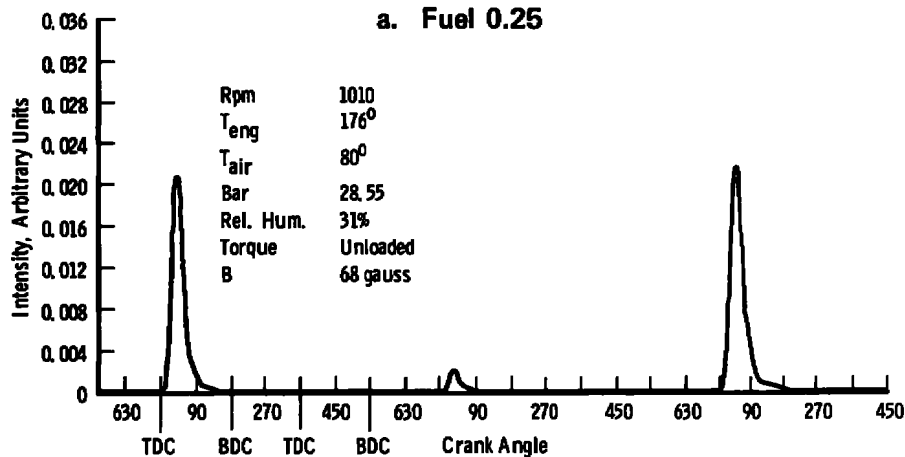
b. Fuel 0.30
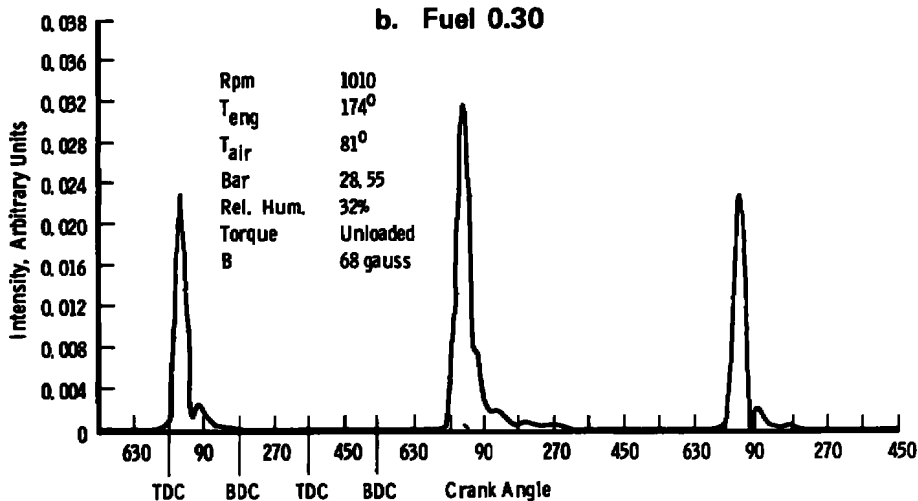
c. Fuel 0.35

Figure 84. Relative emission for fuel settings
of 0.25, 0.30, and 0.35.
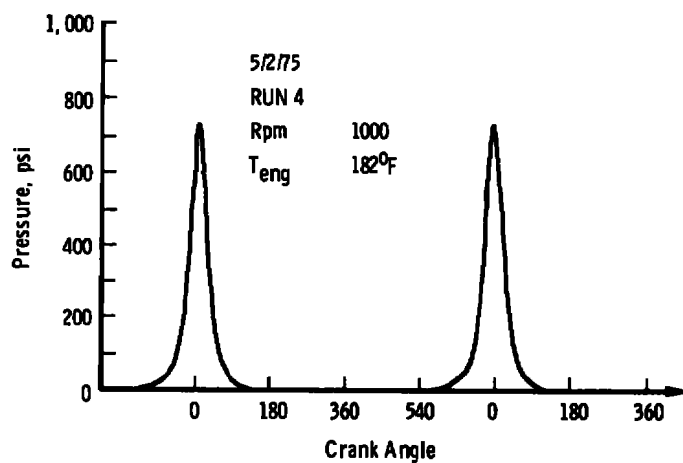
a. Fuel = 0
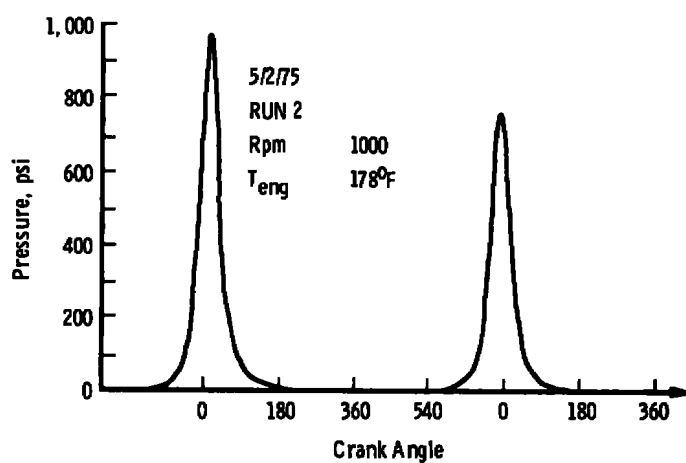
b. Fuel = 0.30
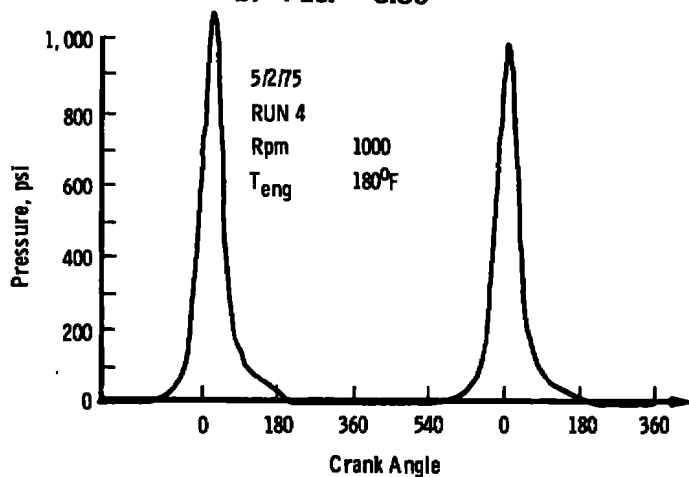
c. Fuel = 0.40

Figure 85. Pressure versus crank angle for various
fuel settings.
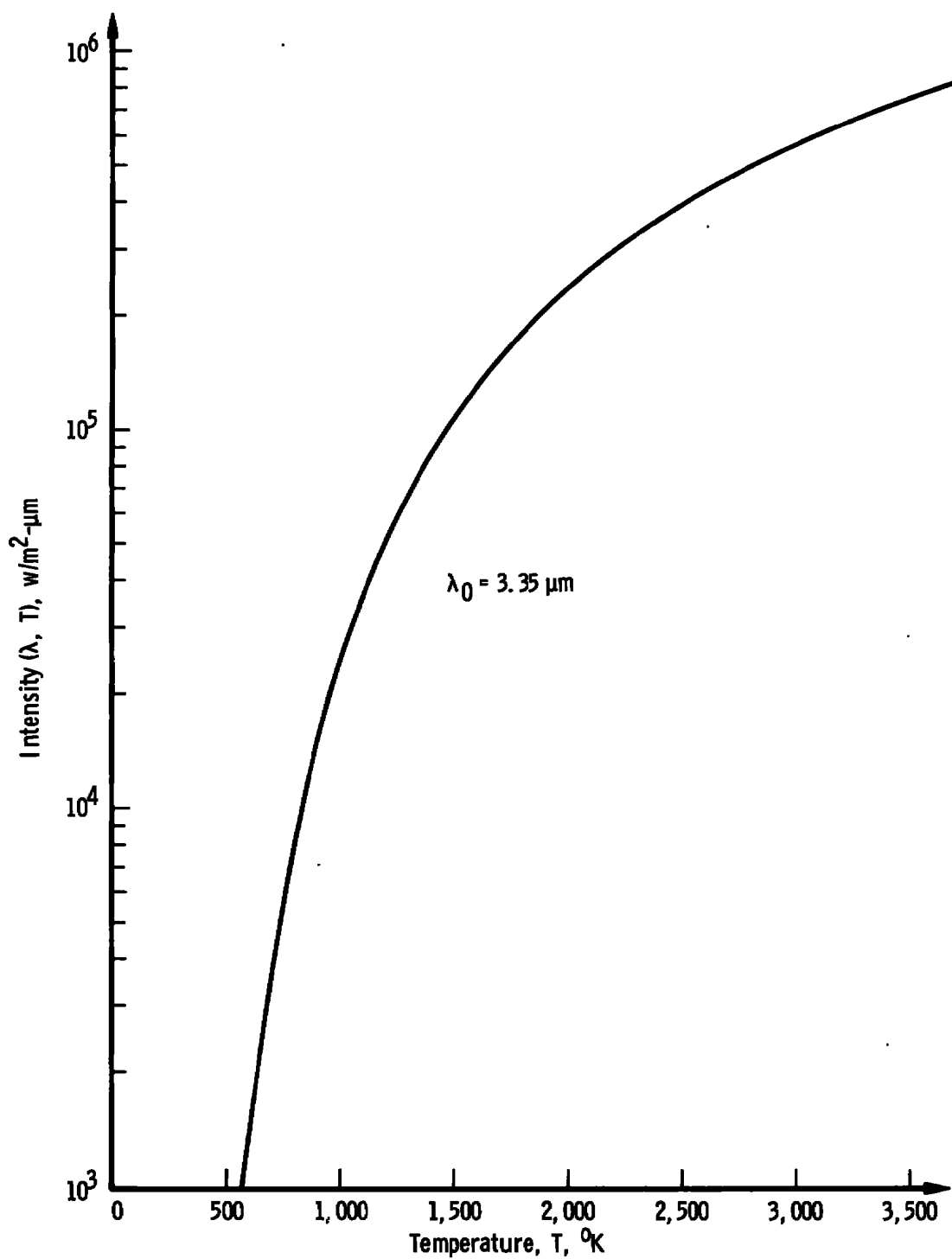
Figure 86. Intensity versus temperature.
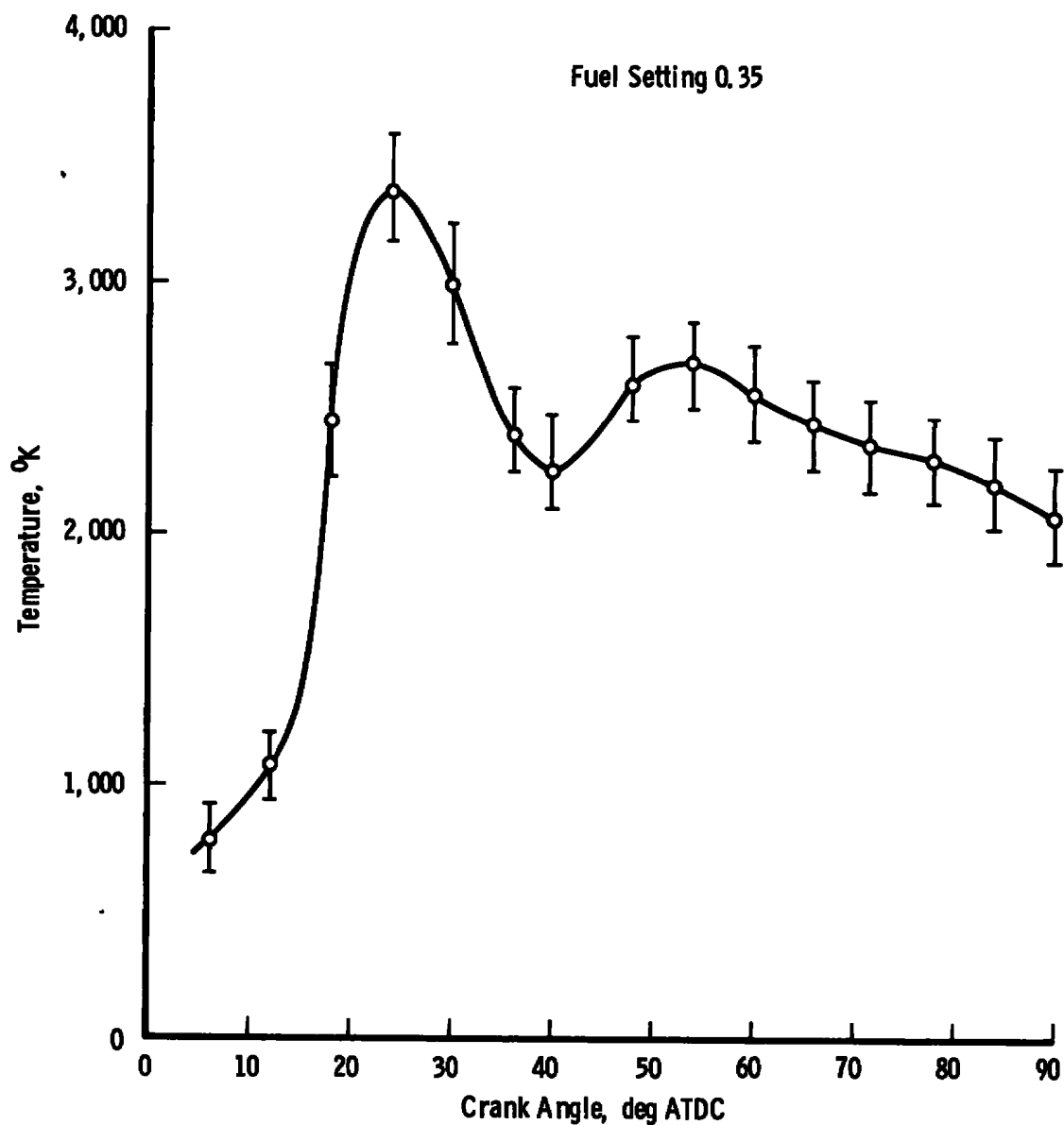
Figure 87. Temperature versus crank angle normalized to peak
temperature of 3,360°K.

9.0 CONCLUSIONS

9.1 GENERAL

The results of the many experiments and analyses that were performed to ascertain the feasibility of applying electro-optic diagnostic techniques (Fig. 88) to study diesel engine combustion phenomena verify that most of these may be immediately applied. Each of the techniques provides particular information that is complementary to the others in addition to being complementary to conventional measuring techniques.
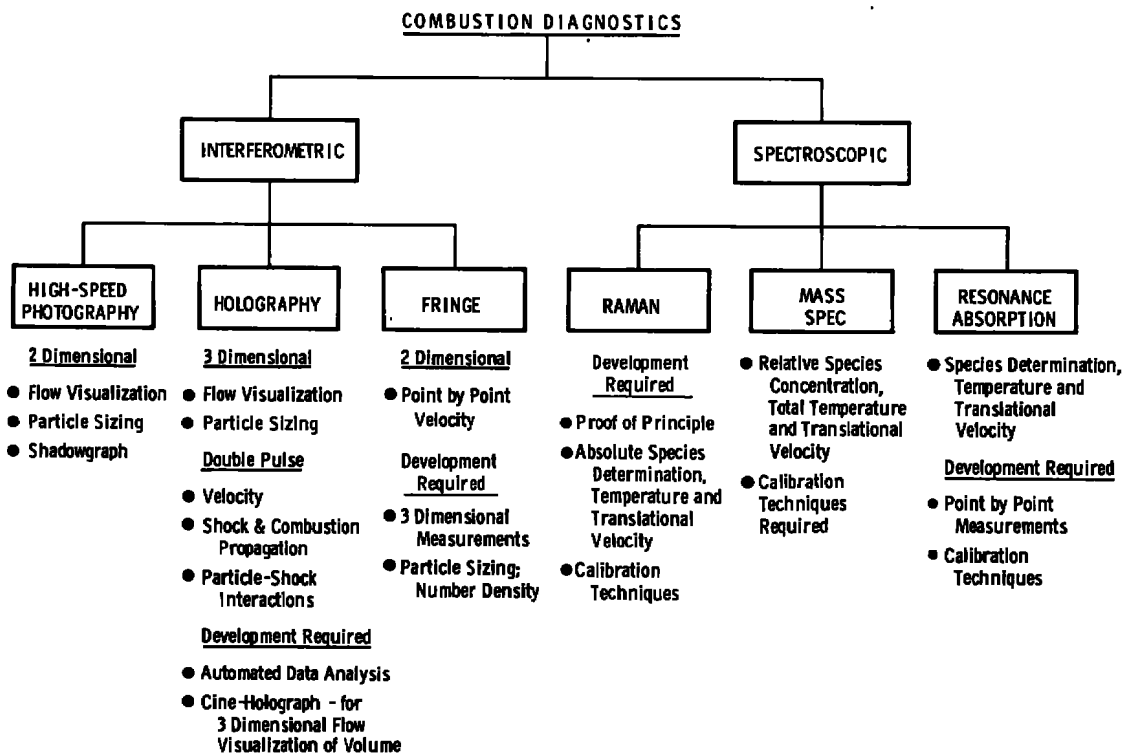
Figure 88. Electro-optical combustion diagnostics.

Engine modifications that were required to optically probe the interior of the cylinder did not prove to be too difficult a task. With the establishment of proper operating procedures, outlined in previous sections, it was possible to make velocimeter measurements during engine operation for at least 10 minutes before window fogging occurred. At this time, the engine was shut down and the windows replaced with clean units. In the case of holography and resonance absorption the operating time was reduced to approximately 3 minutes before window fogging degraded the measurements. Insofar as the other spectroscopic techniques, e.g., mass spectrometer, etc., are concerned, where the combustion chamber is not probed, there is no window-fogging problem. In the subsequent paragraphs the performance of each of the techniques is evaluated and recommendations for future activities are presented.

9.2 HIGH-SPEED PHOTOGRAPHY

High-speed photography has been successfully applied to both the Turner and the TACOM diesel engines. The technique provides information concerning fuel injection and flow characteristics, swirl, droplet sizes, ignition and combustion, etc., in a plane. The technique is presently limited in that only particles having a minimum diameter of approximately 30 μ could be resolved. This is considered the present state-of-the-art threshold for the diesel engine application. A number of frame speeds were used in the present study, e.g., 2,500, 5,000, and 10,000 frames per second. The optimum combination of time and spatial resolution was obtained using a frame speed of 5,000 frames per second. By manual analysis of data, it was possible to acquire quantitative data with regard to the motion of the spray plume across the field-of-view, thus providing data of the initiation and duration of the combustion process. Placement of timing and crank-shaft angle position markers on the edge of the film allows these data to be correlated.

9.3 HOLOGRAPHY

The extension of the photographic process from two to three dimensions is accomplished with holographic techniques. Reconstructed images indicate that sideband holography can be applied to studies of fuel droplets on the order of 8 μ and larger. In-line holographic techniques and/or front-lighted holography do not appear to be applicable for the determination of fuel droplet sizes. The limitations of the holographic techniques are also evident in optically dense regions or regions of high fuel-droplet density. The results of the measurements indicate that only those droplets around the periphery of the fuel spray could be resolved with maximum resolution. During the combustion process itself, the light traversing the combustion chamber is diffusely scattered, thereby making the individual droplet images difficult to resolve. Experiments are still required to ascertain the maximum gas density, or degree of combustion, that can be tolerated before the technique is no longer applicable.

Although microscopic details about the fuel spray could not be resolved within its core, gross field characteristics were discernible such as the regions of high and low number, or gas, densities and spray angle. The areas where shearing forces attributable to swirl cause droplet breakup can be identified and analyzed. Although the droplets below 8 μ could not be resolved, an indication of their collective presence around the periphery of the spray was evidenced in the reconstruction. In order to improve the resolution for droplets less than 8 μ in diameter, a smaller f/# optical system is required. The limited depth of field of the smaller f/# system is then extended by the holographic recording. However, in order to maintain resolution on the hologram, the images must be magnified before being recorded. As a result, the reconstructed distance increases as a square of the magnification and the long depth-of-field required for the analysis would be limited by the physical length of the reconstruction bench.

Despite the fact that front-lighted holography does not appear applicable for determining the size of a droplet directly, it was found that an indirect size measurement, in addition to its trajectory or propagation path, could be determined.

9.4 FRINGE TECHNIQUES (VELOCIMETRY AND PARTICLE SIZING)

High-speed photography and holographic techniques provide an overall view of the region under study and provide information about where to probe the flow in more detail. Detailed, on-line probing is then performed with a multicomponent velocimeter. The feasibility of making two-component velocity measurements, simultaneously, throughout the combustion cycle has been verified.

During the course of the studies some basic problems arose in making velocity measurements because of the rapidly varying particle density and background light intensity throughout the engine cycle. Modifications to the experimental technique were made so that now the acquisition of a large sample of velocity data over a small, e.g., 10-deg, interval can be realized. A series of velocity measurements was made over a number of 10-deg crank-angle intervals with each series taken until sufficient statistical data of the flow characteristics in the measurement volume were obtained. Step-wise scanning over the volume of interest provides flow profile data.

One problem that was encountered during the course of the velocimeter experiments was the drifting of the engine rpm. This was a characteristic of the Turner engine operation since only two of the three cylinders were firing. An external drive unit on the Turner engine would alleviate this situation. Rigid engine mounting was also found to be important, particularly when making LV measurements, since engine motion relative to the LV optics system produces uncertainties in the measurement location within the cylinder. The LV can be considered operational; a magnetic tape-computer system is available and computer programs have been developed to expedite data acquisition and analysis.

Attempts to apply the fringe particle-sizing system to the diesel engine to acquire on-line particle-sizing information were not too successful. The determination of particle sizes is based on the ratio between the a-c and d-c signals. Therefore, since the background light is variable during the engine cycle, means are required to eliminate this contribution to the signal. This instrument is only in the prototype stage, and considerable developmental effort is still required before it will become an operational tool for combustion diagnostics.

9.5   MASS SPECTROSCOPY

The mass spectrometer was successfully used to measure chemical species stemming from the combustion process in both the Turner and the TACOM diesel engines. Oscilloscope traces were analyzed to determine the occurrence of individual species throughout the combustion cycle using a lean fuel mixture. From the data, N_2/CO, O_2, NO, CO_2, and H_2O concentrations were qualitatively identified. The evaluation of these data as a function of crank-shaft angle indicated that during the expansion, after TDC, the O_2 depleted much more rapidly than did nitrogen. During the course of the engine cycle, abrupt transitions occurred in H_2O and NO at approximately the time of ignition. It was also found that NO is formed in significant amounts only for a portion of the combustion time. And finally, CO_2, if formed at ignition, continues to form for approximately 30 crank-angle degrees after ignition.

9.6   RAMAN SPECTROSCOPY

The feasibility of applying the Raman spectroscopic technique was not established during this portion of the program. Nevertheless, from past experience there are no foreseen difficulties in successfully applying the technique for absolute species concentration determinations for those where the Raman cross sections are sufficiently large.

9.7   RESONANCE ABSORPTION

The basic instrumentation techniques and equipment for resonance absorption studies were acquired and successfully interfaced with the TACOM diesel engine. Analytical techniques, with particular emphasis on determination of methane concentration, were also developed. An x-y scanning technique was devised and used in the measurements. The resonance absorption technique, as currently developed, also provides data concerning total hydrocarbon concentration in addition to methane. Absorption occurring before injection revealed a carryover of unburned hydrocarbons from the previous cycle.

Attempts were made to ascertain gas temperature using the infrared laser as a calibration source. Although the preliminary results were marginal they were encouraging.

10.0   RECOMMENDATIONS

Efforts over the past several years have been involved with modification of diesel engines, adaption of electro-optical instrumentation to diesel engines, and a series of verifying experiments. No attempt was made to evaluate the detailed performance of a single engine while the techniques were unproven in the hostile combustion and cyclical environment. The point has now been attained such that efforts can now be concentrated on performance evaluation. To this end, the objective of the present section is to recommend activities to realize this goal.

It is recommended that future experimental activities be concentrated on performing detailed measurements on development-type engines such as the Texaco, Southwest Research, and White stratified charge engines in addition to any new prototype systems. The experimental program entails the use of high-speed photography, single and multiple pulse holography, and multi-component velocity measurements applied sequentially to a single engine. The data will be acquired, in particular for the latter technique, using high-speed data acquisition and data reduction techniques. Computer programs have already been developed for this application. The data should be analyzed in detail to evaluate engine performance under the various parameters outlined in the research program, e.g., varying fuel/air ratios, engine loading conditions, engine fuel types, etc.

Insofar as spectroscopic measurements are concerned, particular emphasis should be focused upon proof-of-principle Raman measurements. In this manner absolute species determination can be realized. The Raman technique would then be used as a calibration tool for further mass spectroscopy measurements.

Although considerable progress has been made in developing the electro-optical instrumentation, considerable effort is still required. In general, the techniques are basically laboratory tools and have not found wide-spread use in combustion research. In order to increase their applicability, specific recommendations for future development are outlined in the following paragraphs.

10.1 HOLOGRAPHY

The extent to which the reconstructed hologram can provide information concerning burning droplets should also be investigated under carefully controlled conditions. Double-pulse holograms should be taken for information on propagation of the spark and combustion wavefronts through the droplet volume to provide additional information of the combustion process. The presence or absence of reconstructed image pairs, on either side of the wavefront, would provide insight into the wavefront-droplet interactions. To follow droplet trajectories, or propagation paths, multiple-pulse, front- or side-lighted holographic techniques would be applied. Regions and the degree of turbulent intensity would be determined from a study of the interference fringes resulting from density changes between two or more exposures.

A sideband holocamera system should be applied to the stratified charge engine where the onset of combustion can be controlled and holograms recorded during this time. Reconstruction of low number density regions could then be analyzed to determine the effects of droplet size on the combustion process.

Quantitative data reduction and analysis of a droplet field hologram is at present an extremely slow, time-consuming, process. Machine-assisted analysis of the droplet field would facilitate the transfer of data from the reconstructed hologram - to a computer - to a final usable form. Means for semi- or completely automated data acquisition of droplet sizes should be investigated and developed.

10.2 VELOCIMETRY

Although the two-component velocimeter is feasible for immediate application to diesel engine combustion studies, additional development of the third component is required. The turbulent flow field, within the cylinder, is three-dimensional, and hence a more complete understanding of the flow processes requires the third component (Ref. 58). The development could be effected, as a piggy-back process, during the course of the experimental activities using the two-component system. This not only reduces the time and cost of the development but also expedites the amount of data that can be recorded and analyzed.

Various techniques can be applied to improve the signal quality, although this was not a dictating problem during the course of the studies. Some of these techniques are to control the air intake and filtering, injecting particles into the air intake having a distinct size distribution and number density. However, the injection of particulates might be objectionable since they could affect the normal combustion process.

10.3 MASS AND RAMAN SPECTROSCOPY

Additional effort should be expended on enhancing the mass spectrometer signal in addition to developing signal-averaging techniques.

Considerable experimental work is still required to determine (1) species intensities as a function of crank-shaft angle for fixed mass numbers and (2) species intensity for fixed crank-shaft angles for the entire spectrum of mass numbers. These measurements should be taken under varying engine operating conditions, sampling nozzle variations, and combustion bowl sampling location. In addition the analysis should also yield kinetic temperature and velocity data. Feasibility of the Raman technique should be established and an experimental program devised to obtain temporal and spatial species intensities, quantitatively, under varying operating conditions.

10.4 RESONANCE ABSORPTION

Activities in this area should be focused on determining the total hydrocarbon content in the cylinder as a function of crank-shaft angle. This requires the development of a suitable calibration technique which would not be too difficult a task. Additional effort

should be focused on developing analytical techniques, and further refinement of the experimental capabilities should be minimized.

REFERENCES

1. Belz, R. A. and Dougherty, N. S. "In-Line Holography of Reacting Liquid Sprays." Proceedings of the Engineering Applications of Holography. Symposium sponsored by ARPA, 1972.

2. Bowditch, Fred W. "A New Tool for Combustion Research: A Quartz Piston Engine." SAE Transactions, Vol. 69, 1961, pp. 7-23.

3. Rochrock, A. M. and Waldron, D. C. "Effects of Air Fuel Ratio on Fuel Spray and Flame Propagation and Flame Formation in a Compression Ignition Engine." NACA Report No. 545, 1936.

4. Trolinger, J. D., Bentley, H. T., Lennert, A. E. and Sowls, R. E. "Application of Electro-Optical Techniques in Diesel Engine Research." SAE Paper No. 740125, 1974.

5. Scott, W. M. "Looking in on Diesel Combustion." SAE Paper No. 690002, 1969.

6. Scott, W. M. "Color Movies Help Engineers See What Goes On in Diesel Chamber During Combustion Process." SAE Journal, Vol. 78, No. 1, 1970, pp. 52-58.

7. Witzky, J. E. and Clark, John M., Jr. "A Study of the Swirl Stratified Combustion Principle." SAE Paper No. 660092, 1966.

8. Witzky, Julius and Clark, John M., Jr. "Jeep Engine Gets Stratified Charge Combustion." SAE Journal, Vol. 75, No. 4, 1967, pp. 63-67.

9. Streeter, Robert L. and Lichty, Lester C. Internal Combustion Engines. McGraw-Hill, 1933, pp. 428-529 (Fourth Edition).

10. Develis, J. B. and G. O. Reynolds. Theory and Applications of Holography. Addison-Wesley Publishing Co., Reading, Mass., 1967.

11. Thomas, Woodlief, Jr. SPSE Handbook of Photographic Science and Engineering, Sect. 22, "Holography." H. M. Smith, Ed., John Wiley & Sons, New York, 1973.

12. Graube, A. "Advances in Bleaching Methods for Photographically Recorded Holograms." Applied Optics, Vol. 13, No. 12, December 13, 1974, pp. 2942-2946.

13. Straselko, D. I. and Kosnikovshii, V. A. "Holographic Recording of Three-Dimensional Ensembles of Fast-Moving Particles." Optics and Spectroscopy, Vol. 34, No. 2, February 1973.

14. Born, M. and Wolf, E. Principles of Optics. Pergamon Press, Oxford, England, 1965.

15. Matthews, B. J., and Lear, C. N. "Application of Holographic Methods to the Measurement of Flames and Particulate, Vol. 2, Final Report." April 1974, PB-235675/6; TRW-23523-6001-TN-00-Vol. 2, EPA-650/2-74-031-b-Vol. 2.

16. Royer, H. "Particle Velocity Measurements via High-Speed Holography." Proceedings of the 11 Congress in High Speed Photography, September 1974, London, England.

17. Dougherty, N. S. and Belz, R. A. "In-Line Holography of Liquid Propellant Injection During Combustion." Proceedings of the Ninth JANNAF Combustion Meeting, September 11-15, 1972, Monterey, Calif.

18. Trolinger, J. D., et al. "Application of Electro-Optical Techniques in Diesel Engine Research." Proceedings of the SAE Automotive Engineering Congress, Detroit, Mich., February 25 - March 1, 1974.

19. Brayton, D. B. and Goethert, W. H. "A New Dual-Scatter Doppler-Shift Velocity Measuring Technique." Transactions Instrument Society of America, Vol. 10, No. 1, 1971, pp. 40-50.

20. Lennert, A. E., et al. "Summary Report of the Development of a Laser Velocimeter to Be Used in AEDC Wind Tunnels." AEDC-TR-70-101 (AD871321), Also published in AGARD Lecture Series No. 49.

21. Smith, F. H. and Parsons, J. A. "Velocity Measurements in the AEDC Low Speed Wind Tunnel Using a Laser Doppler Velocimeter." AEDC-TR-70-119 (AD708717), July 1970.

22. Cline, V. A., Jr. "Dust Particle Velocity Measurements Using a Laser Velocimeter." AEDC-TR-72-159 (AD752225), December 1972.

23. Cline, V. A., Jr. and Bentley, H. T., III. "Application of a Dual Beam Laser Velocimeter to Turbulent Flow Measurements." AEDC-TR-74-56 (AD785352), September 1974.

24. Stevenson, W. H. "Optical Frequency Shifting by Means of a Rotating Diffraction Grating." Appl. Opt., Vol. 9, No. 3, March 1970, pp. 649-652.

25. Mayo, W. T., Jr. "Spatial Filtering Properties of the Reference Beam in an Optical Heterodyne Receiver." Appl. Opt., Vol. 9, No. 5, May 1970, pp. 1159-1162.

26. Durst, F. "Scattering Phenomena and Their Application in Optical Anemometry." Journal of Applied Mathematics and Physics (ZAMP), Vol. 24, FASC. 4, July 25, 1973, pp. 619-643.

27. Durst, F. and Whitelaw, J. H. "Optimization of Optical Anemometers." Proceedings of the Royal Society A(G-B), London, England, Vol. 324, No. 1557, July 1971, pp. 157-181.

28. Mazumder, M. K. "Laser Doppler Velcoity Measurement without Directional Ambiguity by Using Frequency Shifted Incident Beams." Applied Physics Letters , Vol. 16, No. 11, July 1970, pp. 462-464.

29. Brayton, D. B., Kalb, H. T. and Crosswy, F. L. "Two-Component Dual-Scatter Laser Doppler Velocimeter with Frequency Burst Signal Readout." Applied Optics, Vol. 12, No. 6, June 1973, pp. 1145-1156.

30. Treacy, E. B. "Laser Doppler Ambiguity and Its Effect on Turbulence Measurement." ISA Conference on Aerospace Instrumentation, 1971.

31. Kalb, H. T., Brayton, D. B., and McClure, J. A. "Laser Velocimetry Data Processing." AEDC-TR-73-116 (AD766418), September 1973.

32. Farmér, W. M. "Determination of a Third Orthogonal Velocity Component Using Two Rotationally Displaced Laser Doppler Velocimeter Systems." Applied Optics, Vol. 11, April 1972, pp. 770-774.

33. Farmer, W. M. and Hornkohl, J. O. "Two-Component, Self-Aligning Laser Vector Velocimeter." Applied Optics, Vol. 12, No. 11, November 1973, pp. 2636-2640.

34. Farmer, W. M. "Measurement of Particle Size, Number Density, and Velocity Using a Laser Interferometer." Applied Optics, Vol. 11, No. 11, November 1972, pp. 2603-2612.

35. Roberds, D. W., Farmer, W. M. and Lennert, A. E. "Interferometric Instrumentation for Particle Size Analysis." AEDC-TR-74-82 (AD-A006136), February 1975.

36. Brown, R. F. and Heald, J. H., Jr. "Description and Performance of a Molecular Beam Chamber Used for Cryopumping and Adsorption Pumping Studies." AEDC-TR-66-135 (AD641388), October 1966.

37. Brown, R. F. and Heald, J. H., Jr. "Background Gas Scattering and Skimmer Interaction Studies Using a Cryogencially Pumped Molecular Beam Generator." Rarefied Gas Dynamics Fifth Symposium, C. L. Brundin, Ed., Academic Press, Inc. New York, pp. 1407-1424.

38. Heald, J. H., Jr. "The Performance of a Mass Spectrometric Modulated Beam Detector for Gas Surface Interaction Measurements" Vacuum, Vol. 17, No. 9, September 1967, pp. 511-515.

39. Powell, H. M. and Heald, J. H., Jr. "A System for the Measurement of Velocity Distributions of Molecular Beams." AEDC-TR-68-151 (AD675306), September 1968.

40. Ruby, E. C. "An Experimental Study of the Velocity Distribution and Relative Abundances of Argon Molecular Clusters in the Condensation Region of a Free Jet." University of Tennessee Master's Thesis, December 1969.

41. Ruby, E. C., Brown, R. F., and Busby, M. R. "The Effects of Condensation on the Flow Field Properties in Free Jet Expansion of Argon." AEDC-TR-70-142 (AD710616), August 1970.

42. Bailey, A. B., Busby, M. R., and Dawbarn, R. "Cluster Formation in Free-Jet Expansions." AEDC-TR-72-32 (AD740898), April 1972.

43. Bailey, A. B. "Mass Spectrometric Sampling of the Free-Jet Expansions of Gas Mixtures." AEDC-TR-73-88 (AD761811), June 1973.

44. Bailey, A. B., Busby, M. R., and Dawbarn, R. "Effect of Skimmer Interaction on the Properties of Partially Condensed Molecular Beams." AEDC-TR-72-100 (AD746292), August 1972.

45. Golomb, D., Good, R. E., Bailey, A. B., Busby, M. R., and Dawbarn, R. "Dimers, Clusters and Condensation in Free Jets II." Journal of Chemical Physics, Vol. 57, No. 9, November 1972, pp. 3844-3852.

46. Gerritsen, H. J. and Heller, M. E. "High Resolution Tuned Laser Spectroscope." Applied Optics, Supplement 2, 1965, Chemical Lasers, pp. 73-77.

47. Gerritsen, H. J. "Tuned Laser Spectroscopy of Organic Vapors." Published in the Proceedings of the Physics of Quantum Electronics Conference held in San Juan, Puerto Rico, June 28-30, 1965.

48. McGregor, W. K., Few, J. D., and Litton, C. D. "Resonance Line Absorption Method for Determination of Nitric Oxide Concentration." AEDC-TR-73-182 (AD771642), December 1973.

49. Herzberg, G. Molecular Spectra and Molecular Structure, II Infrared and Raman Spectra of Polyatomic Molecules. D. Van Nostrand Co., Inc., N. J., 1950.

50. Plyler, E. K., Tidwell, E. D., and Blaine, L. R. "Infrared Absorption Spectrum of Methane from 2470 to 3200 cm^{-1}." Journal of Research of the Nat. Bur. of Stand. A Physics and Chem. Vol. 64A, No. 3, May-June 1960, pp. 201-212.

51. Allen, H. C., Jr. and Plyler, E. K. "ν_3 Band of Methane." Journal of Chemical Physics, Vol. 26, No. 4, April 1957, p. 972-973.

52. Mitchell, A. C. G. and Zemansky, M. C. O. Resonance Radiation and Excited Atoms. University Press, Cambridge, England. 1971.

53. Armstrong, R. L. and Welsh, H. L. "Absolute Intensities of the Infrared Fundamentals of Methane." Spectrochim ACTA, Vol. 16, 1960, pp. 840-852.

54. Penner, S. S. Quantitative Molecular Spectroscopy and Gas Emissivities. Addison & Wesley Publ Co., Inc., Reading, Mass., 1959.

55. Gaydon, A. G. The Spectroscopy of Flames. John Wiley & Sons, Inc., 1957.

56. Bell, W. E., and Bloom, A. L. "Zeeman Effect at 3.39 Microns in a Helium-Neon Laser." Applied Optics, Vol. 3, No. 3, March 1964, pp. 413-415.

57. Hum, R. W. "Air Pollution and the Compression Ignition Engine." 12th Symposium International (On Combustion), The Combustion Institute of Pittsburgh, Pa., 1969, pp. 677-687.

58. Lennert, A. E., Crosswy, F. L., and Kalb, H. T. "Application of the Laser Velocimeter for Trailing Vortex Measurements." AEDC-TR-74-26 (AD-A002151), December 1974.

APPENDIX A
THEORETICAL DEVELOPMENT

INTRODUCTION

The theoretical basis necessary for quantitative evaluation of the molecular concentration of absorber gas will be developed in this section. However, evaluation will be deferred to a later section. Three specific regimes will be evaluated with a classification being made on the basis of the dominant broadening mechanism for the absorption line. It will be shown that these regimes for a particular type of environment, i.e., diesel engine operation, can be classified into thermal, pressure, or thermal-pressure dominant regimes. A summary of the salient portions of the theory as it applies to molecular infrared absorption when the laser line is much narrower than the absorption line, i.e., the narrow line technique, will be treated. A detailed description of the theory will be presented sake of completeness.

Absorption Line

When radiation of frequency ν is incident on a gas with an absorption coefficient $k(x, \nu)$ then from Lambert's Law

$$I(\nu) = I_o \exp\left[-\int_{X_1}^{X_2} k(x,\nu)\,dx\right] \qquad \text{(A-1)}$$

where I_o is the incident intensity, $I(\nu)$ is the intensity upon absorption, and x is measured along the optical path through the gas. If the gas properties are uniform along the optical path, this equation reduces to

$$I(\nu) = I_o \exp\left[-k(\nu)x\right] \qquad \text{(A-2)}$$

where x is now the total pathlength through the gas. In general, k, the absorption coefficient, is a function of the state variables, temperature, and pressure (Fig. A-1).

### Einstein Theory of Radiation

To obtain $k(\nu)$, first consider system of isotropic radiation of a frequency between ν and $\nu+d\nu$ with an intensity of $I(\nu)$ and of molecules capable of being elevated from a normal state 1 to an excited state 2 through the absorption of radiation. Following closely the development of Ref. 52, the transition probability coefficients are defined as follows:

149

$B_{1 \to 2}$ $I(\nu)$ is the probability per second that a molecule in state 1, subject to radiation which has the frequency range between ν and $\nu + d\nu$ and intensity $I(\nu)$, will absorb a quantum $h\nu$ and pass to state 2.

$A_{2 \to 1}$ is the probability per second that a molecule in state 2 will spontaneously (on its own) emit a quantum $h\nu$ and pass to state 1.

$B_{2 \to 1}$ $I(\nu)$ is the probability per second that a molecule in state 2 will undergo a transition to state 1 when exposed to radiation of frequency between ν and $\nu + d\nu$ of intensity $I(\nu)$ and simultaneously emitting a quantum in the same direction as the stimulating quantum.

a. I versus ν

b. k(ν) versus ν
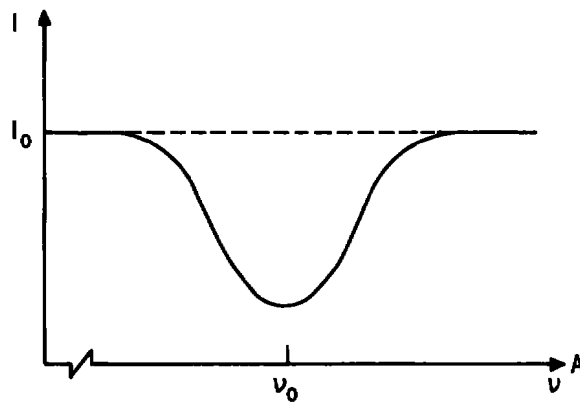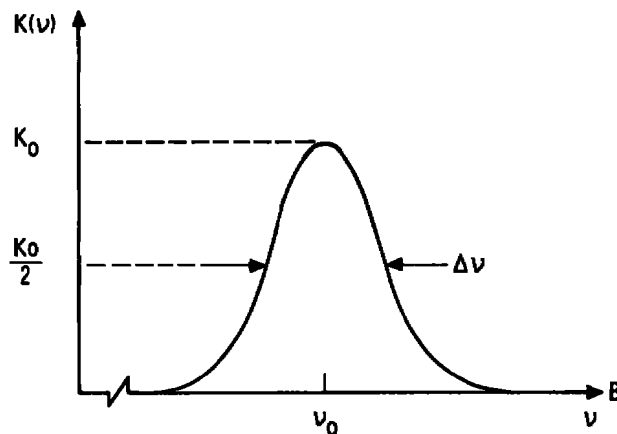
Figure A-1. Schematic of absorption profile.

The Einstein relationships between the transition coefficients are

$$\frac{A_{2\to 1}}{B_{1\to 2}} = \frac{2h\nu^3}{c^2} \frac{g_1}{g_2} \qquad (A\text{-}3)$$

$$\frac{B_{2\to 1}}{B_{1\to 2}} = \frac{g_1}{g_2} \qquad (A\text{-}4)$$

$$A_{2\to 1} = \frac{1}{\tau} \qquad (A\text{-}5)$$

where g_1 and g_2 are the statistical weights of the normal and excited states, respectively, and τ is the radiative lifetime of the excited state (having a value of 0.037 sec for the ν_3 band of methane (Ref. 53).

Now consider the radiation to be passing through an isotropic gas of pathlength dx. Suppose that there are N_1 normal-state molecules per unit volume of which δN_1 are capable of absorbing within the frequency range ν to $\nu+d\nu$. Also, there exists N_2 excited-state atoms of which δN_2 are capable of emitting in the same frequency range. The net decrease in beam intensity is given by

$$d\left[h(\nu)\,d\nu\right] = \partial N_2\, dxh\nu\, B_{2\to 1} \frac{I(\nu)}{4\pi} - \partial N_1\, dxh\nu\, B_{1\to 2} \frac{I(\nu)}{4\pi} \qquad (A\text{-}6)$$

Upon simplification, Eq. (A-6) becomes

$$\frac{-dI(\nu)}{dx} \frac{\partial \nu}{I(\nu)} = \frac{h\nu}{4\pi}\left(B_{1\to 2}\delta N_1 - B_{2\to 1}\delta N_2\right) \qquad (A\text{-}7)$$

Upon differentiation of Eq. (A-2) and combining it with Eq. (A-7), the following definition for $k(\nu)$ is obtained:

$$k(\nu)\,d\nu = \frac{h\nu}{4\pi}\left(B_{1\to 2}dN_1 - B_{2\to 1}dN_2\right) \qquad (A\text{-}8)$$

Now integrating over the whole absorption line and neglecting slight variations in ν throughout the line

$$\int_0^\infty k(\nu)\,d\nu = \frac{h\nu_0}{4\pi}\left(B_{1\to 2}N_1 - B_{2\to 1}N_2\right) \qquad (A\text{-}9)$$

151

Upon substitution for $B_{1 \to 2}$ and $B_{2 \to 1}$ from Eqs. (A-3) through (A-5), Eq. (A-9) can be written as

$$S \equiv \int_0^\infty k(\nu)d\nu = \frac{c^2}{8\pi\nu_0^2} \; r \; \frac{g_2}{g_1} N_1 \left(1 - \frac{g_1}{g_2}\frac{N_2}{N_1}\right) \qquad (A\text{-}10)$$

This equation is of fundamental importance as its validity is independent of the physical processes responsible for the formation of the absorption line. In cases where the temperature is low and/or the energy difference between the excited and normal state is large then the term $(g_1/g_2)(N_2/N_1)$ becomes small and can be neglected. However, conditions found in diesel engines do not permit such as simplifying conclusion. Temperatures are too high to neglect the upper state emission as an appreciable number of molecules occupy this state.

BROADENING PARAMETERS

In internal combustion engine operation very high temperatures and pressures are encountered. It is at exactly this time in the combustion cycle that information on reactions and species concentrations is desired. The net effect of these high pressures and temperatures is to broaden the absorption line. In general, there are five such processes which can be described as follows:

1. Natural broadening attributable to the finite lifetime of the excited state.

2. Doppler broadening attributable to the thermal kinetic energy of the molecules.

3. Lorentz broadening attributable to collisions with foreign gases.

4. Holtsmark or self-broadening attributable to collisions of like-absorbing molecules.

5. Start broadening attributable to collisions with the electrons and ions.

Natural broadening contributes very little at the pressures and temperatures normally encountered and therefore can be neglected. Holtsmark and Lorentz broadening can be considered as part of pressure broadening as the formalism is the same for both cases. Holtsmark or self-broadening would be negligible as most gases of present interest constitute only a small fraction of the total pressure. Finally, Stark broadening can be neglected as the degree of ionization is very low. Therefore, the broadening regimes to be considered are pure Doppler, pure Lorentz broadening, and the special case when both mechanisms must be considered when they have comparable effects.

Doppler Broadening

First the case where only thermal motion of the molecules is important will be considered. The absorption coefficient for the gas can be given by

$$k_D(\nu) = k_o \exp - \left[\frac{2(\nu - \nu_o)}{\Delta\nu_D} (\ln 2)^{1/2} \right]^2 \qquad (A-11)$$

where ν_o is the center frequency of the absorption line, k_o is the maximum value of the absorption coefficient at ν_o, and $\Delta\nu_D$ is the full width at half maximum of the Doppler profile and is defined as follows:

$$\Delta\nu_D = \frac{2(2R \ln 2)^{1/2}}{c} \nu_o \left(\frac{T}{M} \right)^{1/2} \qquad (A-12)$$

where R is the universal gas constant (8.3143×10^7 ergs/gm-mole °K), c is the speed of light, and M is the molecular weight of the broadened gas. It can be seen that the amount of broadening is proportional to $T^{1/2}$ and inversely proportional to the square root of the molecular weight. Therefore, this broadening mechanism becomes less important for the heavier hydrocarbons and lower temperatures as is shown in Fig. A-2.

Integrating Eq. (A-11) yields S, the integrated line strength of the absorption profile:

$$S = \int_o^\infty k(\nu) d\nu = \frac{1}{2} \left(\frac{\pi}{\ln 2} \right)^{1/2} k_o \Delta\nu_D \qquad (A-13)$$

Lorentz Broadening

When collision broadening is predominant because of high pressures, the absorption coefficient (Ref. 54) is given by

$$k_L(\nu) = \frac{S}{2\pi} \frac{\Delta\nu L}{(\nu - \nu_o)^2 - \left(\frac{\Delta\nu L}{2} \right)^2} \qquad (A-14)$$

S is defined as before and $\Delta\nu_L$ is the collisional fullwidth at half maximum and is defined as (see Fig. A-3)

$$\Delta\nu_L = \frac{1}{\pi} \sum_{j=1}^N Z_{1j} = \frac{3.326 \times 10^{20}}{\pi} \sum_{j=1}^N \sigma_1 \sigma_j \left(\frac{1}{M_1} + \frac{1}{M_j} \right)^{1/2} \frac{P_j}{\sqrt{T}} \qquad (A-15)$$

where Z_{1j} is the relative collision frequency between the absorber and foreign gas molecule, x is the optical collison diameter in centimeters, p_j is the partial pressure of the broadening
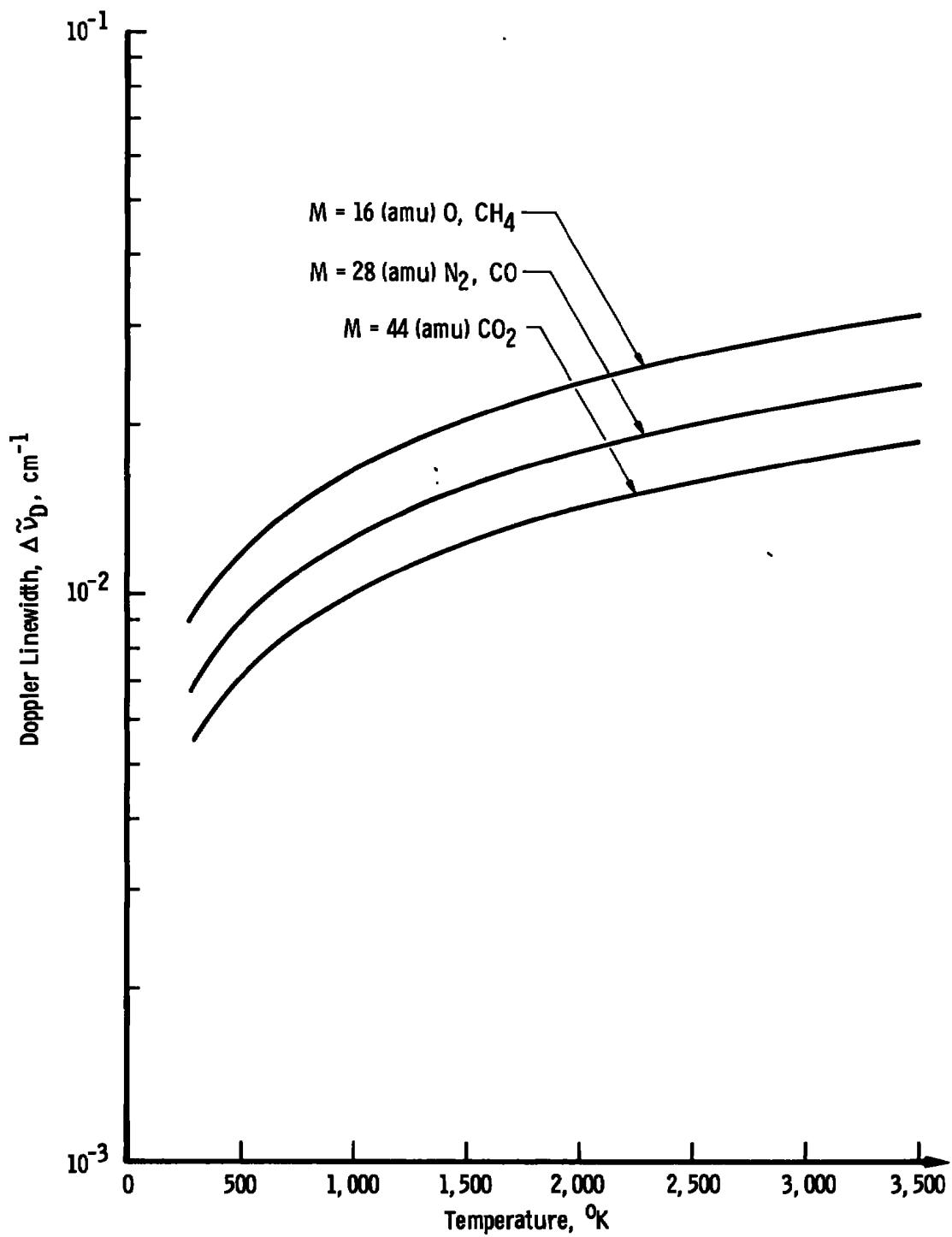
Figure A-2. Doppler linewidths versus temperature for various
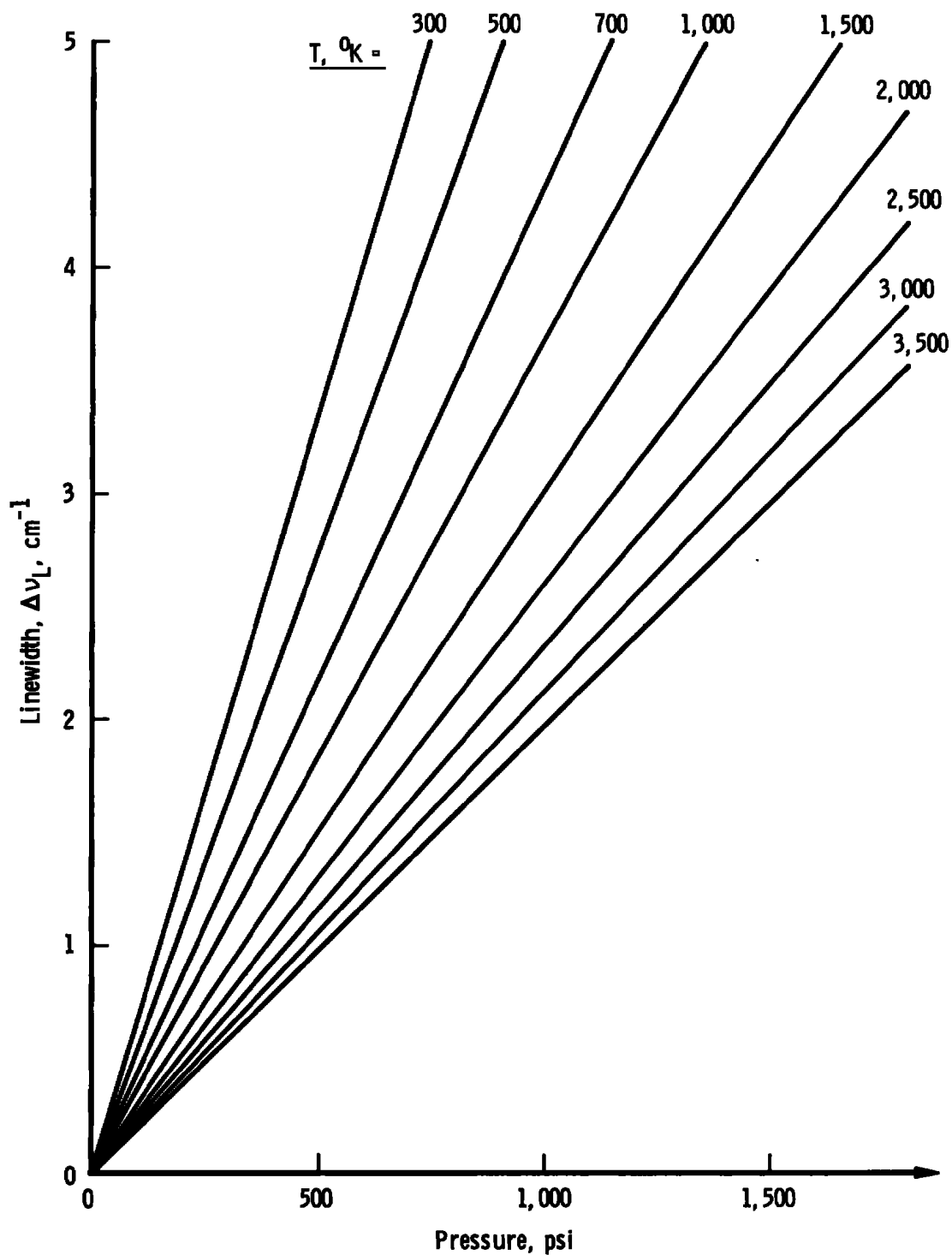molecular weights.

Figure A-3. Lorentz linewidth versus pressure for various temperatures for CH_4.

gas in dynes/cm^2, T is the temperature in °K, and M the gram-molecular weight. As will be shown later, the terms inside the sum can be approximated by a single value and the partial pressures can be replaced by the total pressure.

Combined Doppler and Lorentz Broadening

In those pressure and temperature regimes where the Doppler and pressure-broadening effects are comparable, both effects must be taken into account. Because of the independent nature of these broadening mechanisms, it is necessary to convolve the two profiles in order to obtain a proper representation of k(ν). This class of profiles are generally called Voigt profiles. The convolution is given by

$$k_{D-i}(\nu) = k_D(\nu) * k_L(\nu) = \int_{\infty}^{4\infty} k_D(u) g(\nu - u) du \qquad (A-16)$$

Upon substitution of Eq. (A-11) and Eq. (A-14), Eq. (A-16) becomes

$$k_{o-i}(\nu) = \frac{2 k_o}{\pi(\Delta\nu_L + \Delta\nu_N)} \int_{-\infty}^{\infty} \frac{\exp\left[-\left(\frac{2u}{\Delta\nu_o}\sqrt{\ln 2}\right)^2\right]}{1 + \left[\frac{2}{\Delta\nu_L + \Delta\nu_N}(\nu - \nu_o - u)\right]^2} du \qquad (A-17)$$

where $\Delta\nu_N$ is the natural broadening halfwidth denoted as

$$\Delta\nu_N = \tfrac{1}{2}\pi\tau$$

The natural broadening profile has the same form as the Lorentz broadening profile, and it can be shown that the halfwidths are additive and were included in Eq. (A-16).

Upon application of Parseval's theorem and evaluation at line center the equation reduces to

$$k_o = \frac{2 S}{\Delta\nu_D}\left(\frac{\ln 2}{\pi}\right)^{1/2} \exp(a^2) \operatorname{erfc}(a) \qquad (A-18)$$

where

$$a = \left(\frac{\Delta\nu_N + \Delta\nu_L}{\Delta\nu_D}\right)(\ln 2)^{1/2} \qquad (A-19)$$

S the line strength in Eq. (A-10) is defined as before, and erfc is the complementary error function

$$\frac{2}{\sqrt{\pi}} \int_{x}^{\infty} e^{-u^2} \, du$$

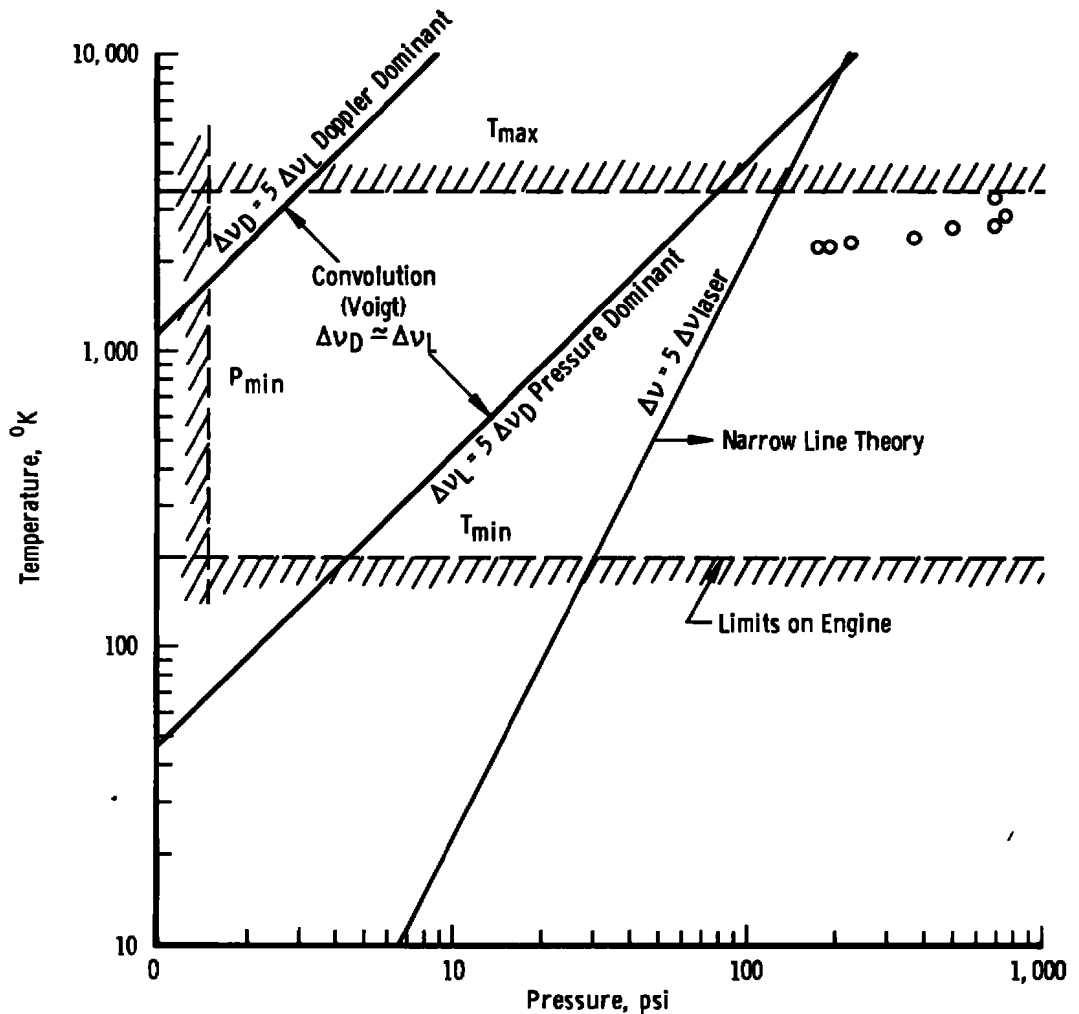The regimes where each of the broadening mechanisms apply are shown in Fig. A-4.

Figure A-4. Criteria for broadening mechanisms.

SPECIES CONCENTRATION

Depending upon the pressure-temperature regime, either Eqs. (A-13), (A-14), or (A-15) will apply. In each of these equations, the line strength, S, appears. Equation (A-10) relates this line strength to N_1 and N_2. The excited-state number density can be described as (Ref. 55)

$$N_2 = N_1 \frac{g_2}{g_1} \exp\left[-\frac{h\nu_o}{kT}\right] \qquad (A-20)$$

The number of molecules, N_1, in a vibrational-electronic ground state with rotational quantum number J for a condition of rotational equilibrium is given by

$$N_1 = N_o \left(\frac{(2J+1)^2}{Q_r Q_v}\right) \exp\left[\frac{-E_1}{kT}\right] \qquad (A-21)$$

where E_1 is the energy level of the ith rotation state and is given by Eq. (A-5), and Q_v is the vibrational partition function (Ref. 49) is shown in Fig. A-5.

$$Q_u = \pi \left[1 - \exp\left(-\frac{\nu_i h}{kT}\right)\right]^{-d_i} \qquad (A-22)$$

where ν_i is the frequency of the band centers and d_i is the degree of degeneracy of the vibrational frequency ν_i. The rotational partition function can be defined as (Fig. A-6)

$$Q_r = \sqrt{\frac{\pi}{B^3}\left(\frac{kT}{hc}\right)^3} = 1.02718 \left(\frac{T}{B}\right)^{3/2} \qquad (A-23)$$

which corresponds to the classical value and is valid where $T/B \gg 1$.

Upon substitution of the above relations into Eq. (A-13) for the Doppler-broadened absorption coefficient

$$N_o = \frac{4\pi \nu_o^2 \Delta\nu_o Tk_o\left(\frac{\pi}{\ell n\, 2}\right)^{1/2}}{\left[1 - \exp\left(-\frac{h\nu_o}{kT}\right)\right]c^2} \frac{g_1}{g_2} \exp\left(\frac{E_1}{kT}\right)\frac{Q_r Q_v}{(2J+1)^2} \qquad (A-24)$$
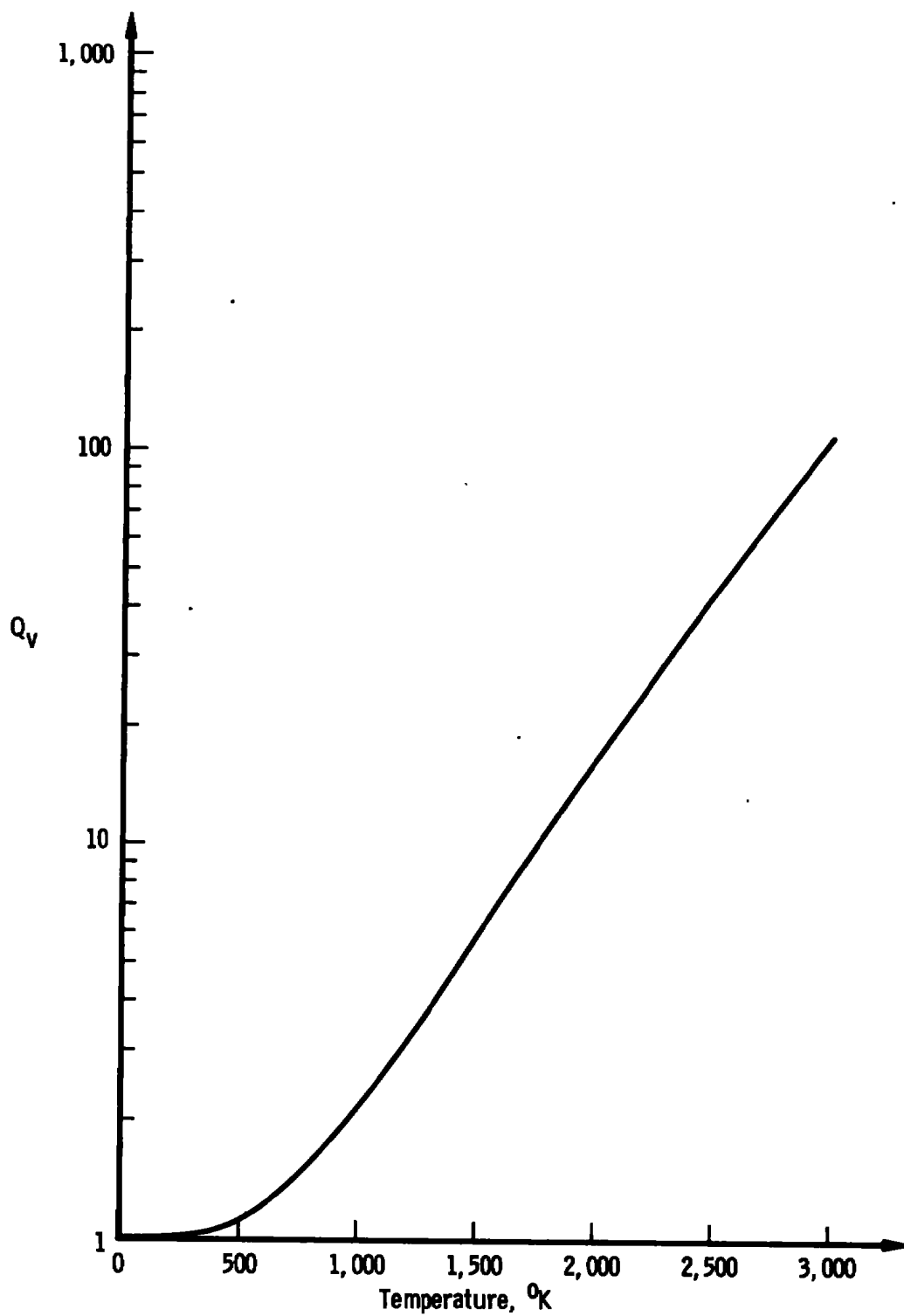
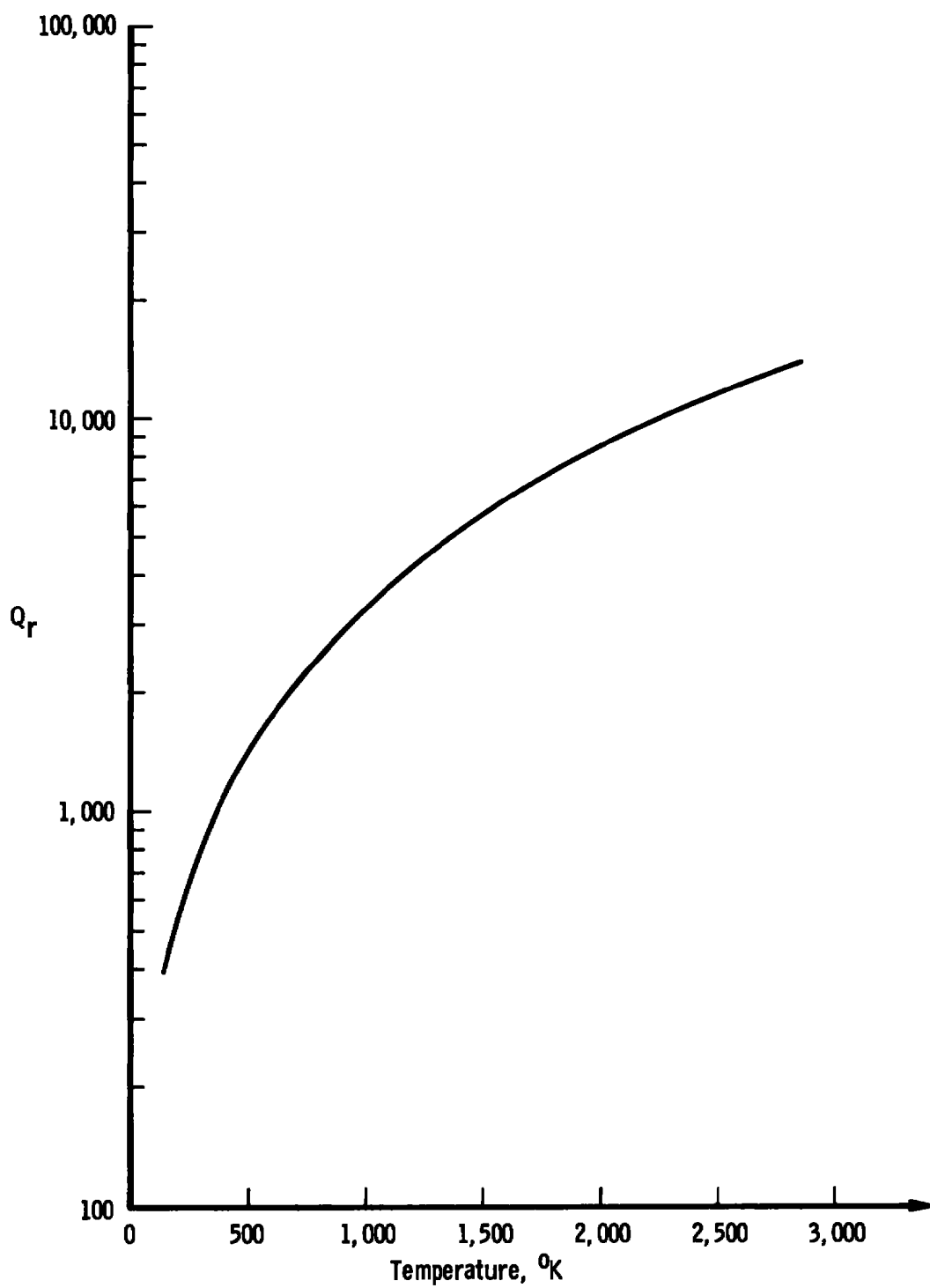Figure A-5. Q_V versus temperature for CH_4.

Figure A-6. Q_r versus temperature for CH_4.

Substituting Eq. (A-24) into Eq. (A-14), for the Lorentz-broadened line, one obtains

$$N_o = \frac{4\pi^2 \nu_o^2 \Delta\nu_L \, rk_o}{\left[1 - \exp\left(-\frac{h\nu_o}{kT}\right)\right] c^2} \quad \frac{g_1}{g_2} \frac{Q_r Q_v}{(2J+1)^2} \quad \exp\left(\frac{E_1}{kT}\right) \tag{A-25}$$

And upon substitution into the equation for the combined Doppler-Lorentz-broadened line, Eq. (A-18),

$$N_o = \frac{4\pi\nu_o^2 \Delta\nu_o \, rk_o \left(\frac{\pi}{\ell n \, 2}\right)^{1/2}}{\left[\exp(a^2) + \mathrm{erfc}(a)\right]\left[1 - \exp\left(-\frac{h\nu_o}{kT}\right)\right] c^2} \quad \frac{g_1}{g_2} \frac{Q_r Q_v}{(2J+1)^2} \quad \exp\left(\frac{E_1}{kT}\right) \tag{A-26}$$

Although the equations look somewhat formidable, all of the parameters for methane are published or can be measured.

161